

**Subsystem Integration for Efficient Power Flow
In 21st Century Airlifters**

Final Report

For the period
April, 1997 to May, 1999

Sponsored By

Air Force Office of Scientific Research
New World Vistas Program
Subsystem Integration and Power

AFOSR Grant Number: F49620-97-1-0254

Dr. Spencer Wu, Program Manager
AFOSR/NA
801 N. Randolph St., Rm 732
Arlington, VA 22203-1977

September 1, 1999

Prepared by

Dr. Douglas K. Lindner, Dr. Dusan Boroyevich
Mr. Konstantin Louganski, Mr. Sriram Chandrasekaran

Center for Power Electronics Systems
The Bradley Department of Electrical and Computer Engineering
657, Whittemore Hall
Blacksburg, VA 24061 - 0111

Mr. George Korba, Ms Catherine Frederick, Mr. Gordon Lu
Lockheed Martin Control Systems
600 Main Street
Johnson City, NY 13790-1888

19990928 080

Executive Summary

Introduction

In this project we are concerned with the modeling, simulation and dynamic stability of next generation DC power distribution systems for 21st century airlifters. These new power distribution systems are novel in that they allow for two way power flow between the generator, power distribution system, and loads including the actuators, avionics, and the environmental control system. This two way power flow implies that all of these subsystems dynamically interact with each other. In fact these subsystems are tightly coupled and they exhibit strongly nonlinear behavior. The thrust of this project was to model and simulate this nonlinear behavior and develop a methodology to evaluate the stability of this nonlinear interaction. The results of this investigation can be broadly classified into four categories: 1) a typical power distribution system architecture was identified along with the generation units and the loads, 2) a simulation block library was developed for this prototypical power distribution system based on a multi-level modeling concept, 3) the destabilizing effects of regenerative energy on the power bus was identified as a focus problem for further study, and 4) a methodology for investigating the nonlinear stability of subsystem interaction was developed.

Baseline System Architecture

A baseline DC power distribution system architecture was identified in conjunction with Lockheed Martin Control Systems. This system was based on the power distribution system being developed under the MADMEL program, but scaled for a typical airlifter. Next generation electromechanical and electrohydraulic actuators, developed for a More Electric Aircraft (MEA), were included as the loads of the power distribution system. Other loads included in this study are so-called smart actuators that are being developed for mitigating tail buffet on twin tail aircraft. Finally, switched reluctance starter/generators as well as conventional generators were included as power sources. This baseline architecture is described in Chapter 2.

Simulation Block Library

In order to investigate the subsystem interaction problems in the baseline power distribution system, an extensive simulation block library was developed in Simulink. The basic idea was to develop a block for every component of the baseline system and standard interconnection links. With this block library subsystems in the power distribution system can be easily synthesized from the basic building blocks. This block library is described in detail in the Addendum to the final report.

In addition, a multilevel modeling concept was incorporated into the block library. The basic idea is that each component should be represented by three models of varying complexity: a detailed (switching) model, an "average" (nonlinear) model, and a linear model. Using these multilevel models, simulations of varying complexity can be built up as is needed in a particular study. Each component in Chapter 3 is described at these three levels.

The components in the block library include, passive elements, linear networks, diode/transistor switches, switching power converters of several types, electric motors, electromechanical actuators (EMA), electrohydraulic actuators (EHA), switched reluctance generators, and a DC power bus. The models for all of these components are described in Chapter 3.

Regenerative Energy

One type of subsystem interaction that is unique to DC power distribution systems is two way power flow. All power systems are designed to deliver power to the load. The power converters that control the flow of power on the DC bus support reverse power flow as well. This bidirectional power flow dynamically couples the loads with the power bus. When a particular actuator is delivering power to the bus (regenerating power), the bus voltage can fluctuate widely. This fluctuation may even be so violent so as to cause the bus to violate its mil specs (MIL SPEC 704E). Lockheed Martin has identified this phenomenon of regenerative energy as a potential problem in the development of the DC power distribution system for the MEA. The control of this regenerative energy has now become a major focus of the follow-on effort to this project.

The effects of regenerative energy on the power distribution system were investigated using the simulation block library. The voltage spiking on the bus due to the regenerative energy from the actuators can be traced to various capacitors on the bus. The effect of these capacitors on the bus voltage fluctuations was investigated in anticipation to control strategies to control the effects of regenerative energy. The results of these investigations can be found in Chapter 4.

Piezoelectric actuators offer a new kind of solid state actuator for controlling vibrations on an aircraft. These actuators act as transducers exchanging electrical and mechanical energy. When these actuators are employed for vibration suppression, and a switching amplifier is used to drive them, the amplifier returns a significant amount of energy back to the bus. The effects of regenerative energy from piezoelectric actuators were investigated [4-5], and several methods for mitigating voltage fluctuations on the power bus are proposed in Chapter 4.

Nonlinear Stability Methodology

The bidirectional power flow in a DC power distribution system introduces strong dynamic interaction between subsystems. When two subsystems strongly interact, stability is always concern. Since the subsystems in the baseline power distribution system are governed by nonlinear differential equations, the global stability of the entire system is in question.

It is of interest to clearly understand the effects of energy regeneration on the stability and the performance of the power distribution system. Nonlinear stability analysis was performed on an interconnected system consisting of an input filter and a regulated power converter and it was found that the reversal of power flow does not result in loss of stability. However, this analysis did not study the effect on the performance characteristics of the DC bus due to the regeneration of energy.

In addition, we have investigated the stability of these interacting subsystems using methodologies based on bifurcation analysis. These methods yield a global understanding of the behavior of the system, unlike stability results based on linear (or small signal) models. Hence, the estimates of the stability region may be less conservative than those estimates based on linear analysis. The interaction between an input filter and a regulated DC-DC buck converter was studied using bifurcation analysis. This same analysis is applied to the interaction at the DC bus between the bus regulator and a load converter in the presence of a changing load impedance. It is found that the results of bifurcation analysis yield a significantly better understanding than the linear analysis [1]. These results are reported in Chapter 5.

Publications

This research project has produced the following publications.

1. Sriram Chandrasekaran, Douglas K. Lindner, Konstantin Louganski and, Dushan Boroyevich, "Subsystem Interaction Analysis in Power Distribution Systems of Next Generation Airlifters", To be presented at the European Power Electronics Conference, EPE '99, Lausanne, Switzerland, September 1999.
2. Sriram Chandrasekaran, Dusan Borojevic, Douglas. K. Lindner, "Input Filter Interaction in Three phase AC-DC Converters", Proceedings of the Power Electronics Specialists Conference, PESC '99, Charleston, South Carolina, June 1999, pp. 987-992.
3. Sriram Chandrasekaran, Douglas. K. Lindner, Dushan Boroyevich, "Analysis of Subsystem Integration in Aircraft Power Distribution Systems", Proceedings of the International Symposium of Circuits and Systems, ISCAS '99, Orlando, Florida, May 1999, vol. 5, pp. 82-85.
4. Douglas K. Lindner, Sriram Chandrasekaran, "Control of Regenerative Power from Piezoelectric Actuators", Proceedings of the AIAA Adaptive Structures Forum in the 40th SDM Conference, St. Louis, Missouri, April 1999.
5. Douglas K. Lindner, Sriram Chandrasekaran, "Power System Design Issues for Smart Materials", Proceedings of the 1999 SPIE conference, Newport Beach, California, March, 1999.

TABLE OF CONTENTS

EXECUTIVE SUMMARY	1
1 INTRODUCTION	6
2 BASELINE SYSTEM ARCHITECTURE.....	10
2.1 Introduction.....	10
2.2 Power Distribution System.....	10
2.2.1 EHAs and EMAs.....	13
2.2.2 Smart Actuators	15
2.3 Generation Units	16
2.4 Regenerative Energy.....	17
3 SIMULATION BLOCK LIBRARY	19
3.1 Introduction.....	19
3.2 Multi-level Modeling of Power Distribution System Components	19
3.3 Power Distribution System Analysis and Simulation Tools	21
3.4 Modeling of Subsystem Elements	24
3.5 Modeling of DC-DC Switching Power Converters.....	29
3.5.1 DC-DC Buck Converter Modeling	29
3.5.2 DC-DC Boost Converter Modeling	30
3.6 Modeling of Three Phase Subsystems	32
3.6.1 Three Phase Subsystem Modeling Approach	32
3.6.2 Three Phase Synchronous Generator Modeling.....	34
3.6.3 Three Phase Boost Rectifier Modeling	37
3.7 Switched Reluctance Generator Modeling	41
3.8 Modeling of Flight Actuators	45
3.8.1 Electromechanical Actuator Modeling	45
3.8.2 Electrohydrostatic Actuator Modeling.....	48
3.9 Smart Actuator Modeling	50
3.9.1 Introduction.....	50
3.9.2 Modeling.....	50
3.9.3 Drive Amplifier.....	54
3.9.4 Controller Design.....	55
3.9.5 Interaction with DC Bus	57
3.10 DC Power Distribution Bus Modeling	58
3.11 Conclusions	59
4 REGENERATIVE POWER.....	60
4.1 Introduction.....	60
4.2 System Configuration	61
4.3 Overall System Performance Characteristics and Methodology	64
4.4 Effect of the Input Filter Capacitor.....	67
4.5 Effect of the Boost Rectifier Capacitor	75
4.6 Control of Bidirectional Power from Smart Actuators	81
4.6.1 Variation of System Parameters.....	81
4.6.2 Bus Conditioners.....	83
4.7 Conclusions.....	85

5	NONLINEAR ANALYSIS METHODOLOGY	86
5.1	Introduction.....	86
5.2	Impedance Ratio Criterion	87
5.3	Input Filter Interaction in Three-Phase AC-DC Converters.....	88
5.4	Stability Analysis of Sample System.....	100
5.5	Sample Power Distribution System	100
5.6	Simulation Results.....	101
5.7	Nonlinear Analysis	104
5.8	Stability under Bidirectional Power Flow.....	104
5.9	Bifurcation Methods	109
5.9.1	Input Filter Interaction	109
5.9.2	Interaction at the DC Bus.....	118
5.10	Conclusions	122
6	CONCLUSIONS	123
7	REFERENCES	124
8	APPENDICES	126

1 Introduction

The "More Electric Aircraft Initiative" has become a leading design concept for future aircraft. It assumes using electrical energy instead of hydraulic, pneumatic, and mechanical means to power virtually all aircraft subsystems including flight control actuation, environmental control system, and utility functions. The concept offers advantages of reduced overall aircraft weight, reduced need for ground support equipment and maintenance personnel, increased reliability, and reduced susceptibility to battle damage in military applications [1-7]. As the result of this initiative many components and subsystems of the next generation aircraft are being redesigned based on recent technological advances.

One of the aircraft's subsystems most strongly affected by the MEA is the power distribution system. In fact, a new type of power distribution system is being proposed for next generation aircraft based on a DC bus. (A prototype of a DC power distribution system has been built under the MADMEL program.) In a DC power distribution system the power is distributed at zero (0) frequency, hence the name. The power is regulated on the bus by switching power converters, which act as an interface between the generator and the bus as well as the bus and the loads. These switching power converters replace the transformers in a conventional AC power distribution system. This type of power distribution system has many advantages over conventional AC power distribution systems including ?

The presence of switching power converters in a DC power distribution system has a significant impact on the dynamics of the power bus, the dynamics of the loads, and the dynamics of the subsystem interaction between the bus and the loads. The tight coupling between the power distribution system, the loads, and the generation sources can be explained by the fact that the switching power converters support bidirectional power flow. (Bidirectional power flow is closely related to their high efficiencies.) Normally, the power flows from the sources (generators) to the loads (actuators, ECS, battery, utility loads). However, in certain modes of operation, certain loads can work in regenerative mode, thus supplying electric power to the DC distribution bus. For example, a flight control actuator works in regenerative mode when it has to slow down a moving flight control surface, or when the surface is being moved by the air flow. Another example is using the battery as an energy source and the APU starter/generator as a motor to start the APU engine. Hence, all electrically powered subsystems become parts of an electric power distribution system, which unites all electrical sources and loads of an aircraft by means of a power distribution bus.

We call the energy that is delivered from the load to the bus regenerative energy. The regenerative power has potential advantages since the power regenerated by one subsystem can potentially be used to power the other loads or it can be stored in the power distribution system for future use. However, it also has potential problems since unused regenerative power may create voltage spikes and swings on the DC bus well beyond the limits set by the standard (MIL-STD-704E [8]). These voltage spikes may affect normal

operation or even damage equipment connected to the bus. The voltage spikes result from the inability of the power distribution system to absorb the regenerative energy or deliver it to another load. There is experimental evidence from Lockheed Martin that the regenerative energy from their electromechanical actuators does cause voltage transients large enough to be a concern. At the present time acceptable methods for controlling voltage transients on the bus do not exist.

A second concern with a DC power distribution system is the overall stability of this system. Again, these stability issues can be traced to the bidirectional power flow. Bidirectional power flow essentially means the subsystems are tightly coupled and hence, stability is an issue. The stability problem is further compounded here because the components are highly nonlinear. Thus, the standard linear analysis methods yield only local estimate of the stability region. Because of the large transients generated by the regenerative energy, it is desirable to have an estimate of the global stability characteristics of the power distribution system.

The impedance ratio criterion has been traditionally used to study the stability of two interconnected subsystems. This criterion was primarily used to study interaction between an input filter and a regulated power converter, and only guarantees stability in the neighborhood of an equilibrium point. We have investigated the stability of these interacting nonlinear subsystems using methodologies based on bifurcation analysis [?]. These methods yield a global understanding of the behavior of the system yielding estimates of the stability region that may be less conservative than those estimates based on linear analysis. The goal of this project is to understand the subsystem interaction introduced by the next generation DC power distribution system. To focus the effort, the research is directed towards understanding the effects of regenerative energy on the stability and performance of the power bus. The intention is to develop a nonlinear stability analysis methodology to assess the stability of the coupled system and to develop tools for optimization and control of the regenerative energy.

The thrust of this project was to model and simulate this nonlinear behavior and develop a methodology to evaluate the stability of this nonlinear interaction. The results of this investigation can be broadly classified into four categories: 1) a typical power distribution system architecture was identified along with the generation units and the loads, 2) a simulation block library was developed for this prototypical power distribution system based on a multi-level modeling concept, 3) the destabilizing effects of regenerative energy on the power bus was identified as a focus problem for further study, and 4) a methodology for investigating the nonlinear stability of subsystem interaction was developed.

A baseline DC power distribution system architecture was identified in conjunction with Lockheed Martin Control Systems. This system was based on the power distribution system being developed under the MADMEL program, but scaled for a typical airlifter. The main components of this baseline system include a 270 V DC power bus with a 270 V battery, two engine starter/generators (500 kW each) with split/parallel bus, APU channel starter/generator (200 kW), and smart load management. Next generation

electromechanical and electrohydraulic actuators, developed under the MEA initiative, were included as the loads of the power distribution system along with negative impedance avionics loads and environmental control systems. Other loads included in this study are so-called smart actuators that are being developed for mitigating tail buffet on twin tail aircraft. Finally, switched reluctance starter/generators as well as conventional generators were included as power sources. This baseline architecture is described in Chapter 2.

In order to investigate the subsystem interaction problems in the baseline power distribution system, an extensive simulation block library was developed in Simulink. The basic idea was to develop a block for every component of the baseline system and standard interconnection links. With this block library, subsystems in the power distribution system can be easily synthesized from the basic building blocks. This block library is described in detail in the Addendum to the final report.

The components in the block library include, passive elements, linear networks, diode/transistor switches, switching power converters of several types, electric motors, and a DC power bus. This block library also contains models of electromechanical actuators (EMA), electrohydraulic actuators (EHA) which were provided by Lockheed Martin. The models for the power generation units consist of conventional three phase synchronous generators and the next generation switched reluctance integral starter/generators. The model of a switched reluctance machine is generally very complicated because it is based on a detailed analysis of the physics. The model of the switched reluctance starter/generator included in the block library is derived from a simpler "average" model of this machine developed in [21].

The power distribution system is too large and complex that simulation using detailed models of each component becomes computationally very expensive. To address this complexity issue, the block library is built using the concept of multi-level models. The basic idea is that each component should be represented by three models of varying complexity: a detailed (switching) model, an "average" (nonlinear) model, and a linear model. Using these multilevel models, simulations of varying complexity can be built up as is needed in a particular study. Each component in the block library is described at these three levels.

The effects of regenerative energy on the power distribution system were investigated using the simulation block library. The voltage spiking on the bus due to the regenerative energy from the actuators can be traced to various capacitors on the bus. The effect of these capacitors on the bus voltage fluctuations was investigated in anticipation to control strategies to control the effects of regenerative energy.

Piezoelectric actuators offer a new kind of solid state actuator for controlling vibrations on an aircraft. These actuators act as transducers exchanging electrical and mechanical energy. When these actuators are employed for vibration suppression, and a switching amplifier is used to drive them, the amplifier returns a significant amount of energy back to the bus. The effects of regenerative energy from piezoelectric

actuators were investigated [45,46], and several methods for mitigating voltage fluctuations on the power bus are proposed.

It is of interest to clearly understand the effects of energy regeneration on the stability and the performance of the power distribution system. The commonly used impedance ratio criterion is only applicable to DC-DC converter systems, which are essentially SISO systems. A detailed analysis was performed to extend this criterion to three phase AC-DC converters. Specifically, conditions for stability and minimal interaction between a three phase input filter and a regulated three phase AC-DC rectifier were obtained [43]. The criterion was used to analyze stability in a sample power distribution system consisting of an electromechanical actuator drive for the spoiler surface of the aircraft. Simulation examples are shown that demonstrate the inability of the criterion to predict unstable behavior of the system when excited by large signal disturbances [42]. These examples motivate the nonlinear analysis methods.

Nonlinear stability analysis was performed on an interconnected system consisting of an input filter and a regulated power converter and it was found that the reversal of power flow does not result in loss of stability. However, this analysis did not study the effect of the performance characteristics of the DC bus due to the regeneration of energy.

We have investigated the stability of these interacting subsystems using methodologies based on bifurcation analysis. These methods yield a global understanding of the behavior of the system, unlike stability results based on linear (or small signal) models. Hence, the estimates of the stability region may be less conservative than those estimates based on linear analysis. The interaction between an input filter and a regulated DC-DC buck converter was studied using bifurcation analysis. This same analysis is applied to the interaction at the DC bus between the bus regulator and a load converter in the presence of a changing load impedance. It is found that the results of bifurcation analysis yield a significantly better understanding than the linear analysis [44].

In Chapter 2 the baseline power distribution system architecture is described in detail. In Chapter 3 the models for the block simulation library are developed. The block simulation library itself is described in an addendum to this report. In Chapter 4 several simulations are undertaken to demonstrate the effects of the regenerative energy. In Chapter 5 the nonlinear stability analysis is reported. Chapter 6 contains the conclusions.

2 Baseline System Architecture

2.1 Introduction

The baseline system being considered in this study consists of the power distribution system, electromechanical actuators (EMAs), electrohydraulic actuators (EHAs), and smart actuators. The baseline power distribution system is based on a proposed next generation 270 DC bus. The EMA and EHA actuators have been specifically developed for use with this type of DC power distribution system under the More Electric Aircraft initiative. The power distribution system, EMA's, and the EHA's have been sized for an airlifter. This study also includes smart actuators which consist of piezoelectric patches embedded or attached to the aircraft structure. Due to the innovative nature of these actuators, the models in this report are based on wind tunnel experiments (although full-scale ground tests have been conducted with these actuators).

One of the distinguishing characteristics of the proposed dc power distribution bus is that power can readily flow in both directions. Often the regenerative energy, power flowing from the loads into the bus, is considered to have a negative effect on the power bus because it may cause unacceptably large voltage swings as the examples below show. However, there is also the promise of being able to capture and/or reuse this energy for other purposes. A major thrust of the proposed research effort is to determine if this bidirectional power flow can be controlled to some advantage in the next generation aircraft by organizing the subsystem interactions in the proper way.

In this section we will briefly describe the baseline architecture of the power distribution system. Then a brief overview of the various actuators under consideration is presented including a discussion of smart actuators. Finally, the nature and origins of regenerative energy are discussed.

2.2 Power Distribution System

The baseline power distribution system architecture was developed jointly with Lockheed Martin Control Systems (LMCS) and the following specifications were agreed upon:

1. 270 V DC power bus with a 270 V battery
2. Two Engine Starter/Generators (500 kW each) with Split/Parallel Bus
3. APU Channel Starter/Generator (200 kW)
4. Smart Load Management
5. Loads
 - Electric Actuation
 - Cargo Bay Pressurization
 - Negative Impedance Avionics Loads
 - Environmental Control System

Conceptually, this system is shown in Figure 2.1.

The characteristics of aircraft electric loads in a typical commercial transport aircraft are given in Table 2.1.

Table 2.1 Characteristics of Aircraft Electric Loads

Load Group	Characteristics of the Load	Percentage of Total Load
Motor (ECS, Pumps)	<ul style="list-style-type: none"> Mainly squirrel-cage induction motor at present. Brushless DC motor with power converter will compete with the induction motor Fixed Frequency ac or dc with power converter; coarsely regulated, insensitive to waveform and transients for ac induction motor Power Flow in bidirectional 	Represents the largest portion of aircraft electrical loads
Heating	<ul style="list-style-type: none"> Constant voltage ac; constant or variable frequency, or dc; tolerate low quality, coarsely regulated power Power Flow in one direction 	Represent large segment of electric loads in commercial transports
Lighting	<ul style="list-style-type: none"> Incandescent lamps prefer low voltage ac or dc; tolerate transients and poor waveform Power flow in one direction 	
Electronics	<ul style="list-style-type: none"> Closely regulated, clean dc or ac; input power ultimately transformed to low voltage dc for utilization Power Flow in one direction 	
Control	<ul style="list-style-type: none"> Consists of relays, actuators, indicators and some lights and electronics. Part of this load requires closely regulated power, ac or dc; the remainder can tolerate low quality power Power Flow of actuator load is bidirectional 	Represent a small portion of the total load, usually less than 5% of the total load

This distribution system is built around a dual 270 V/500 kW DC bus with an APU and battery backup auxiliary bus. This system has both a right and left starter/generator. Several different loads are included in the architecture. Both EMA and EHA actuators are present in the system. Models and parameters of these actuators were developed under the MADMEL program and they were provided by LMCS. Also included are conventional motor loads associated with the ECS system. Novel actuators built using so-called smart materials are under consideration.

The key electrical components for the regulation of the power bus are the bidirectional power converters (BDC). One BDC provides the interface between the starter/generator and the distribution bus. Typically there is a BDC between the power bus and the load. The primary function of these devices is to change the power from one form into another and to regulate the power flow. For example, the BDC between the starter/generator and the power distribution bus converts 110 V three phase 400Hz power from the generator to 270V DC power for the distribution bus.

It is also the function of this BDC to regulate the voltage on the bus to a prescribed percentage of 270V in the face of fluctuations in the generator and the loads. The presence of BDCs in the power distribution system induces a significant change in the properties of these next generation power distribution systems.

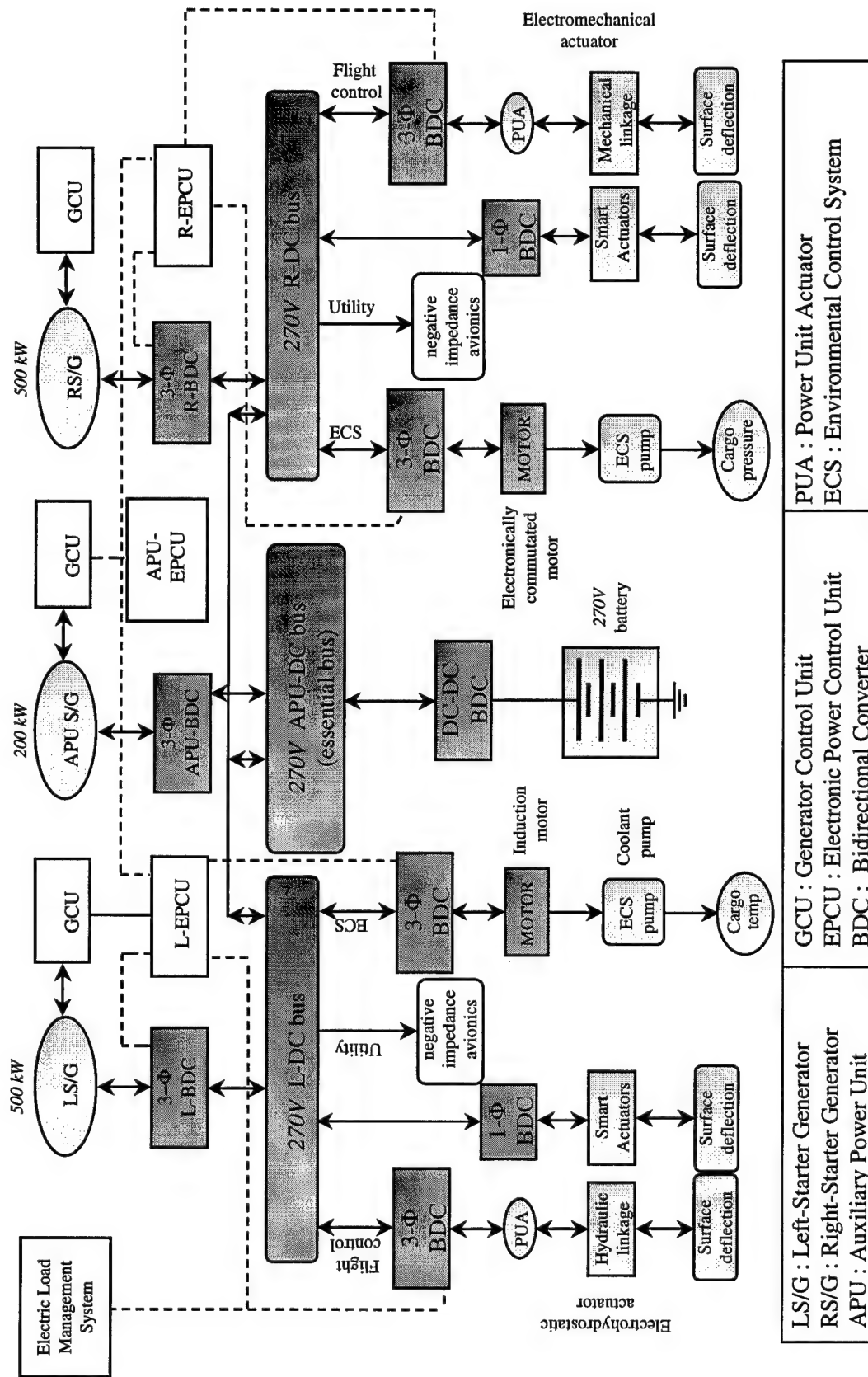


Figure 2.1: Power Distribution System with Generators and Loads

The one significant change on which we are focussing is the bidirectional power flow. The origins of this bidirectional power flow are in the BDCs. These devices function by turning on and off electronic switches at carefully timed moments to control the characteristics of the output voltage waveform. When the switches are closed, the input terminals of the BDC are directly connected to the output terminals and current can flow in either direction. Here is the origin of the bidirectional power flow on a DC distribution bus.

2.2.1 EHAs and EMAs

Because these actuators are the source of the regenerative energy, it is important that the good models be available for the optimization methodology. Models and parameters of the actuators described next were developed under the MADMEL program and they were provided by LMCS. Electro-Hydraulic Actuators (EHAs) will drive the primary control surfaces of the airlifter. Two EHAs will drive each surface panel for the elevator, aileron, and flaperon, while three EHAs will drive the rudder. In total, there will be 15 EHAs driving the seven primary flight control surfaces. Figure 2.2 depicts the actuator location for each of the primary surfaces.

2.2.1.1 Secondary Surface Configuration

The secondary flight control surfaces consist of 14 spoiler panels. Electro-Mechanical Actuators (EMAs) will drive these panels. Each of these EMAs will have one output shaft connecting to a particular surface panel.

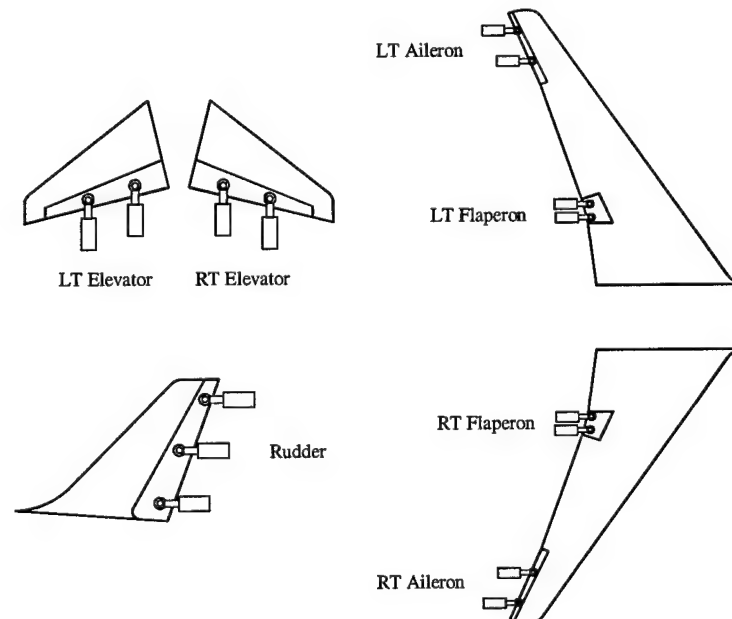


Figure 2.2. Primary Actuator Configuration

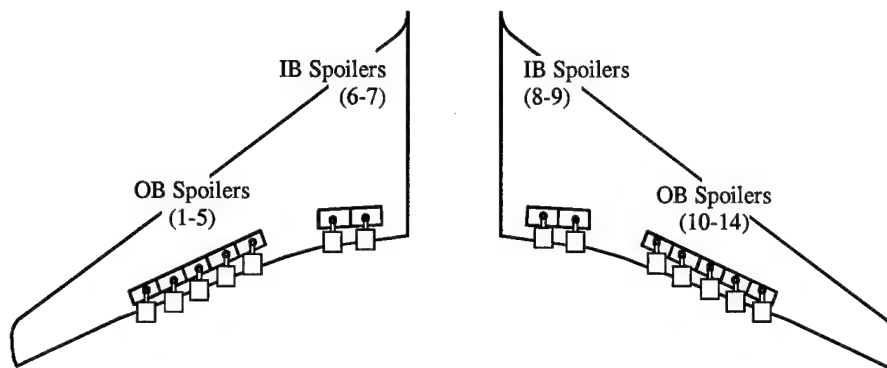


Figure 2.3. Secondary Actuator Configuration

Table 2.2. Selected Actuator Duty Cycles for Regeneration Study

Flight Phase	Elevator (EHA) 4 x 10 hp	Aileron (EHA) 4 x 10 hp	Flaperon (EHA) 4 x 9 hp	Rudder (EHA) 3 x 15 hp	Outboard Spoiler (EMA) 4 x 6 hp	Inboard Spoiler (EMA) 10 x 6 hp	
Bypass Test on Ground	-15 to +10	+10 to -10	-10 to +10	-15 to +10			Surface Deflection (deg)
	+210 to -220	-230 to +230	-60 to +110	+1530 to -1590			Hinge Moment (ft-lbs)
Control Check on Ground	-30 to +25	+15 to -30	+36 to -10	-25 to +25			Surface Deflection (deg)
	+1670 to -1750	-90 to +90	+500 to -1120	-4740 to 4940			Hinge Moment (ft-lbs)
Roll Maneuver		+6 to -9	+24 to +36		0 to +4.5	0 to +1.0	Surface Deflection (deg)
		-990 to -350	-8520 to -10420		0 to +154	0 to -324	Hinge Moment (ft-lbs)
Yaw Maneuver		+3 to -5	+30 to -36	-5.5 to +5.5			Surface Deflection (deg)
		-790 to -510	-9610 to -10140	+17610 to -14280			Hinge Moment (ft-lbs)
Landing Rollout		-30 to 0	-10 to 0		0 to +45	0 to +60	Surface Deflection (deg)
		+230 to 0	-370 to 0		-5310 to +492	-1035 to +1482	Hinge Moment (ft-lbs)

This configuration differs from that of the primary surfaces, where two or three separate EHA RAM output shafts connect to the same control surface. Figure 2.3 depicts the secondary control surfaces and their

actuator locations. The operating duty cycles of each of the deflection surfaces and the associated hinge moments are given in Table 2.2. The associated power levels in hp for each of the deflection surfaces are also provided in Table 2.2.

2.2.2 Smart Actuators

The last few years have seen the beginning of the development of a whole new class of actuators for future aircraft. These actuators are built around so-called "smart materials." These materials are just transducers that change their shape in response to an applied field. These materials include piezoelectric and electrostrictive materials that change their shape in response to an electric field, magnetostrictive materials that change their shape in response to a magnetic field, and shape memory alloys that change their shape in response to heat. These materials have garnered some interest because they offer the possibility of solid state induced-strain actuators with the attendant benefits of high energy density and reliability. While these actuators are clearly in the early stages of development, we note there are several large DARPA and Air Force programs that are developing these actuators. In some cases these actuators are going into flight testing. These actuators are of direct interest to this proposed research effort because the smart materials support two way power flow.

These smart materials are being used in two primary ways. First, the smart material is being integrated into a mechanical assembly to enhance its performance. This mechanical component is similar to a conventional actuator and it is used in a similar manner. Both magnetostrictive and piezoelectric based actuators are being developed. Two prototypes of these actuators are included in the DARPA sponsored Smart Wing Program at Northrop Grumman. The goal of this program is to develop a conformal wing to optimize the performance over several flight regimes. Second, the smart material is integrated with a structural material to improve the properties of structural component. Both shape memory alloys and piezoelectric patches have been used in this manner. The shape memory alloys are included as part of the Smart Wing Program. In another application both the Air Force and NASA Langley have programs to alleviate the fatigue in the tail due to buffeting by integrating the actuators directly into the tail. By using the piezoelectric actuators to reduce the vibrations in the tail the peak stress is also reduced, increasing the life of the tail. The outcomes of both of these programs could have a major impact on 21st Century airlifters through tailoring the wing profile to improve the lift capabilities and by increasing the in-service lifetime of the structural materials.

All of the actuators employing smart materials are electrically driven. The electrical load that these actuators present to the power system has not been characterized, however. Each of these actuators has different electrical characteristics. Shape memory alloys are heated by a dc current, so this load is resistive. Piezoelectric and electrostrictive actuators are basically capacitors (in which some of the electrical energy is changed into mechanical energy) so that the load is almost purely reactive. Strain is induced in the

actuation material by cycling charge in and out of the actuator. Clearly, the drive electronics must be carefully designed for this type of electrical load. Furthermore, these smart materials also support the reverse power flow by changing mechanical energy into electrical energy. Therefore, there is a potential regenerative energy flow from the mechanical load back into the power system. Strain is induced in magnetorestrictive actuators by applied magnetic fields. Therefore, most magnetorestrictive actuators employ a coil to generate the magnetic field. The electrical impedance is primarily inductive rather than capacitive as in piezoelectric actuators. Thus, the design of the drive electronics is in some sense dual to the drive electronics for piezoelectric actuators. The issues associated with the regenerative power flow are the same.

The drive amplifiers for piezoelectric and electrostrictor actuators have received some attention lately. The design of these amplifiers must take into account the reactive (capacitive) nature of the smart actuators. These reactive loads require a significant amount of electrical energy to be cycled between the actuator and amplifier. The amplifier must not only deliver power but it must be able to accept regenerative power from the actuator. Switching amplifiers offer attractive alternatives for these actuators when efficiency is required. They also appear to be naturally suited for integration into the next generation power distribution systems on aircraft. Switching amplifiers achieve their efficiency by essentially connecting the actuator directly to the power bus. This topology allows the energy to be circulated between the actuator and the power bus. Since these actuators are ultimately configured to reduce structural vibrations, the actuators effectively convert the mechanical energy to electrical energy, and drive the energy back into the power distribution system – these actuators regenerate power. Hence these actuators naturally fall into the scope of the project.

2.3 Generation Units

Two distinct starter/generator units were considered under this project namely,

1. The three phase synchronous generator which generates 110V/400Hz three phase AC voltage and,
2. The switched reluctance integral starter generator which generates 270V DC to be fed to the DC distribution bus.

The three phase synchronous generator requires a three phase-to-DC rectifier to provide the tightly regulated 270 DC voltage required at the DC bus. A three pha

se bidirectional boost rectifier was used as the bus regulator to convert the 110V/400Hz AC to 270V DC. This combination of generator/bus regulator was used in most simulation examples and stability studies. The switched reluctance integral starter/generator provides regulated the 270V DC bus voltage through a bidirectional converter connected to its windings. The models of both these generating units have been

developed and are explained in detail in Chapter 3. The models of the three phase synchronous generator and of the boost rectifier can be built independently and connected together as shown schematically in Figure 2.1. However, the switched reluctance starter/generator model has to be coupled with that the bidirectional converter that regulates the DC bus. This is due to some fundamental differences in the way the bidirectional converters associated with the respective generating units are controlled. These details are explained in Chapter 3.

2.4 Regenerative Energy

The key components that control the 270 V DC power distribution bus are the bidirectional power converters. These devices, which are briefly described above, occur in two primary locations. First, the bus converter provides an interface between the starter/generator and the distribution bus. The generator produces unregulated 110 V AC three phase sinusoidal power at 400 Hz. The bus converter accepts this raw power, regulates it to 270 V DC, and puts out power to the bus. The bus converter tries to maintain the bus voltage at 270 V. Second, the load converter accepts the power from the power bus and converts this power into a usable form for the load. For example, the EMAs are three phase brushless DC motors. The load converters for each of these actuators converts the 270 V DC power to 120 V three phase power for the motors and supplies this power on demand from the surface deflection control system.

These power converters have the property that the current can flow in both directions through the converters. Hence, power can flow in both directions through the converters. This characteristic of these converters leads to the phenomena of *regenerative power flow* in DC power distribution systems. As the name implies, power is generated by the load and flows back into the power distribution system. The origin of this regenerated power is easily explained with an EMA. When the motor accelerates the control surface, the motor draws power. To stop the surface the motor provides a braking action, effectively acting as a generator. During this action the motor regenerates power which is transmitted onto the bus through the load converter. The amount of regenerative power is strongly affected by the wind load on the control surface, as the simulations below show. Regenerative power can also occur during verification and testing of the actuators performed by the flight crew on the ground.

The drive amplifiers for piezoelectric and electrostrictor actuators have received some attention lately. The design of these amplifiers must take into account the reactive (capacitive) nature of the smart actuators. These reactive loads require a significant amount of electrical energy to be cycled between the actuator and amplifier. The amplifier must not only deliver power but it must be able to accept regenerative power from the actuator. Switching amplifiers, which are a small variation of the bidirectional power converter concept, offer attractive alternatives for these actuators when efficiency is required. They also appear to be naturally suited for integration into the next generation power distribution systems on aircraft. Since these actuators are ultimately configured to reduce structural vibrations, the actuators effectively convert the

mechanical energy to electrical energy, and drive the energy back into the power distribution system – these actuators regenerate power. Hence these actuators naturally fall into the scope of the project.

It would appear that regenerative power is a positive feature of a DC power distribution system because it would make more power available to the system, and/or it would increase the efficiency of the system. However, if the power distribution system is not designed to accept this power, the effects can be quite detrimental. The regenerative power will be stored in the available energy storage elements, mainly capacitors, driving up the bus voltage to unacceptably high levels and causing transient voltage swings on the bus. These voltage disturbances on the bus can cause damage to other components designed to operate within set voltage limits. (Mil Spec 704E [8]). These surface deflections are much larger and faster than in the regular flight conditions, so that much larger regenerative power flows are encountered.

3 Simulation Block Library

3.1 Introduction

The development of the SIMULINK block library of models for the subsystems in the baseline system architecture is described in this chapter. A multi-level modeling approach is used to describe each of the subsystems at varying levels of complexity. The basic idea is that each component should be represented by three models of varying complexity: a detailed (switching) model, an “average” (nonlinear) model, and a linear model. Using these multilevel models, simulations of varying complexity can be built up as is needed in a particular study. Each component is described at these three levels. A standard set of interconnection rules is developed that enables the user to develop a model for an interconnected system by a “drag and drop” procedure from the block library. This block library is described in detail in the Addendum to the final report. The components in the block library include, passive elements, linear networks, diode/transistor switches, switching power converters of several types, electric motors, electromechanical actuators (EMA), electrohydraulic actuators (EHA), switched reluctance generators, smart actuators and a DC power bus. The models for all of these components are described in detail in this chapter.

3.2 Multi-level Modeling of Power Distribution System Components

In order to achieve the research goals, a model of the PDS that allows studying subsystem interactions has to be developed. This model should provide efficient ways for analysis, simulation, optimization, and control system design of subsystems interacting with each other within the PDS. Although good models for all subsystems already exist or can be readily developed with the use of known modeling techniques, simply putting all the subsystem models together would not provide an acceptable solution to the problem. The global system model built this way would be overcomplicated, with many unnecessary details not helpful in most cases of studying subsystem interactions. Since the available system modeling software does have limitations, this model will likely be very computationally intensive, slow, inefficient, or sometimes inoperable at all due to numerical convergence problems.

The multi-level modeling concept allows us to overcome this drawback. In this approach, a model reduction procedure is used to obtain models of different level of complexity for each subsystem. Three levels of models are available: the detailed model, the behavioral model, and the reduced order model. For a particular type of analysis, a model of an appropriate level will be chosen for each subsystem.

A detailed model is based on equations derived from the subsystem structure and electrical circuit. For a subsystem whose configuration or topology changes during its operational cycle, there will be a separate

set of equations for each configuration. A detailed model reflects both low and high frequency dynamics of the subsystem and may include effects of secondary importance such as parasitics. An example of a detailed model for a switching power converter would be a model that exactly describes all voltage and current waveforms in the circuit produced by the switching action of the semiconductor switches. For switching power converters, a detailed model is often called a “switching” model. A detailed model is very computationally intensive in computer simulations. Since a detailed model often includes discrete and discontinuous functions, it cannot be used for control loop design based on linearization and frequency domain techniques. For this reason, a detailed model is used only in simulations when a detailed study of the subsystem operation is required.

A behavioral model is derived from the detailed model by time averaging of high-frequency periodical waveforms such as switching waveforms [9]. The behavioral model corresponds to a subsystem whose terminal behavior is identical to the original subsystem at frequencies much lower than the switching frequency and excluding the switching ripple in waveforms. The behavioral model preserves nonlinearities and low-frequency dynamics of the original subsystem. It may or may not reflect the subsystem nonidealities and parasitic effects. Since the high-frequency behavior no longer has to be obtained in the process of numerical integration, the behavioral model is much more computationally efficient than the detailed model. The low-frequency dynamics of the behavioral model are described by continuous functions, which can be linearized and used for control design. A behavioral model of a switching converter is often called an “average” model.

A reduced order model is obtained from a behavioral model by linearizing it around an equilibrium point. Therefore, it is often called a “linearized” or a “small-signal” model. A large signal model is reduced to a small signal model valid in a small neighborhood of this operating point. A standard procedure of perturbation and linearization of nonlinear continuous equations of a behavioral model is employed to obtain the linearized model [9]. Most commercial software packages can perform this procedure automatically. The reduced order model allows frequency domain analysis and design tools to be applied. The reduced order model is often used as a generic model of a subsystem (for example, sources and loads) in cases when having a more detailed model is not essential.

The mixed-level modeling concept provides a convenient way to study subsystem interactions under a particular scenario without overcomplicating the global model of the system. As mentioned before, it is neither feasible nor necessary to use detailed models for all subsystems for every particular scenario. Instead of trying to simulate the whole system “as it is” in all its complexity, we concentrate our attention on a particular aspect of the system operation that we want to study, select the appropriate level of modeling of the interacting subsystems that would allow to capture the essential features of the phenomenon under investigation, and use reduced level models for the rest of the subsystems involved in this scenario. Figure 3.1 illustrates the usage of this concept. We would use the reduced order model for

each subsystem if we want to simulate only the global system states. The second scenario could be used to study how the second subsystem interacts with the third subsystem with a contribution from the first subsystem. In this scenario, we would select the behavioral model of the second and third subsystems and the reduced order model of the first subsystem. The third scenario describes the case when we want to know exactly how the first subsystem responds to the second subsystem with a contribution from the third subsystem. To study this case, we would use the detailed model of the first subsystem, the behavioral model of the second subsystem, and the reduced order model of the third subsystem.

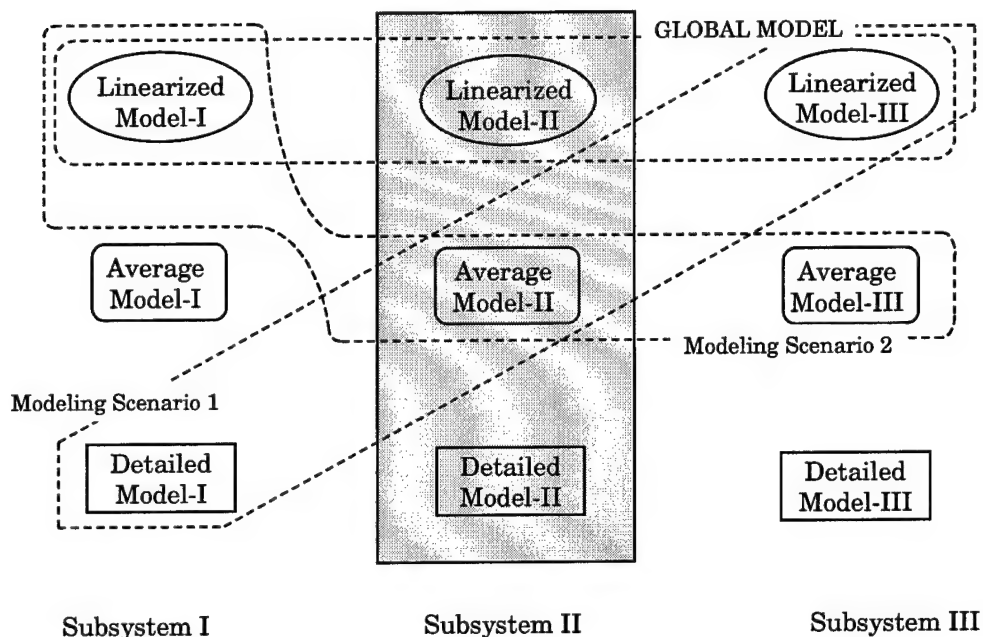


Figure 3.1. Mixed-level modeling concept.

As illustrated above, the mixed-level modeling concept provides an efficient way to investigate all aspects of the system behavior. Instead of having just one global system model, we build particular system models at the levels that suit our needs.

3.3 Power Distribution System Analysis and Simulation Tools

In order to take advantage of the multi-level and mixed-level modeling concepts described above, a computer-aided analysis and simulation tool has to be developed. There are a number of commercial software packages possessing necessary capabilities, most of them are application-specific. The PDS of an aircraft consists of elements with diverse physical nature, both electrical and non-electrical, such as power generators and converters, electromechanical devices, hydraulic and mechanical actuators. This calls for a generic modeling and simulation tool that allows diverse physical systems to be modeled in a uniform environment. Based on these considerations, MATLAB/SIMULINK was chosen as a software platform.

MATLAB is a numerical analysis software, which is ideally suited for system level analysis and simulation [10]. It contains a variety of toolboxes for many kinds of specialized analysis including optimization and control design. SIMULINK, a toolbox of MATLAB, is a dynamic system simulation software, which provides a convenient graphical user interface for building system models [11]. Stability and transient behavior, which are the key issues in studying subsystem interactions, can be conveniently analyzed using these tools.

The system analysis based on the mixed-level modeling concept requires the capability of the software environment to provide an easy way of building simulation models for various system configurations using different level models for the subsystems. This is achieved by employing a modular approach for building SIMULINK models for the subsystems and their parts. Basic models of electric circuit elements and low-level subsystems are designed as modules, which are used as building blocks for creating models of subsystems that are more complicated and the whole system. Each block has input and output ports, through which it interchanges input and output variables with other blocks connected to it. Generally, each block has its own specific input and output variables, but the majority of variables being exchanged are voltages and currents. Since any subsystem containing an electrical two-port network has both voltages and currents as both inputs and outputs, a special convention about voltage and current variable exchange needs to be made. It is agreed that each block receives its input voltage and output current from the adjacent blocks as its input variables and supplies its input current and output voltage to the adjacent blocks as its output variables, as illustrated in Figure 3.2. All the SIMULINK blocks developed must satisfy this convention, which is known as interconnection rules. This is a novel modeling concept developed in this research for greater flexibility in modeling different PDS configurations. Other variables exchanged between the subsystems have similar interconnection rules.

Each subsystem, in general, has three types of models as discussed above: detailed, average, and linearized. A general procedure for a subsystem model development includes the following steps:

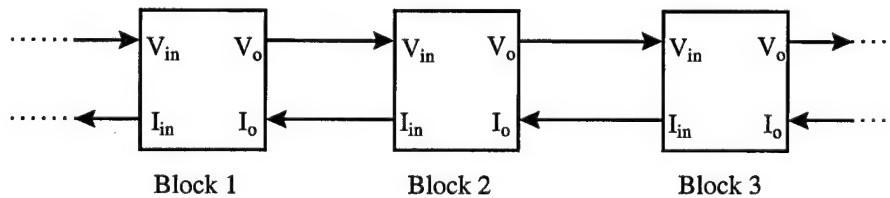


Figure 3.2. Interconnection rules for two-port networks.

- partitioning of the subsystem into generic (elementary) blocks,
- developing analytical expressions for each block at both detailed and average model level,
- implementing the models in SIMULINK,
- using MATLAB to obtain a linearized model.

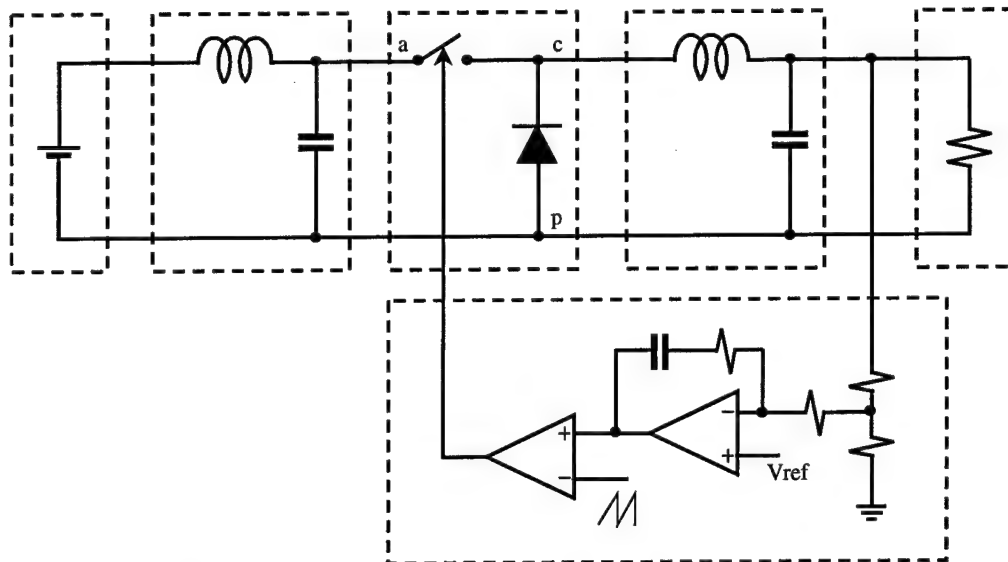


Figure 3.3. Buck converter – partitioning into generic blocks.

An example of partitioning of the system into generic blocks is shown in Figure 3.3. It represents a buck converter with feedback control. The converter is partitioned into the following blocks: input filter, PWM switch, output filter, feedback controller, in addition to the blocks for the voltage source and the load. For each of these blocks, a SIMULINK model is obtained based on their equations. Then the models are tied together into the whole system model according to the interconnection rules as shown in Figure 3.4. The detailed and the average models for the PWM switch will be different, while they will appear to be the same to other blocks. This provides the user with a very convenient plug-and-place capability. All these blocks are typical for power converters; thus the developed SIMULINK models can be used as building blocks for building models of different systems.

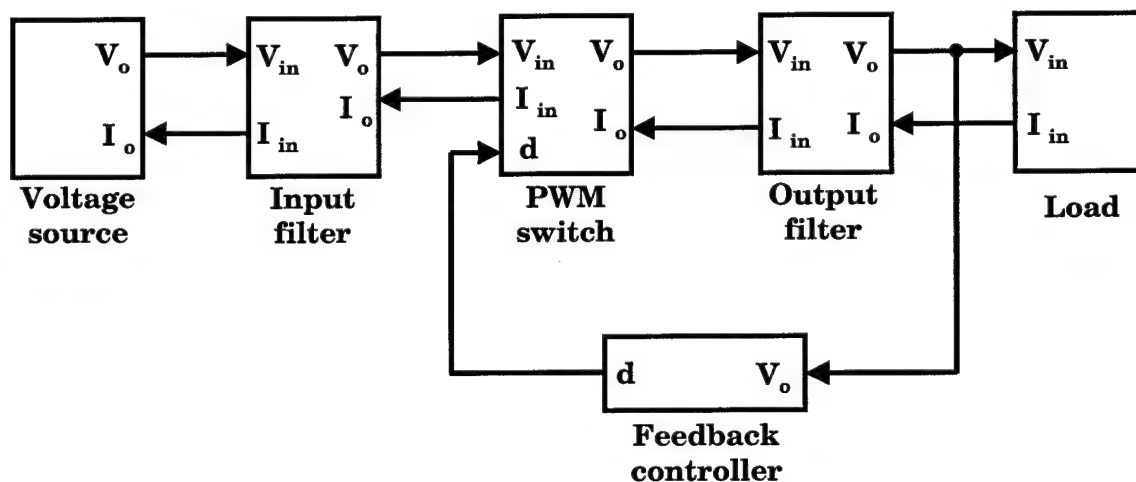


Figure 3.4. SIMULINK block diagram for the buck converter in Figure 3.3.

A linearized model of a subsystem can be obtained from its average model using the MATLAB's Control System Toolbox commands [12]. Usually, a linearized model is obtained for the purpose of a control loop design and can be defined within MATLAB, without implementation in SIMULINK. A linearized model intended for simulation as a part of the whole system model will be implemented in SIMULINK.

3.4 Modeling of Subsystem Elements

As we have seen in the previous section, elementary blocks typical for switching power converters are PWM switches and RLC networks (usually low-pass filters). These elements are two-ports, therefore, the interconnection rules for voltages and currents should be observed. We will show how to use modeling capabilities of SIMULINK to build models for these elements.

As an example of an RLC network, we will consider a low-pass L-C filter (Figure 3.5), which is a generic component for many types of power converters. The circuit is described by equations:

$$L \frac{di_{in}}{dt} = v_{in} - v_o - i_{in} R_l \quad \dots (3.1)$$

$$C \frac{dv_c}{dt} = i_{in} - i_o$$

$$v_o = v_c + R_c (i_{in} - i_o)$$

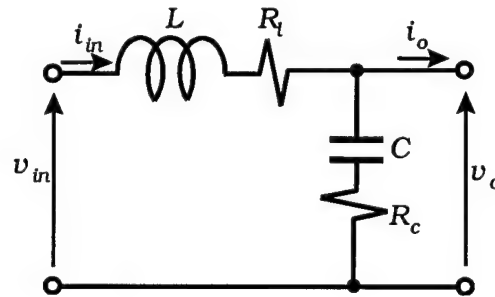


Figure 3.5. Low-pass L-C filter.

The implementation of Equation 3.1 and the application of the interconnection rules in the SIMULINK model of the filter are shown in Figure 3.6. For convenience, it is further enclosed into the “Subsystem” block and used as illustrated in Figure 3.4. Another way of building a model for this network is to represent it as a linear system using the “State-space” SIMULINK block as shown in Figure 3.7. To do this, we need to identify state-space matrices for the network by writing its equations in the state-space form as:

$$\frac{d}{dt} \begin{bmatrix} i_{in} \\ v_c \end{bmatrix} = \begin{bmatrix} -\frac{R_c + R_l}{L} & -\frac{1}{L} \\ \frac{1}{C} & 0 \end{bmatrix} \begin{bmatrix} i_{in} \\ v_c \end{bmatrix} + \begin{bmatrix} \frac{1}{L} & -\frac{R_c}{L} \\ 0 & -\frac{1}{C} \end{bmatrix} \begin{bmatrix} v_{in} \\ i_o \end{bmatrix} \quad \dots (3.2)$$

$$\begin{bmatrix} i_{in} \\ v_o \end{bmatrix} = \begin{bmatrix} 1 & 0 \\ R_c & 1 \end{bmatrix} \begin{bmatrix} i_{in} \\ v_c \end{bmatrix} + \begin{bmatrix} 0 & 0 \\ 0 & R_c \end{bmatrix} \begin{bmatrix} v_{in} \\ i_o \end{bmatrix}$$

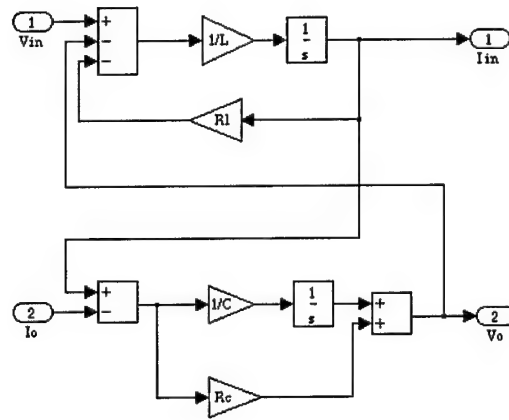


Figure 3.6. SIMULINK model of the L-C filter.

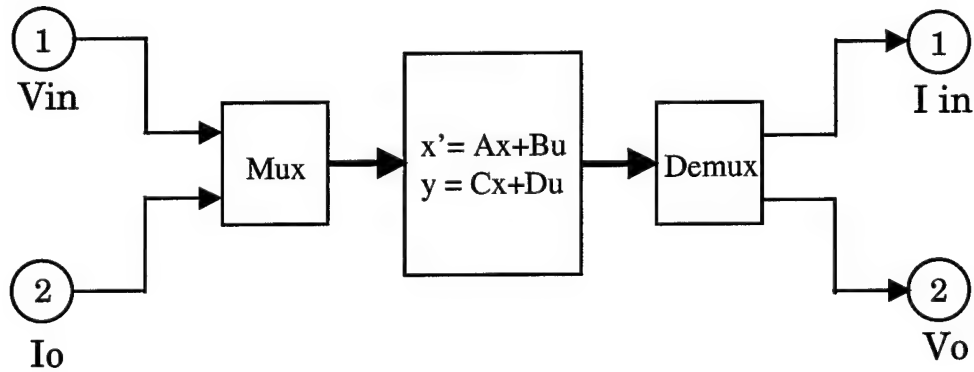


Figure 3.7. Alternative SIMULINK model of the L-C filter based on state-space representation. The models in Figure 3.6 and Figure 3.7 are equivalent. The model in Figure 3.6 represents a general approach for model building based on the system equations, which is generally used in this research. The other approach is applicable only to linear systems represented in state-space form. It can be convenient for modeling of high-order systems with a large number of parameters, for which using the previous

approach may be too cumbersome. In addition, it may be more computationally efficient since it reduces the number of algebraic operations in the simulation process.

The models for the L-C filter developed above are detailed, average, and linearized at the same time because no switching or nonlinearities are present in the network. The models for the PWM switch that we will consider next are different at the detailed and average levels.

The PWM switch configuration used in the buck converter (Figure 3.3) is a two-port switching network with three terminals: active, passive, and common. The switching action of the PWM switch is described by the switching function s , which accepts the values of 0 and 1 as shown in Figure 3.8. The terminal behavior of the PWM switch, therefore, is described by the following equations upon which the detailed model of the switch is based:

$$\begin{aligned} i_a &= s \cdot i_c \\ v_{cp} &= s \cdot v_{ap} \end{aligned} \quad \dots (3.3)$$

The switching voltage and current waveforms produced by the PWM switch are averaged by the low-pass filtering action of the input and output filters of the converter as they are seen at the load and source terminals. This presents a physical basis for using an average model of the switch, which neglects its switching action while preserving quantitative relationships between average values of voltages and currents at its terminals [9]. Mathematically, averaging of a periodical function $x(t)$ is defined as

$$\bar{x} = \frac{1}{T} \int_{t-T}^t x(\tau) d\tau \quad \dots (3.4)$$

The operation of averaging, being applied to the discrete switching function $s(t)$ with a discrete value of duty cycle d for each switching period, results in the continuous duty cycle function $d(t)$, and the following equations for the PWM switch, which constitute its average model (Figure 3.8):

$$\begin{aligned} \bar{i}_a &= d \cdot \bar{i}_c \\ \bar{v}_{cp} &= d \cdot \bar{v}_{ap} \end{aligned} \quad \dots (3.5)$$

The SIMULINK implementations of the detailed and average PWM switch models are shown in Figure 3.9. Besides the terminal voltages and currents, the models have an additional input – the duty cycle command. The detailed model then turns this command into the output voltage and current switching waveforms by comparing it with a ramp generator signal, in a manner very similar to the operation of real PWM modulator circuits. The average SIMULINK model is based on the average model equations (Equation 3.5). Note that the interconnection rules for voltages and currents are observed.

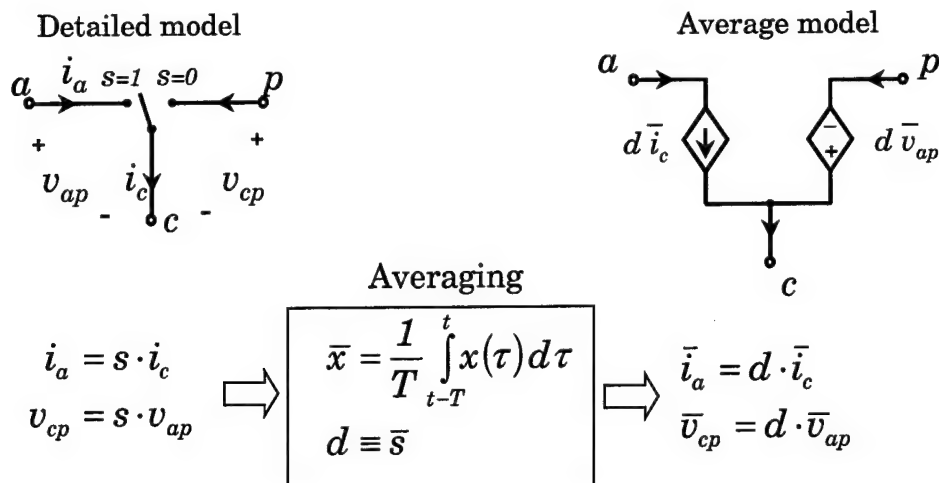


Figure 3.8. Development of detailed and average models for the PWM switch.

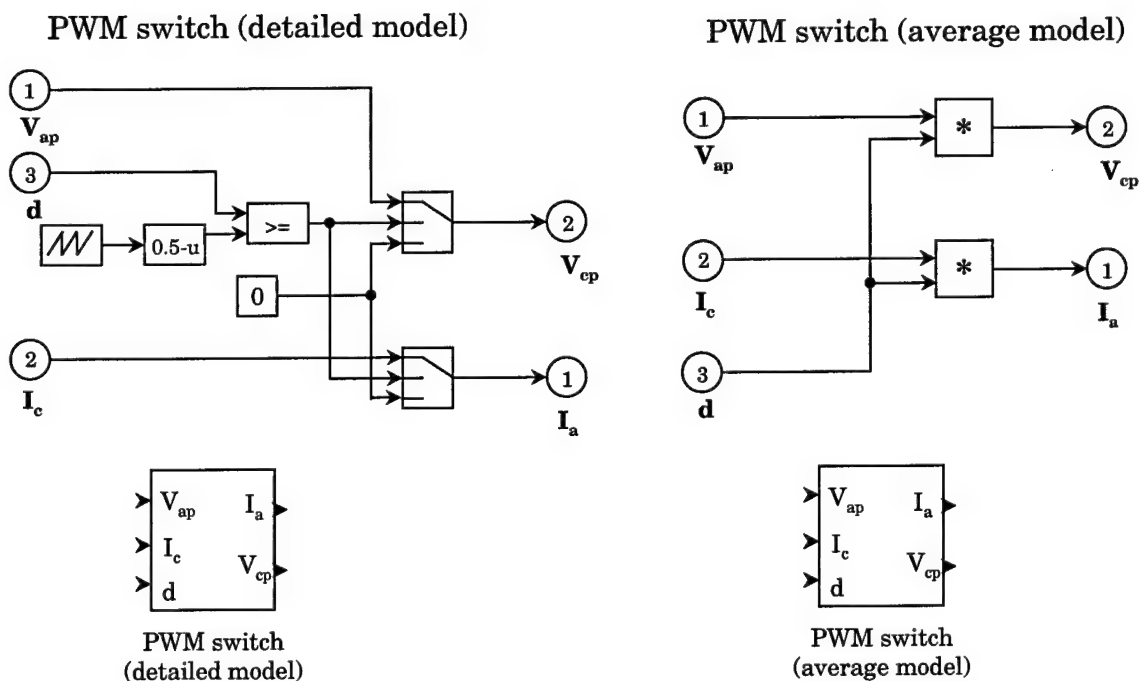


Figure 3.9. Detailed and average SIMULINK models for the PWM switch.

The SIMULINK model for the system in Figure 3.4 may employ either detailed or average model for the PWM switch developed above. Both models will preserve the low-frequency dynamics of the system, but without the switching ripple in the state variables' waveforms in case of using the average model. Figure 3.10 illustrates this point. It shows the simulated output filter capacitor voltage and inductor current transients of the buck converter obtained with both detailed and average models of the PWM switch. It is

seen that the current response obtained with the average model reflects all the details of the current response obtained with the detailed model except the switching ripple.

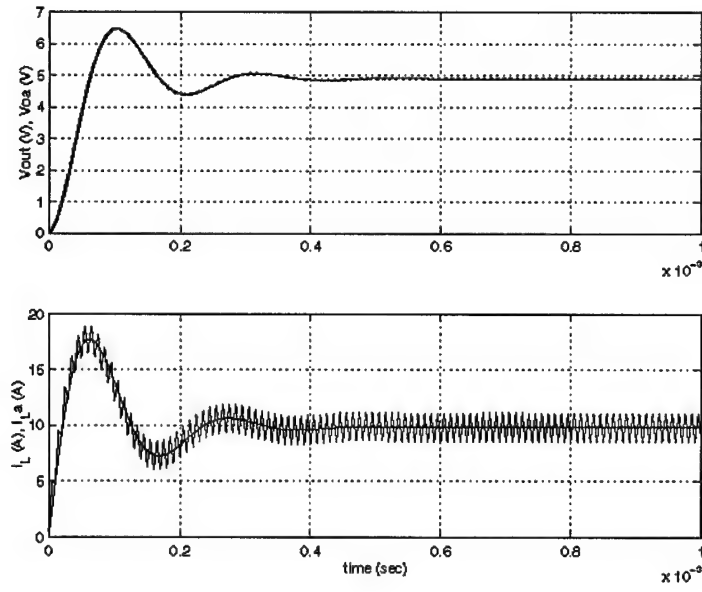


Figure 3.10. Buck converter example of simulation with detailed and average models for the PWM switch.

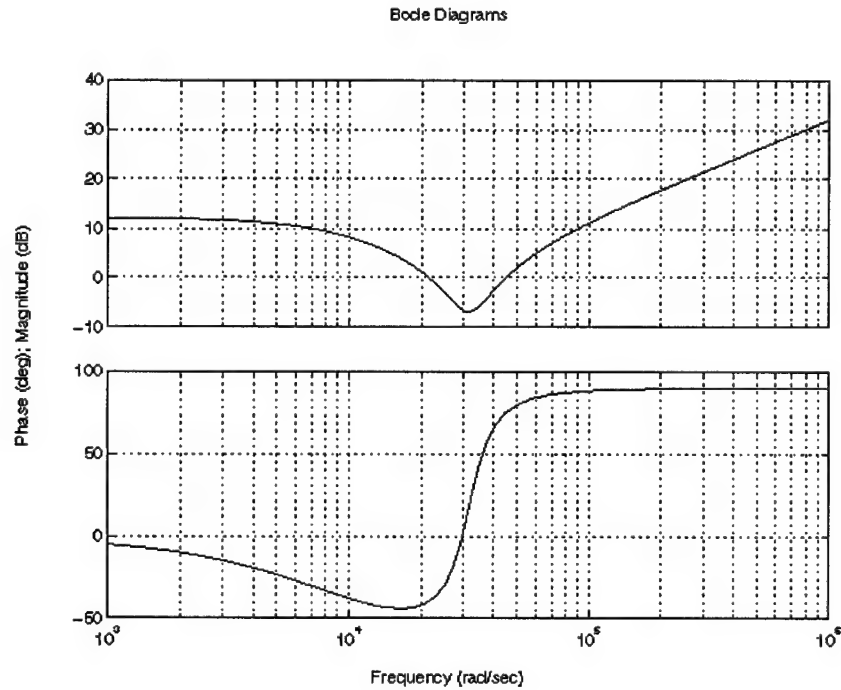


Figure 3.11. Buck converter open loop input impedance.

This is also true for the output voltage waveforms. The switching ripple of the output voltage is so small that both curves almost coincide on the plot. Although the average model does not show the switching ripple, it provides much faster simulation and an additional opportunity for small-signal analysis and control design using MATLAB Control System Toolbox [12]. A nonlinear system such as the buck converter can be linearized at an equilibrium point, and a number of transfer functions can be obtained. For example, Figure 3.11 shows the input impedance transfer function of the buck converter in open loop configuration obtained by using the Control System Toolbox.

3.5 Modeling of DC-DC Switching Power Converters

3.5.1 DC-DC Buck Converter Modeling

The buck converter topology was discussed earlier (Figure 3.3). A complete SIMULINK model of the buck converter is shown in Figure 3.12. The model features the input and output L-C filters and the average model of the PWM switch. The converter model can use a different input filter topology with the proper SIMULINK model. The model has an improved two-pole, two-zero feedback compensator, which provides voltage mode control to the converter. The feedback controller includes the integrator anti-windup feature and provides a soft start with the reference voltage rising from zero.

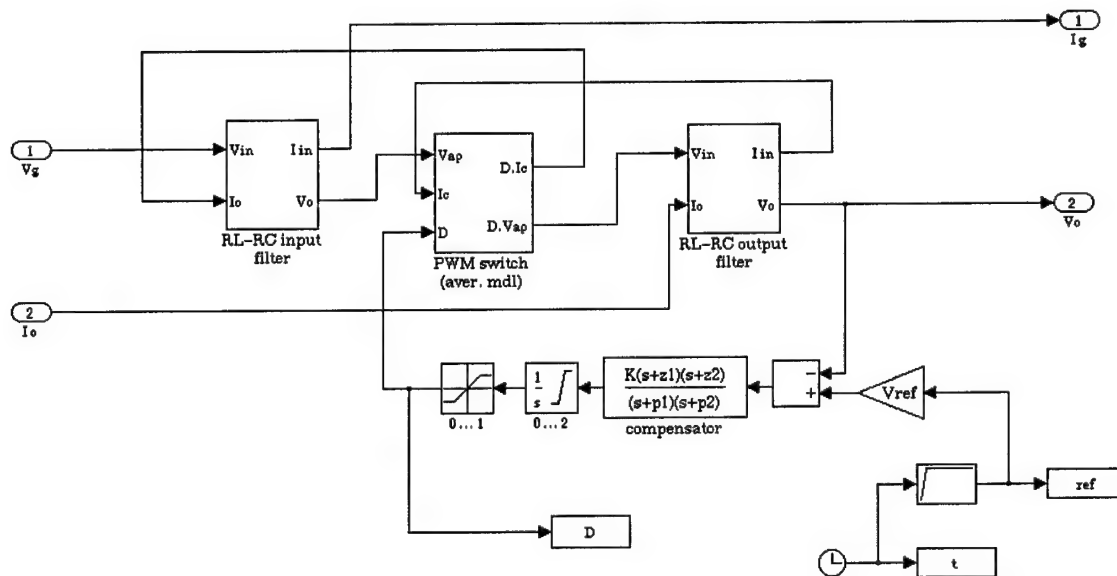


Figure 3.12. Bidirectional buck converter SIMULINK model.

The model supports bidirectional power flow, and can be used in the aircraft power distribution system simulations to power low-voltage DC applications such as avionics from 270V DC bus. The model can

also be used for bidirectional DC-DC full-bridge buck converter topologies, provided the lower limit of duty cycle in the feedback loop is set to -1 .

3.5.2 DC-DC Boost Converter Modeling

The boost converter has an output filter split by the PWM switch (Figure 3.13), therefore the power stage model cannot be obtained by interconnecting the existing PWM switch and L-C filter models. A separate SIMULINK model (Figure 3.15) for the power stage of the boost converter (Figure 3.14) is developed based on the circuit equations given below.

$$L \frac{di_g}{dt} = v_g - v_o(1-d) - i_g R_l \quad \dots (3.6)$$

$$C \frac{dv_c}{dt} = i_g(1-d) - i_o$$

$$v_o = v_c + R_c(i_g(1-d) - i_o)$$

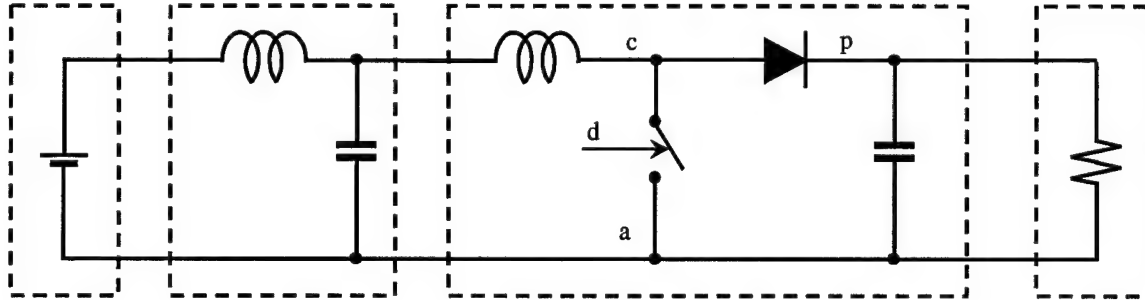


Figure 3.13. Boost converter topology.

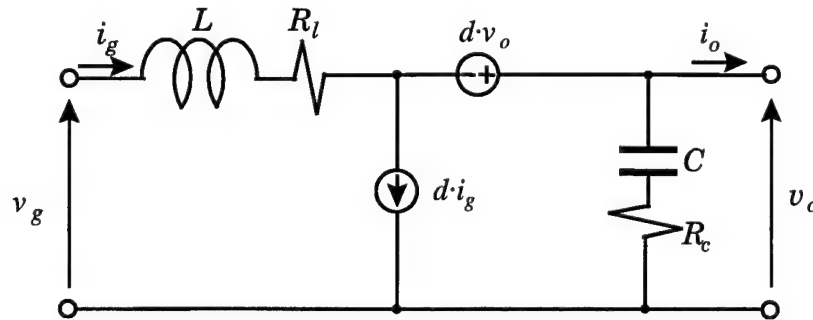


Figure 3.14. Equivalent circuit of the boost converter power stage.

A complete model of the boost converter with voltage feedback loop is shown in Figure 3.16. It is composed of the average model of the boost converter power stage, the input filter model, and the feedback controller. The compensator with anti-windup is very similar to the one used in the buck converter. Of course, the compensator zeros, poles, and gain should be designed individually for a particular converter.

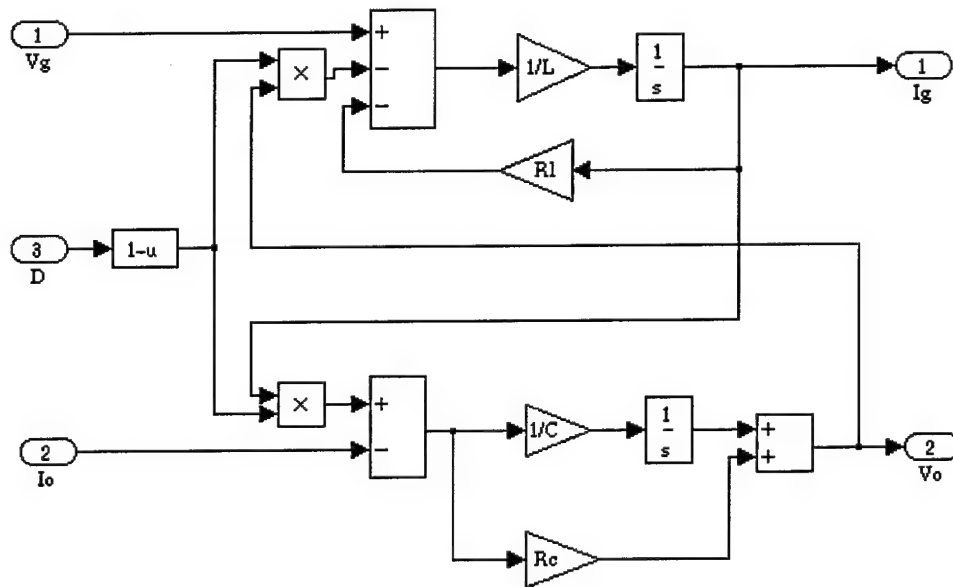


Figure 3.15. SIMULINK average model for the boost converter power stage.

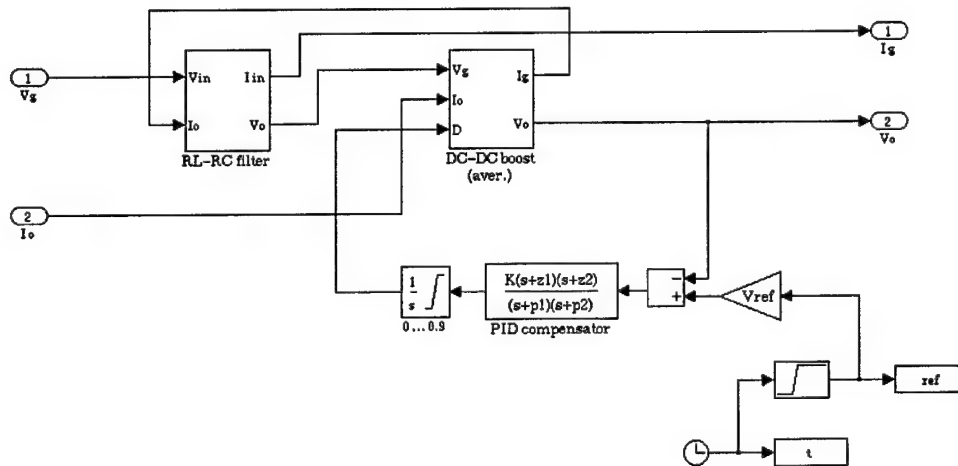


Figure 3.16. Bidirectional boost converter SIMULINK model.

3.6 Modeling of Three Phase Subsystems

3.6.1 Three Phase Subsystem Modeling Approach

Three phase subsystems of the PDS considered in this research include three phase synchronous motors/generators and three phase bidirectional converters. We will take a close look at modeling and simulation techniques for a three phase synchronous starter/generator loaded by a three phase-to-dc boost rectifier. The models should reflect bidirectional power flow in the subsystems (both generating and motoring) found under different scenarios.

Direct modeling of three phase systems by writing their circuit equations in the three-phase reference frame is undesirable for several reasons. For a synchronous machine, this would result in equations with time-varying parameters because the self-inductances and mutual inductances of the machine windings depend on the rotor position. For the boost rectifier, even after averaging of the switching ripple, a three-phase model would not allow using the linearization and feedback control design techniques since the steady state waveforms of the system variables are sinusoidal, and a dc operating point cannot be specified.

If we assume the waveforms to be purely sinusoidal by neglecting the nonidealities of subsystems, these problems may be overcome by modeling them in the synchronously rotating reference frame commonly known as dq coordinates. Modeling of the synchronous machine and the boost rectifier in dq coordinates is well covered in literature [13,14]. The relationship between a set of dq variables and the corresponding set of abc variables is provided by the transformation matrix T . Since the three phase systems studied in this research are balanced, no 0-axis components are present, and we may use a simplified version of dq transformation given by Equations 3.7 and 3.8.

$$\begin{bmatrix} X_d \\ X_q \end{bmatrix} = T \begin{bmatrix} X_a \\ X_b \\ X_c \end{bmatrix} \quad \dots (3.7)$$
$$T = \frac{2}{3} \begin{bmatrix} \cos \omega t & \cos(\omega t - \frac{2\pi}{3}) & \cos(\omega t + \frac{2\pi}{3}) \\ -\sin \omega t & -\sin(\omega t - \frac{2\pi}{3}) & -\sin(\omega t + \frac{2\pi}{3}) \end{bmatrix}$$

The inverse transformation from dq to abc coordinates is defined as

$$\begin{bmatrix} X_a \\ X_b \\ X_c \end{bmatrix} = T' \begin{bmatrix} X_d \\ X_q \end{bmatrix} \quad \dots (3.8)$$

$$T' = \begin{bmatrix} \cos \omega t & -\sin \omega t \\ \cos(\omega t - \frac{2\pi}{3}) & -\sin(\omega t - \frac{2\pi}{3}) \\ \cos(\omega t + \frac{2\pi}{3}) & -\sin(\omega t + \frac{2\pi}{3}) \end{bmatrix}$$

To provide a means for abc-dq and dq-abc transformation of variables during simulation process, two SIMULINK blocks “ABC-to-DQ” (Figure 3.17) and “DQ-to-ABC” (Figure 3.18) are developed. However, their usage is limited to modeling only separate subsystems or simple systems since the transformation blocks contain sinusoidal signal sources and must be used only with fixed-step integration routines. For complex systems that have to take advantage of robust variable-step integrators three phase systems should be modeled completely in dq coordinates. After the simulation is done, the results in dq variables may be converted to abc variables using the inverse transformation matrix T' . A special MATLAB function “dq2abc” described in Appendix B has been developed for this purpose.

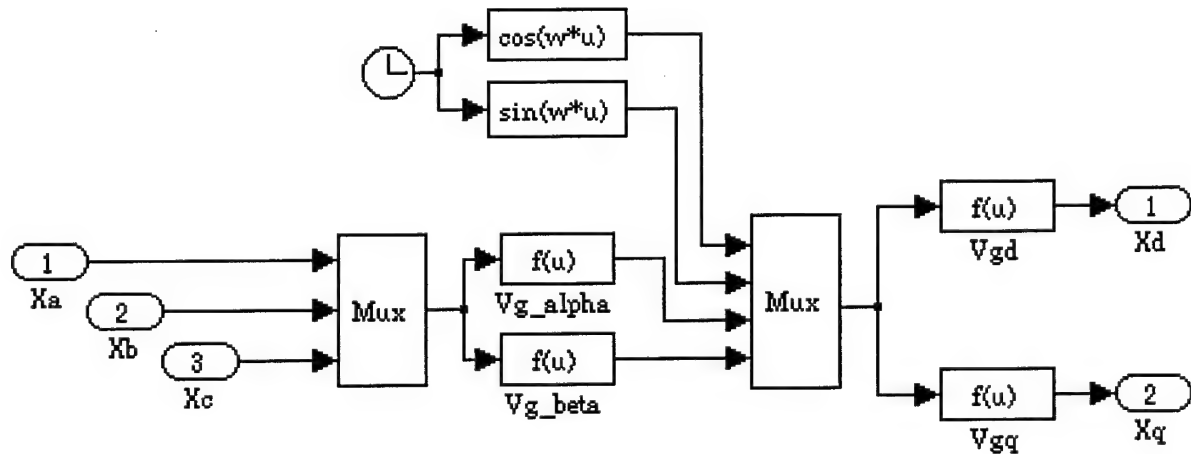


Figure 3.17. ABC-to-DQ transformation SIMULINK block.

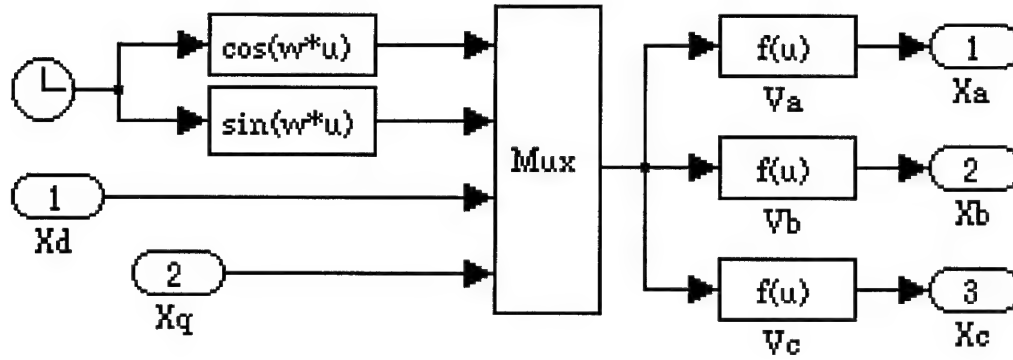


Figure 3.18. DQ-to-ABC transformation SIMULINK block.

3.6.2 Three Phase Synchronous Generator Modeling

An equivalent circuit of the synchronous generator with a balanced load is presented in Figure 3.19. As mentioned above, modeling of a synchronous machine in dq coordinate frame avoids the problem of time-variance of the winding inductances. It converts the ac system variables into equivalent dc variables, which relate to the magnitude of the sinusoids in the steady state operation and in transients.

The machine is described by the following equations corresponding to the equivalent circuit [13]:

$$v_d = (i_{sd} - i_d)R_a$$

$$v_q = (i_{sq} - i_q)R_a$$

$$0 = R_a i_d - (R_a + R_s) i_{sd} + \omega(L_{ls} + L_{mq}) i_{sq} - \omega L_{mq} i_{kq} - (L_{ls} + L_{md}) \frac{di_{sd}}{dt} + L_{md} \frac{di_{fd}}{dt} + L_{md} \frac{di_{kd}}{dt}$$

$$0 = R_a i_q - (R_a + R_s) i_{sq} - \omega(L_{ls} + L_{md}) i_{sd} + \omega L_{md} i_{fd} + \omega L_{md} i_{kd} - (L_{ls} + L_{mq}) \frac{di_{sq}}{dt} + L_{mq} \frac{di_{kq}}{dt}$$

$$v_{fd} = R_{fd} i_{fd} - L_{md} \frac{di_{sd}}{dt} + (L_{fd} + L_{md}) \frac{di_{fd}}{dt} + L_{md} \frac{di_{kd}}{dt}$$

$$0 = R_{kd} i_{kd} - L_{md} \frac{di_{sd}}{dt} + (L_{kd} + L_{md}) \frac{di_{kd}}{dt} + L_{md} \frac{di_{fd}}{dt}$$

$$0 = R_{kq} i_{kq} - L_{mq} \frac{di_{sq}}{dt} + (L_{kq} + L_{mq}) \frac{di_{kq}}{dt}$$

..... (3.9)

where

R_s - armature phase resistance,

- ω - rotor speed,
- v_d - armature d axis terminal voltage,
- v_q - armature q axis terminal voltage,
- i_d - armature d axis terminal current,
- i_q - armature q axis terminal current,
- i_{sd} - d axis phase current,
- i_{sq} - q axis phase current,
- v_{fd} - field winding terminal voltage (reflected to the stator),
- i_{fd} - field winding terminal current (reflected to the stator),
- i_{kd} - d axis damper winding current (reflected to the stator),
- i_{kq} - q axis damper winding current (reflected to the stator),
- Λ_d - total armature flux in d axis,
- Λ_q - total armature flux in q axis.

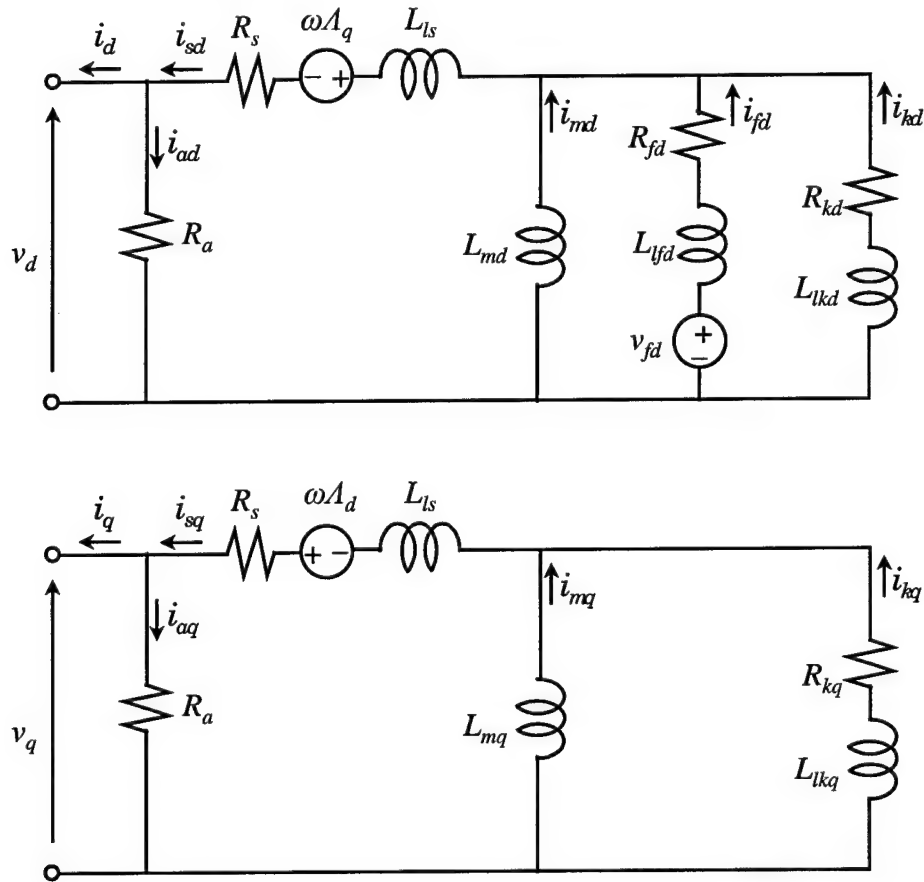


Figure 3.19. Equivalent circuit of the synchronous generator in dq coordinates.

In this model, we assume a constant rotor speed. This is justified for studying dynamic behavior of the PDS since changes in the generator load would not likely affect the aircraft engine speed. If it is necessary to include mechanical dynamics into consideration, a mechanical equation of motion should be added to the equations above. According to the interconnection rules for voltages and currents specified above, a SIMULINK model for the generator must have a current port as an input and a voltage port as an output. They will be coupled with the boost rectifier's input voltage port and the output current port. The phase

currents i_{sd} and i_{sq} , being state variables, cannot be the input variables at the same time. Therefore, a fictitious terminal resistance R_a was added to the model. This resistance has a relatively high value and does not affect other variables. It can also account for magnetic losses in the generator.

A SIMULINK model for this subsystem could be built directly by drawing a block diagram corresponding to the equations (Equation 3.9) similarly to the block diagram for the L-C filter in Figure 3.6. However, because of complexity of the equations, this approach would be too cumbersome. An alternative approach of building a SIMULINK model uses the state-space SIMULINK block. Equation 3.9 represent a linear system with state variables i_{sd} , i_{sq} , i_{kd} , i_{kq} , i_{fd} , input variables i_d , i_q , v_{fd} , and output variables v_d , v_q . The equations are solved for the state derivatives and represented in state-space form (the details of the solution are given in Appendix C):

$$\begin{aligned} \frac{d}{dt} \begin{bmatrix} i_{sd} \\ i_{sq} \\ i_{kd} \\ i_{kq} \\ i_{fd} \end{bmatrix} &= A_g \begin{bmatrix} i_{sd} \\ i_{sq} \\ i_{kd} \\ i_{kq} \\ i_{fd} \end{bmatrix} + B_g \begin{bmatrix} i_d \\ i_q \\ v_{fd} \end{bmatrix} \\ \begin{bmatrix} v_d \\ v_q \end{bmatrix} &= C_g \begin{bmatrix} i_{sd} \\ i_{sq} \\ i_{kd} \\ i_{kq} \\ i_{fd} \end{bmatrix} + D_g \begin{bmatrix} i_d \\ i_q \\ v_{fd} \end{bmatrix}, \end{aligned} \quad \dots (3.10)$$

where A_g , B_g , C_g , D_g are the state-space matrices.

It can be seen from Equation 3.9 that the output voltage of the synchronous generator significantly depends on its load current. In order to keep the output voltage at a specified level regardless of load conditions, a voltage feedback loop is introduced into the SIMULINK model. The feedback provides the rms value of the output voltage calculated from its dq components according to the formula,

$$v_{rms} = \frac{1}{\sqrt{2}} \sqrt{v_d^2 + v_q^2} \quad \dots (3.11)$$

The field winding voltage controller, which is modeled here as a simple gain, uses the output voltage error signal. Since the dc distribution bus voltage is precisely regulated by the boost rectifier, the presence of a small steady-state error in the generator output voltage is not a problem.

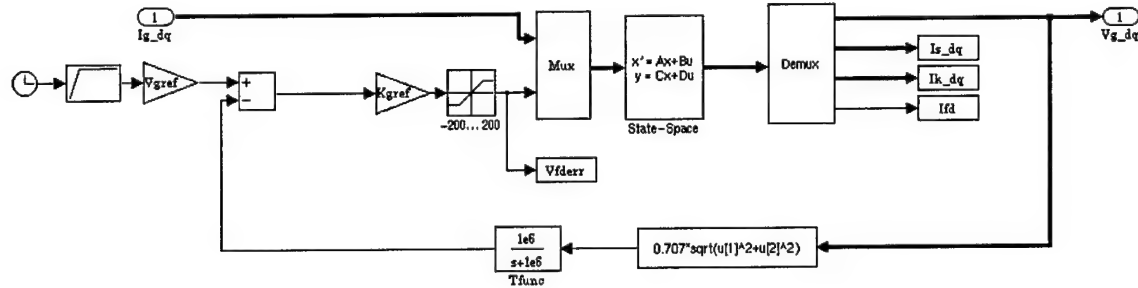


Figure 3.20. Closed-loop SIMULINK model of the synchronous generator in dq coordinates.

A complete SIMULINK model of the synchronous generator is presented in Figure 3.20. A soft-start feature is added to avoid large transients in the beginning of simulation. The transfer function T_{func} with a very high frequency pole is introduced into the feedback path in order to break an algebraic loop in the model, which may cause numerical problems in large system simulations. The transfer function does not affect the model operation otherwise.

3.6.3 Three Phase Boost Rectifier Modeling

The boost rectifier provides front-end three phase-to-dc power conversion from the synchronous generator to the dc distribution bus. The rectifier operates with unity power factor and draws sinusoidal currents from the three phase source. When the output current reverses its direction, the boost rectifier reverses the power flow through it and operates as a voltage source inverter.

The power stage of the boost rectifier as modeled in this research is shown in Figure 23. The output capacitor ESR is taken into consideration to reflect the converter dynamics more accurately. By averaging the switching action of the semiconductor switches and applying the dq transformation to the resulting average model, a large signal

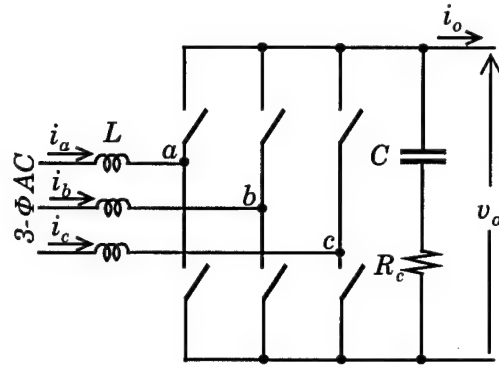


Figure 3.21. Power stage topology of the boost rectifier.

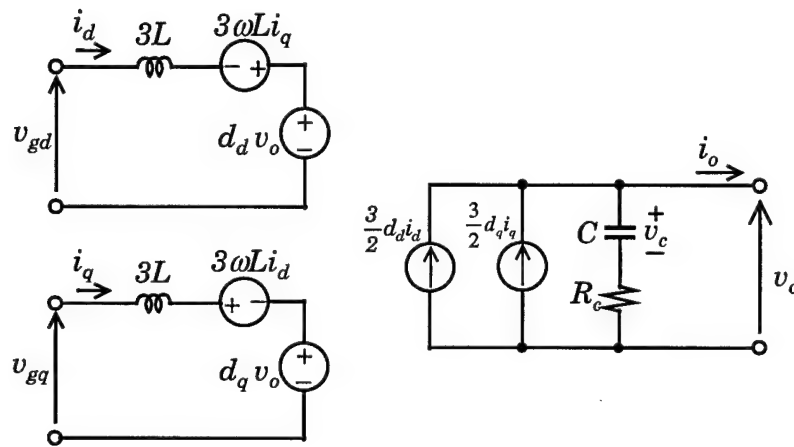


Figure 3.22. Average model of the boost rectifier in dq coordinates.

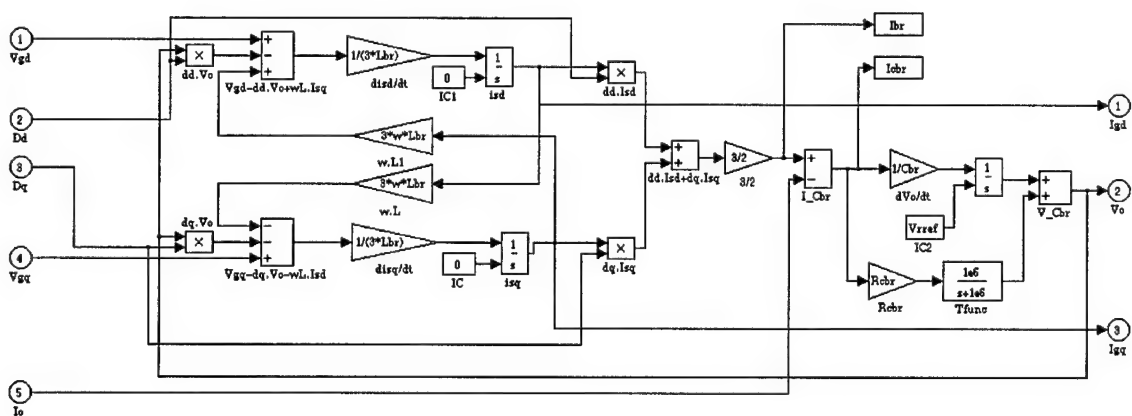


Figure 3.23. SIMULINK model of the boost rectifier power stage in dq coordinates.

average model in dq coordinates is obtained [14,15]. The equivalent circuit is shown in Figure 3.22 and described by equations,

$$\begin{aligned}
\frac{di_d}{dt} &= \frac{1}{3L}(v_{gd} + 3\omega Li_q - d_d v_o) \\
\frac{di_q}{dt} &= \frac{1}{3L}(v_{gq} - 3\omega Li_d - d_q v_o) \\
\frac{dv_c}{dt} &= \frac{1}{C}\left(\frac{3}{2}(d_d i_d + d_q i_q) - i_o\right) \\
v_o &= v_c + R_c\left(\frac{3}{2}(d_d i_d + d_q i_q) - i_o\right),
\end{aligned}
\tag{3.12}$$

where,

- i_d, i_q - input currents in dq coordinates,
- v_{gd}, v_{gq} - input voltages in dq coordinates,
- i_o - output dc current,
- v_o - output dc voltage,
- d_d, d_q - duty cycle in dq coordinates,
- ω - angular frequency,
- L - phase inductance,
- C - output capacitance,
- R_c - capacitor ESR.

A SIMULINK model derived from these equations is shown in Figure 3.23. The model accepts dq voltages, dq duty cycles, and dc output current as input variables and supplies dc voltage and dq currents as output variables.

The control diagram for the boost rectifier is shown in Figure 3.24. It includes the decoupling terms $3\omega L/V_o$ to eliminate cross-coupling between the d and q channels so that they could be controlled independently [15]. Perfect decoupling is achieved at a specified line frequency and output voltage and is load-independent, which satisfies the conditions of this research.

The voltage mode feedback control is provided with a feedback voltage loop and two current loops. The current loops control the decoupled channels of the power stage independently by adjusting their duty cycles. They both use proportional controllers with the same gain K_{dq} . The reference signal for the q channel is set to zero since the input currents should be in phase with the input voltages. The reference signal for the d channel is provided by the voltage loop compensator. The closed-loop transfer functions for both current loops are load-independent. The voltage loop uses a proportional-integral compensator with a transfer function

$$H_v(s) = K_{vp} + \frac{K_{vi}}{s} \tag{3.13}$$

which provides fast response and no steady-state error in the output voltage..

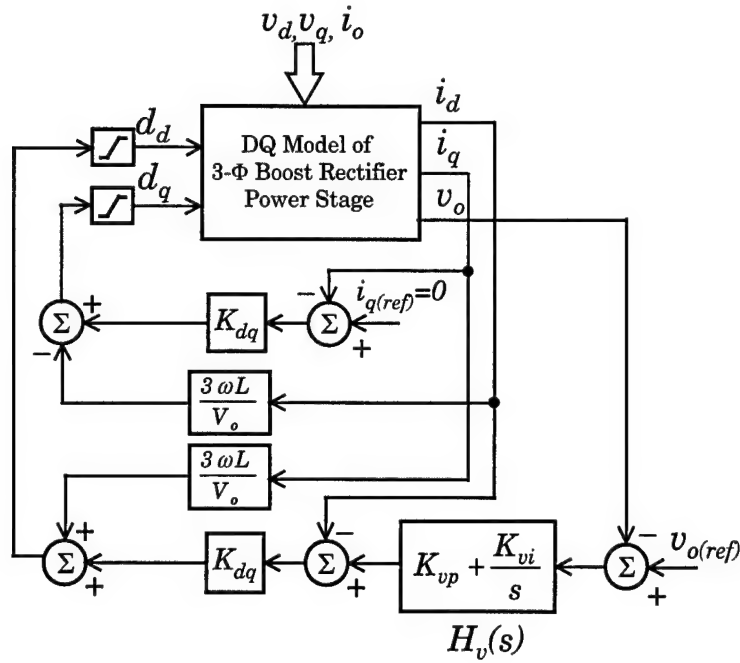


Figure 3.24. Control diagram of the boost rectifier.

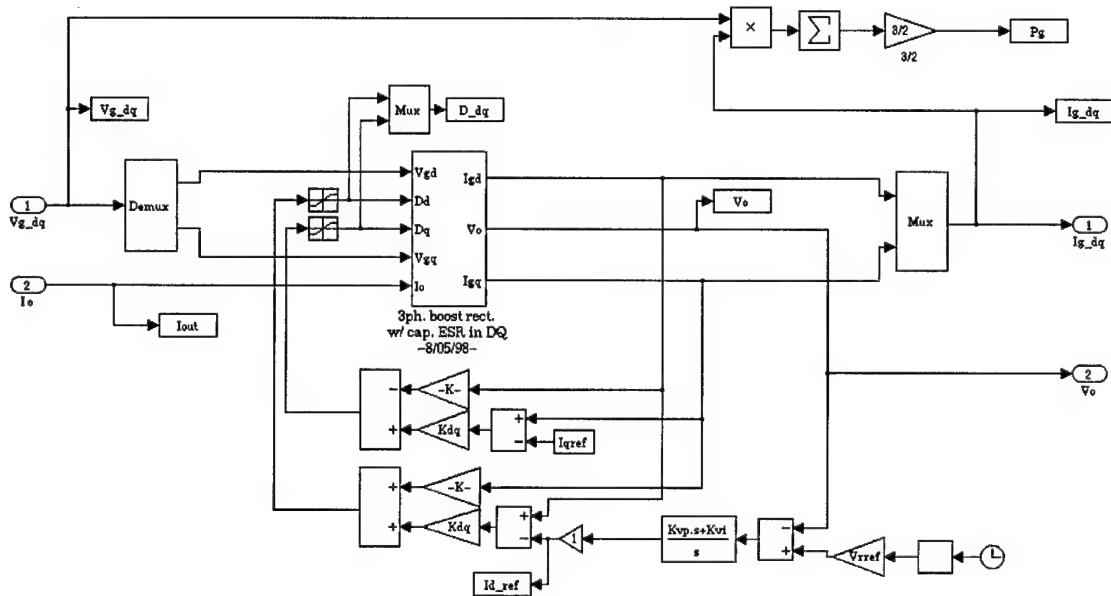


Figure 3.25. Closed-loop SIMULINK model of the boost rectifier in dq coordinates.

The control-to-output transfer function v_o/i_{dref} significantly depends on the load and direction of the power flow, therefore the voltage loop compensator can be optimized only for a specific load. In order to use this type of control for the whole range of loads under bidirectional power flow conditions as assumed in this research, a compromise in the compensator design was required. The resulting design provided a low

closed-loop bandwidth yet stable operation and acceptable transient response under all load conditions. The complete closed-loop SIMULINK model for the boost rectifier in dq coordinates is shown in Figure 3.25. It uses the SIMULINK model of the rectifier power stage as a subsystem.

3.7 Switched Reluctance Generator Modeling

A switched reluctance machine can be used as a starter/generator in the PDS instead of a synchronous generator. This approach eliminates the need in a three-phase-to-dc converter (boost rectifier), discussed above. The switched reluctance generator (SRG) is connected directly to the DC bus through its own inverter, which is a mandatory part of the machine. A schematic of one channel of an SRG developed for aircraft applications is shown in Figure 3.26; the details of its operation and testing results are covered in [16-19]. Another advantage of an SRG compared with a synchronous generator-boost rectifier combination is that the SRG has a simpler rotor design (no windings), which improves its reliability and makes simpler its maintenance. A certain effort was made in the framework of this research in order to develop a SIMULINK model of the SRG that can be effectively used for simulation and analysis as a part of the global PDS model.

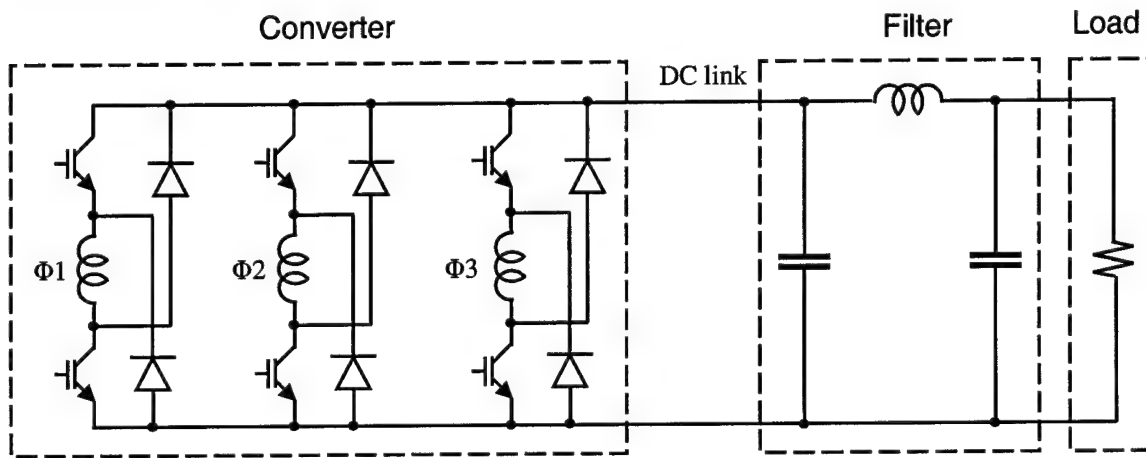


Figure 3.26. Switched reluctance starter/generator converter circuit diagram.

The SRG presents unique challenges in modeling. Like in a synchronous generator, the winding inductances of the SRG depend on the rotor position. In addition, they depend on the phase current because the magnetic flux of a phase always saturates in the aligned position and returns to non-saturated state when the phase goes out of alignment. Therefore, magnetic properties of the material must be taken into account. The phase voltage and current waveforms are not sinusoidal. Unlike the synchronous machine, there is no transformation of variables that could transform the SRG voltages and currents into dc variables. The majority of models built for a switched reluctance machine (for example, [20]) follow a straightforward approach that includes modeling of all details of its operation. This results in a detailed

model, which is very complex, computationally intensive, not suitable for control design, and cannot be used as a part of the global PDS model for simulation and analysis.

An average type of model for the SRG could be built based on assumption made in [21]. Figure 3.27 shows how the DC link current is made up of individual phases' currents. With a certain degree of idealization, this current may be viewed as a discrete function of time, in which each step corresponds to the current of the phase active at this moment. This approach results in a discrete average model of a SRG [21] shown in Figure 3.28. In this model, the DC link current is represented by a current source controlled with a discrete controller. The rest of the model is a low-pass DC link filter. The value of the current is constant over one electrical cycle but may change from cycle to cycle. The controller adjusts the DC link current in order to maintain the output voltage at a specified level. The discrete controller incorporates two time delays: a constant delay introduced by the microprocessor control, and a variable delay, which comes from a discrete nature of the model and depends on the SRG speed. As shown in [21], the model produced results in a good agreement with the experimental results.

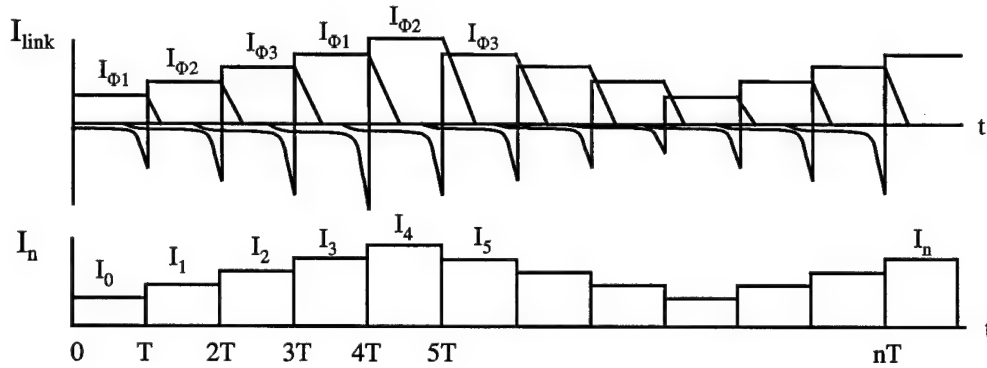


Figure 3.27. Switched reluctance starter/generator converter discrete average modeling concept.

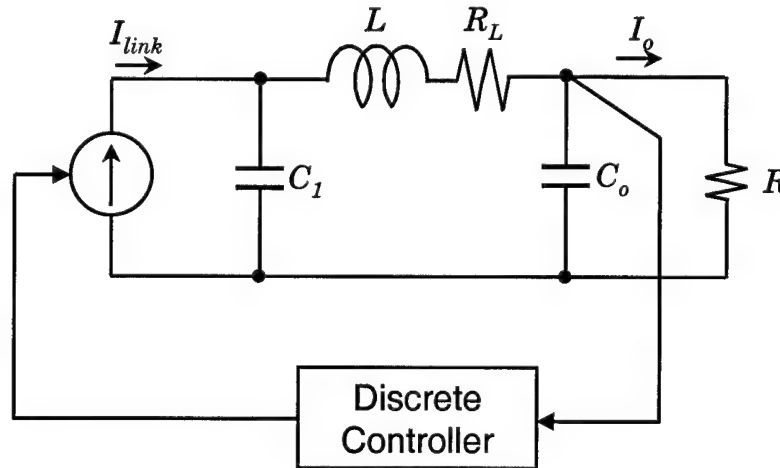


Figure 3.28. Switched reluctance starter/generator converter discrete average model.

Although the model in Figure 3.28 is a considerable step from the detailed model towards a simple, computationally efficient average model of the SRG, the discrete nature of the model still makes it unsuitable for the purpose of this research. A discrete model of the SRG included into the overall PDS model will make it computationally inefficient because all the discrete steps will have to be processed by the integration routine. The discrete model as a part of the PDS will not allow using frequency domain techniques for stability analysis and control design. To overcome these difficulties, a continuous SRG model was built in this research by further developing of the discrete averaging concept presented above.

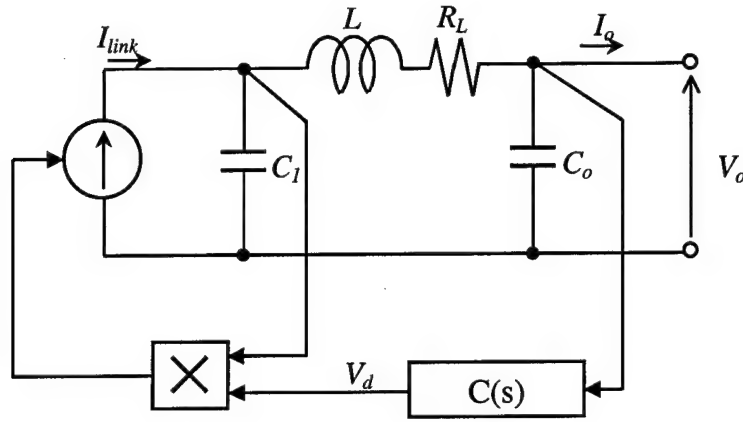


Figure 3.29. Switched reluctance starter/generator converter continuous average model.

The new model is based on a further simplification of the discrete DC link current waveform shown in Figure 3.27 with an assumption that the current changes continuously. This assumption significantly limits the frequency range in which this model is valid since the lowest phase current frequency, which occurs at ground idle engine speed, is only 5.4kHz. Although different control strategies are possible for the SRG, we assume that the output voltage feedback control is used. The model is shown in Figure 3.29. An analog compensator with transfer function $C(s)$ processes the output voltage error and produces the control signal V_d . Voltage across the capacitor C_1 is the DC link voltage. As shown in [18], current generated by a phase during its generation period is determined by current built up in the phase during its excitation period (Figure 3.30). The current built up in the phase (the amount of excitation energy) depends both on the time when the switches are closed during the excitation period and the DC link voltage. For an inductor, the current built up in it is proportional to the voltage across the inductor and the time during which the voltage is applied, according to the formula,

$$V = L \frac{\Delta I}{\Delta t} \quad \dots (3.14)$$

Therefore, an assumption that the generated DC link current is equal to the product of the DC link voltage and the feedback control signal V_d as shown in Figure 3.29s made. This is an analogy with a PWM switch

that controls excitation of the phase. V_d is a control signal proportional to the time duration of the excitation switches (Figure 3.26) being closed. It may also be viewed as duty cycle of the switches within the electrical cycle of the phase.

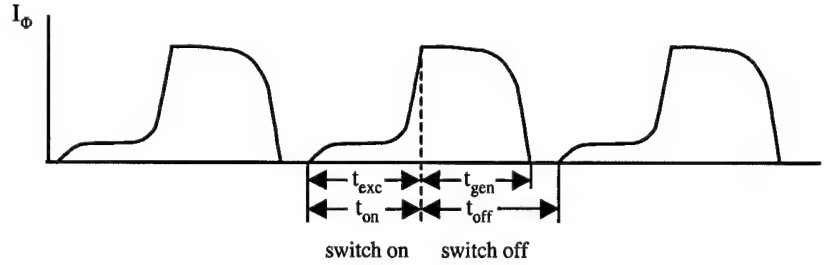


Figure 3.30. Switched reluctance generator phase current waveform.

It is seen from the model that with constant excitation time (open loop operation) the system may be unstable depending on the load, which agrees with the analysis given in [18]. The model equations are as follows,

$$i_{link} = v_{C_1} \cdot v_d \quad \dots (3.15)$$

$$v_d(s) = C(s)v_o(s)$$

$$L \frac{di_L}{dt} = v_{C_1} - v_o - R_L i_L$$

$$C_1 \frac{dv_{C_1}}{dt} = i_{link} - i_L$$

$$C_o \frac{dv_o}{dt} = i_L - i_o$$

where,

- i_{link} - DC link current,
- v_{C_1} - DC link voltage,
- v_d - control signal,
- v_o - output voltage,
- i_L - inductor current,
- i_o - output current,
- L - filter inductance,
- R_L - filter inductor ESR,
- C_1 - DC link capacitor,
- C_o - output capacitor.

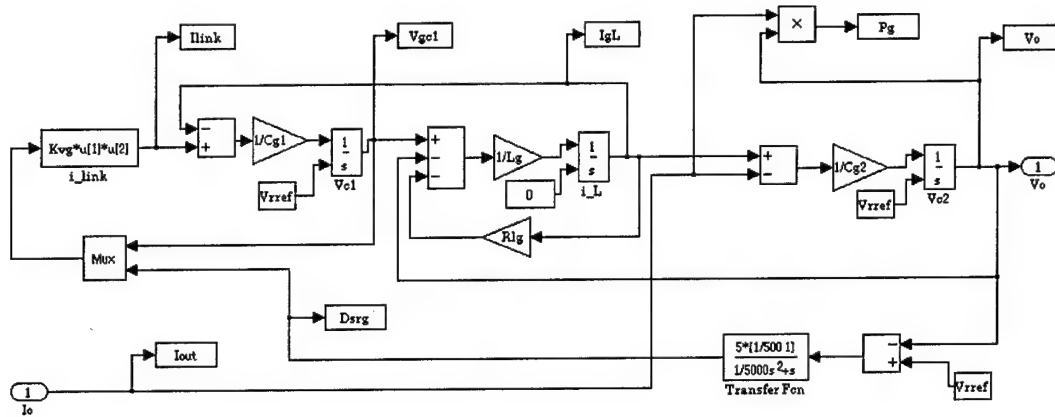


Figure 3.31. SIMULINK model of the switched reluctance starter/generator converter.

A SIMULINK block diagram based on the model in Figure 3.29 is shown in Figure 3.31.

3.8 Modeling of Flight Actuators

3.8.1 Electromechanical Actuator Modeling

An electromechanical actuator driving an inboard spoiler surface of an aircraft was chosen in this research as an example of a flight actuator as a part of the PDS. A SIMULINK model of the actuator-surface system was developed by Lockheed Martin Control Systems in Johnson City, New York.

A system diagram of the electromechanical actuator (EMA) is shown in Figure 3.32. It consists of a dc-dc power converter feeding a dc motor, which moves the inboard spoiler surface through a mechanical transmission consisting of a gearbox and a ball screw mechanism. The dc-dc converter is connected to the dc power distribution bus through an input filter, whose purpose is to prevent the switching ripple of the converter from going to the bus. Finally, a multiloop feedback controller is employed to precisely control the surface deflection.

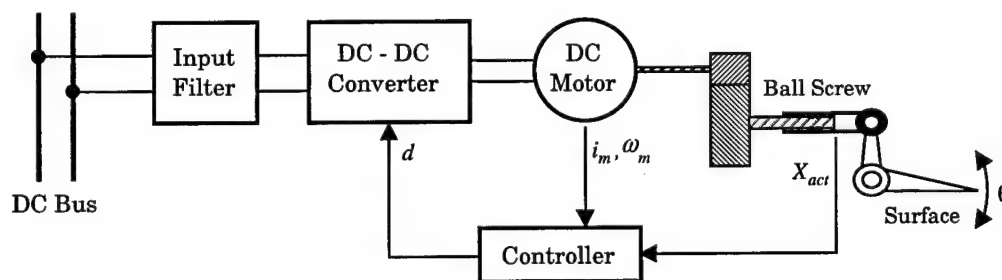


Figure 3.32. Electromechanical actuator system diagram.

A typical EMA architecture of a modern aircraft employs a three-phase dc brushless motor fed by a dc-to-three phase inverter; however, it was agreed that the use of a dc-dc converter and a dc motor models instead will not affect essential features of the subsystem dynamics. A SIMULINK model for the EMA subsystem (Figure 3.33) follows its structure and consists of six functionally complete modules. The input filter is modeled as an L-C filter, whose modeling was already discussed above (Figure 3.5 and Figure 3.6).

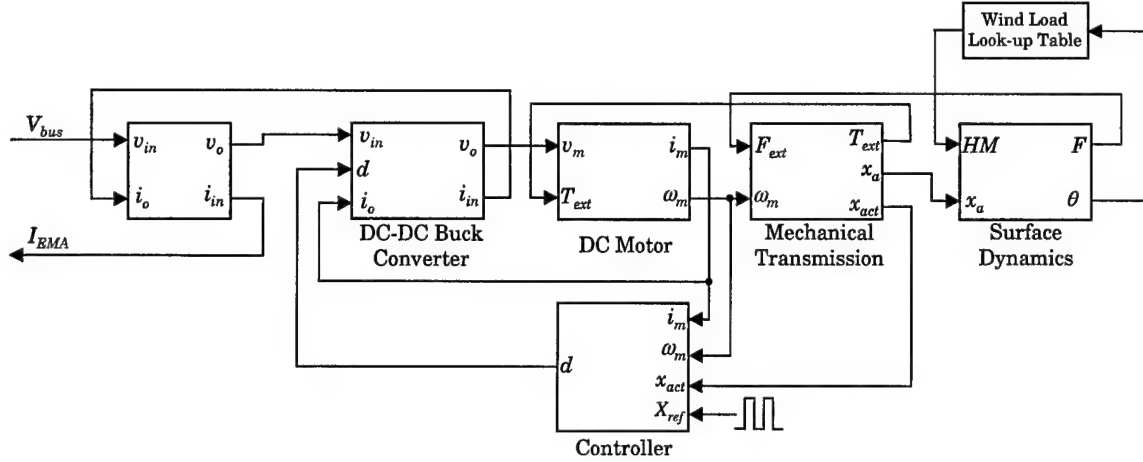


Figure 3.33. Electromechanical actuator SIMULINK block diagram.

The dc-dc converter module represents a power stage of the buck converter without an output L-C filter since its load (dc motor) provides sufficient filtering effect due to its own inductance. Therefore, the average model of the PWM switch shown in Figure 3.8 and Figure 3.9 was used for the dc-dc converter. A SIMULINK model for a separately excited dc motor is shown in Figure 3.34. The model is derived from the motor equations,

$$\begin{aligned} v_m &= K_e \omega_m + i_m R + L \frac{di_m}{dt} \\ K_t i_m - T_{ex} &= B_m \omega_m + J \frac{d\omega_m}{dt} \end{aligned} \quad \dots (3.16)$$

where,

- v_m - armature voltage,
- i_m - armature current,
- ω_m - armature angular speed,
- T_{ex} - external (load) torque applied to the shaft,
- L - armature inductance,
- R - armature resistance,
- J_m - armature inertia,
- B_m - viscous friction coefficient,
- K_e - back-emf constant,
- K_t - electromagnetic torque constant.

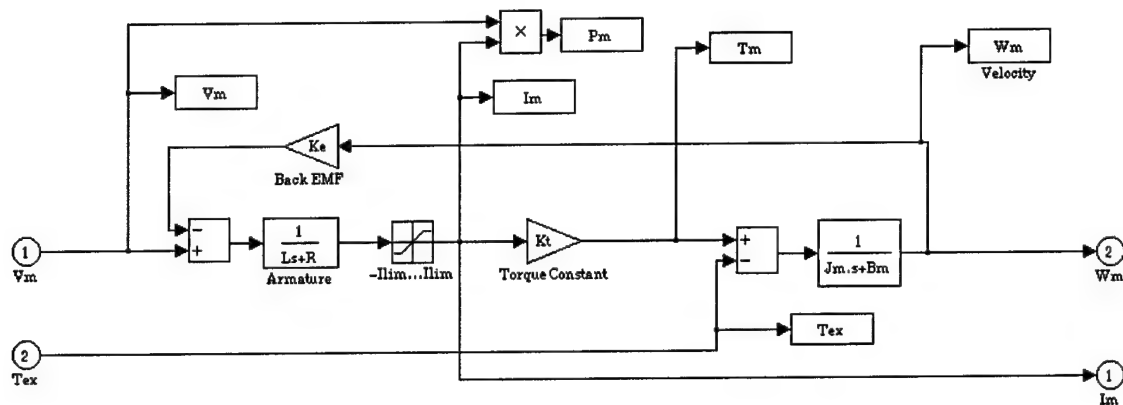


Figure 3.34. SIMULINK model for a separately excited dc motor.

The mechanical actuator module includes the gears and the ball screw mechanism. A SIMULINK model for it (Figure 3.35) takes into account the inertia, damping, and stiffness of the ball screw mechanism as well as stiffness of the bearing structure.

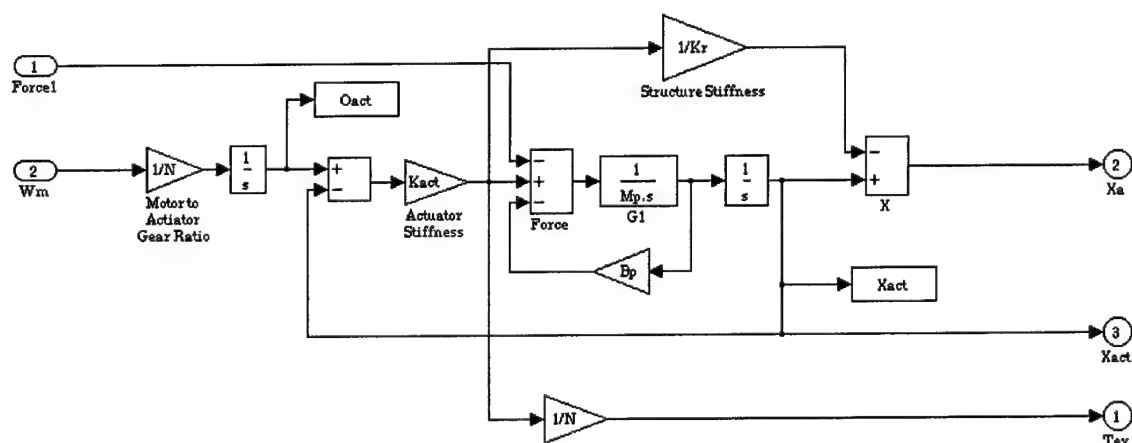


Figure 3.35. SIMULINK model for the mechanical transmission of the EMA.

A SIMULINK model for the surface dynamics is shown in Figure 3.36. The model reflects the horn stiffness, surface inertia and damping, and a nonlinear relationship between the mechanical actuator movement and the surface deflection angle. A feedback controller of the entire EMA subsystem (Figure 3.37) controls the duty cycle of the dc-dc converter according to the actuator position command. The controller employs the motor current, motor speed, and the actuator position feedback loops.

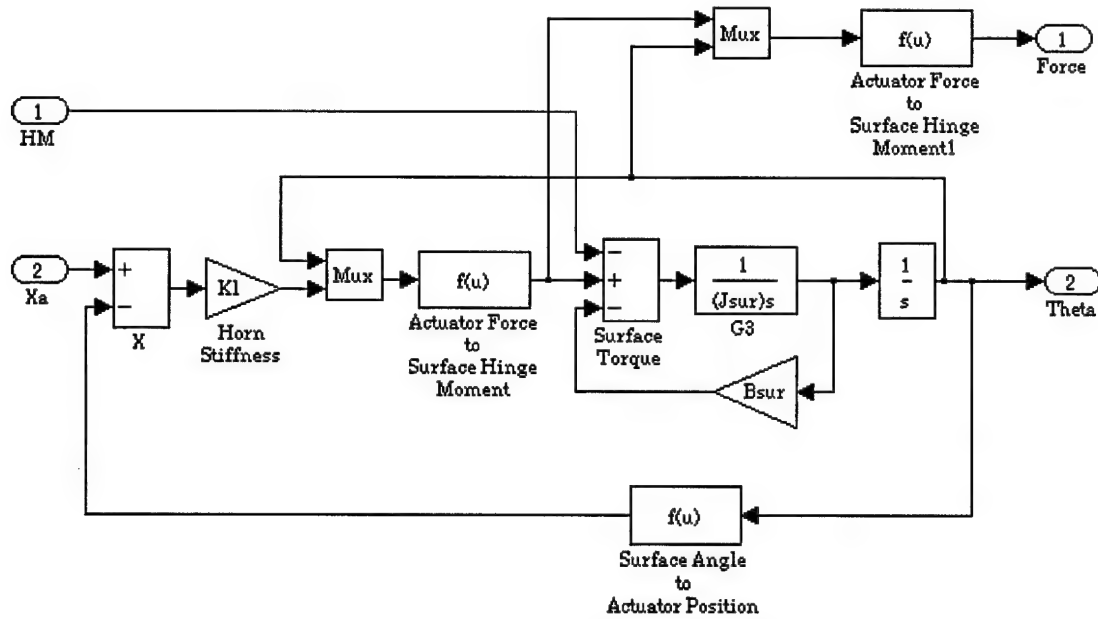


Figure 3.36. SIMULINK model for the surface dynamics.

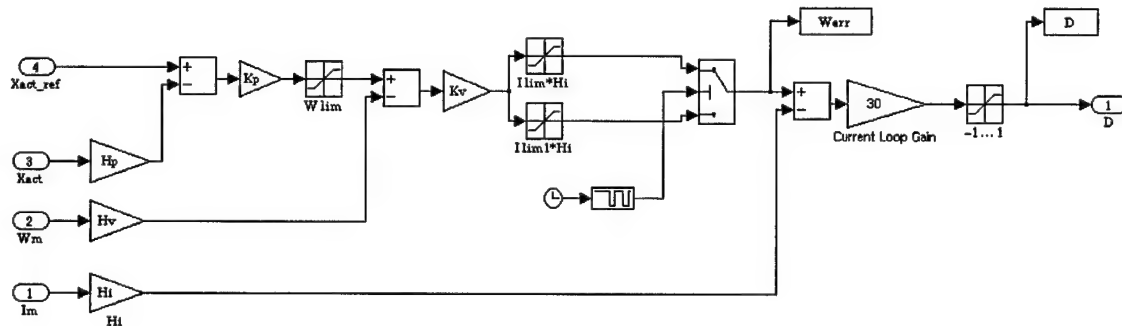


Figure 3.37. SIMULINK model for the feedback controller.

A part of the EMA model is a SIMULINK look-up table containing an approximation of the wind load on the spoiler surface as a function of its deflection angle. This table was used in simulations corresponding to the normal flight conditions. Another possible scenario investigated in this research was testing the system on the ground, which assumed that the wind load to the surface is equal to zero.

3.8.2 Electrohydrostatic Actuator Modeling

Another model developed by Lockheed Martin Control Systems as an example of a flight actuator modeling was an electrohydrostatic actuator driving the elevator surface. A system diagram of the actuator is shown in Figure 3.38, and its SIMULINK model – in Figure 3.39.

The electrohydraulic actuator (EHA) model is very similar to the EMA model described above. The model employs a hydraulic actuator consisting of a hydraulic pump and a cylinder instead of a mechanical actuator to convert the motor rotation to the surface movement.

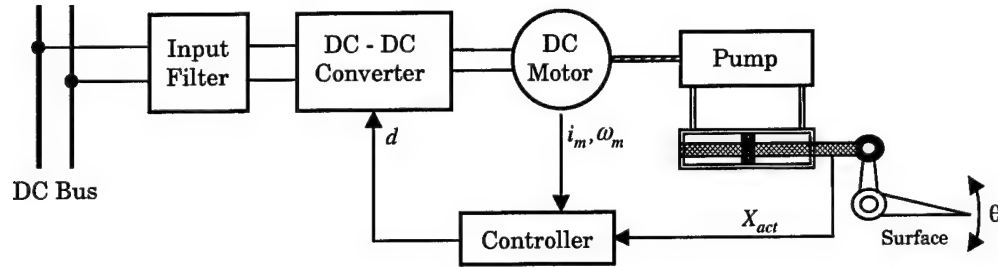


Figure 3.32. Electrohydraulic actuator system diagram.

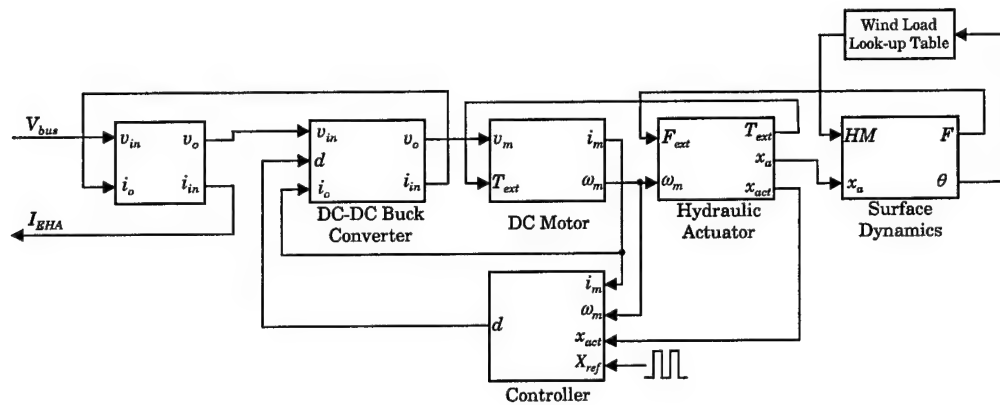


Figure 3.39. Electrohydraulic actuator SIMULINK block diagram.

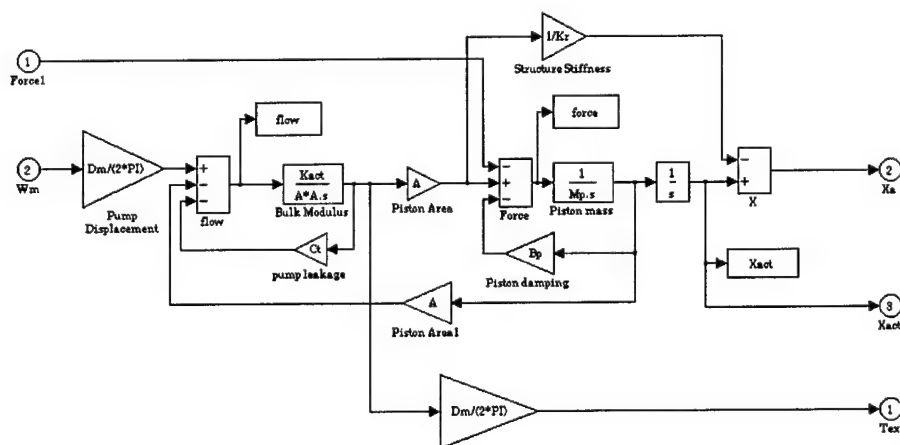


Figure 3.40. Hydraulic actuator SIMULINK model.

A SIMULINK model of the hydraulic actuator is shown in Figure 36. It takes into account the pump leakage, the piston inertia and damping, and the bearing structure stiffness. All the other components of the EHA model have the same structure as the corresponding EMA components but different parameter values. The EHA model was used in simulations in the same way as the EMA model.

3.9 Smart Actuator Modeling

3.9.1 Introduction

Piezoelectric actuators have been widely used for active vibration control of structures. One important application of this technology is the use of piezoelectric actuators for alleviating the “tail buffeting” problem in a twin tail aircraft. The buffet loads acting on the tail surface cause excessive wear and tear that significantly reduce the lifetime of the aircraft and increase repair and maintenance costs. Piezoelectric actuators mounted at the root of the tail and on the surface are controlled to actively suppress the effect of the buffet loads on the tail surface. A simplified schematic of the actively controlled tail-surface is shown in Figure 3.41. The amplifier to drive the piezoelectric actuators is a current controlled switch mode converter. A dynamic model for the actively controlled tail structure has been developed based on data from wind-tunnel tests performed at the NASA-Langley Research Center. This model is then integrated into a power distribution system and its interaction with the DC power bus is studied.

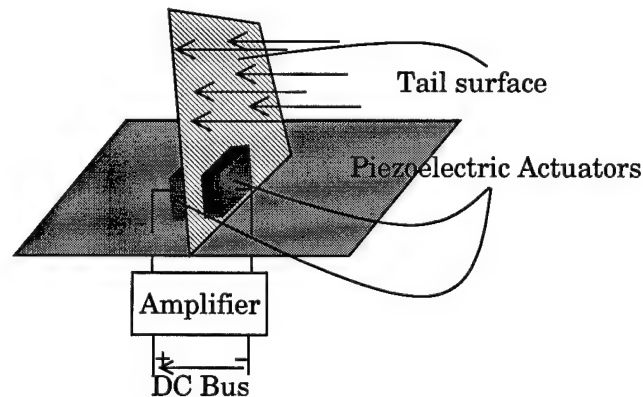


Figure 3.41. Actively controlled tail surface with piezoelectric actuators and amplifier

3.9.2 Modeling

The one-dimensional linear coupled electromechanical constitutive relations between the strain ϵ_1 , stress σ_1 , electric field E_3 , and electric displacement D_3 , are given below:

$$D_3 = K_{33}^\sigma E_3 + d_{31} \sigma_1$$

..... (3.17)a

$$\varepsilon_1 = d_{31} E_3 + s_{11}^E \sigma_1$$

..... (3.17)b

where, K_{33} and s_{11} are the permittivity and compliance (reciprocal of the Young's modulus) respectively and d_{31} is the transverse piezoelectric charge constant. The first index in the subscripts indicates the direction of the electrical component and the second index indicates the mechanical direction. Equation 3.17a states that the electric displacement is the superposition of the direct piezoelectric effect and the applied field times the permittivity. Equation 3.17b states that the strain is the superposition of Hooke's law the indirect effect.

The piezoelectric actuator essentially behaves like a capacitor whose voltage is the sum of two components:

1. The direct capacitive effect where $v = \frac{1}{C} \int i dt$ and
2. A contribution from the mechanical stress.

Figure 3.42 illustrates the voltage contribution from the direct capacitive effect.

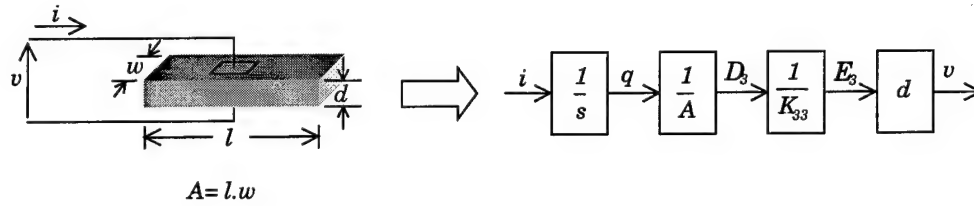


Figure 3.42. Voltage due to direct capacitive effect

The contribution from the mechanical component is derived as follows:

Figure 3.43 shows a schematic of a bending motor. A bending motor is formed by

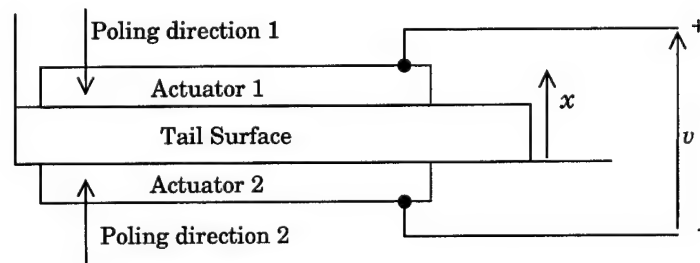


Figure 3.43. Bending Motor

bonding two piezoelectric actuators on either side of the substructure. An electric field applied opposite to the poling direction of the top actuator and along that of the bottom actuator will cause the top material to expand laterally and the bottom material to laterally contract thereby inducing bending of the surface. The total moment at the cross section of the surface is the sum of the moment M_S caused by the bending of the surface and the moment M_A caused by the bending of the actuator mounted on the surface. This sum is equal to the bending moment M_A induced in the structure by the actuators due to the applied electric field as shown in Equation 3.18.

$$M_S + M_A = M_A \quad \dots (3.18)$$

The net mechanical stress σ_m , in the piezoelectric actuators is then given by the difference between the stress induced by the electric field and the stress caused by the bending in the surface. Using Equation 3.17b, the voltage contribution from the mechanical component can then be given by:

$$V_m = \frac{d_{31}}{K_{33}^\sigma} d\sigma_m \quad \dots (3.19)$$

The modal equations are represented by n-uncoupled single degree of freedom systems each with a structural damping and resonant frequency. With reference to Figure 3.41, we assume that the tail surface can be modeled as a single degree of freedom system with a given structural damping and resonant frequency driven by an equivalent generalized force f and the buffet load f_{ext} . The dynamic equations are then given by:

$$\ddot{x} + 2\zeta\omega_n\dot{x} + \omega_n^2x = f + f_{ext} \quad \dots (3.20)$$

The generalized force f is related by a constant to the net mechanical stress σ_m . The complete block diagram of the actuator-tail structure is shown in Figure 3.44. The constant K_1 relates the tip displacement of the tail surface to the stress on the piezoelectric actuators and K_2 relates the net mechanical stress σ_m on the actuators to the generalized force acting on the tail surface. An important feature of this particular model is that explicitly identifies both the forward and reverse power flow through the piezoelectric actuator.

The objective of the active vibration control problem is to minimize the effect of the net force f_{ext} on the acceleration a , of the tip of the tail (Figure 3.41). Thus, a closed loop system is required that will effectively minimize the transfer function between the external force and the tip acceleration. The mechanical dynamics of the tail surface, represented by the transfer function in Figure 3.44, can be equivalently represented by the block diagram shown in Figure 3.45.

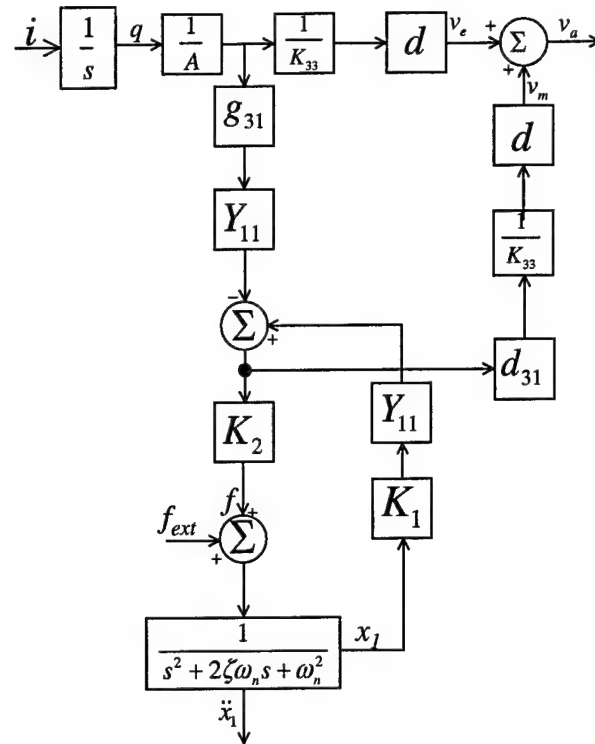


Figure 3.44. Block diagram of the piezoelectric actuator.

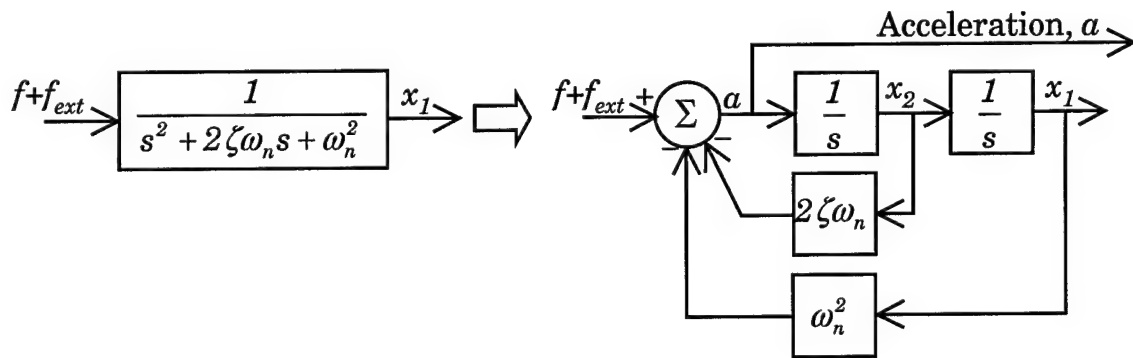


Figure 3.45. Equivalent representation of the mechanical dynamics

The closed loop system will involve a switched mode power amplifier that will drive the piezoelectric actuator such that an equivalent compensating force is applied to the tail to minimize the tip acceleration and hence reduce wear and tear. The power amplifier will be current controlled with the reference current provided by an outer tip-acceleration feedback loop.

3.9.3 Drive Amplifier

The power amplifier used to provide the required drive current to the piezoelectric actuator is a single-phase DC-AC inverter that feeds off a 270V DC bus. A schematic of the amplifier is shown Figure 3.46.

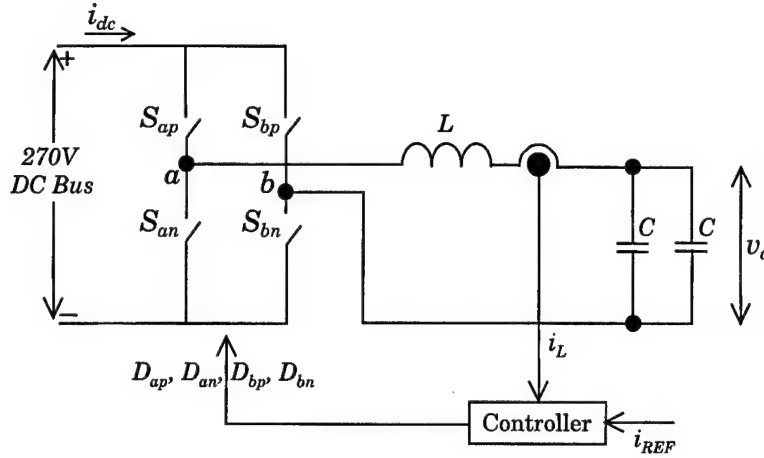


Figure 3.46. Schematic of amplifier

The amplifier supplies a sinusoidally pulse width modulated voltage whose fundamental is at the required magnitude and frequency. The average voltage applied between a and b can be written in terms of the DC bus voltage and the duty cycles of the switches S_{ap} and S_{bp} as follows:

$$v_{ab} = (d_{ap} - d_{bp}) V_{dc} = d_{ab} V_{dc} \quad \dots (3.21)$$

The controller provides the duty cycles to the inverter in response to a reference current command to be driven into the actuator. The two capacitors in parallel shown in Figure 3.46 represent the two piezoelectric actuators on either side of the beam in the bending motor configuration (Figure 3.43). The poling directions of the two actuators are opposite to one another to induce bending in the beam. But their electrical characteristics as capacitive elements do not depend on their poling directions. Hence, if the contribution to the voltage across the actuators is neglected the two actuators simply appear as two capacitors in parallel loading the amplifier. The state equations for the amplifier model shown in Figure 3.46 are given below:

$$\begin{aligned} \frac{di_L}{dt} &= \frac{1}{L} (d_{ab} \cdot V_g - v_a) \\ \frac{dv_a}{dt} &= \frac{1}{2C} i_L \end{aligned} \quad \dots (3.22)$$

3.9.4 Controller Design

The goal of the active control problem as mentioned in the previous sections is to minimize the tip acceleration of the wing in response to the external force input. The closed loop controller essentially determines a command current to be driven into the piezoelectric actuators, which in turn generate an equivalent compensating force. The design of the controller involves the determination of the relevant open-loop transfer functions. A block diagram of the open-loop plant to be controlled is shown in Figure 3.47.

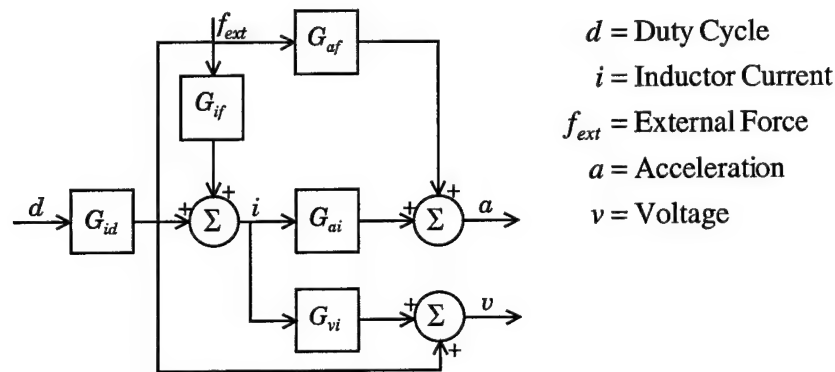


Figure 3.47. Block Diagram of Open Loop System

The multi-loop controller with current, voltage and acceleration control loops as shown in Figure 3.48 was designed. The bode plot of transfer function between the external force and the tip acceleration of the wing is shown in Figure 3.49.

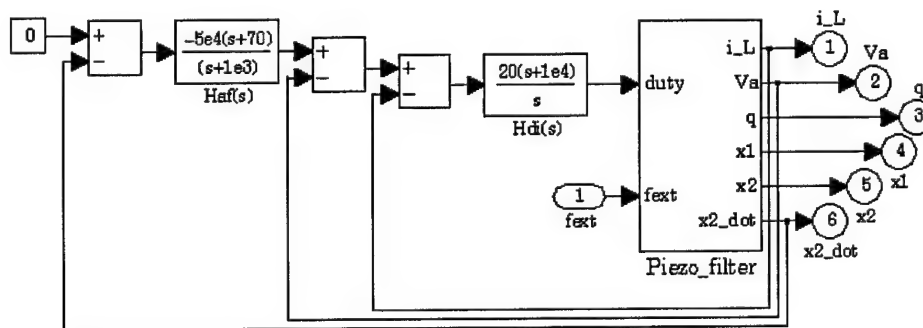


Figure 3.48. Block Diagram of the Closed Loop System

It can be seen that the controller introduces additional damping into the dynamics of the tail surface. The acceleration response of the tip under open and closed loop conditions when the tail is subjected to an

external force input at its resonant frequency of 14Hz is shown in Figure 3.50. It can be seen that for the same external force input, the tip acceleration is minimized appreciably by the closed loop controller.

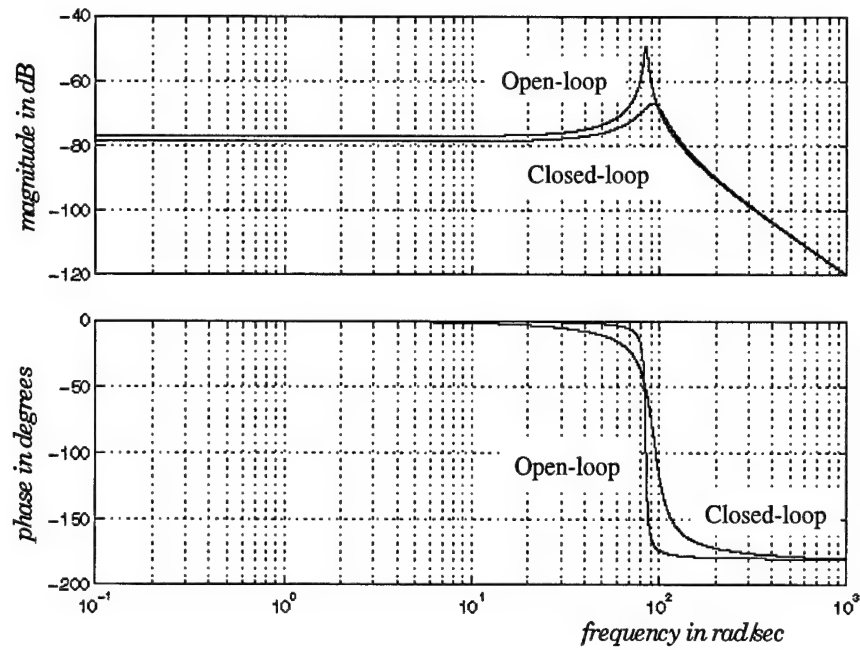


Figure 3.49. Transfer Function between External Force and Tip-Acceleration of Tail Surface

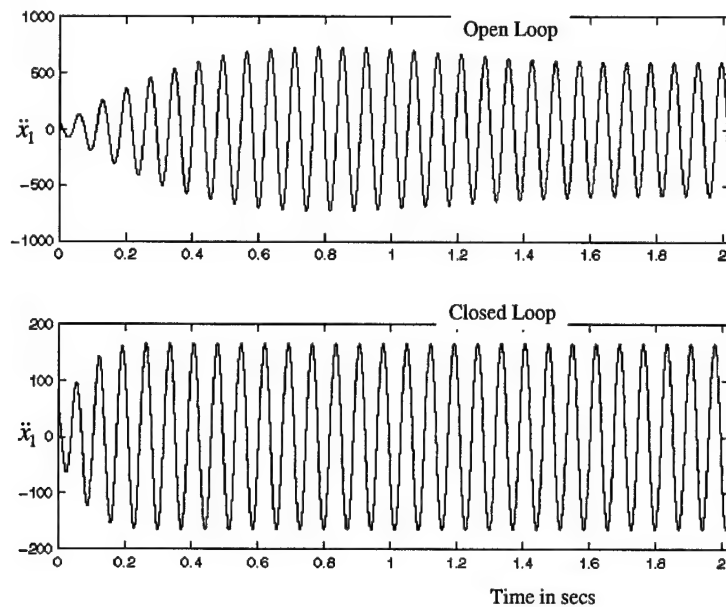


Figure 3.50. Tip-Acceleration Response under Closed Loop and Open-Loop Conditions

3.9.5 Interaction with DC Bus

A simplified block diagram of interconnection of the piezoelectric actuator to DC bus of power distribution system is shown in Figure 3.51.

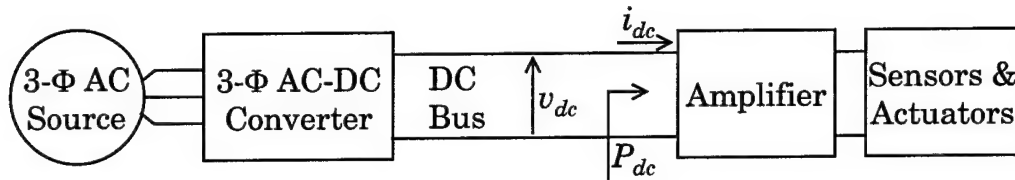


Figure 3.51. Interconnection of Piezoelectric Actuator with DC Bus

In addition to the model of the amplifier and piezoelectric actuator, this system includes a three phase AC generator, a three phase to DC converter, and a 270 V DC power distribution bus. The power distribution system model is based on the next generation power distribution system currently under development for the F-22. The piezoelectric actuator appears as a reactive load to the amplifier. Consequently, a considerable amount of power circulates between the DC bus and the “amplifier-actuator” subsystem. One of the main concerns in the design of the power distribution system is the development of methods to handle this bidirectional flow of power between the source and the load. The power P_{dc} flowing out of the DC bus is shown in Figure 3.52. Positive values of represent the flow of power from the DC bus to the amplifier and negative values represent the regenerated energy flowing back into the bus.

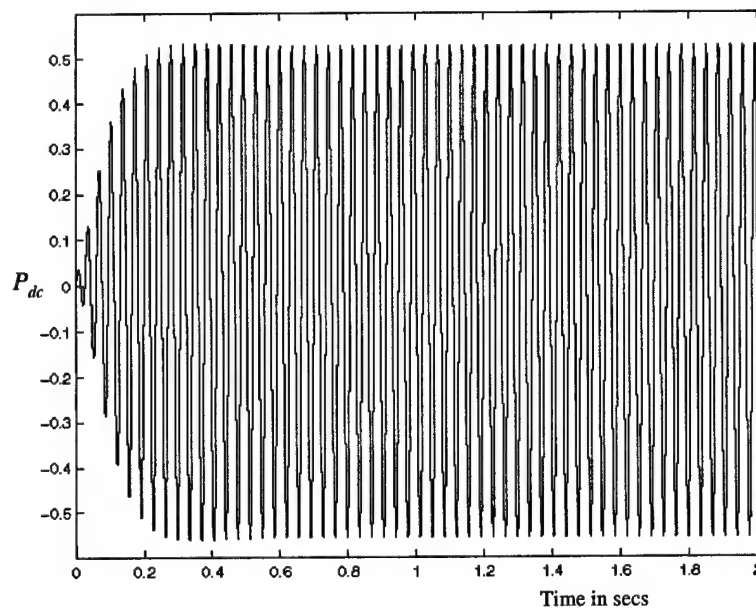


Figure 3.52. Regenerative Power at the DC Bus.

The magnitude of power shown in Figure 3.52 is not representative of the actual regenerated power in the power distribution system. This is because the choice of actuators and design of the control was based on a wind-tunnel model of the aircraft. The number, placement of the actuators would be significantly different on a full-scale model of the aircraft and hence would result in appreciably higher magnitudes of power to be fed back into the DC bus. The regenerative energy that flows back into the DC bus from the actuators results in undesirable distortion in the DC bus voltage. In addition to methods required to characterize the regenerative energy, appropriate storage or redirection techniques need to be determined for its efficient use for other applications.

3.10 DC Power Distribution Bus Modeling

The dc bus as viewed in this research consists of wires and cables transmitting dc power between the three-phase-to-dc converters and the loads. These connection elements are characterized by R, L, C parameters distributed along their lengths. Although these parameters are fairly small compared to the corresponding lumped parameters of the subsystems connected by the bus, under certain scenarios they do affect the processes in the PDS and therefore must be taken into account.

Since we are not interested in studying propagation of voltages and currents along the bus, there is no need in modeling it as a transmission line. A much more computationally effective bus model may be obtained by modeling any piece of the bus between two adjacent subsystems connected to it as a network with lumped parameters. In order to account for attenuation and phase delay produced by such a segment, a simple L-C filter model would suffice. The L-C filter network (Figure 3.5) and its SIMULINK model (Figure 3.6) were already discussed earlier.

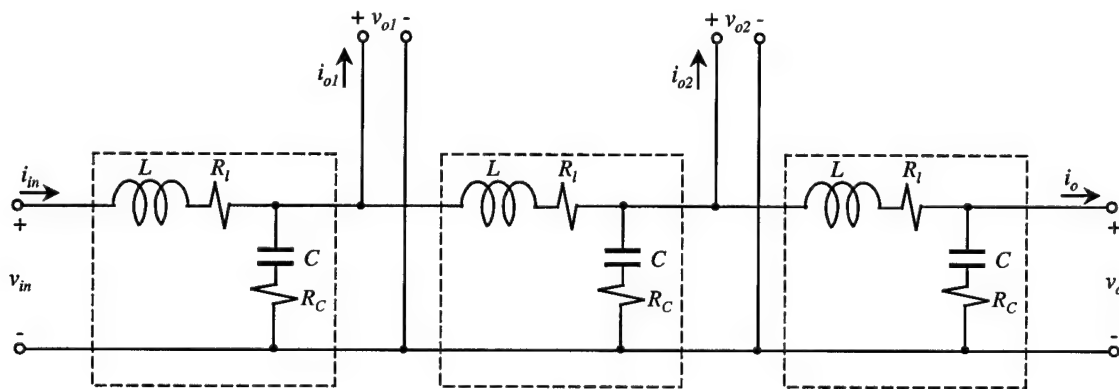


Figure 3.53. Three-section dc bus equivalent circuit.

Figure 3.53 shows a three-section dc distribution bus with two subsystems connected to its ends and two others connected in the middle. Each section is modeled as an L-C filter network whose parameters should be determined specifically for each section based on the section length and the distributed parameter

values. The leakage conductance between wires is not modeled since it is negligible for aircraft busses. A corresponding SIMULINK model shown in Figure 3.54 is based on the L-C filter models assembled into the system model according to the interconnection rules.

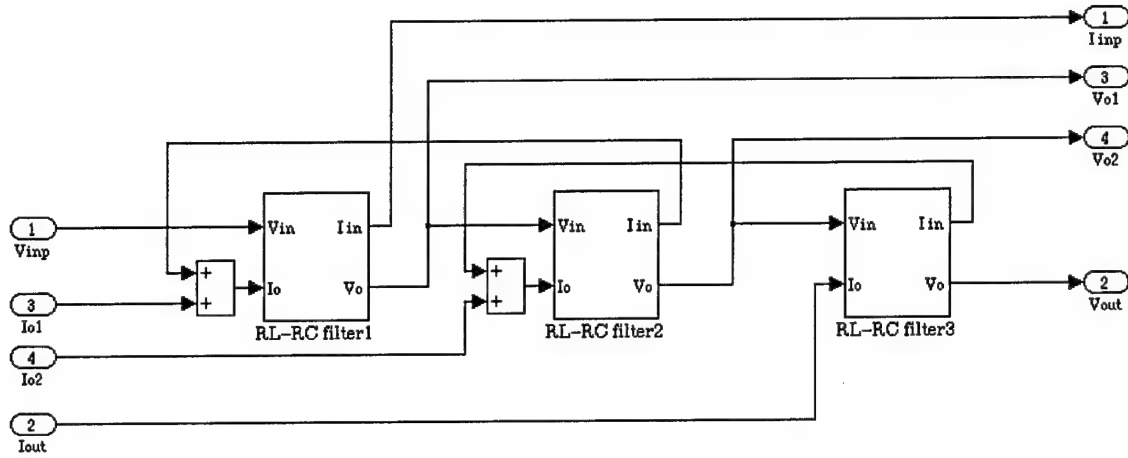


Figure 3.54. SIMULINK model of a three-section dc bus.

3.11 Conclusions

The development of the SIMULINK block library was described in this chapter. The block library consists of multi-level models of all the subsystems in the baseline power system architecture. The concept of multi-level models was introduced and its application in simulating systems at various levels of complexity was demonstrated. The detailed derivation of models of subsystems in the baseline architecture was presented. In the subsequent chapters, this modeling concept will be used extensively in the study of bidirectional power flow and in developing nonlinear methods of stability and subsystem interaction analysis.

4 Regenerative Power

4.1 Introduction

A prominent feature of the PDS is bidirectional power flow in its subsystems and the DC bus. As opposed to the normal power flow from the sources to the loads, the reverse power flow occurs when certain loads in the system work in regenerative mode. For example, this mode of operation is typical for flight control actuators, which alternate between normal and regenerative modes during their operational cycle. In this chapter, we will consider how the overall system performance characteristics such as DC bus power quality and system efficiency are affected by the regenerative power flow from an electromechanical actuator drive. The dependence of these performance measures on the parameters of the system is described. The effects of bidirectional power flow from smart actuators is also explained in detail in the latter sections of this chapter. Possible methods of controlling the regenerative power from these actuators are outlined.

The energy coming from a regenerating subsystem tends to raise the DC bus voltage unless this energy is utilized by certain means. If no other load with sufficient power consumption is present during regeneration, and no measures are taken to utilize the regenerative energy, the bus voltage can easily rise beyond the allowable limits specified in the MIL-STD-704E [8]. This may affect normal operation of the PDS and cause damage to the equipment connected to the bus. An attractive solution would be to store this energy in the battery for future use. However, allowable rates of charging the battery will have to be taken into account because the regenerative energy appears as a transient disturbance. There are several possible ways to deal with regenerative energy in the system:

- to dissipate it in resistors connected to the bus at the time of regeneration,
- to let it go back to the engine by using the generator and three-phase-to-dc power converter in regenerative mode,
- to use large capacitors in order to store the regenerative energy either in the DC bus, or in the regenerating subsystem,
- to use a DC bus conditioner (a power converter that stores the extra energy from the bus in a large capacitor and returns the energy to the bus when loads are available).

Currently, industry uses the first approach with damping resistors dissipating the regenerative energy. Unfortunately, the amount of this energy is so high that the resistors require liquid cooling. This complicates the system and reduces the benefits of the “more electric approach” in aircraft design. This chapter considers utilizing the regenerative energy in the power source (the engine) with the use of

additional capacitors in the DC bus and in the regenerating subsystem in order to alleviate transient voltage spikes caused by regenerative power flow.

4.2 System Configuration

The system configuration shown in Figure 4.1 was used to study the effects of the additional capacitors on the DC bus power quality and the system efficiency under bidirectional power flow conditions. The system consists of a three-phase synchronous generator, three-phase-to-dc boost rectifier, resistive load on the DC bus, and the EMA with an input filter. The development of models for each of the subsystems in Figure 4.1 is described in detail in Chapter 3.

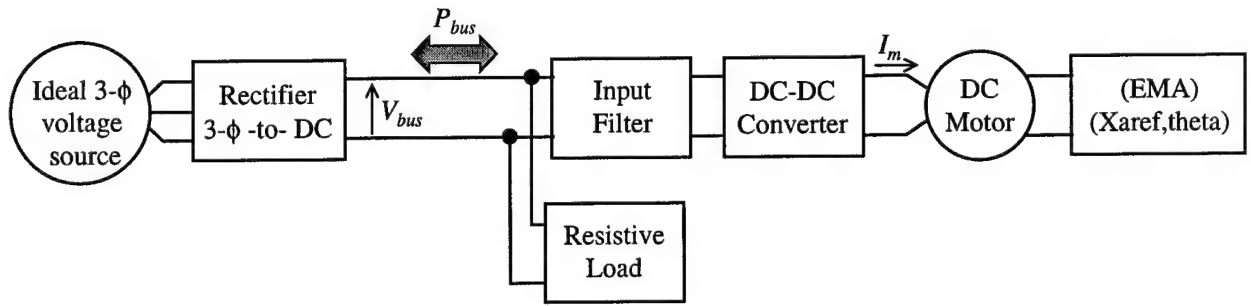


Figure 4.1. System Configuration for Bidirectional Power Flow Analysis

For the simulation example shown, the resistive load is on the bus is assumed to 1kW. The actuator deflection cycle is explained below:

1. The actuator deflection cycle occurs from $t = 0.5s$ to $t = 2.5s$, which corresponds to the full cycle of the EMA. X_{aref} and θ in the EMA block in Figure 4.1 are the reference command and the actual deflection of the surface respectively. The period from $t = 0$ to $t = 0.5s$ is a "start-up" period; it is used to bring the simulation model to the initial conditions corresponding to the beginning of the cycle. This period is not taken into consideration.
2. At $t = 0.5s$, a surface deflection command X_{aref} , is issued to the actuator drive system. As the deflection surface accelerates from rest, the drive motor draws a large current I_m . This appears as a transient load disturbance on the DC bus resulting in a spike in the voltage V_{bus} . The motor current reduces to close to zero, as the motor speed becomes constant.
3. As the deflection surface reaches its final commanded position, the motor decelerates acting as a generator. This braking action resulting in a regenerative surge of energy as can be seen in the negative excursion in the motor current I_m . This results in another spike on the DC bus voltage V_{bus} . The same sequence of events occur when a command X_{aref} to return to the zero position is issued at

$t=1.5$ s. The amount of energy regenerated is significantly dependent on the presence or absence of wind loading on the deflection surface. In the presence of wind load, the amount of regenerative energy increases appreciably compared to case without wind load.

The system waveforms during one operating cycle of the EMA are shown in Figure 4.2 (operation without the wind load) and Figure 4.3 (operation with the wind load). As was explained above, the major phenomena under investigation such as regenerative energy flow and voltage disturbances on the bus occur at times when the actuator reference signal changes abruptly and the actual position of the actuator reaches its commanded value. This causes the actuator motor to speed up or to slow down, thus consuming or regenerating a certain amount of energy, which causes significant current flow in the system and, as a result, voltage disturbances on the DC bus.

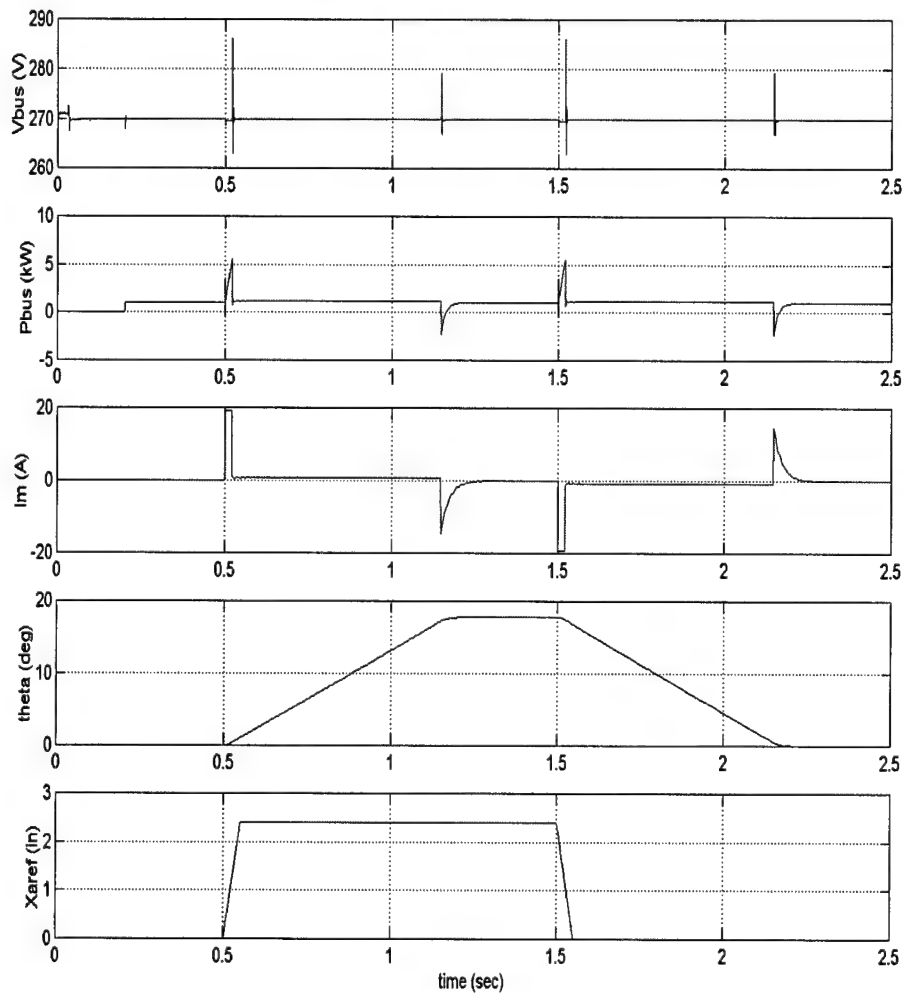


Figure 4.2. System operation without the wind load

What happens to the regenerative energy in this particular system configuration depends primarily on the value of the resistive load on the DC bus. If the load is large enough such that the power that it draws from the bus exceeds the peak value of the actuator regenerative power, the power drawn from the boost rectifier remains positive at all times. The actuator regenerative power is completely consumed by the resistive load, thus merely decreasing the power drawn from the boost rectifier.

If the peak actuator regenerative power exceeds the load power requirement, the excessive power will be transferred back to the generator by the boost rectifier. If the rectifier does not possess bidirectional energy flow capability, the excess energy will be stored in the rectifier output capacitor and the input filter capacitor, which will cause the DC bus voltage to increase.

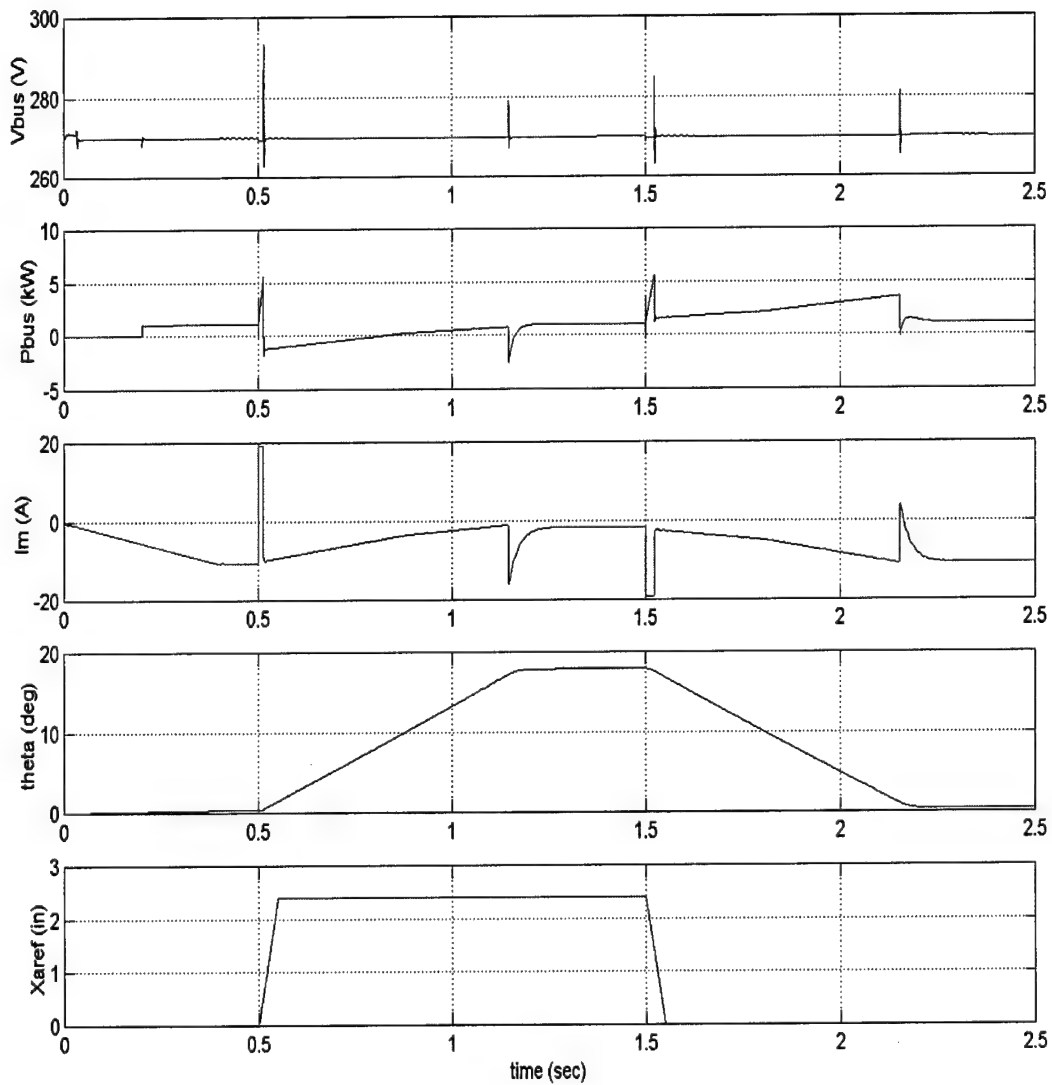


Figure 4.3. System operation with the wind load

In order to characterize quantitatively the process of energy distribution and regeneration in the sample PDS (Figure 4.1), the complete energy flow analysis was performed. Energy flow in the system is described in terms of energy flow at subsystem boundaries (Figure 4.5). Energy is computed at each boundary by integrating the corresponding power as a function of time during the EMA operating cycle.

Mechanical power, supplied by the engine to the generator: (4.1)

$$P_{gm} = P_g + P_{gl}$$

where, P_g – power transferred from the generator to the boost rectifier,

P_{gl} – total power losses in the generator.

Power, supplied by the generator to the boost rectifier: (4.2)

$$P_g = \left(\frac{3}{2} \right) (V_{gd} I_{gd} + V_{gq} I_{gq})$$

where, V_{gd} V_{gq} – generator output voltages in dq coordinates,

I_{gd} I_{gq} – generator output currents in dq coordinates.

Generator electrical losses are calculated as a sum of losses in phase windings, damper winding, and the excitation winding. Total generator losses are obtained by multiplying the electrical losses by two to account for magnetic and other types of losses.

Losses in phase resistances: (4.3)

$$P_{gls} = \left(\frac{3}{2} \right) (I_{gd}^2 + I_{gq}^2) R_s$$

where I_{gd} I_{gq} – phase currents in dq coordinates,

R_s – resistance per phase in the equivalent circuit.

Losses in the damper winding: (4.4)

$$P_{gls} = \left(\frac{3}{2} \right) (I_{kd}^2 R_{kd} + I_{kq}^2 R_{kq})$$

where I_{kd} I_{kq} – damper winding currents in dq coordinates,

R_{kd} R_{kq} – damper winding resistances in dq coordinates.

Losses in the field winding: (4.5)

$$P_{glf} = I_{fd}^2 R_{fd}$$

where I_{fd} – field winding current referenced to the stator,

R_{fd} – field winding resistance referenced to the stator.

Total generator losses: (4.6)

$$P_{gl} = 2(P_{gls} + P_{glk} + P_{glf})$$

Power transferred from the boost rectifier to the load: (4.7)

$$P_{bus} = V_{bus} I_{bus}$$

where V_{bus} – dc bus voltage,

I_{bus} – dc bus current.

Power transferred from the load to the input filter: (4.8)

$$P_{fi} = V_{bus} (I_{bus} - I_{load})$$

where I_{load} – load current.

Power transferred from the input filter to the EMA: (4.9)

$$P_{act} = V_{act} I_{act}$$

where V_{act} , I_{act} – EMA input voltage and current, respectively.

Power transferred from the actuator to the air: (4.10)

$$P_{wind} = H_m \omega_{sur}$$

where H_m – external moment from the air flow,

ω_{sur} – actuation surface angular speed.

Energy flowing from the left to the right is considered positive, flowing in the opposite direction – negative (regenerative). Based on the energy flow analysis at the boundaries, the energy balance for each subsystem is calculated.

Energy balance for the engine, which is the net energy coming from the engine to the generator: (4.11)

$$W_{eng} = (W_{gmp} - W_{gmn})$$

where W_{gmp} – positive energy, coming from the engine,

W_{gmn} – negative (regenerative) energy, going back to the engine from the generator.

Energy balance for the generator, equal to the total losses in the generator: (4.12)

$$W_{gen} = (W_{gmp} - W_{gmn}) - (W_{gp} - W_{gn})$$

where W_{gp} – positive energy, going from the generator to the boost rectifier,

W_{gn} – negative (regenerative) energy, going back to the generator from the boost rectifier.

Energy balance for the boost rectifier, equal to its losses: (4.13)

$$W_{brec} = (W_{gp} - W_{gn}) - (W_{busp} - W_{busn})$$

where W_{busp} – positive energy, going from the boost rectifier to the bus,

W_{busn} – negative (regenerative) energy, going back to the boost rectifier from the bus.

Energy balance for the resistive load: (4.14)

$$W_{load} = (W_{busp} - W_{busn}) - (W_{fip} - W_{fin})$$

where W_{fip} – positive energy, going from the bus to the input filter,

W_{fin} – negative (regenerative) energy, going back from the input filter to the bus.

Energy balance for the input filter, equal to its losses: (4.15)

$$W_{iftl} = (W_{fip} - W_{fin}) - (W_{actp} - W_{actn})$$

where W_{actp} – positive energy, going from the input filter to the EMA,

W_{actn} – negative (regenerative) energy, going back from the EMA to the input filter.

Energy balance for the EMA, equal to its losses:

..... (4.16)

$$W_{actr} = (W_{actp} - W_{actn}) - (W_{windp} - W_{windn})$$

where W_{windp} – positive energy, going from the EMA to the air,

W_{windn} – negative (regenerative) energy, going from the air flow to the EMA.

Energy balance for the air flow, equal to the net energy passed by the EMA to the air:

..... (4.17)

$$W_{wnd} = (W_{windp} - W_{windn})$$

The overall system efficiency is obtained as

..... (4.18)

$$\eta = \frac{W_{gmp} - (W_{gen} + W_{brec} + W_{iflt} + W_{actr})}{W_{gmp}}$$

Efficiency is calculated for total energy coming from the engine. Total losses include the losses in the generator, boost rectifier, input filter, and the actuator. Energy dissipated in the resistive load, passed to the air by the actuator, and regenerative energy returned into the engine is considered to be usefully spent.

4.4 Effect of the Input Filter Capacitor

At the first stage of analysis, the influence of the EMA input filter capacitance on the system performance was studied by using the parametric sweep technique. The system operation was simulated repeatedly for different values of the capacitance, with and without the wind load. The capacitance value range was chosen with the lowest value based on necessary switching ripple attenuation and the highest value approaching 1F. The system performance measures such as energy flow and voltage disturbance characteristics then were analyzed based on the simulation results.

The study showed that voltage spikes on the DC bus produced by the EMA cyclic operation are significantly reduced with the increase of the capacitance value. For example, Figure 4.2 and Figure 4.3 show the system operation with the lowest value of the capacitance, equal to 63μF. Figure 4.6 and Figure 4.7 show the system waveforms for a capacitance value of 63mF. It is seen that the voltage disturbances produced on the bus become lower in magnitude and longer in time with the increase of the capacitance. The EMA waveforms are preserved regardless of the capacitance value due to the EMA feedback control. The results of parametric sweep analysis of a voltage disturbance caused by regenerative power flow are shown in Figure 4.8 and Figure 4.9. Figure 4.8 shows the magnitude of the voltage transients, around the equilibrium value of 270V, as a function of the input filter capacitance. Excursions above 270V are represented by the positive curve and those below 270V by the negative curve. The voltage excursions reduce almost to zero when the capacitance value becomes large enough. Figure 4.9 shows the settling time of these disturbances vs. input filter capacitance. The figure shows that for low capacitance values, the

settling time increases with the increase of the capacitance since the time constant of the circuit increases. At the same time, the magnitude of the disturbances decreases as it is seen from Figure 4.8. When this magnitude falls below the allowable limit $\pm\Delta V$, the settling time becomes zero, according to our definition of the DC bus transients. The analysis showed that the same type of dependence is observed for all voltage disturbances on the bus, both regenerative and non-regenerative, during the operating cycle.

The analysis of energy flow in the system showed that the amount of energy drawn by the system from the source (the engine) depends on the input filter capacitance. The results are illustrated in Figure 4.10 and Figure 4.11 for operation without and with the wind load, respectively.

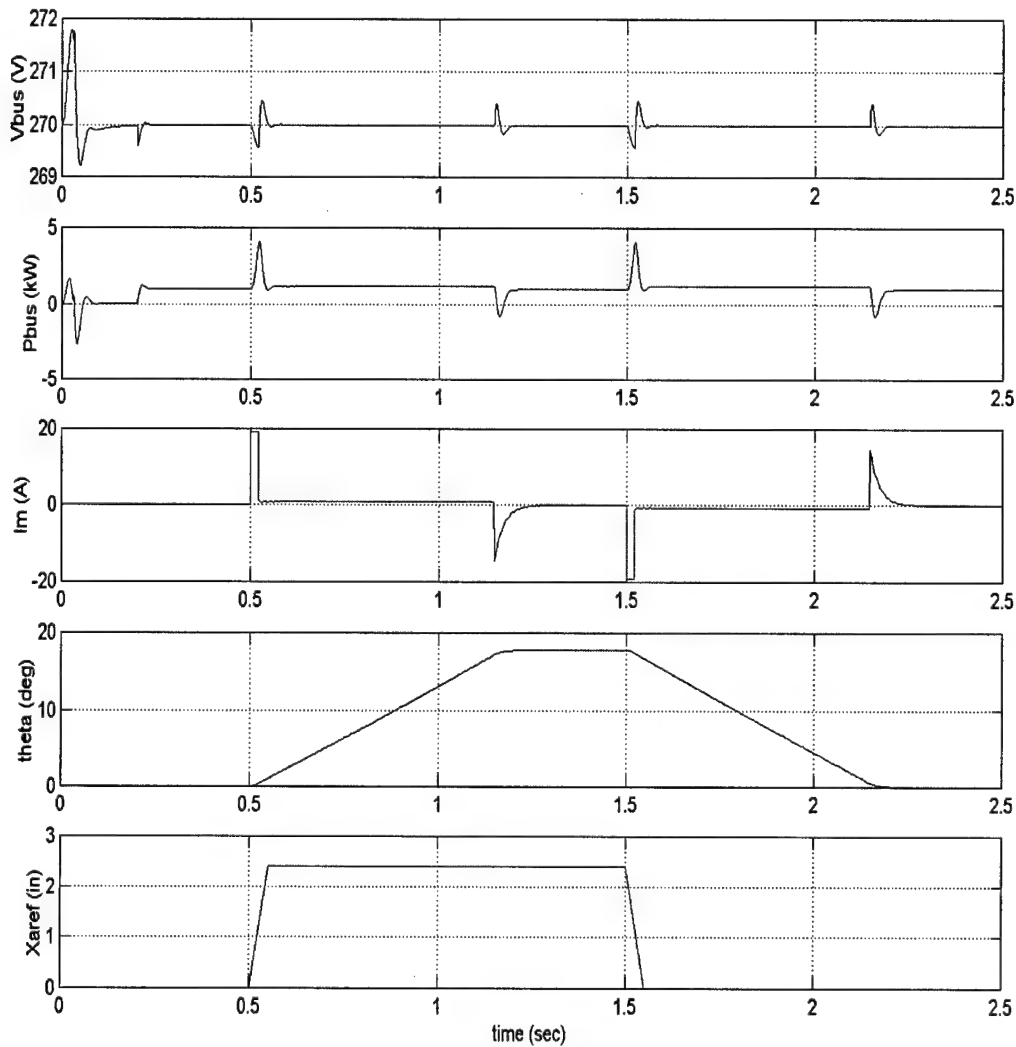


Figure 4.6. System operation without the wind load; $C_{if} = 63\text{mF}$

The figures show the total energy passed from the engine to the system, the amount of regenerative energy passed back to the engine and percentage of the regenerative energy in the total energy drawn by the

system. At large capacitance values, the regenerative energy is almost fully absorbed by the capacitor without going back to the engine; the transient and losses associated with them are reduced. The amount of regenerative energy going back to the engine at large values of the capacitance decreases to zero for operation without the wind load. In the case with the wind load, the amount of regenerative energy is much higher. This energy cannot be fully absorbed by the capacitor; however, its amount is reduced significantly.

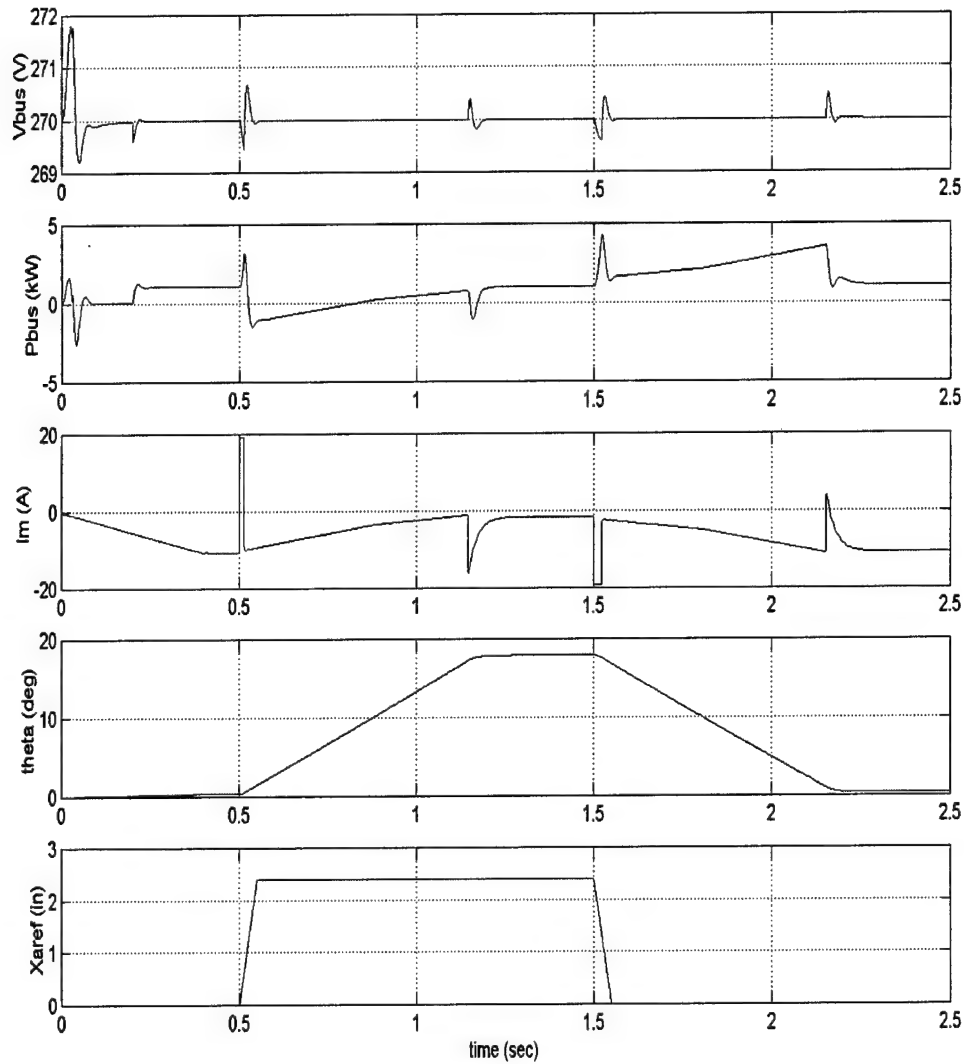


Figure 4.7. System operation with the wind load; $C_{if} = 63\text{mF}$

The air flow driving the actuator surface contributes a substantial amount of regenerative energy to the system. The figures show that the percentage of regenerative energy in the system operating with the wind load is six times higher than in the system operating without the wind load, where regenerative energy is contributed only by moving masses.

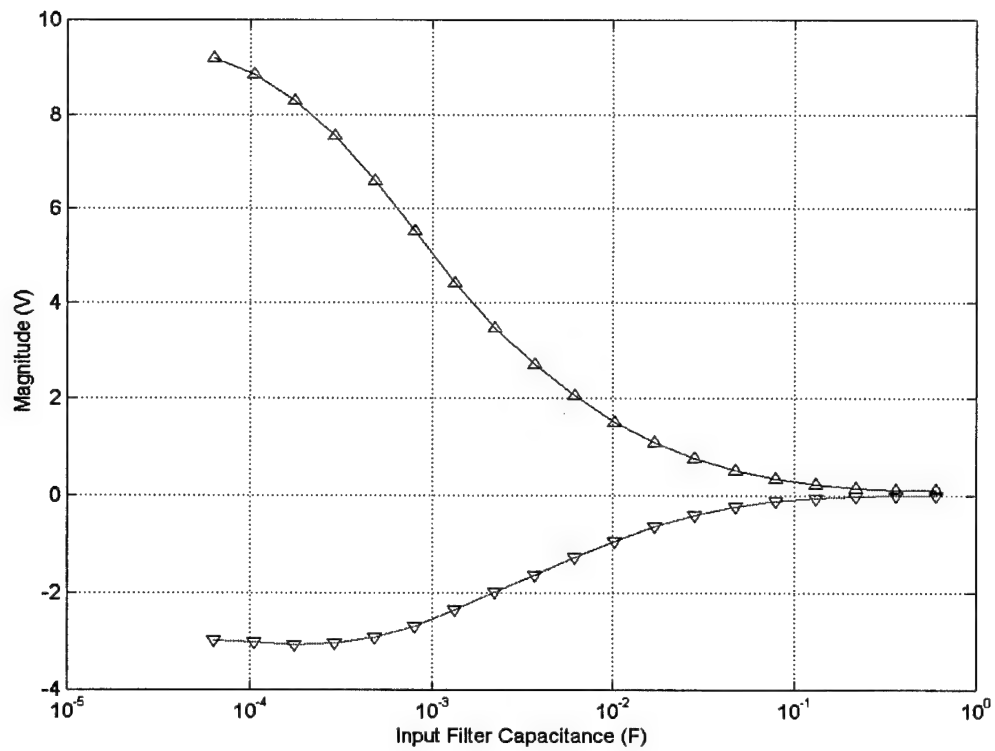


Figure 4.8. Voltage spikes magnitude vs. input filter capacitance

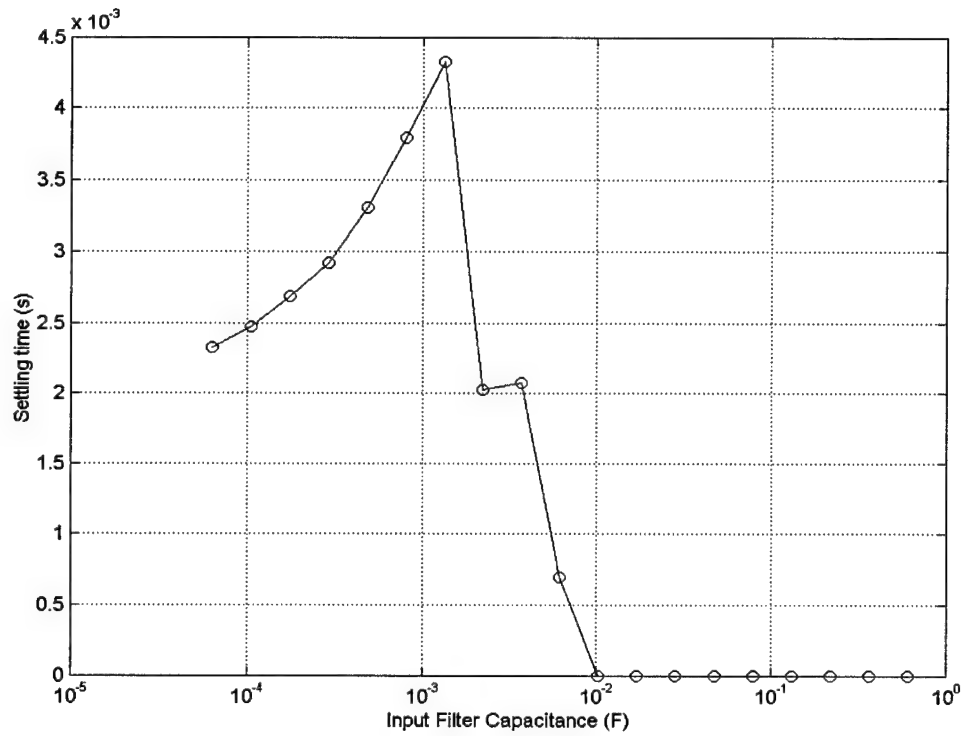


Figure 4.9. Settling time of the transients vs. input filter capacitance

Figure 4.12 shows energy balance for subsystems. For the generator, boost rectifier, input filter, and actuator the energy balance represents losses in the respective subsystem. It is seen that for the generator, boost rectifier, and the input filter the losses tend to decrease at large capacitance value for both with and without the wind load operation. This phenomenon contributes to reduction of the total energy consumed by the system as was shown previously. The actuator losses are not significantly affected by the capacitance value. Although the DC bus voltage transients are affected by the input filter capacitance, the actuator's feedback control makes its operation unaffected by the bus voltage variations. It is seen that losses in the generator, boost rectifier, input filter, and actuator are noticeably higher in case with the wind load, because the extra energy processed by these subsystems is accompanied by extra losses.

The resistive load is considered a payload; its energy balance decreases due to the decrease in the bus voltage rms value when the transients become smaller at large capacitance values. The air flow energy balance represents the net energy passed to the air by the actuator surface. This amount is equal to zero for operation without the wind load. When the system operates with the wind load, this amount is very small and independent of capacitance value. A special consideration is given to the generator losses, which have an increase in the middle of the capacitance range. Figure 4.13 shows the losses that constitute the total generator losses. Losses in the phase resistances and field winding are almost constant in the whole range of capacitance with a slight trend to decrease at large capacitance values because of a decrease in the amount of regenerative energy transferred back to the engine. However, losses in the damper winding experience an increase in the middle of the capacitance range. It is known that the damper winding does not carry current in steady state operation of the generator. The purpose of the damper winding is to damp transients by dissipating their energy. For low values of the capacitance, the transients, although high in magnitude, are relatively short in duration, and do not produce much dissipation in the damper winding. For very large capacitance values, the transients become very small. It is in the middle of the capacitance range, when the transients are still relatively high and their duration is long because of the time constant increased by the large capacitance, the damper winding losses experience an increase. This phenomenon explains why the generator losses in Figure 4.12 have an increase in the middle of the range. This increase in losses produces an increase in energy drawn from the engine, as shown in Figure 4.10 and Figure 4.11, and a corresponding decrease in the overall system efficiency curves as will be shown later. The overall system efficiency is plotted in Figure 4.14. The variation of the efficiency as a function of the input filter capacitance is very small – within 1% of the initial value. The increase in the generator losses produces a decrease in the efficiency for both with and without the wind load operation. At the same time, a global trend in increase of the overall efficiency at very high capacitance values can be seen, especially for operation without the wind load. Efficiency of the system operating with the wind load is approximately 1% lower than without the wind load. The results show that there is no advantage in using larger values of the input filter capacitance to improve the overall system efficiency, although the DC bus power quality can be improved.

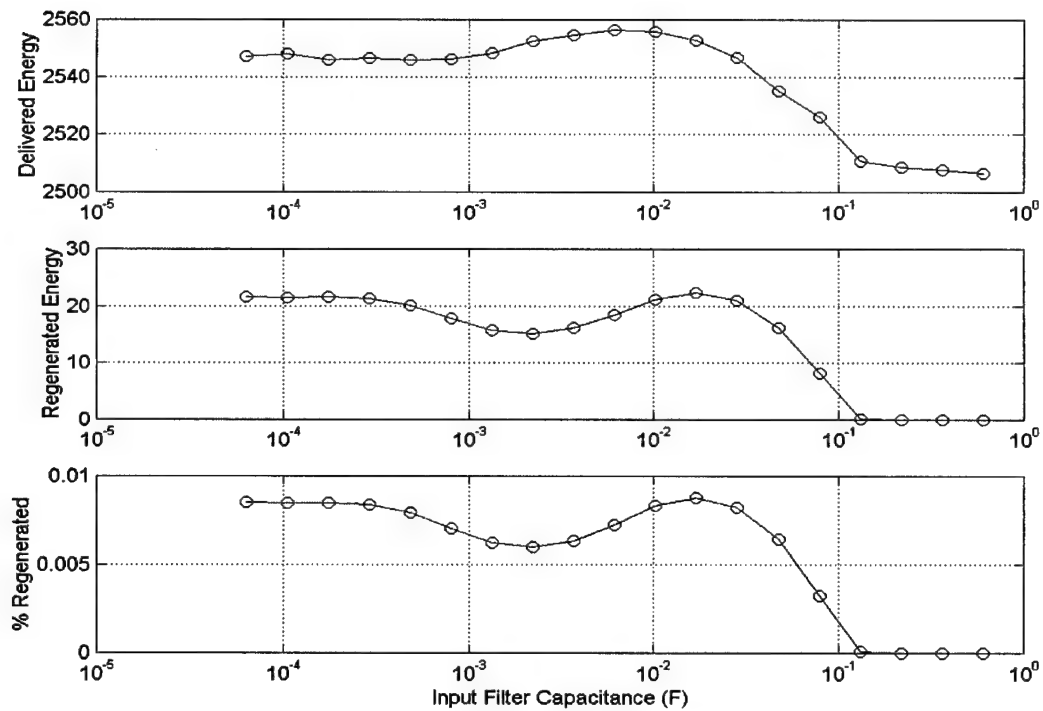


Figure 4.10. Total energy delivered from the engine and regenerated back (J) in the system without the wind load

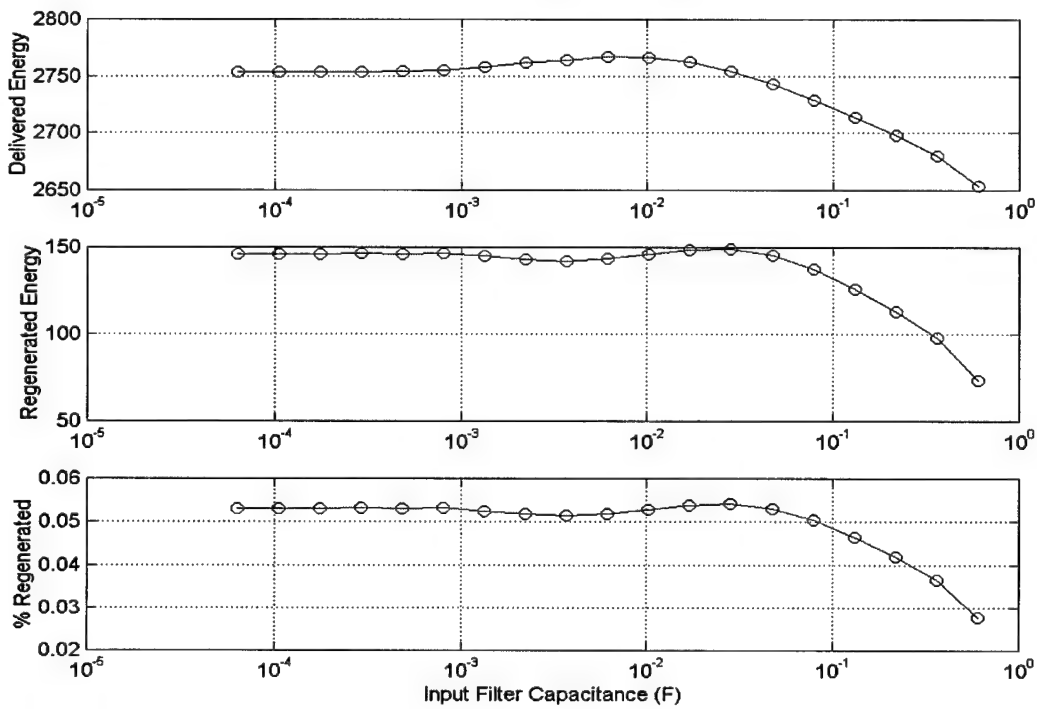


Figure 4.11. Total energy delivered from the engine and regenerated back (J) in the system with the wind load

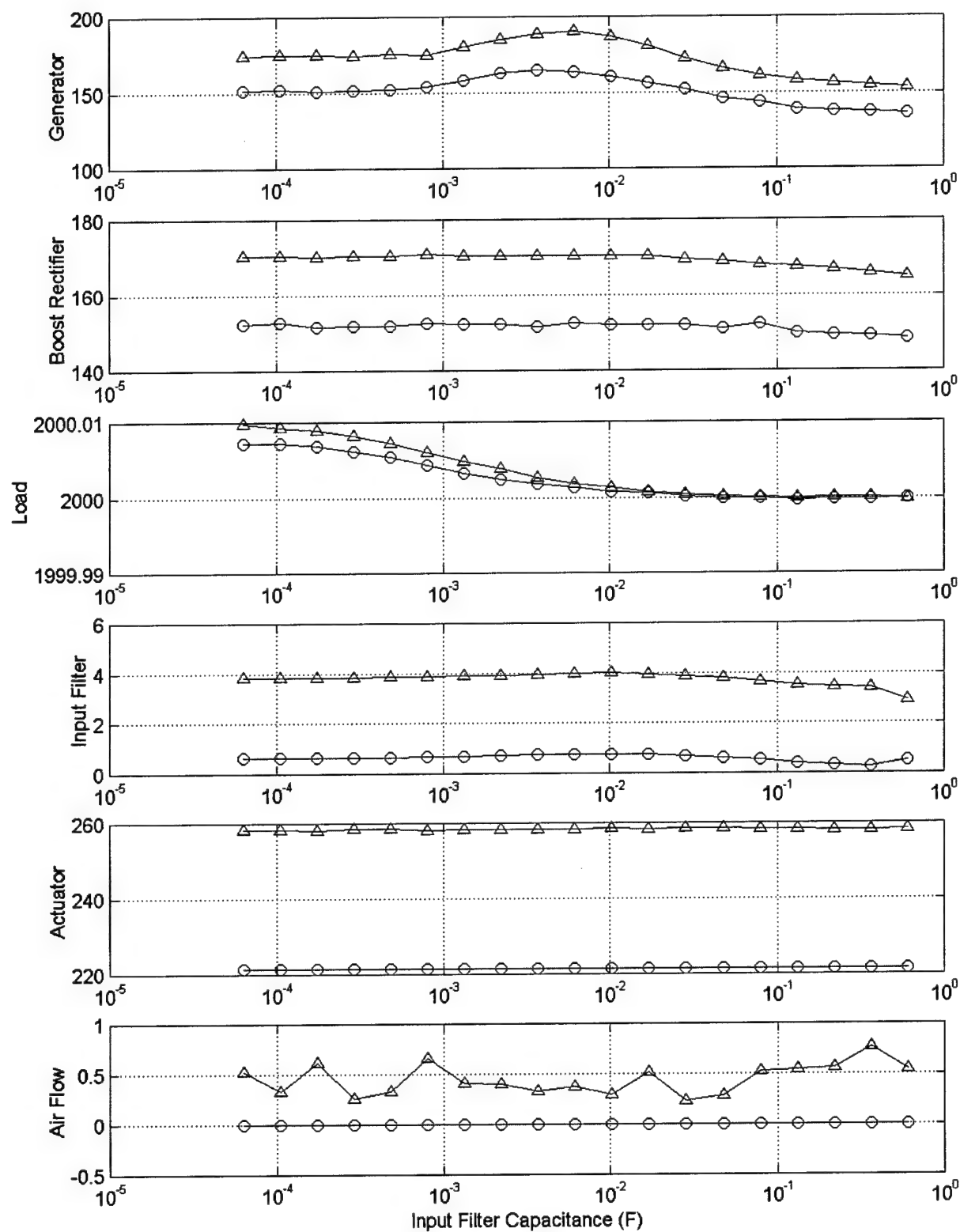


Figure 4.12. Energy balance (J) for subsystems with (Δ) and without (\circ) the wind load

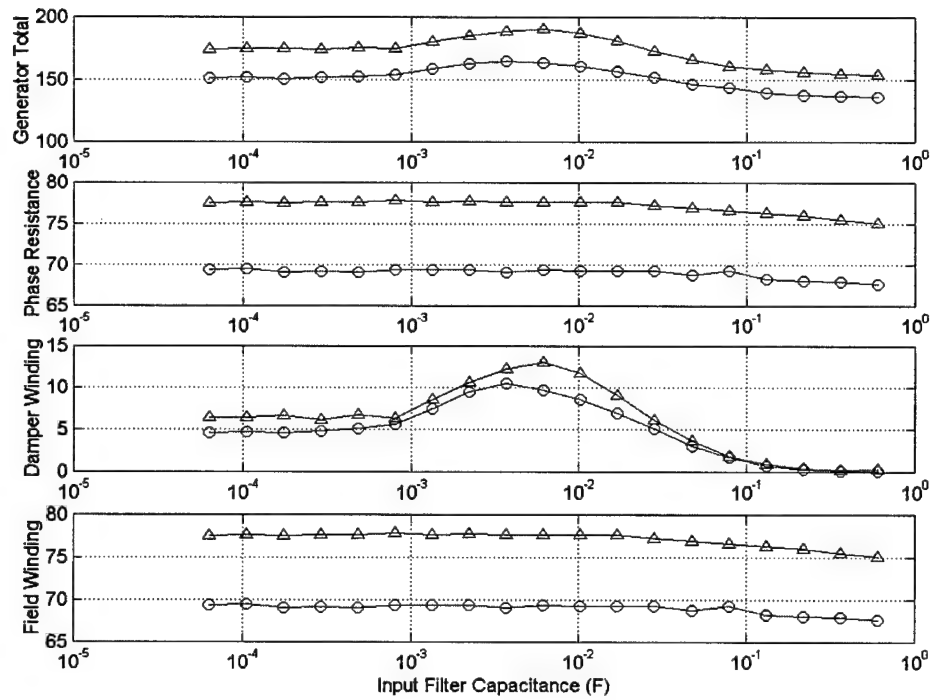


Figure 4.13. Generator losses in the system with (Δ) and without (o) the wind load

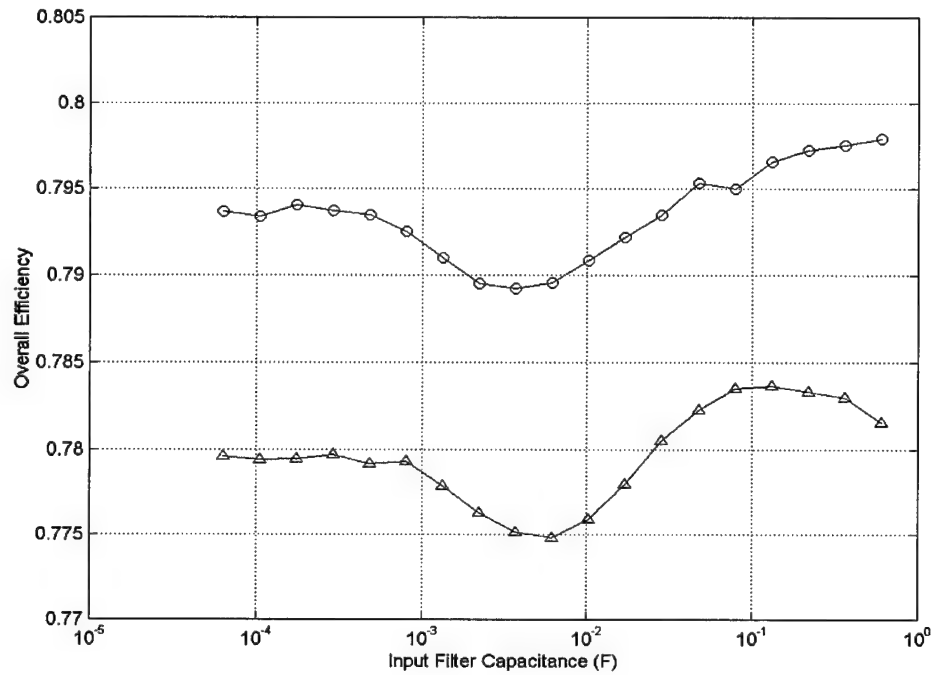


Figure 4.14. Overall efficiency of the system with (Δ) and without (o) the wind load

4.5 Effect of the Boost Rectifier Capacitor

The effect of the boost rectifier capacitor on the bidirectional power flow characteristics was studied by using the parametric sweep technique, similarly to the previous case with the input filter capacitor. The results obtained were very similar. Figure 4.15 and Figure 4.16 show waveforms of the system, operating without and with the wind load, respectively. Compared with waveforms of the system with a nominal set of parameters (Figure 4.2 and Figure 4.3), the results show that the DC bus voltage disturbances produced by both direct and regenerative power flow become lower in magnitude and longer in duration with the increase of the capacitance. This is illustrated in Figure 4.17 and Figure 4.18 showing the voltage spikes magnitude and settling time of the transients. As explained before, the positive and negative curves represent the peaks of transient excursions above and below the equilibrium value of 270V respectively. The figures show the same type of dependence as observed in Figure 4.8 and Figure 4.9 for the case with the variation of the input filter capacitance. It is noticeable that the magnitude curve in Figure 4.17 goes down steeper than in Figure 4.8. This is because the boost rectifier capacitor is connected directly to the bus, without an inductor as in case of the input filter capacitor.

The energy flow analysis yields the results very similar to the case with the input filter capacitance variation. Figure 4.19 and Figure 4.20 are similar to the corresponding Figure 4.10 and Figure 4.11, although the rise in power consumption in the middle of the capacitance range is more prominent. It is seen from comparing Figure 4.13 and Figure 4.14 that the losses in the damper winding in the latter case rise many more times over the initial value than in the former. A comparison of Figure 4.6 and Figure 4.7 with the corresponding Figure 4.15 and Figure 4.16 show that the DC bus transients have more oscillatory behavior with $C_{br} = 350\text{mF}$ than with $C_{if} = 63\text{mF}$. In the latter case, the input filter inductance with its ESR provides an additional filtering and damping action when the regenerative power flow causes transients on the DC bus. The long, poorly damped oscillations, which occur on the bus when a large boost rectifier capacitor is used, increase rms values of voltages and currents in the generator and the boost rectifier. This leads to increased losses in their phase resistances in addition to the increase in the damper winding losses as seen in Figure 4.21 and Figure 4.22. As a result, the overall efficiency curves in Figure 4.23 experience a decrease in the middle of the capacitance range as much as three times larger than the corresponding curves in Figure 4.14. The drop in efficiency is up to 1.5% in case with the wind load, and it is hardly recovered with very large capacitance values at the end of the range. The results of bidirectional power flow analysis showed that increased values of the input filter capacitance and the boost rectifier capacitance can be effectively used to reduce the magnitude of voltage spikes on the DC bus. At the same time, the large capacitors do not provide any advantage in utilizing the regenerative power flow in the system. In fact, the overall system efficiency reduces insignificantly when the capacitance values are increased up to two orders of magnitude against their initial values. This is especially noticeable in case of using a large boost rectifier capacitor, which creates long, poorly damped, large time-constant

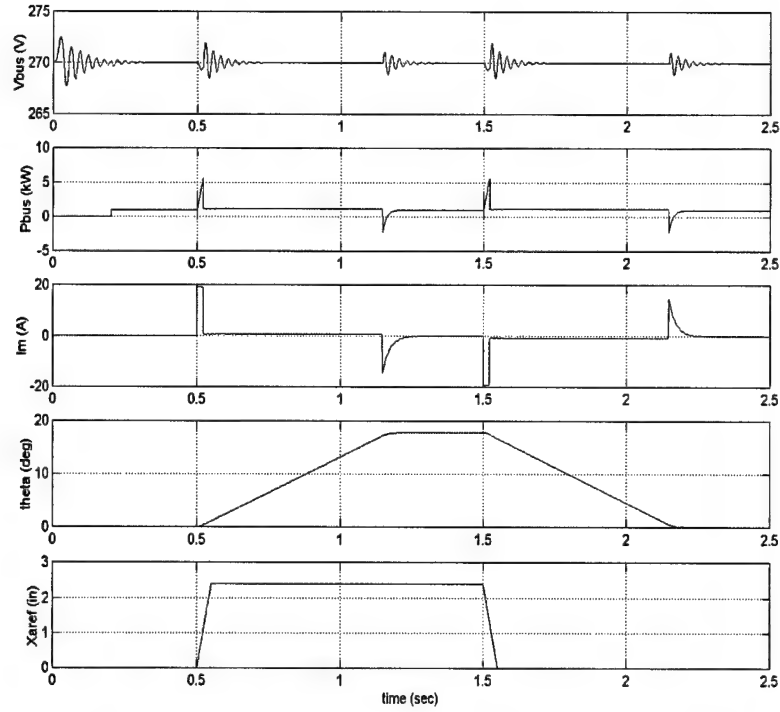


Figure 4.15 System operation without the wind load; $C_{br} = 350\text{mF}$

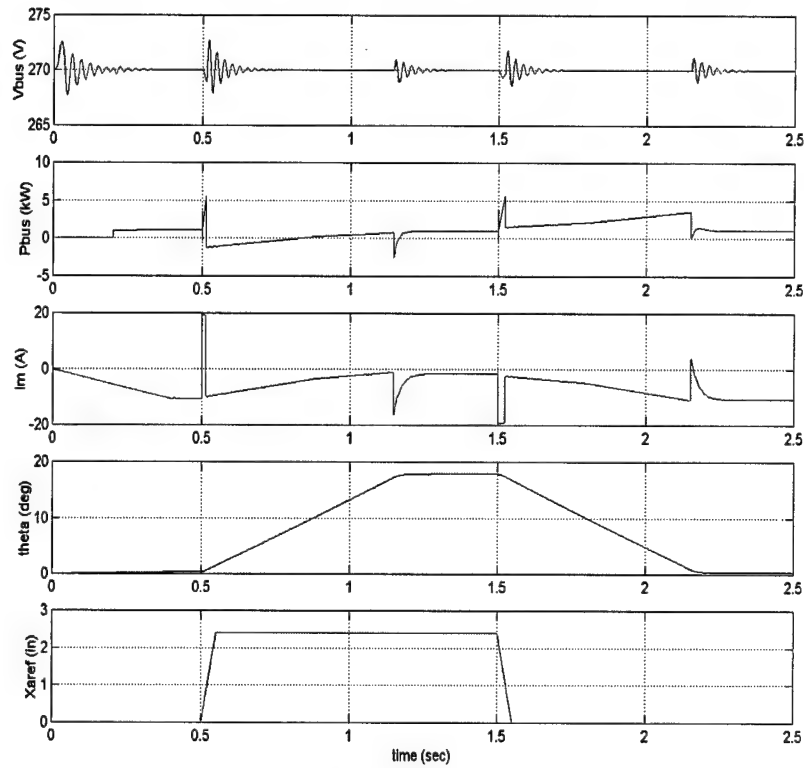


Figure 4.16. System operation with the wind load; $C_{br} = 350\text{mF}$

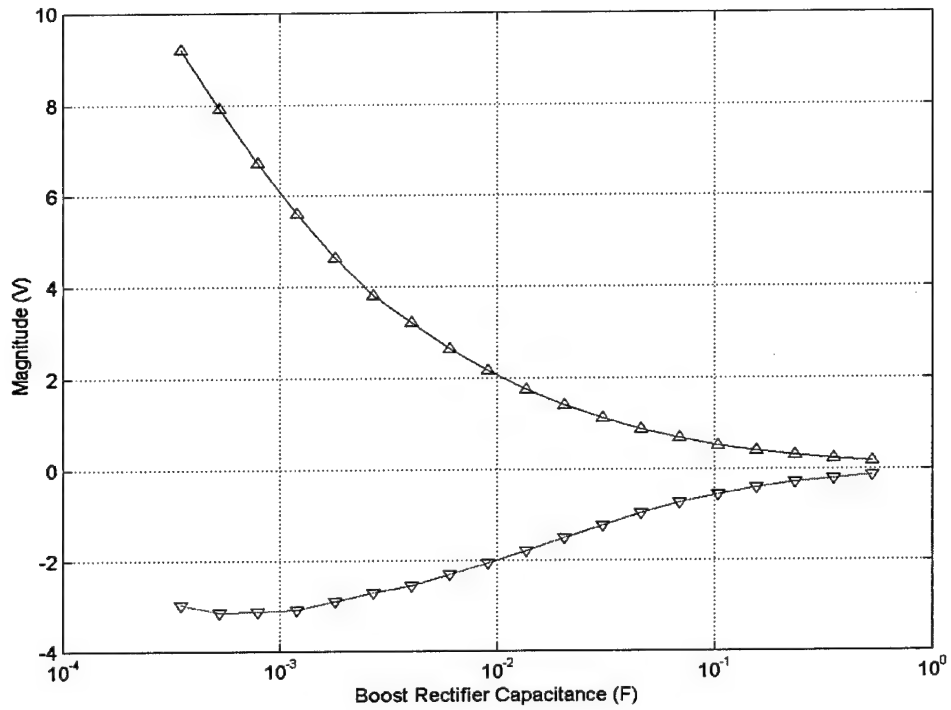


Figure 4.17. Voltage spikes magnitude vs. boost rectifier capacitance

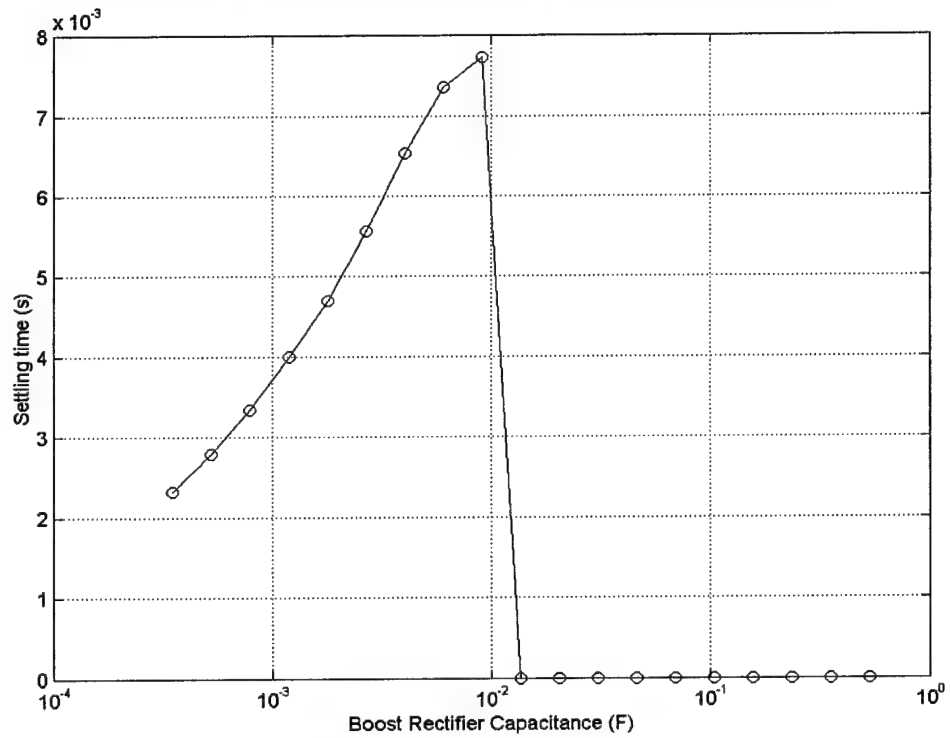


Figure 4.18. Settling time of the transients vs. boost rectifier capacitance

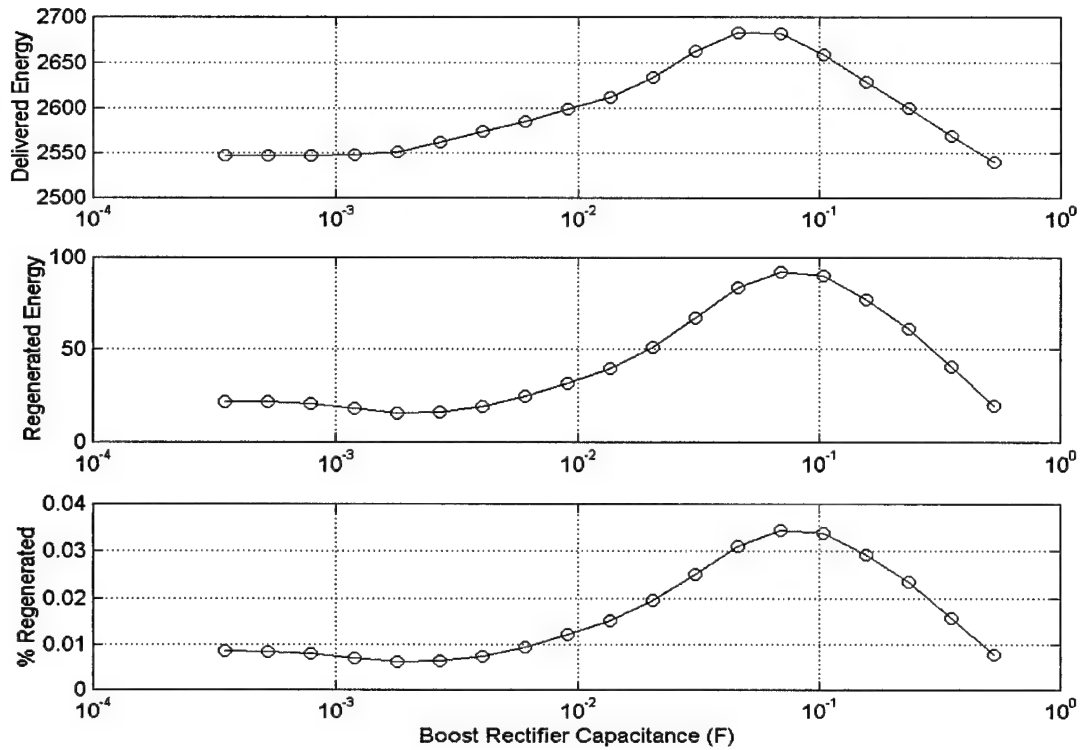


Figure 4.19. Total energy delivered from the engine and regenerated back (J) in the system without the wind load

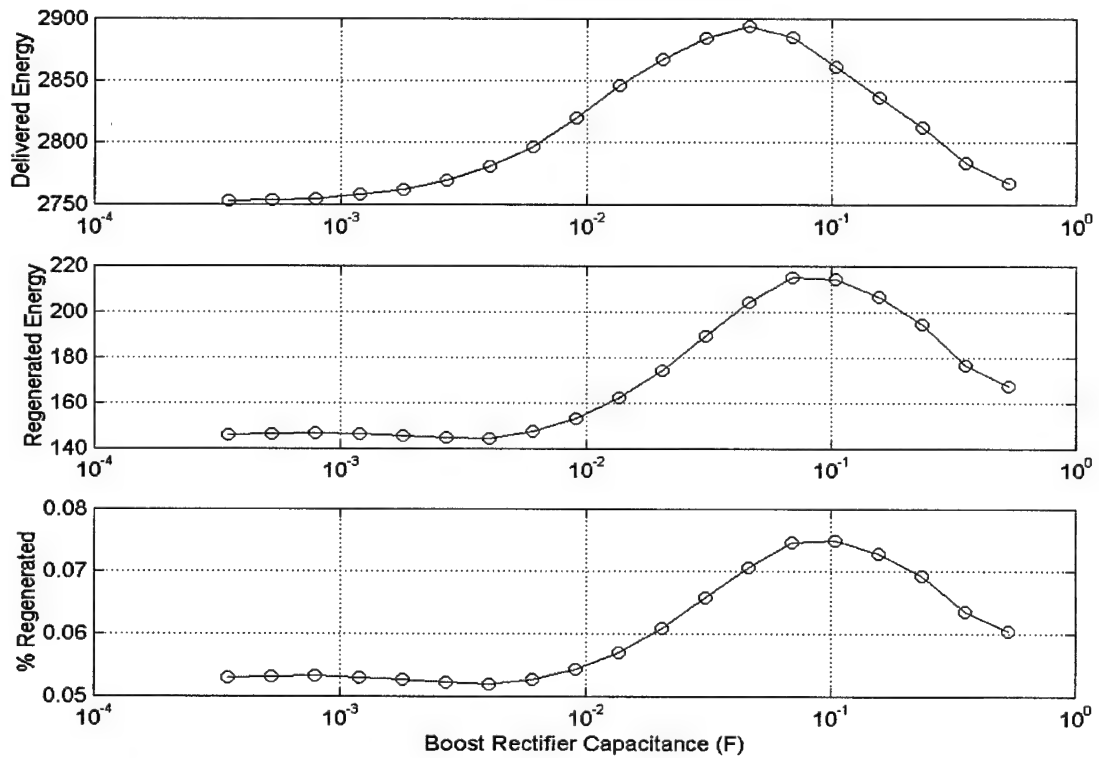


Figure 4.20. Total energy delivered from the engine and regenerated back (J) in the system with the wind load

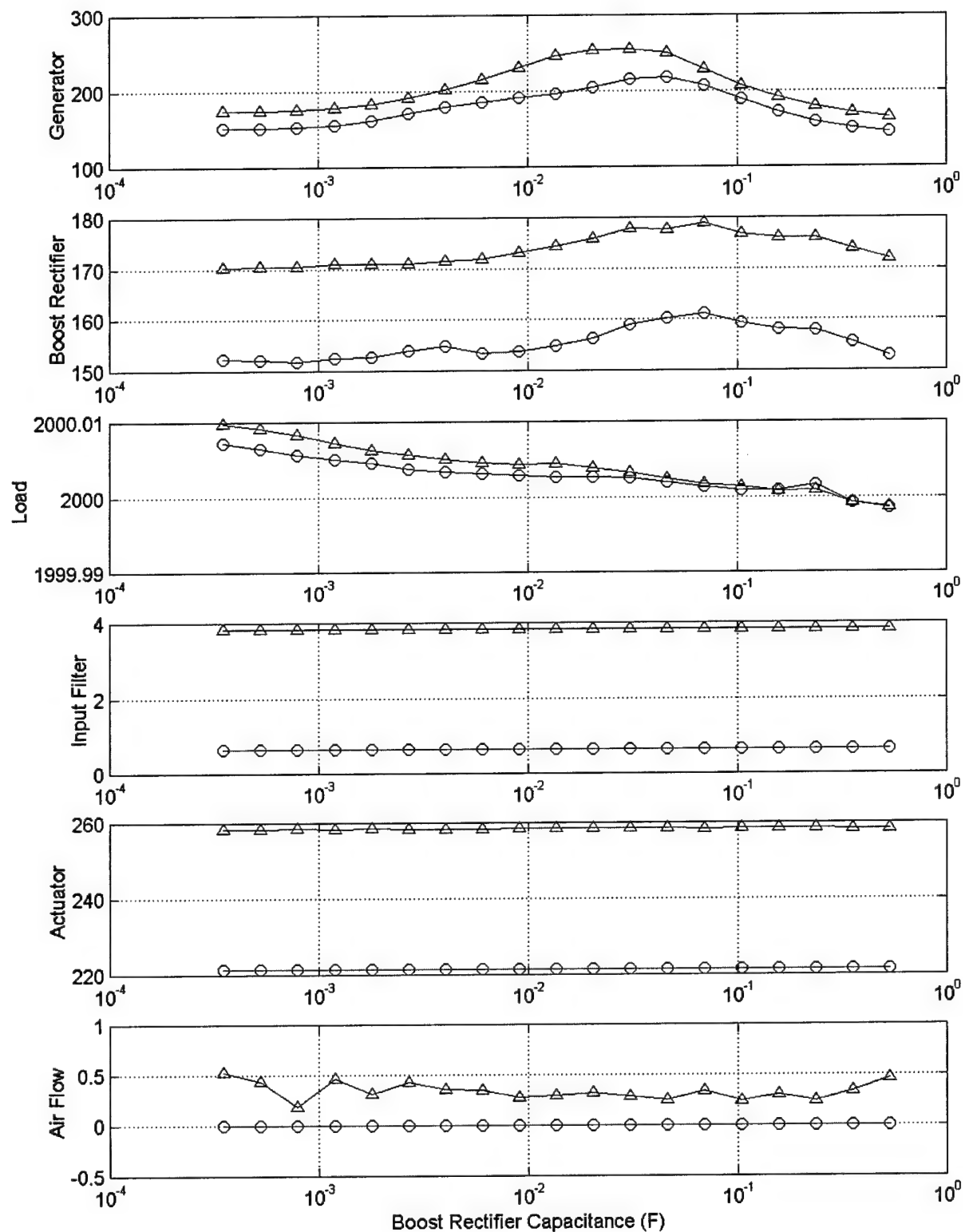


Figure 4.21. Energy balance (J) for subsystems with (Δ) and without (\circ) the wind load

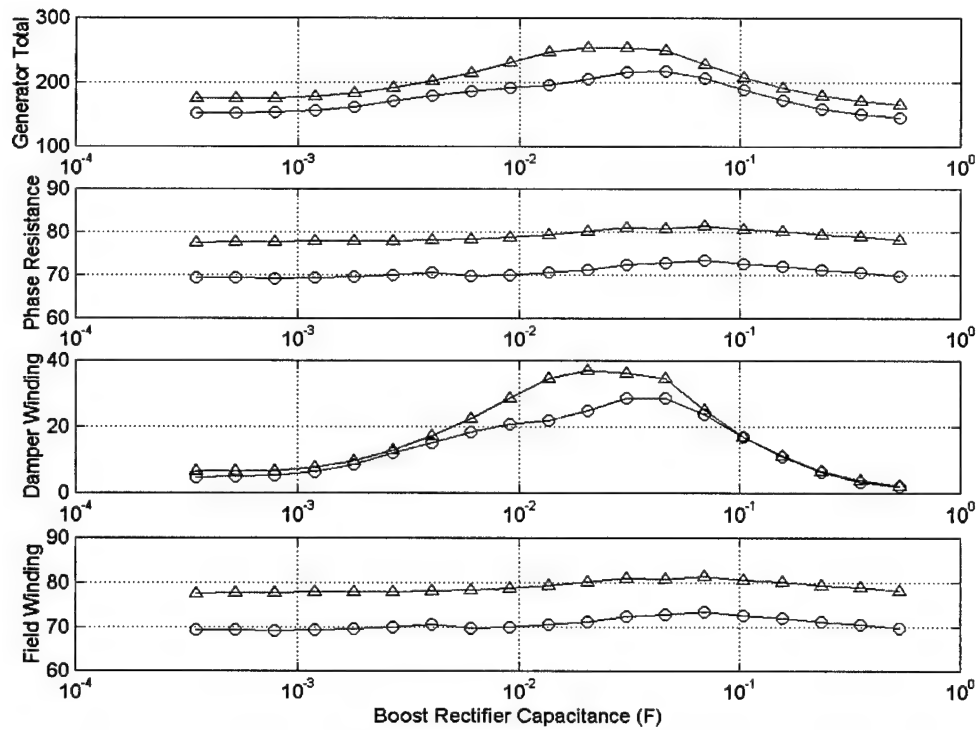


Figure 4.22. Generator losses in the system with (Δ) and without (o) the wind load

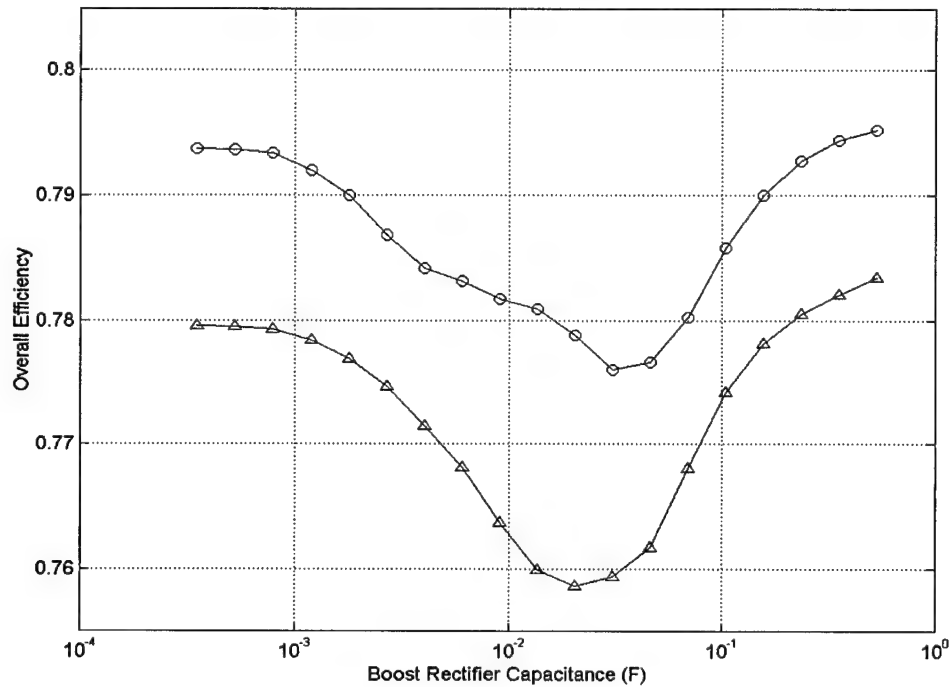


Figure 4.23. Overall efficiency of the system with (Δ) and without (o) the wind load

oscillations on the bus. For this reason, it is better to use a larger input filter capacitor than the boost rectifier capacitor to reduce the magnitude of voltage spikes on the bus.

4.6 Control of Bidirectional Power from Smart Actuators

4.6.1 Variation of System Parameters

The block diagram of the baseline power system architecture is shown in Figure 4.24. The baseline power system consists of a three phase AC generator represented by an ideal three phase sinusoidal voltage source, a three phase to DC rectifier [10] feeding the DC distribution bus, the piezoelectric actuator system and other constant current i_o , constant power Z , and resistive R , loads .

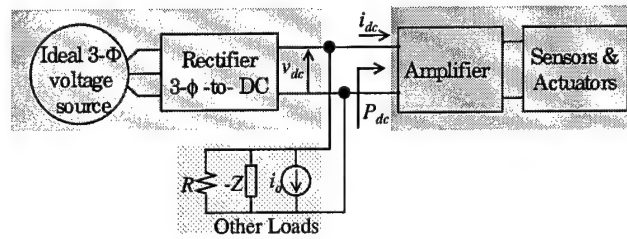


Figure 4.24. Baseline Power System Architecture with Piezoelectric Actuator

The power distribution system model shown in Figure 4.24 is based on the next generation power distribution system currently under development for the F-22.

The piezoelectric actuator appears as a reactive load to the amplifier. Consequently, a considerable amount of power circulates between the DC bus and the “amplifier-actuator” subsystem. One of the main concerns in the design of the power distribution system is the development of methods to handle this bidirectional flow of power between the source and the load. The signals i_{dc} and P_{dc} respectively represent the current and power flowing into and out of the “amplifier-actuator” subsystem shown in Figure 4.24. Positive values of represent the flow of power from the DC bus to the amplifier and negative values represent the regenerated energy flowing back into the bus. The circulating power between the DC bus and the amplifier appears as a pulsating load current to the three-phase rectifier feeding the DC bus. This pulsating current can lead to undesirable distortion in the DC bus voltage. The magnitude and nature of the distortion in the voltage depends on the parameters of the rectifier and other loads feeding off the bus. Simulation results that illustrate the effect a pulsating load current can have on the DC bus are shown in Figure 4.25.

The response of the DC bus voltage to a pulsating load current depends upon the impedance Z_o , looking into the output terminals of the rectifier. The output impedance Z_o depends critically on the regulation bandwidth ω_p , of the rectifier, the DC bus capacitor at the output of the rectifier and the other loads connected to the DC bus. Since the three-phase rectifier is essentially a nonlinear system, the output impedance and regulation bandwidth are determined after linearizing the system around a steady state operating point. The other loads on the system

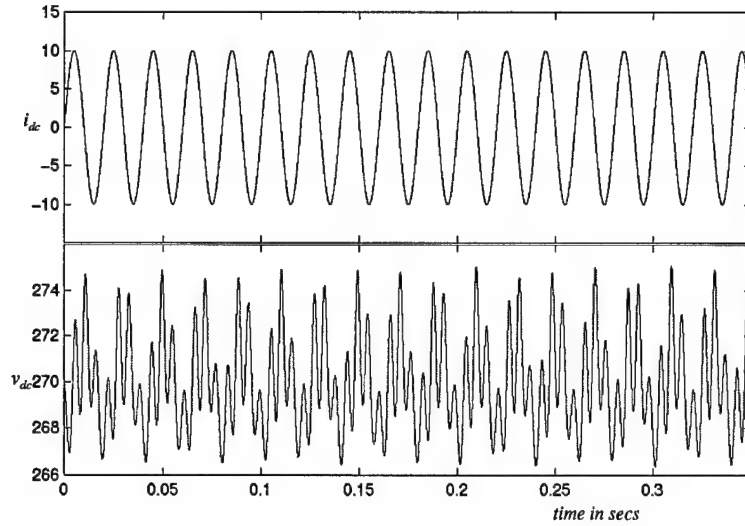


Figure 4.25. Effect of Pulsating Load Current on DC Bus Voltage

are assumed to be constant in this study. The variation of the output impedance Z_o of the rectifier as a function of the regulation bandwidth and output capacitor value is shown in Figure 4.26 and Figure 4.27.

It can be observed that the output impedance reduces as the regulation bandwidth increases. Hence, an increase in regulation bandwidth can be expected to result in lesser distortion of the DC bus voltage. However, increase in bandwidth is accompanied by the risk of instability. This effect is illustrated in Figure 4.28 where the phase margin of the rectifier is shown as a function of the regulation bandwidth. As the value of the DC bus capacitor is increased, the output impedance falls. However, a large DC bus capacitance allows a very narrow regulation

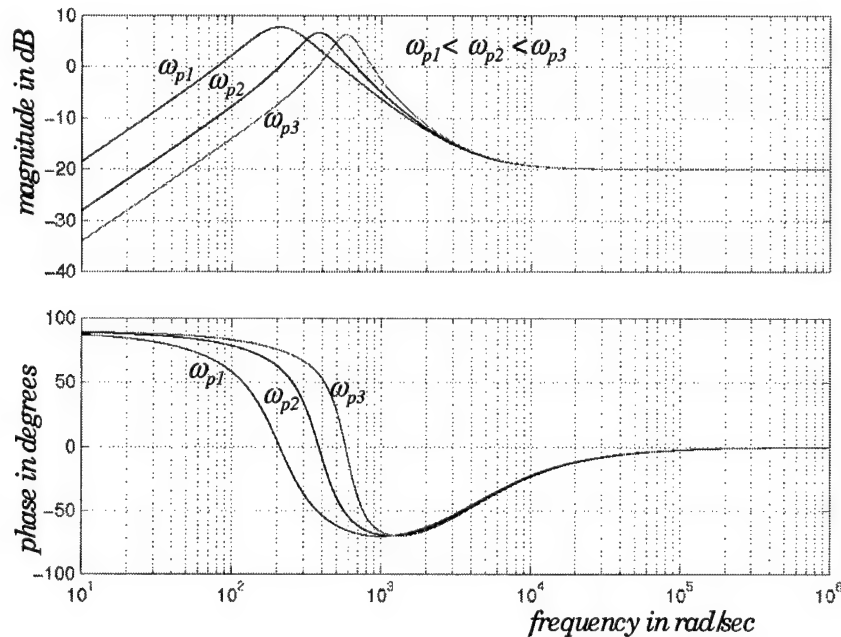


Figure 4.26. Variation of Z_o as a Function of Regulation Bandwidth of Rectifier

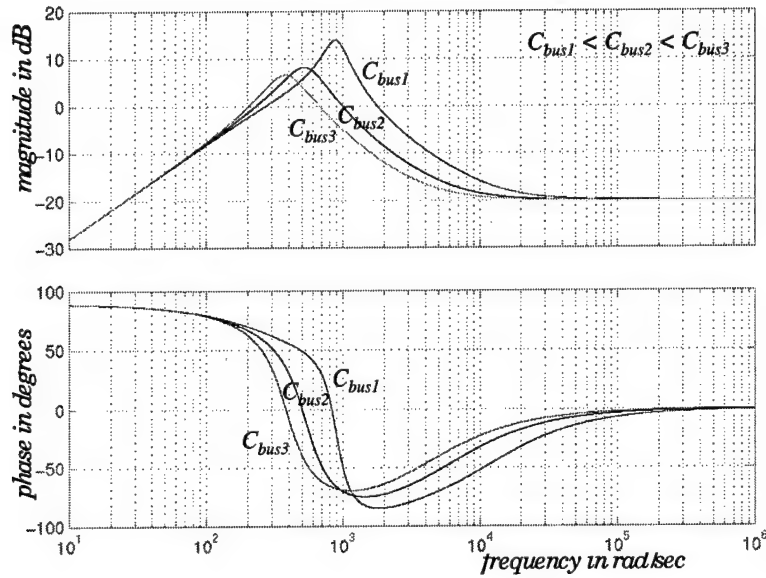


Figure 4.27. Variation of Z_o as a Function of Bus Capacitor

bandwidth resulting in a very sluggish response of the DC bus voltage to disturbances. Thus, a trade-off between bandwidth and bus capacitor value has to be achieved while maintaining stability and satisfactory speed of response.

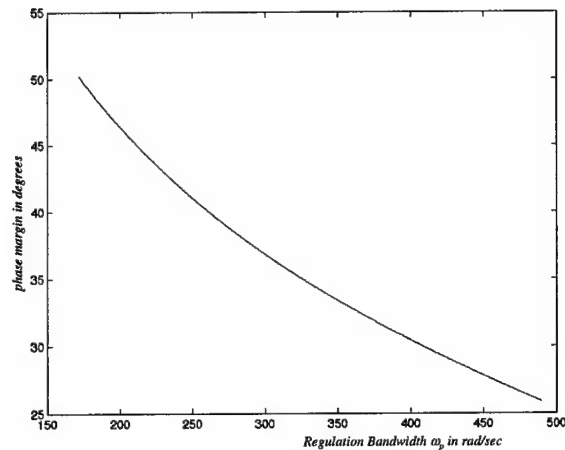


Figure 4.28. Phase Margin of Three-Phase Rectifier as a function of ω_p .

4.6.2 Bus Conditioners

Another way to handle the bidirectional power flow from the actuators is to use a bus conditioner to cancel the pulsating current of the actuator [45,46]. Bus Conditioners are controlled power electronic converters

that are connected to the DC bus of a distributed power system to alleviate disturbances arising due to pulsating or harmonic loads, system transients such as load switching etc. The simplified schematic shown in Figure 4.29 explains the concept of the active bus conditioners.

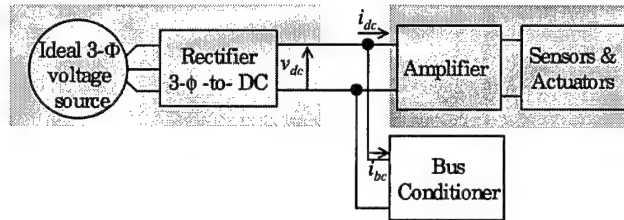


Figure 4.29. The concept of a bus conditioner

The control of a bus conditioner is different from that of a conventional regulated power converter. On sensing harmonic or pulsating power required by loads from the DC bus, the bus conditioner provides these loads with the required power thus helping maintain the stability of the DC bus. The bus conditioner hence, essentially serves as an actively controlled storage device that can source and sink energy to and from the DC bus. The circuit schematic of the bus conditioner is shown in Figure 4.30.

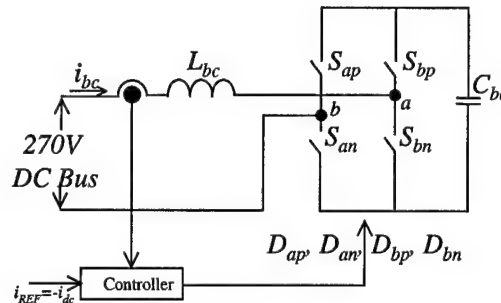


Figure 4.30. Schematic of Active Bus Conditioner

The controller for the bus conditioner consists of a high bandwidth current loop that drives the current flowing in and out of the bus conditioner to follow a reference. The reference current is tailored to cancel out the unwanted disturbance loads on the DC bus.

Since, a capacitive storage mechanism is usually preferred, a very slow voltage loop is closed around the current loop to ensure adequate energy on the capacitor during periods of inactivity on the bus. Figure 4.31 shows the response of the DC bus voltage when loaded by a pulsating current with and without a DC bus conditioner. The other loads in the system are assumed to be zero for the results shown in Figure 4.31. It can be seen that bus conditioner reduces the amplitude of the oscillations in the bus voltage considerably. The disadvantage of using a bus conditioner is the need for an additional converter and its associated control circuitry.

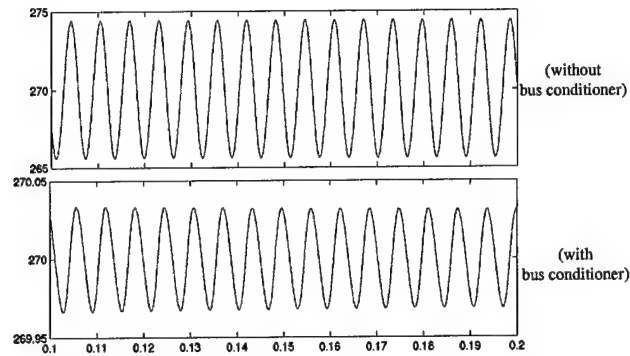


Figure 4.31. Effect of Bus Conditioner of Response of DC Bus Voltage

4.7 Conclusions

In this chapter, detailed simulation studies of the effects of bidirectional power flow on the power distribution system were presented. A sample system configuration consisting of an electromechanical actuator drive was introduced and extensive simulations of the same were performed to study the dependence of the performance characteristics of the system on parameters. Specifically, the characteristics of the DC bus voltage in terms of magnitude and settling time of voltage spikes due to regenerative transient disturbances were examined as the capacitances in the input filter and the boost rectifier were varied. The simulation example show that the amount of regenerative energy and hence its effects are critically dependent on the presence or absence of wind load on the deflection surface. Thus, the analyses of the effects of the same were performed for both with and without wind load. The paths of energy flow through the various subsystems in the sample system configuration were traced and the amount of regenerative energy consumed by each of the subsystems is studied. The results of this analysis are expected to be very useful in designing storage mechanisms for optimal handling of the regenerative energy.

The bidirectional power flow from smart actuators was considered next. Unlike the electromechanical actuator drive where the regenerative power flow occurs as a transient disturbance, smart actuators result in the flow of pulsating power on the DC bus. The effects of such a pulsating power on the DC bus voltage were described. The variation of the output impedance of the boost rectifier in the as a function of its output capacitor and regulation bandwidth were studied. The use of the bus conditioner as an alternative to mitigate the disturbances on the DC bus due to the pulsating load from the smart actuators was then described. It can be seen that a single solution cannot solve all the problems associated with regenerative energy. Since, the process of regeneration takes place in two distinct ways, a combination of solutions need to be used to optimally use the energy and minimize its detrimental effects.

5 Nonlinear Analysis Methodology

5.1 Introduction

The baseline power distribution system shown in Figure 2.1 consists of several complex systems that interact with each other. Although each of these individual subsystems are designed to be stable for standalone operation, their performance when integrated into a bigger system needs to be investigated. The first step in the analysis of subsystem interaction is to study the stability of interconnected systems. As mentioned earlier, the bidirectional power converter (BDC) form an integral part of the baseline power distribution system. The bidirectional power converter connected between the starter/generator and the DC distribution bus (henceforth called the bus regulator) converts 110/400Hz three-phase AC power from the generator to tightly regulated 270V. Converters that form part of motor drives connected to flight control surfaces, however, are not directly controlled to provide a fixed voltage at their output. But they are driven by a voltage command generated by the control loops of the actuator. In most cases, these converters can be shown to have constant power characteristics, which will be explained in detail in this chapter.

The Middlebrook Impedance Ratio Criterion [22], the conventional method used to determine the stability properties of interconnected systems is described in section 5.1. The study of subsystem interaction, using the impedance ratio criterion, has traditionally focussed on the interconnection between an input filter and a regulated power converter [22-27]. The effects of the inclusion of the input filter on the performance and stability properties of the regulated converter have been addressed. The bus regulator is a three phase AC-DC rectifier as mentioned above and is invariably preceded by an input filter. The impedance ratio criterion, as it is known, is applicable only to a SISO case and hence cannot be directly applied to study interaction in three phase systems because of their multivariable nature. The extension of the criterion to study input filter interaction in three phase AC-DC rectifiers to account for their multivariable nature is presented in section 5.2. The application of the impedance ratio criterion to analyze the stability of the sample power distribution system introduced in Chapter 4 is described in section 5.3. The impedance ratio criterion uses linearized models and hence provides only local stability information in a small neighborhood around the operating point. The failure of the impedance ratio criterion to accurately predict large signal behavior of the sample power system is demonstrated through a simulation example. To obtain large signal stability information, methods that recognize the nonlinear nature of the subsystems need to be used. The application on nonlinear methods to analyze the stability of the system is presented in section 5.4. To start with, the stability of a simple input filter-converter system under bidirectional flow of power is studied. Bifurcation methods that analyze global system behavior as a function of a set of control parameters are then presented to analyze the stability of a sample power system. Specifically, interaction between an input filter and DC-DC converter and at the DC bus of the sample power system is studied. The advantages and disadvantages of using these methods to study interaction are outlined.

5.2 Impedance Ratio Criterion

In this section, a generic subsystem interface is introduced and the classical impedance ratio criterion that ensures minimal interaction between the two subsystems and stability of the interconnected system is presented [22]. A generic subsystem interface is shown in Figure 5.1. Subsystems 1 and 2 are represented by their linearized small signal models around an operating point.

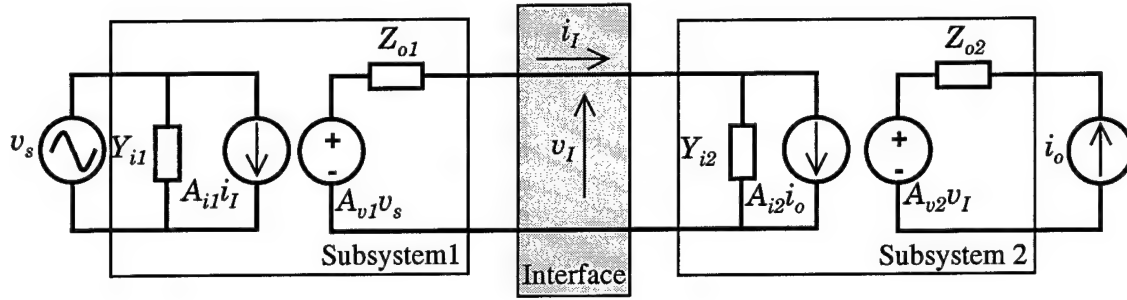


Figure 5.1. Generic Subsystem Interface

The variables i_I and v_I at the interface are given by:

$$\begin{aligned} i_I &= -(Y_{i2}v_I + A_{i2}i_o) \\ v_I &= A_{v1}v_s + Z_{o1}i_I \end{aligned} \quad \dots (5.1)$$

Equation (5.1) indicates the presence of a feedback loop as shown in Figure 5.2. The stability of this feedback loop determines the stability of the interconnected system, which can be determined by counting the number of counterclockwise encirclements of the $(-1+j0)$ point of the Nyquist contour of the loop gain, $Z_{o1}Y_{i2}$. However, a sufficient and a much simpler condition for stability can be obtained from the small gain theorem, which can be written as:

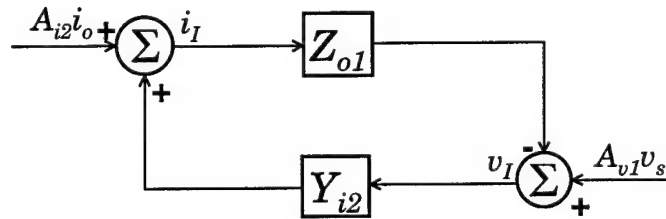


Figure 5.2. Equivalent feedback representation of subsystem interface

$$\begin{aligned} Z_{o1}Y_{i2} &< 1 \\ \Rightarrow \frac{Z_{o1}}{Z_{i2}} &< 1 \end{aligned} \quad \dots (5.2)$$

Satisfying the inequality in Equation 5.2, not only ensures the stability of the interconnected system but also guarantees minimal performance degradation of either of the two subsystems due to interaction.

5.3 Input Filter Interaction in Three-Phase AC-DC Converters

In this section, the interaction between the bus regulator and the three-phase input filter is discussed. A linear impedance ratio criterion similar to that presented above, but extended to accommodate the multivariable nature of three phase AC-DC converters is presented. Studies of input filter interaction in three phase rectifiers were performed in [28,29], but the results presented therein were not applied to three phase AC-DC converters in general. The design of input filters for power factor correction circuits was introduced in [30]. The factors affecting the choice of the filter topology for power factor correction circuits were outlined. In [31], the three phase converter was treated as a multivariable system and criteria for the stability of the interconnected filter-converter system were derived based on the eigenvalue loci and singular values of the relevant transfer function matrices. However, the analysis presented in [31] did not clearly identify the effects of the inclusion of the input filter on the performance indices of the system. The analysis presented here is general but is described using the example of a three phase boost rectifier represented by its average model in rotating dq coordinates [32].

AC-DC converters both three phase and single phase, are basically posed with two control objectives: (1) tight regulation of output DC voltage and (2) regulation of input power factor to unity. The power drawn by the converter from the AC source is, hence, purely real and is equal to the power required by the load on the DC side. The schematic of a three phase AC-DC converter supplied from an AC source through an input filter is shown in Figure 5.3. v_b and v_c , not shown in Figure 5.3, represent the voltages of phase b and c at the converter input.

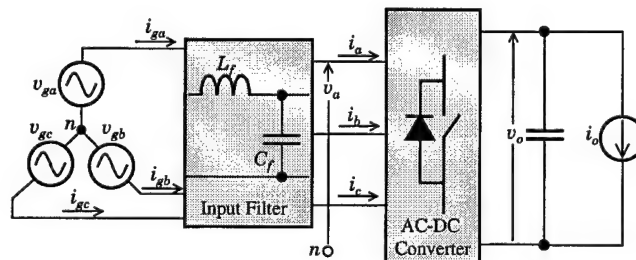


Figure 5.3. Schematic of three-phase AC-DC Converter with input filter

In the absence of an input filter, the voltage $v_{ga} = v_a$ and the current $i_{ga} = i_a$. With the power factor regulated to unity, the current i_{ga} and the voltage v_{ga} are in phase. The phasor diagram showing the voltages and currents at sinusoidal steady state are shown in Figure 5.4a. With the inclusion of the input filter, if the input current is required to be in phase with the voltage, as in Figure 5.4b, the converter must be forced to draw a current that is not in phase with the voltage at its input.

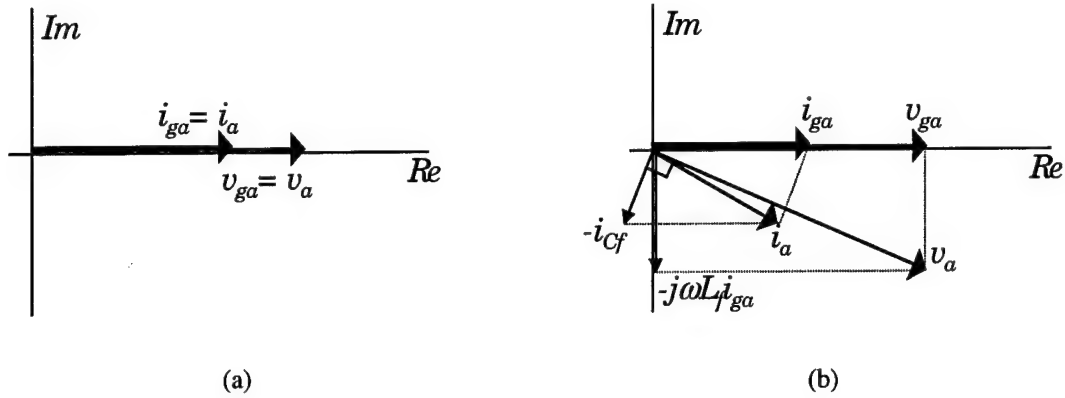


Figure 5.1. Phasor Diagram of phase current and voltage (a) without input filter, (b) with input filter

Thus, some reactive power has to be circulated between the converter and the input filter to achieve unity power factor at the source. Figure 5.5 shows a block diagram of a three phase rectifier fed from an AC source through an input filter. The rectifier, input filter and the AC source are represented by their corresponding dq models. The development of dq models of three phase systems is explained in detail in Chapter 2.

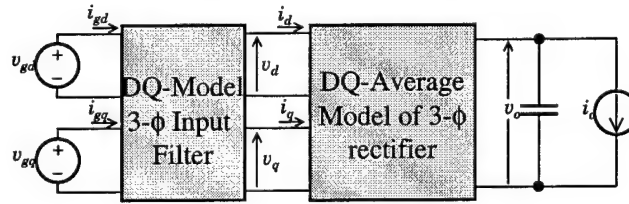


Figure 5.5. DQ-Model of a three phase rectifier fed from an AC source

The real and reactive powers supplied by the source are given by:

$$P = \left(\frac{1}{2} \right) (v_{gd} i_{gd} + v_{gq} i_{gq})$$

$$Q = \left(\frac{1}{2} \right) (v_{gq} i_{gd} - v_{gd} i_{gq}) \quad \dots (5.3)$$

Regulating the power factor to unity at the input requires driving the reactive power Q to zero. This results in the following relationship between the input voltages and currents:

$$\frac{v_{gd}}{i_{gd}} = \frac{v_{gq}}{i_{gq}} \quad \dots (5.4)$$

If the d-axis is synchronized with the zero crossing of the phase a voltage, then $v_{gq} = 0$ thus resulting in $i_{gq} = 0$ for zero reactive power. The rectifier is usually controlled by a two channel compensator, one channel for

output voltage regulation and the other for regulating i_q to I_{qref} to achieve unity power factor. In the absence of an input filter, $v_{gd,q} = v_{d,q}$ and $i_{gd,q} = i_{d,q}$. Hence, regulating i_q to 0 will ensure unity power factor at the input.

However, as mentioned before, with the inclusion of the input filter, it is necessary to circulate some reactive power between the filter and the converter to achieve unity power factor at the input. This translates to regulating i_q to a value different from zero, dependent on the magnitude of the real power supplied to the load, the input voltage and the component values of the input filter. However, the circulating reactive power between the converter and the input filter may result in larger currents to flow through the switches of the converter if the filter components are not appropriately sized. In addition, the inclusion of the input filter appreciably changes the operating point of the rectifier.

5.3.1.1 Existence and Stability of Equilibrium Solutions

The input filter schematic shown in Figure 5.6 is used as an example for the interaction analysis to be presented in the following. This topology was chosen according to the directions presented in [33] for PFC circuits.

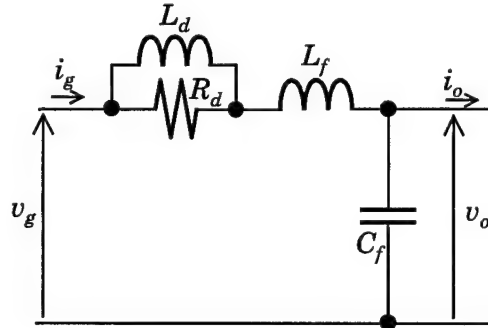


Figure 5.6. Schematic of input filter used in the analysis

Since the dc output voltage of the rectifier is tightly regulated, for a given load, the real power supplied by the rectifier and hence, drawn at the output of the filter (assuming a lossless converter) is constant. If i_q is regulated such that $i_{gq} = 0$, the real power P is then given by the equation,

$$P = \frac{1}{2} \left(V_{gd} I_{gd} - I_{gd}^2 R_d \frac{(\omega/\omega_d)^2}{1 + (\omega/\omega_d)^2} \right) \quad \dots (5.5)$$

where, $\omega_d = \frac{R_d}{L_d}$

From Equation 5.5, it can be seen that real equilibrium solutions exist for the interconnected system if and only if the following condition is satisfied,

$$\frac{V_{gd}^2}{8R_d} > P \frac{(\omega/\omega_d)^2}{1 + (\omega/\omega_d)^2} \quad \dots (5.6)$$

Uppercase letters in Equations 5.5 and 5.6 represent the operating point values of the corresponding variables. The operating point values for the input voltages and currents of the converter are given in Equation 5.7.

$$\begin{aligned} V_d &= V_{gd} - I_{gd} R_d \frac{(\omega/\omega_d)^2}{1 + (\omega/\omega_d)^2}, \\ V_q &= -\omega L_f I_{gd} - I_{gd} R_d \frac{(\omega/\omega_d)}{1 + (\omega/\omega_d)^2}, \\ I_d &= I_{gd} + \omega C_f V_q, I_q = -\omega C_f V_d \end{aligned} \quad \dots (5.7)$$

Figure 5.7 and Figure 5.8 show the effects of changing R_d and C_f on the q-axis input current I_q to the rectifier, power dissipated in the filter, reactive power and the input current drawn by the rectifier. The control design for the rectifier is usually done at a single operating point given by $V_d=V_{gd}$, $V_q=V_{gq}=0$, $I_d=2P/V_d$, $I_q=0$. The filter components must hence be chosen such that the variation in the operating point after the inclusion of the input filter is not appreciable.

It is obvious from Equation 5.7 that C_f does not affect the power loss in the resistor. Increasing R_d reduces the power loss in the filter, at the cost of reduction in damping. To achieve the same damping ratios with a higher R_d requires a higher L_d and hence a bigger filter.

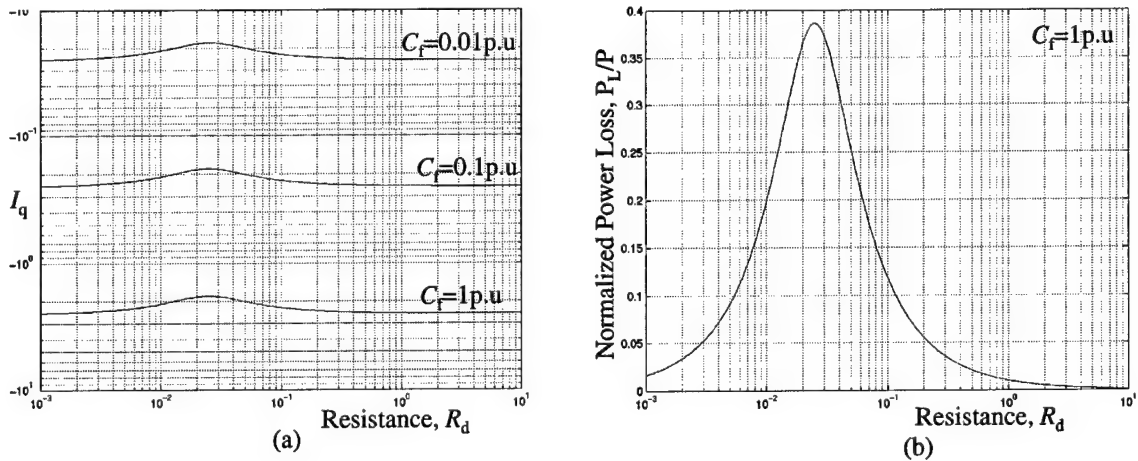


Figure 5.7. (a) Variation of I_q as a function of R_d for different values of C_f .
(b) Variation of power loss in filter as a function of R_d .

The variation of the resonant frequency, bandwidth and the damping ratios of the filter as a function of the component values are well known and hence, are not included here. A comparison of different filter topologies for PFC circuits is presented in [31].

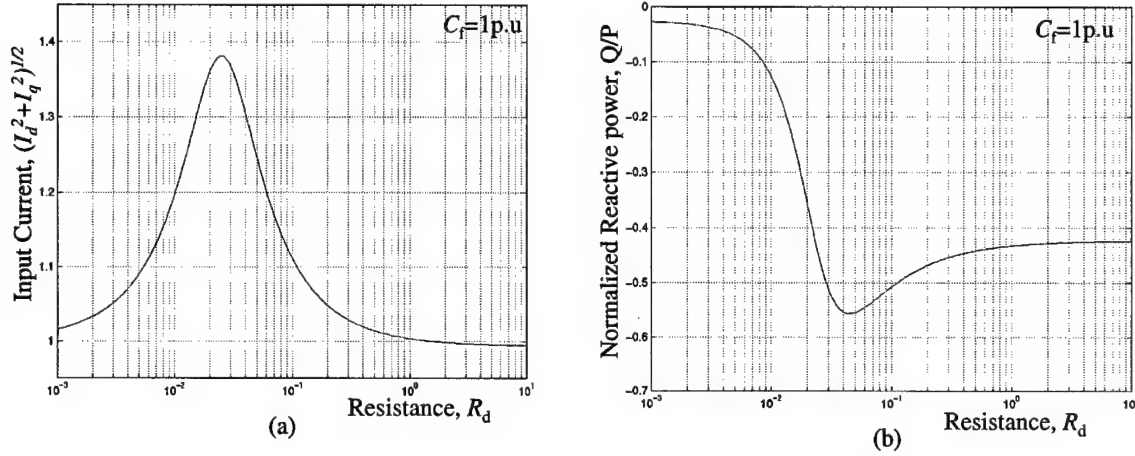


Figure 5.8. (a) Variation of $(I_d^2 + I_q^2)^{1/2}$ as a function of R_d .
(b) Variation of reactive power as a function of R_d .

5.3.1.2 Three Phase Boost Rectifier

The three phase boost rectifier is chosen as an example to illustrate the variation of loop gain, output impedance and stability of the system due to the interaction with the input filter.

The average model of the three phase boost rectifier in rotating dq-coordinates is given by Equation 5.8.

$$\begin{aligned} L \frac{di_d}{dt} &= v_d - d'_d v_o \\ L \frac{di_q}{dt} &= v_q - d'_q v_o \\ C \frac{dv_o}{dt} &= \left(\frac{1}{2} \right) (d'_d i_d + d'_q i_q) - i_o \end{aligned} \quad \dots (5.8)$$

If the duty cycles d_d and d_q are modified as follows,

$$d_d = d'_d + \frac{\omega L i_q}{v_o}, \quad d_q = d'_q - \frac{\omega L i_d}{v_o} \quad \dots (5.9)$$

the state equations reduce to,

$$\begin{aligned} L \frac{di_d}{dt} &= v_d - d'_d v_o \\ L \frac{di_q}{dt} &= v_q - d'_q v_o \\ C \frac{dv_o}{dt} &= \left(\frac{1}{2} \right) (d'_d i_d + d'_q i_q) - i_o \end{aligned} \quad \dots (5.10)$$

For notational simplicity, the primes for the modified duty cycles are dropped and they are used as the original duty cycles. Linearizing the system of differential equations around an operating point, we get

$$\frac{d}{dt} \begin{bmatrix} \hat{i}_d \\ \hat{i}_q \\ \hat{v}_o \end{bmatrix} = \begin{bmatrix} 0 & 0 & -\frac{D_d}{L} \\ 0 & 0 & -\frac{D_q}{L} \\ \frac{D_d}{2C} & \frac{D_q}{2C} & 0 \end{bmatrix} \begin{bmatrix} \hat{i}_d \\ \hat{i}_q \\ \hat{v}_o \end{bmatrix} + \begin{bmatrix} -\frac{V_o}{L} & 0 \\ 0 & -\frac{V_o}{L} \\ \frac{I_d}{2C} & \frac{I_q}{2C} \end{bmatrix} \begin{bmatrix} \hat{d}_d \\ \hat{d}_q \end{bmatrix} + \begin{bmatrix} \frac{1}{L} & 0 & 0 \\ 0 & \frac{1}{L} & 0 \\ 0 & 0 & -\frac{1}{C} \end{bmatrix} \begin{bmatrix} \hat{v}_d \\ \hat{v}_q \\ \hat{i}_o \end{bmatrix} \quad \dots (5.11)$$

The variables D_d , D_q , I_d , I_q and V_o denote the operating point values of corresponding duty cycles, currents and voltage. The transfer function representation of the linearized system of equations given by Equation 5.11 is given below:

$$\begin{bmatrix} I_d(s) \\ I_q(s) \\ V_o(s) \end{bmatrix} = \begin{bmatrix} G_{idd} & G_{idq} \\ G_{iqd} & G_{iqq} \\ G_{vod} & G_{voq} \end{bmatrix} \begin{bmatrix} D_d(s) \\ D_q(s) \end{bmatrix} + \begin{bmatrix} Y_{dd} & Y_{dq} & A_{id} \\ Y_{qd} & Y_{qq} & A_{iq} \\ A_{vd} & A_{vq} & Z_o \end{bmatrix} \begin{bmatrix} V_d(s) \\ V_q(s) \\ I_o(s) \end{bmatrix} \quad \dots (5.12)$$

The boost rectifier is usually controlled by a two channel compensator, one for the regulation of the output voltage v_o and the other for the q -axis input current i_q . A block diagram representation of a controlled three phase boost rectifier system is shown in Figure 5.9. H_{vo} represents the output voltage controller and H_{id} and H_{iq} , the current controllers.

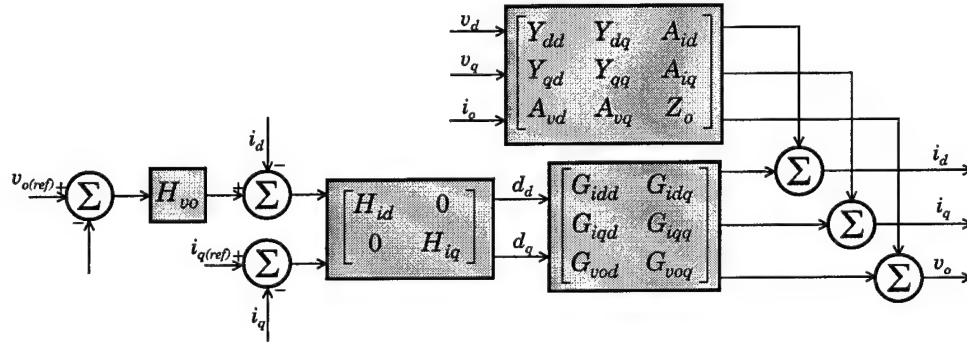


Figure 5.9. Block diagram of the controlled 3- Φ boost rectifier

The output variables I_d , I_q and V_o are determined below after making the following definitions:

$$\begin{aligned} \begin{bmatrix} I_d \\ I_q \end{bmatrix} &= I_c, \begin{bmatrix} V_d \\ V_q \end{bmatrix} = V_c, \begin{bmatrix} G_{idd} & G_{idq} \\ G_{iqd} & G_{iqq} \end{bmatrix} = G_{id}, \begin{bmatrix} G_{vod} & G_{voq} \end{bmatrix} = G_{vd}, \\ \begin{bmatrix} Y_{dd} & Y_{dq} \\ Y_{qd} & Y_{qq} \end{bmatrix} &= Y_i, \begin{bmatrix} A_{vd} & A_{vq} \end{bmatrix} = A_v, \begin{bmatrix} A_{id} \\ A_{iq} \end{bmatrix} = A_i, \\ \begin{bmatrix} H_{id} & 0 \\ 0 & H_{iq} \end{bmatrix} &= H_i, H_v = \begin{bmatrix} H_{id} H_{vo} \\ 0 \end{bmatrix}, \quad \dots (5.13) \end{aligned}$$

$$\begin{aligned}
\begin{bmatrix} D_d \\ D_q \end{bmatrix} &= -\begin{bmatrix} H_i & H_v \end{bmatrix} \begin{bmatrix} I_c \\ V_o \end{bmatrix} \\
\begin{bmatrix} I_c \\ V_o \end{bmatrix} &= -\begin{bmatrix} G_{id} \\ G_{vd} \end{bmatrix} \begin{bmatrix} H_i & H_v \end{bmatrix} \begin{bmatrix} I_c \\ V_o \end{bmatrix} + \begin{bmatrix} Y_i & A_i \\ A_v & Z_o \end{bmatrix} \begin{bmatrix} V_c \\ I_o \end{bmatrix} \\
&= \begin{bmatrix} I + G_{id}H_i & G_{id}H_v \\ G_{vd}H_i & 1 + G_{vd}H_v \end{bmatrix}^{-1} \begin{bmatrix} Y_i & A_i \\ A_v & Z_o \end{bmatrix} \begin{bmatrix} V_c \\ I_o \end{bmatrix}
\end{aligned} \tag{5.14}$$

The reference vector is omitted from the Equation 5.13 because it does not affect the loop gain. The loop gain in Equation 5.14, is not a single transfer function as in the case of a DC-DC converter, but a transfer function matrix given by:

$$T(s) = \begin{bmatrix} G_{id}H_i & G_{id}H_v \\ G_{vd}H_i & G_{vd}H_v \end{bmatrix} \tag{5.15}$$

The diagonal elements of $T(s)$ represent the current and voltage loop gains and the off-diagonal elements, the coupling between the two channels. The characteristic polynomial, the eigenvalues of which determine the stability of the closed loop system is given by:

$$\begin{aligned}
\Phi_{CL} &= \det(I + T(s)) \\
&= \det((I + G_{id}H_i)(1 + G_{vd}H_v) - G_{id}H_vG_{vd}H_i)
\end{aligned} \tag{5.16}$$

The closed loop output impedance, audiosusceptibility and input admittance determined from Equation 5.14 are given in Equation 5.17. The modifications in the above expressions due to the interaction with the input filter are determined in the next section.

$$\begin{aligned}
\begin{bmatrix} Y_i & A_i \\ A_v & Z_o \end{bmatrix}^{CL} &= (I + T(s))^{-1} \begin{bmatrix} Y_i & A_i \\ A_v & Z_o \end{bmatrix} \\
(I + T(s))^{-1} &= \begin{bmatrix} S^{-1}(1 + G_{vd}H_v) & -S^{-1}G_{id}H_v \\ -G_{vd}H_iS^{-1} & \frac{(I + G_{vd}H_iS^{-1}G_{id}H_v)}{(1 + G_{vd}H_v)} \end{bmatrix} \\
S &= (I + G_{id}H_i)(1 + G_{vd}H_v) - G_{id}H_vG_{vd}H_i
\end{aligned} \tag{5.17}$$

5.3.1.3 Effect of Input Filter on Rectifier Performance

The circuit schematic of one phase of a typical input filter is shown in Figure 5.6. The corresponding state space representation of one phase is given by Equation 5.18.

$$\dot{x} = A_f x + Bu \quad \dots (5.18)$$

$$y = C_f x$$

The dq model of the input filter derived based on the directions presented in Chapter 3 is shown in Figure 5.10.

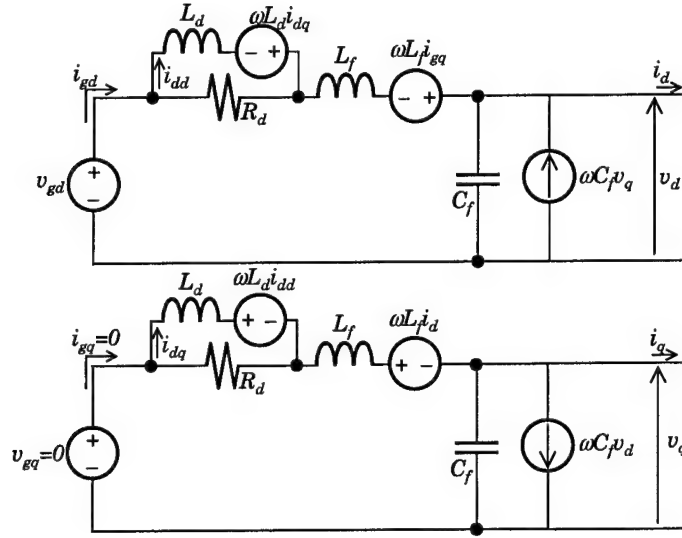


Figure 5.10. DQ -Equivalent circuit model of three phase input filter

The corresponding state space representation of the dq model is given by Equation 5.19.

$$\begin{bmatrix} \dot{x}_d \\ \dot{x}_q \end{bmatrix} = \begin{bmatrix} A_f & \omega_s I \\ -\omega_s I & A_f \end{bmatrix} \begin{bmatrix} x_d \\ x_q \end{bmatrix} + \begin{bmatrix} B_f & 0 \\ 0 & B_f \end{bmatrix} \begin{bmatrix} u_d \\ u_q \end{bmatrix} \quad \dots (5.19)$$

$$\begin{bmatrix} y_d \\ y_q \end{bmatrix} = \begin{bmatrix} C_f & 0 \\ 0 & C_f \end{bmatrix} \begin{bmatrix} x_d \\ x_q \end{bmatrix}$$

The transfer function representation of the Equation 5.19 is then,

$$\begin{bmatrix} Y_d(s) \\ Y_q(s) \end{bmatrix} = \begin{bmatrix} M(s) & N(s) \\ -N(s) & M(s) \end{bmatrix} \begin{bmatrix} U_d(s) \\ U_q(s) \end{bmatrix} \quad \dots (5.20)$$

where,

$$M(s) = C_f (sI - A_f) [(sI - A_f)^2 + \omega_s^2 I]^{-1} B_f$$

$$N(s) = \omega_s C_f [(sI - A_f)^2 + \omega_s^2 I]^{-1} B_f \quad \dots (5.21)$$

ω_s , the angular frequency of the input supply voltage. Figure 5.11 shows how the input filter affects the input currents and output voltage of the boost rectifier.

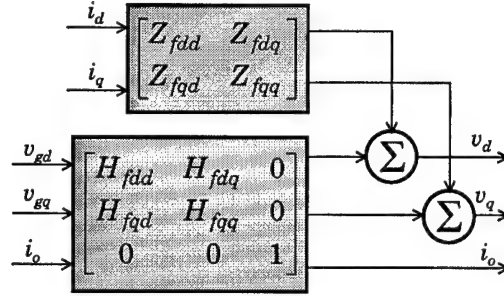


Figure 5.11. Effect of input filter on output variables of the rectifier

Due to the interaction with the input filter, Equation 5.14 gets modified as follows.

$$\begin{bmatrix} I_c \\ V_o \end{bmatrix} = \begin{bmatrix} I + G_{id}H_i + Y_iZ_{of} & G_{id}H_v \\ G_{vd}H_i + A_vZ_{of} & 1 + G_{vd}H_v \end{bmatrix}^{-1} \begin{bmatrix} Y_iH_f & A_i \\ A_vH_f & Z_o \end{bmatrix} \begin{bmatrix} V_g \\ I_o \end{bmatrix} \quad .. (5.22)$$

The characteristic polynomial is given by Equation 5.23. The last part of Equation 5.23 is obtained from the expression derived in Equation 5.17 for the closed loop input admittance. The origin of the minor loop gain, “ $Y_i^{CL}Z_{of}$ ” can be clearly seen in Equation 5.23.

The stability of the interconnected system is now given by stability of the controller loops and of the minor loop due to the interaction. Thus, the stability of interconnection is determined by the zeros of $\det(I + Y_i^{CL}Z_{of})$. It is obvious that the smaller the “magnitude” of the minor loop gain is compared to unity, lesser is the effect of the interaction due to the input filter on the performance and stability of the converter.

$$\begin{aligned} \Phi_{CL(filt)} &= \det((I + G_{id}H_i + Y_iZ_{of})(1 + G_{vd}H_v)) \\ &\quad - G_{id}H_v(G_{vd}H_i + A_vZ_{of}) \\ &= \det(I + T(s)) \times \\ &\quad \det\left(I + \left((I + G_{id}H_i)^{-1}Y_i - \frac{G_{id}H_vA_v}{\det(I + T(s))}\right)Z_{of}\right) \\ &= \det(I + T(s))\det(I + Y_i^{CL}Z_{of}) \end{aligned} \quad .. (5.23)$$

5.3.1.4 Sufficient Condition for Stability

According to the multivariable Nyquist criterion [33], the interconnected system is internally stable if the number of counterclockwise encirclements of the origin made by the Nyquist contour of $\det(I + Y_i^{CL}Z_{of})$ is equal to the number of right half plane poles of Y_i^{CL} and Z_{of} . Since Y_i^{CL} and Z_{of} are transfer function matrices, it is quite difficult to relate their individual elements to the characteristic polynomial

$\det(I + Y_i^{CL} Z_{of})$. Hence, the criterion for stability must be simplified so that it lends itself to direct physical insight and can be used efficiently in a design procedure. In the following, a sufficient condition for stability is derived based on the singular values of input admittance Y_i^{CL} , and output impedance Z_{of} matrices. From Figure 5.9 and Equation 5.14,

$$\begin{bmatrix} V_d \\ V_q \end{bmatrix} = \left[I + \underbrace{\begin{bmatrix} Z_{fdd} & Z_{fdq} \\ Z_{fqd} & Z_{fqq} \end{bmatrix}}_{Z_{of}} \underbrace{\begin{bmatrix} Y_{dd}^{CL} & Y_{dq}^{CL} \\ Y_{qd}^{CL} & Y_{qq}^{CL} \end{bmatrix}}_{Y_i^{CL}} \right]^{-1} \underbrace{\begin{bmatrix} H_{fdd} & H_{fdq} \\ H_{fqd} & H_{fqq} \end{bmatrix}}_{\begin{bmatrix} V_{sd} \\ V_{sq} \end{bmatrix}} \begin{bmatrix} V_{gd} \\ V_{gq} \end{bmatrix} \bigg|_{I_o=0}$$

$$\begin{bmatrix} V_d \\ V_q \end{bmatrix} = [I + Z_{of} Y_i^{CL}]^{-1} \begin{bmatrix} V_{sd} \\ V_{sq} \end{bmatrix} \quad \dots (5.24)$$

Equation 5.24 shows the existence of a feedback loop as shown in Figure 5.2, the only difference in this case being that the elements of the feedback loop are transfer function matrices. According to the small gain theorem, a sufficient condition for stability is to ensure that the product of the incremental gains of the systems comprising the feedback loop is less than unity for all ω . The incremental gain of a linear, time invariant, stable system is its maximum singular value. The theory of singular values of a matrix and its application to the study of multivariable systems has been well established [33]. In simple terms, the singular values of a matrix represent its “modulus” or “gain” similar to the modulus of a scalar constant. Hence, the sufficient condition for stability is given by

$$\bar{\sigma}(Y_i^{CL}(j\omega)) \bar{\sigma}(Z_{of}(j\omega)) < 1 \quad \dots (5.25)$$

The sufficient condition for stability also turns out to be the condition that ensures minimal interaction between the input filter and the converter as shown below.

$$\left| \det(I + Y_i^{CL}(j\omega) Z_{of}(j\omega)) \right| \leq (1 + \bar{\sigma}(Y_i^{CL}(j\omega)) \bar{\sigma}(Z_{of}(j\omega)))^2 \quad \dots (5.26)$$

Hence, satisfying Equation 5.25 not only ensures the stability of the minor loop gain (and hence of the integrated system), but also that its modulus is closer to 1 than to zero so that the characteristic polynomial given by Equation 5.23 is not appreciably different from that given by Equation 5.16.

5.3.1.5 Simplifying Approximations

In this section, approximate expressions for the singular values of Y_i^{CL} and Z_{of} are derived based on the knowledge of the physical properties of the system.

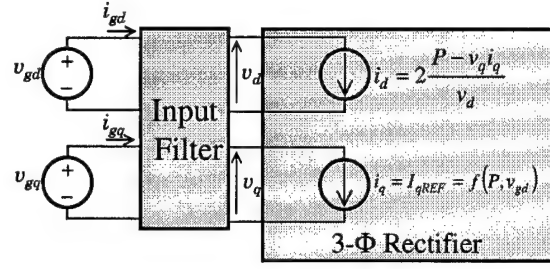


Figure 5.12. Low frequency model of 3-Φ rectifier with input filter

The three phase rectifier, as mentioned before, regulates i_q to a reference value to provide unity power factor at the input. This reference value is determined as a function of the real power P , supplied by the rectifier and the input voltage. It provides a tightly regulated DC output and hence constant power for a given load. Thus, a simplified model of the rectifier that is valid at low frequencies can be represented as shown in Figure 5.12.

The function f , in Figure 5.12, used to determine I_q is static with no time dependent dynamics. Hence, the input admittance of the rectifier and its singular values according to Figure 5.12 are then given by,

$$Y_i^{CL} \approx Y_i^{DC} = \begin{bmatrix} Y_{dd} & Y_{dq} \\ 0 & 0 \end{bmatrix} = \begin{bmatrix} -2 \frac{P - V_q I_q}{V_d^2} & 2 \frac{I_q}{V_d} \\ 0 & 0 \end{bmatrix} \quad \dots (5.27)$$

$$\bar{\sigma}(Y_i^{CL}) \approx \bar{\sigma}(Y_i^{DC}) = \sqrt{|Y_{dd}|^2 + |Y_{dq}|^2}$$

The output impedance of the input filter, from Equation 5.20, is given by,

$$Z_{of} = \begin{bmatrix} M(s) & N(s) \\ -N(s) & M(s) \end{bmatrix}$$

$$\bar{\sigma}(Z_{of}(j\omega)) = \sqrt{|M(j\omega)|^2 + |N(j\omega)|^2 + 2|\text{Im}(M^*(j\omega)N(j\omega))|}$$

$$\leq |M(j\omega)| + |N(j\omega)| \quad \dots (5.28)$$

$M(s)$ and $N(s)$ are as defined in Equation 5.20 with the appropriate choice of B_f and C_f matrices. It can be easily shown that the imaginary parts of the eigenvalues of the dq -model of the filter are symmetrically displaced from the values for the single phase model by the angular frequency ω_k of the input voltages. Figure 5.13 shows the input admittance and output impedance transfer functions of the boost rectifier and input filter respectively.

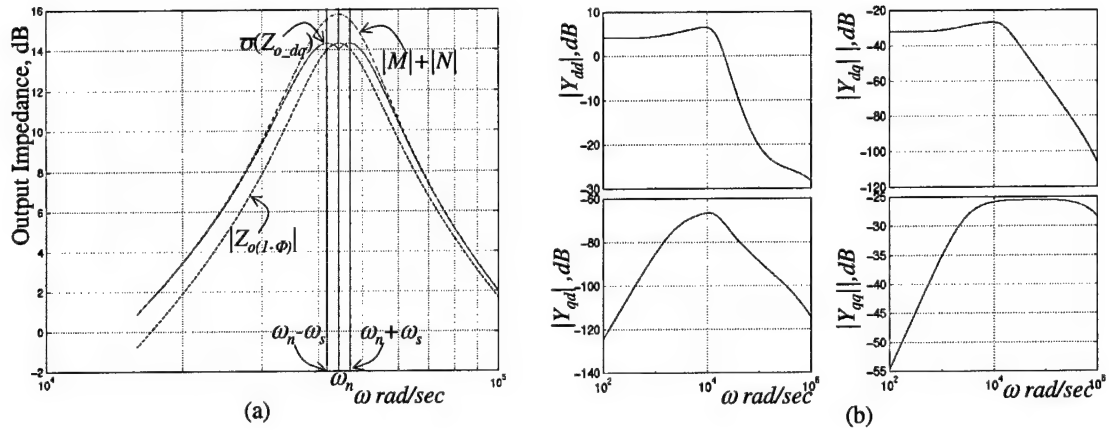


Figure 5.13. (a) Output Impedance of Input Filter (b) Input Admittance of Boost Rectifier

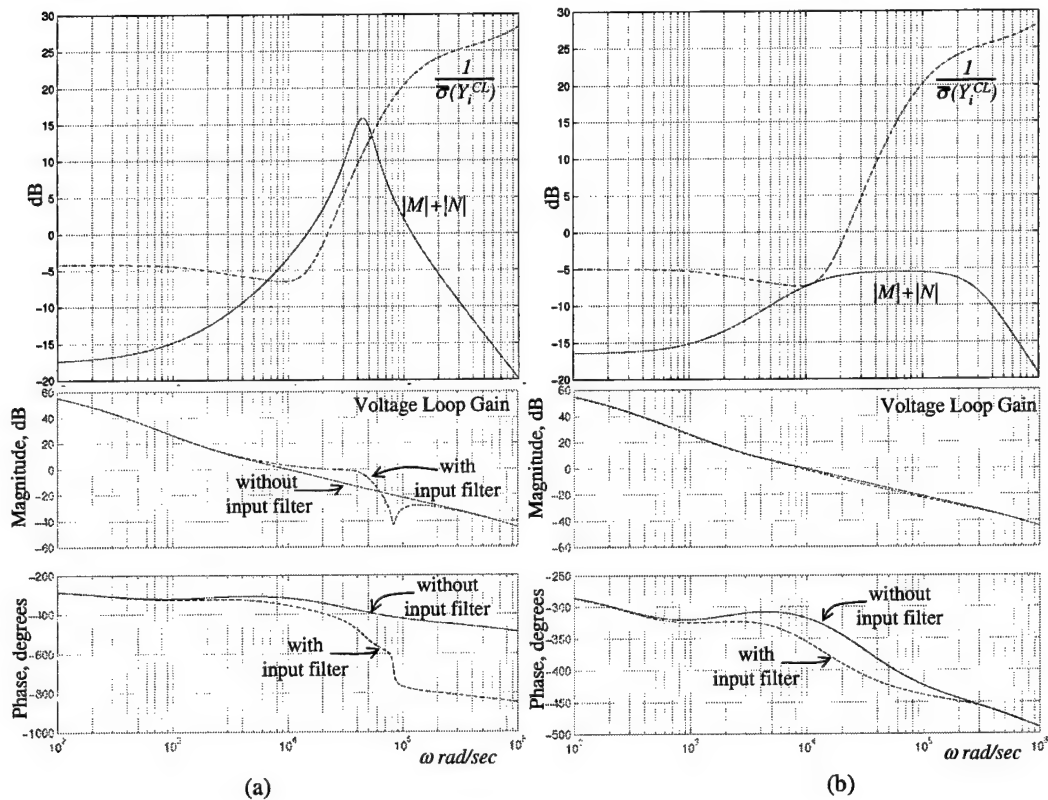


Figure 5.14. Impedance overlap and voltage loop gain of the rectifier system with and without input filter
(a) Strong Interaction (b) Minimal interaction

The interaction between the input filter and the converter is shown in Figure 5.14 for two sets of parameter values for the input filter, one that results in appreciable impedance overlap and hence strong interaction (Figure 5.14a) and another with no impedance overlap and minimal interaction (Figure 5.14b). The singular values of the input admittance and output impedance of the rectifier and the filter respectively are plotted as a function of frequency. The voltage loop gain of the rectifier with and without the input filter is also shown in Figure 5.14 to illustrate the effect of the interaction due to the input filter.

5.4 Stability Analysis of Sample System

In this section, the stability of the sample power distribution system is investigated by the application of the impedance ratio criterion. A source and load subsystem are identified and the criterion is applied to ascertain the stability of the integrated system. Simulation examples are presented to describe the characteristics of the system and to apply the stability criterion appropriately. A simulation example illustrating the loss of stability of the sample power system due to a large signal disturbance is presented to demonstrate the inability of the criterion to guarantee stability under large signal perturbations. This example, in addition, motivates the use of nonlinear methods to obtain a global understanding of the behavior of the system.

5.5 Sample Power Distribution System

The sample power distribution system is shown in Figure 5.15. Each of the independent subsystems in Figure 5.15 is designed for stable operation. However, the stability of the interconnected system remains to be investigated.

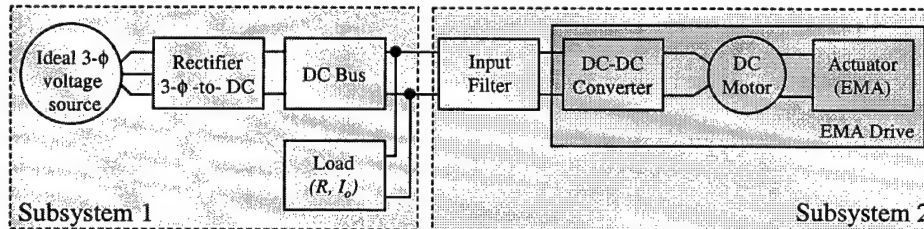


Figure 5.15. Sample Power System Architecture

The DC bus and the three-phase voltage source are considered to be non dynamic elements and are not included in the stability analysis. The impedance ratio criterion is used to determine the stability of sample system. The source subsystem represented by subsystem 1 consists of an ideal three phase voltage source, a three-phase boost rectifier to provide the regulated 270V DC required by the DC bus. The load subsystem represented by Subsystem 2 is an electromechanical actuator used to control the secondary flight control surfaces on the aircraft. The other loads on the DC bus are modeled by a current source, or a simple resistance.

The three-phase boost rectifier is represented by its dq -average model in rotating coordinates synchronized with the input line voltages [32]. A multi-loop controller for the three-phase boost rectifier consists of an outer loop to regulate the output voltage and two inner current loops, one each for the d - and q - axis input currents.

The ElectroMechanical Actuators (EMAs) drive the secondary flight control surfaces consisting of 14 inboard (IB) and outboard (OB) spoiler panels as shown in Figure (something in some chapter). The EMA is driven by a three-phase brushless DC or permanent magnet synchronous motor drive. The inverter-

motor drive is modeled in rotating dq -coordinates that are synchronized with the rotor position. This modeling approach essentially reduces the motor currents and voltages to DC and the resulting model to that of a DC motor. The circuit schematic of the input filter used for the EMA drive in subsystem 2 is shown in Figure 5.16.

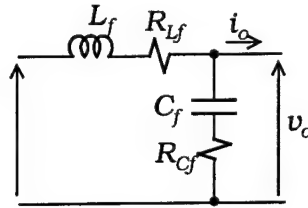


Figure 5.16. Schematic of input filter

5.6 Simulation Results

Typical simulation results for one actuator deflection cycle are shown in Figure 5.17. The change in actuator position from 0 to a commanded reference value is equivalent to a system transition from one equilibrium point to another. Hence, the stability of the sample system has to be guaranteed over a range of equilibrium points. It can be seen that the voltage at the DC bus suffers some spikes due to the transient disturbances caused by the surface deflection command to the actuator. It is critical that the magnitude of the voltage spikes be limited between specified limits and that the system makes a stable transition from one equilibrium point to another. The limits on the transient spikes and the distortion spectra on the DC bus voltage are defined by the specification MIL-STD-704E [34].

The input filter in addition to attenuating the switching ripple, reduces the magnitude of the voltage spike seen on the DC bus according to the size of the filter capacitance and the damping.

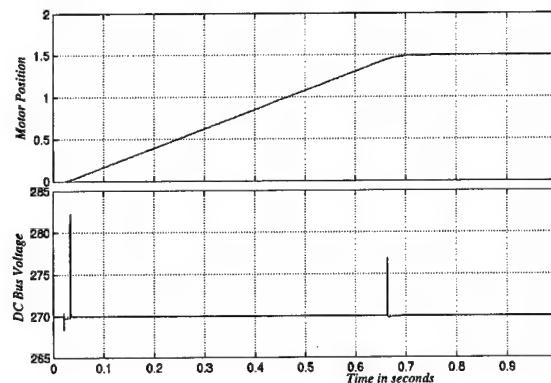


Figure 5.16. Simulation of One Actuator cycle

Other factors that determine the magnitude of the voltage excursions are the regulation bandwidth of the boost rectifier and, the other loads on the bus. It is critical that the stability of the interconnected system is verified against the variation of these parameters. The output impedance of subsystem 1 and input admittance (impedance) of subsystem 2 corresponding to the definitions in Figure 5.1, are identified in Figure 5.18.

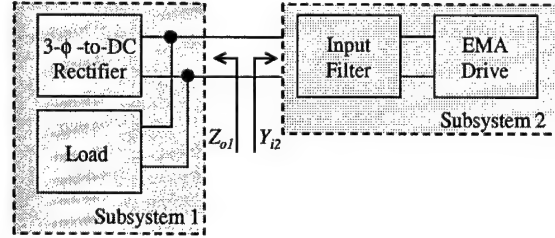


Figure 5.13. Identification of output impedance and input admittance in sample power system.

The input and output impedances of subsystems 2 and 1 respectively as a function of reference surface deflection command are shown in Figure 5.19. It can be seen that the output impedance of subsystem 1 does not vary as appreciably as the input impedance of subsystem 2.

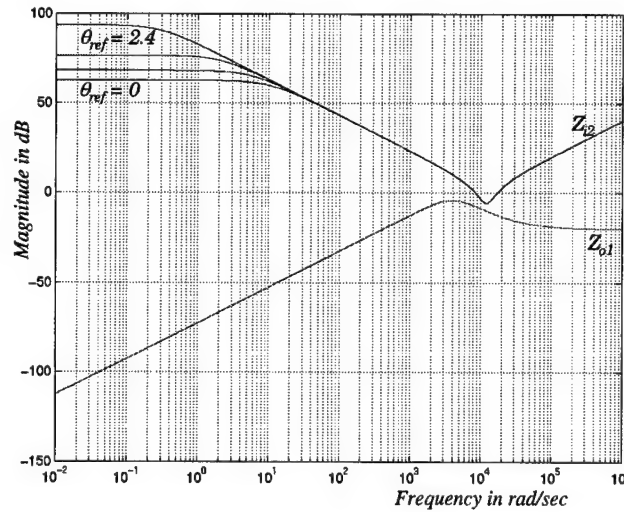


Figure 5.19. Impedance Curves as a function of surface deflection command θ_{ref}

The input impedance is lowest for a $\theta_{ref}=0$, and is hence, the worst case input impedance. As a result, if the stability of the sample system is ensured for $\theta_{ref}=0$, then stability at equilibrium points corresponding to other values of θ_{ref} is guaranteed. The stability of the sample system is tested against the variation of the capacitance in the input filter and in the boost rectifier in Figure 5.20. It is important to keep in mind that an intersection of the impedance curves is not an indication of instability because of the sufficiency of the impedance ratio criterion.

The inability of the impedance ratio criterion to predict the loss of stability due to a large disturbance is illustrated in Figure 5.21. The Nyquist contour of the minor loop gain shown in Figure 5.21a shows that the equilibrium point is stable. A surface deflection command identical to that shown in Figure 5.17 drives the system into sustained oscillations as shown in Figure 5.21b. This behavior cannot be predicted by the impedance ratio criterion.

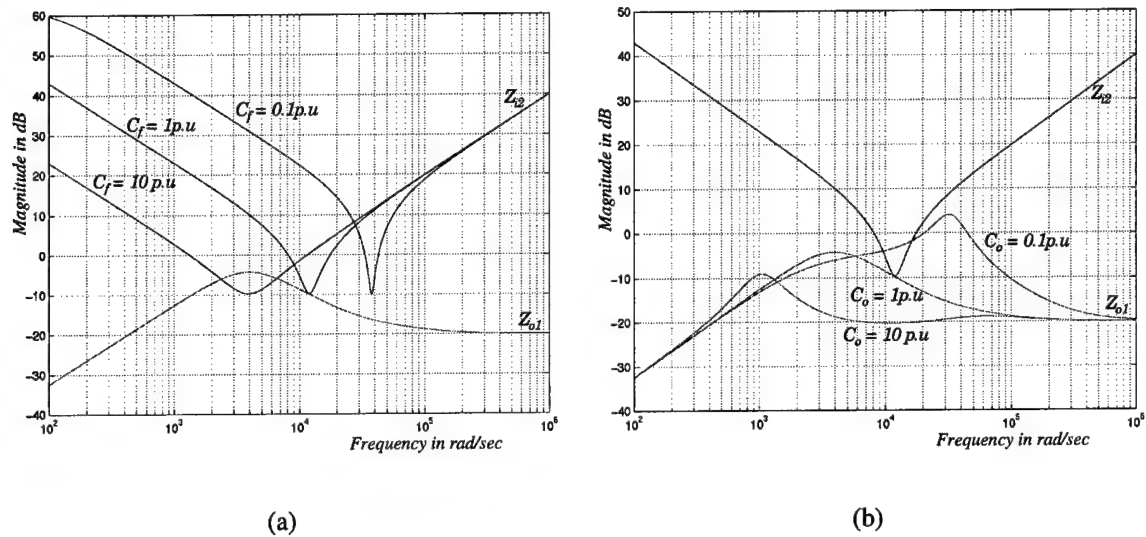
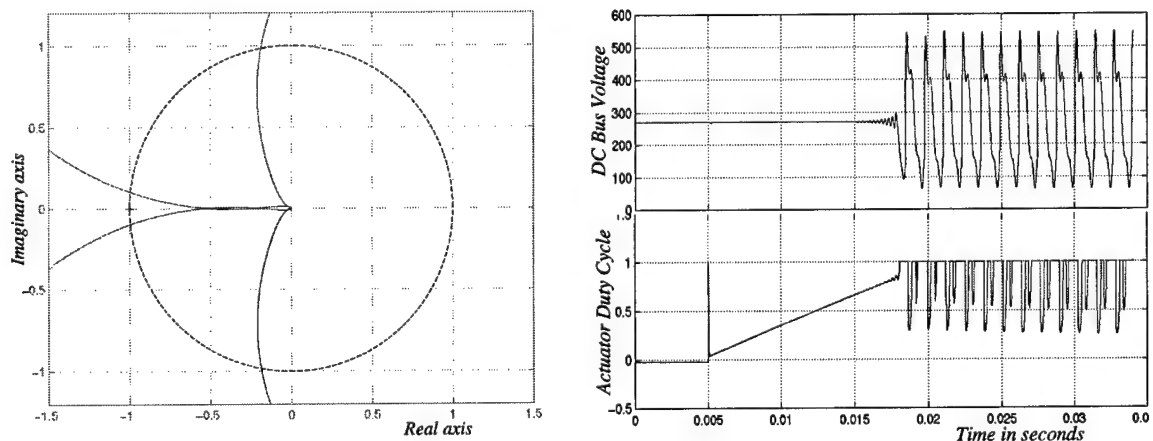


Figure 5.20. Testing the impedance ratio criterion as a function of (a) Filter capacitance C_f (b) Boost Rectifier Capacitance C_o .

The simulation results shown in Figure 5.21 indicate the manifestation of the nonlinear nature of the sample system and entail the application of nonlinear methods to analyze the stability of the system. The application of nonlinear methods to study interaction and stability will be described in the next section. However, the importance of linear methods cannot be completely ignored. Although linear analysis methods yield conservative results, they serve as valuable pointers in identifying critical parameters that can cause strong nonlinear interactions.



(a)

(b)

Figure 5.21. (a) Nyquist contour of minor loop gain (b) Loss of Stability due to large signal disturbance

5.7 Nonlinear Analysis

The simulation examples in the previous section illustrate that the application of linear methods guarantees stability of the system under small disturbances. The behavior of the system when subjected to a large disturbance cannot be predicted. Methods that accommodate the nonlinear characteristics of the system must then be used to obtain a global understanding of the system behavior. The analysis of stability under bidirectional power flow is first studied in this section. The use of bifurcation methods to study system behavior is presented next. The interaction between an input filter and a regulated DC-DC converter and interaction at the DC bus of a modified sample power system are described.

5.8 Stability under Bidirectional Power Flow

The effects of bidirectional power flow on the stability of the converter system are presented in this section. The impedance ratio criterion uses linearized models and hence provides only local stability information in a small neighborhood around the operating point. To obtain large signal stability information, methods that recognize the nonlinear nature of the subsystems need to be used. Figure 5.22 shows a simplified schematic of a regulated power converter with an input filter. The stability of this interconnected system under conditions of bidirectional power flow will be investigated in this section. This system consists of a regulated bidirectional power converter connected to a source through an input filter. The output of the converter is connected to an ideal load modeled by current source. Under constant load conditions, the power delivered to the load is constant because the output voltage of the converter is regulated. The regulated converter thus appears as a constant power load to a system that is connected at its input.

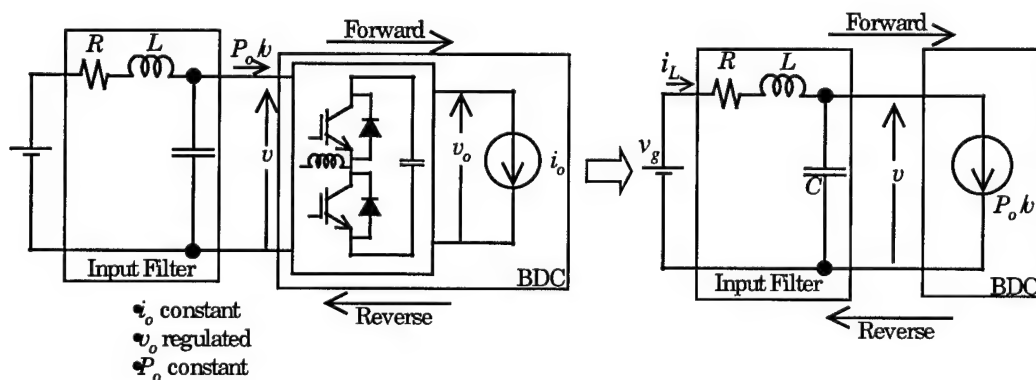


Figure 5.22. Regulated Converter with Input Filter

The constant power curve of this converter is shown in Figure 5.23 by the solid curve when the power is flowing to the load. When the load is regenerating power, the constant power curve is shown by the dotted line in the fourth quadrant of the graph. The constant power curves in Figure 5.23 show that the system in Figure 5.22 is fundamentally a nonlinear system, and that the converter and load appears as a negative impedance to the source when the power is flowing in the forward direction as shown in Figure 5.22. When the direction of power flow reverses, the input impedance of the converter subsystem changes sign as can be clearly observed in Figure 5.23.

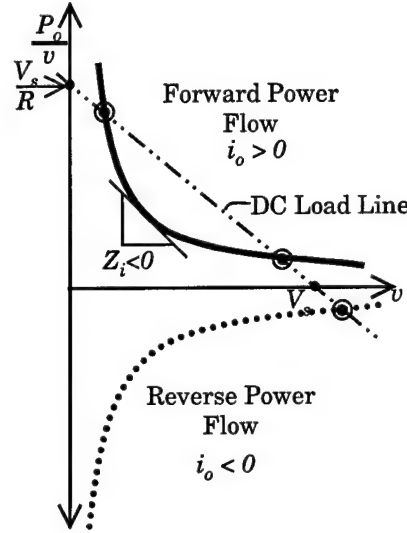


Figure 5.23. Constant Power Characteristics of a Regulated Power Converter

The state equations for the system shown in Figure 5.23 are given below:

$$\begin{aligned} L \frac{di_L}{dt} &= v_g - Ri_L - v \\ C \frac{dv}{dt} &= i_L - \frac{P_o}{v} \end{aligned} \quad \dots (5.29)$$

The equilibrium solutions for the system are given by:

$$\begin{aligned} I_{Le} &= \frac{P_o}{V_e} \\ V_e &= \frac{V_g}{2} \left(1 \pm \sqrt{1 - 4R \frac{P_o}{V_g^2}} \right) \end{aligned} \quad \dots (5.30)$$

The equilibrium points for the system are also determined from the points of intersection between the DC load line and the constant power characteristics of the power converter. This is illustrated in Figure 5.23. Equilibrium solutions exist as long as the load line intersects the constant power curve. In the forward

direction, the load lines for $R \leq V_g^2 / 4P_o$ intersect the constant power curve. Equilibrium points do not exist for $R > V_g^2 / 4P_o$. On the other hand, there exist equilibrium points for all values of R in the reverse direction. This can be inferred from the expressions for the equilibrium solutions in Equation 5.30. Real equilibrium solutions for V_e exist only for $R \leq V_g^2 / 4P_o$. However, for reverse power flow when P_o is negative equilibrium solutions exist for all values of R .

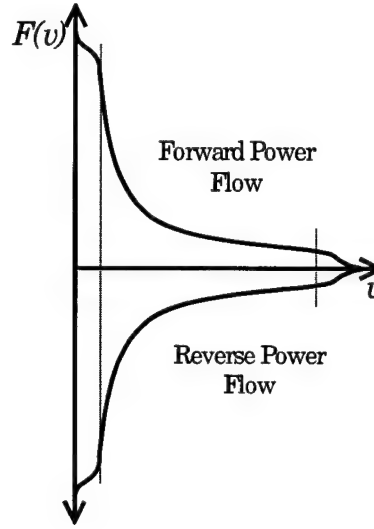


Figure 5.24. Constant Power Characteristics of a Regulated Power Converter

The stability of the equilibrium points depends on the parameter values. To make the stability analysis practical meaningful, the constant power characteristic of the regulated power converter is redrawn to have a finite area under it as shown in Figure 5.24 [37,38].

Definition Complete Stability: A system is said to be “completely stable” if there exist finitely many equilibrium solutions and every solution for the system equations approaches an equilibrium solution.

The criterion for complete stability is given below:

Theorem (Brayton and Moser): A dynamic system described by the state equations

$$\dot{x} = -Ax + Bu$$

$$\dot{y} = Dx - f(y)$$

with the following conditions,

1. A symmetric and positive definite

$$2. B = -D^T$$

..... (5.31)

3. The Jacobian df/dy is symmetric

and $B^T A^{-1} y + f(y) = \text{Grad } G(y)$, if,

1. $\|A^{-1}B\| < 1$ (5.32)
2. $G(y) \rightarrow \infty$ as $|y| \rightarrow \infty$

The system is completely stable. To fit the system in Figure 5.22 within the framework of the theorem given above, the following definitions are made.

$$\begin{aligned} x &:= i_L & y &:= \sqrt{\frac{C}{L}}(v - V_g) \\ A &:= -\frac{R}{L} & B = -D &= -\frac{1}{\sqrt{LC}} \\ f(y) &= \frac{1}{\sqrt{LC}} F\left(\sqrt{\frac{L}{C}} + V_g\right) \end{aligned} \quad \text{..... (5.33)}$$

where, $F(v)$ is as shown in Figure 5.24.

Test for Stability:

1. $\|A^{-1}B\| < 1 \Rightarrow \sqrt{\frac{L}{C}} < R$
2. $G(y) = \frac{1}{2RC} y^2 + \frac{1}{\sqrt{LC}} \int_0^y F\left(\sqrt{\frac{L}{C}}\sigma + V_g\right) \cdot d\sigma$ (5.34)

If $F(v)$ is as shown in Figure 5.24, $G(y) \rightarrow \infty$ as $|y| \rightarrow \infty$ and complete stability is ensured if

$$\sqrt{\frac{L}{C}} < R \quad \text{..... (5.35)}$$

Thus, the stability region can be defined for the forward direction as shown in Figure 5.25. The forward direction of power flow is hence, most critical from the stability standpoint (i.e.) as long as stability is guaranteed in the forward direction, it is preserved in the reverse direction upto the same power level. The reversal of power flow results in the input impedance of the converter system changing sign.

The reasons for potential instability due the negative input impedance of the converter thus cease to exist during regeneration. This result can be further corroborated by the impedance ratio criterion that was introduced in the previous chapter.

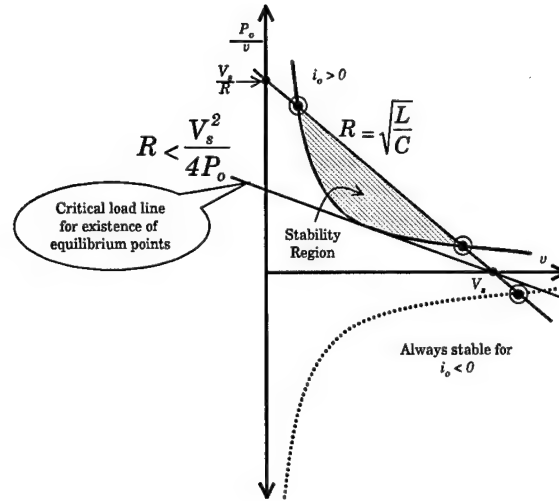


Figure 5.25. Stability of Equilibrium Solutions

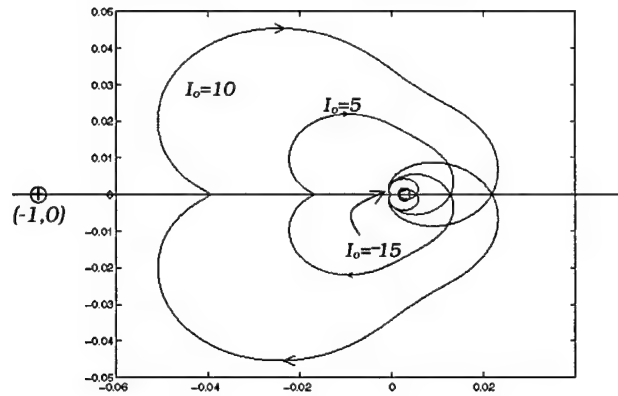


Figure 5.26. Stability of Interconnected System under reversal of power flow

Nyquist contours of the loop gain $Z_{o1}Y_{12}$ are shown in Figure 5.26 as a function of the load current. Z_{o1} and Y_{12} represent the output and input impedances of the input filter and power converter respectively. It can be seen that the Nyquist plots move further away from the $(-1, 0)$ as the load current changes sign and hence reverses the power flow. The foregoing analysis thus suggests that the overall system stability is determined by the stability of the system when the power is flowing in the forward direction. If this result extends to more complicated models, it suggests a simplification in the design process by reducing the complexity of the stability tests.

5.9 Bifurcation Methods

5.9.1 Input Filter Interaction

The circuit schematic of a regulated DC-DC buck converter with an input filter is shown in Figure 5.27 [41]. The resistance R_f in the input filter is chosen as the control parameter and

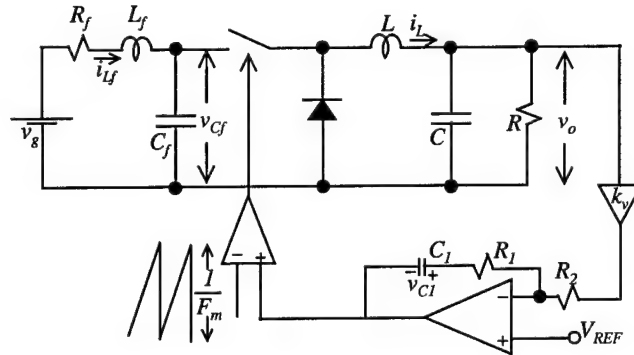


Figure 5.27. DC-DC Buck Converter with Input Filter

the system behavior as a function of R_f is studied.

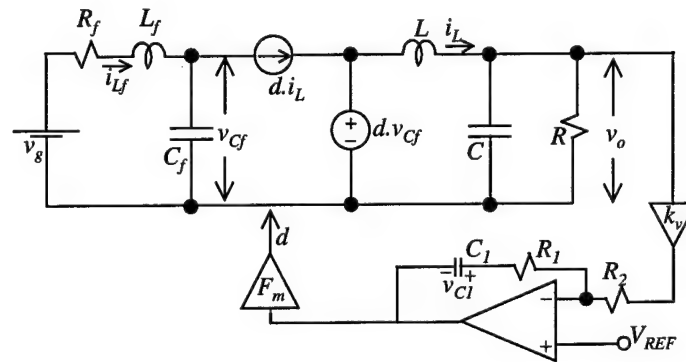


Figure 5.28. Average Model of DC-DC Buck Converter with Input Filter

The PWM switch in Figure 5.27 is replaced by its average model as shown in Figure 5.28. Denoting the gain R_f/R_2 by h_o , the dynamic state space equations of the average model shown in Figure 5.28 are given below:

$$\begin{aligned}
L \frac{di_L}{dt} &= (1+h_o)F_m V_{REF} v_{Cf} - h_o k_v F_m v_o v_{Cf} - F_m v_{C1} v_{Cf} - v_o \\
C \frac{dv_o}{dt} &= i_L - \frac{v_o}{R} \\
L_f \frac{di_{Lf}}{dt} &= v_g - R_f i_{Lf} - v_{Cf} \\
C_f \frac{dv_{Cf}}{dt} &= i_{Lf} - (1+h_o)F_m V_{REF} i_L + h_o k_v F_m i_L v_o + F_m v_{C1} i_L \\
C_1 \frac{dv_{C1}}{dt} &= \frac{1}{R_1} (k_v v_o - V_{REF})
\end{aligned} \tag{5.36}$$

The duty cycle d , is given by:

$$d = [(1+h_o)V_{REF} - h_o k_v v_o - v_{C1}] F_m \tag{5.37}$$

To reduce notational clutter, the state equations for the system are written as:

$$\dot{x} = f(x; R_f) \tag{5.38}$$

where, x , represents the state vector $[i_L \ v_o \ i_{Lf} \ v_{Cf} \ v_{C1}]^T$. The equilibrium solutions $x_e = [I_{Le} \ V_{oe} \ I_{Lfe} \ V_{Cfe} \ V_{C1e}]^T$ for the system are determined by setting the state derivatives in Equation 5.38 equal to zero and solving the resulting system of algebraic equations.

$$0 = f(x; R_f) \Rightarrow x = x_e \tag{5.39}$$

The equilibrium solutions are given by,

$$\begin{aligned}
I_{Le} &= \frac{V_{REF}}{k_v} \cdot \frac{1}{R} \\
V_{oe} &= \frac{V_{REF}}{k_v} \\
I_{Lfe} &= \frac{\left(\frac{V_{REF}}{k_v} \right)^2 \cdot \frac{1}{R}}{V_g \pm \sqrt{V_g^2 - 4 \frac{R_f}{R} \left(\frac{V_{REF}}{k_v} \right)^2}}
\end{aligned}$$

$$V_{Cfe} = V_g \pm \sqrt{V_g^2 - 4 \frac{R_f}{R} \left(\frac{V_{REF}}{k_v} \right)^2} \quad \dots (5.40)$$

$$V_{Cle} = V_{REF} - \frac{V_{REF}}{k_v} \cdot \frac{1}{V_g \pm \sqrt{V_g^2 - 4 \frac{R_f}{R} \left(\frac{V_{REF}}{k_v} \right)^2}}$$

The loci of the equilibrium solutions as a function of R_f is shown in Figure 5.29.

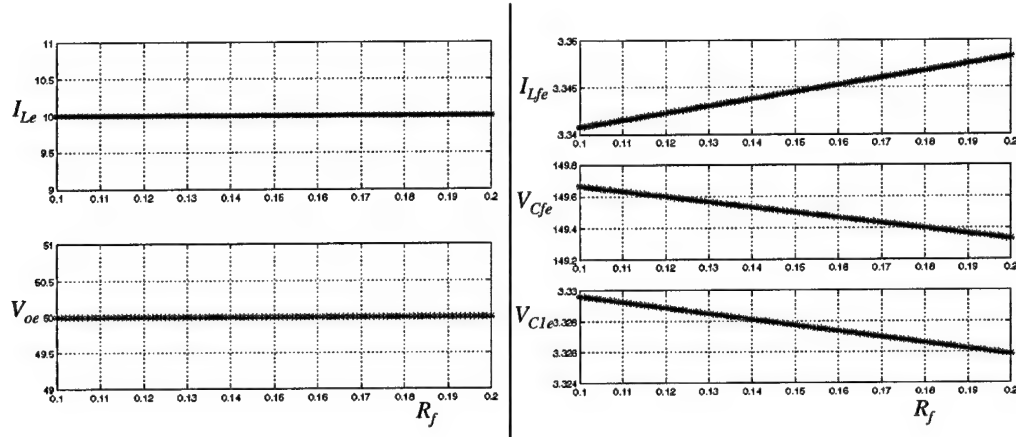


Figure 5.29. Loci of Equilibrium Solutions as a Function of R_f

The linearized system equations around the equilibrium solutions defined by Equation 5.40 are given by Equation 5.41. The location of the eigenvalues of the linearized system determines the stability of the system in the neighborhood of the equilibrium point x_e .

$$J(x_e; R_f) = \left. \frac{\partial f(x; R_f)}{\partial x} \right|_{x=x_e} \quad \dots (5.41)$$

As the eigenvalues move in the complex plane as a function of the control parameter, the system loses stability for a particular value of R_f in one of two ways as shown in Figure 5.30.

An eigenvalue moves to the right half plane through the origin. This is called a static bifurcation.

A pair of complex conjugate eigenvalues move to the right half plane with non-zero imaginary parts. This is called a dynamic or Andronov-Hopf bifurcation.

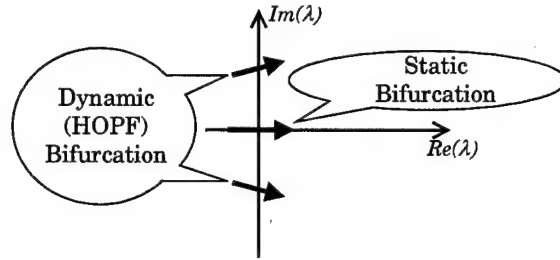


Figure 5.30. Loss of System Stability

The loci of eigenvalues of the linearized system for the DC-DC buck converter with input filter is shown in Figure 5.31.

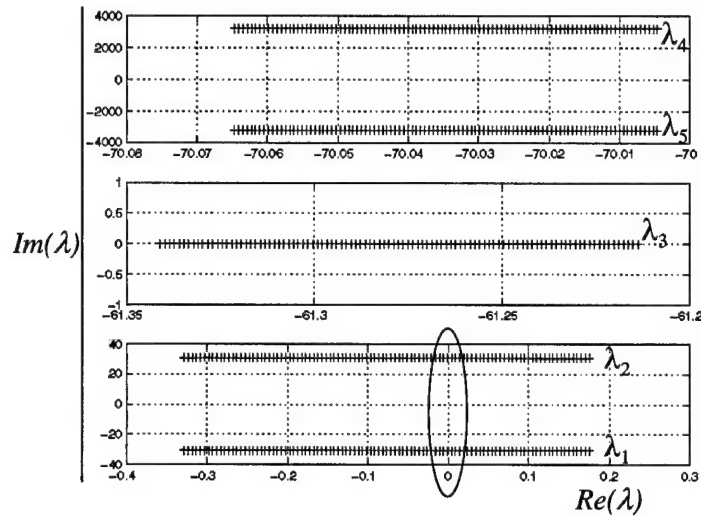


Figure 5.31. Loci of Eigenvalues of Linearized System as a function of R_f

It can be seen that a pair of complex conjugate eigenvalues λ_1 and λ_2 , move to the right half of the complex plane with non-zero imaginary parts. The system thus suffers a dynamic Andronov-Hopf bifurcation. An Andronov-Hopf bifurcation indicates the existence of periodic solutions. The stability of the periodic solutions near the bifurcation point is determined by the type of bifurcation. A Hopf bifurcation is further classified as supercritical and subcritical. By using perturbation methods, "Normal Form" equations that describe the behavior of the system near the bifurcation points are derived. The generic normal form equations for a Hopf bifurcation are given below:

$$\begin{aligned}\dot{a} &= \mu a + \alpha a^3 \\ \dot{\theta} &= \omega + \beta a^2\end{aligned}\quad \dots (5.42)$$

Depending on the sign of α , the bifurcation is supercritical or subcritical. A negative α indicates a supercritical Hopf and a positive α , a subcritical Hopf. A subcritical Hopf bifurcation is characterized by unstable periodic solutions bifurcating from the Hopf point. A supercritical Hopf bifurcation would, on the

other hand, have stable periodic solutions bifurcating from the Hopf point. For the system under study, the bifurcation was found to be subcritical.

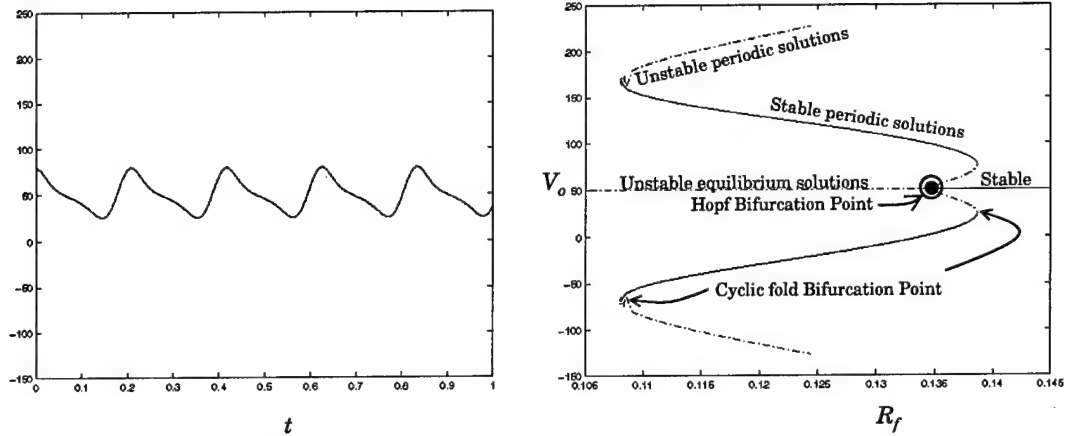


Figure 5.32. Bifurcation Diagram of DC-DC Buck Converter with Input Filter

The complete bifurcation diagram of the DC-DC buck converter with input filter is shown in Figure 5.32. The periodic solutions that bifurcate from the Hopf point are numerically constructed using shooting methods. A branch of periodic solutions as a function of the control parameter R_f can then be traced using one of several methods such as sequential, arc-length or pseudo arc-length continuation. The stability of the bifurcating periodic solutions is determined using Floquet theory. The construction, branch continuation and determination of stability of periodic solutions is explained in detail in the following section.

5.9.1.1 Construction and Stability of Periodic Solutions

The construction of periodic solutions basically involves the determination of initial conditions, x_0 and a solution, $x(t; x_0)$ with a minimal period T for the system equations (Equation 5.2) such that $x(T; x_0) = x_0$. To absorb the problem of determining the minimal period T of the periodic solutions into that of the initial conditions x_0 , the following transformations are performed on the state equations.

$$\begin{aligned}
 t &= \tau T \\
 \frac{dx}{dt} &= \frac{dx}{d\tau} \cdot \frac{d\tau}{dt} = \frac{1}{T} \frac{dx}{d\tau} \\
 \Rightarrow x' &= \frac{dx}{d\tau} = T \frac{dx}{dt} = T \cdot \dot{x} = T \cdot f(x; R_f)
 \end{aligned}
 \tag{5.43}$$

The augmented state equations with initial conditions are given below in Equation 5.44.

$$\begin{aligned} x' &= Tf(x; R_f) \\ T' &= 0 \end{aligned} \quad \begin{bmatrix} x(1; x_o) - x_o \\ x_k(0) - \eta \end{bmatrix} = 0 \quad \dots (5.44)$$

The initial condition, $x_k(0) = \eta$ in Equation 5.44 represents a phase condition for one of the state variables to account for additional state equation that was introduced due to the normalization.

To trace a branch of periodic solutions as a function of the control parameter R_f , the initial condition x_o and the minimal period T need to be determined with R_f as the continuation parameter along the branch. On the other hand, subsequent values of R_f at appropriate intervals along the branch of the periodic solutions can be determined by the continuation algorithm itself if the arc length s , is chosen as the continuation parameter. Hence, R_f is added as an additional state variable to the transformed state equations. The augmented state vector and the dynamic equations are denoted by an underscore as shown in Equation 5.45.

$$\begin{aligned} x' &= Tf(x; R_f) \\ T' &= 0 \\ R_f' &= 0 \end{aligned} \quad \begin{bmatrix} x(1; x_o) - x_o \\ x_k(0) - \eta \\ p(x_o, T, R_f, s) \end{bmatrix} = 0$$

$$\begin{aligned} \underline{x}' &= \underline{f}(\underline{x}) \quad G(\underline{x}_o) = 0 \\ \underline{x} &= [x^T \quad T \quad R_f] \end{aligned} \quad \dots (5.45)$$

The initial conditions x_o , minimal period T and, R_f are determined as a solution to a two-point boundary value problem [39,40]. The problem to be solved is given by Equation 5.45. The additional boundary condition in Equation 5.45 is given by:

$$\begin{aligned} p(x_o, T, R_f, s) &= \zeta \sum_{i=1}^5 (x_{oi} - x_{oi}(s_j)) \frac{dx_{oi}}{ds} + \zeta (T - T(s_j)) \frac{dT}{ds} \\ &\quad + (1 - \zeta) (R_f - R_f(s_j)) \frac{dR_f}{ds} - (s - s_j) \end{aligned} \quad \dots (5.46)$$

The required initial condition $\underline{x}_o = [x_o^T \quad T \quad R_f]^T$ is that for which $G(x_o, T, R_f, x(1; x_o))$ given by Equation 5.47 is equal to zero.

$$G(x_o, T, R_f, x(1; x_o)) = G(\underline{x}_o, x(1; \underline{x}_o)) = \begin{bmatrix} x(1; x_o) - x_o \\ x_k(0) - \eta \\ p(x_o, T, R_f, s) \end{bmatrix} \quad \dots (5.47)$$

A Newton-Raphson iterative procedure explained below is used to determine the initial conditions. A initial guess $\underline{x}_o^{(i)}$ is used as a starting point. The subsequent solutions are found as follows:

$$\begin{aligned}
G^{(i+1)} &= G^{(i)} + (\underline{x}_o^{(i+1)} - \underline{x}_o^{(i)}) G'^{(i)} = 0 \\
\Rightarrow \underline{x}_o^{(i+1)} &= \underline{x}_o^{(i)} - [G'^{(i)}]^{-1} G^{(i)}
\end{aligned}
\quad \dots (5.48)$$

where, $G^{(i)} = G(\underline{x}_o^{(i)}, x(1; \underline{x}_o^{(i)})$. The gradient of G at the i^{th} initial condition is given by:

$$\begin{aligned}
G'^{(i)} &= \frac{\partial G}{\partial \underline{x}_o^{(i)}} + \frac{\partial G}{\partial x} \cdot \frac{\partial x(1; \underline{x}_o^{(i)})}{\partial \underline{x}_o^{(i)}} \\
&= B_o + B_1 \cdot Y(\tau) \Big|_{\tau=1}
\end{aligned}
\quad \dots (5.49)$$

The matrices B_o and B_1 are defined below assuming that the index k in the phase condition in Equation 5.47 is chosen as 4:

$$B_o = \begin{bmatrix} 1 & 0 & 0 & 0 & 0 & 0 & 0 \\ 0 & 1 & 0 & 0 & 0 & 0 & 0 \\ 0 & 0 & 1 & 0 & 0 & 0 & 0 \\ 0 & 0 & 0 & 1 & 0 & 0 & 0 \\ 0 & 0 & 0 & 0 & 1 & 0 & 0 \\ 0 & 0 & 0 & 1 & 0 & 0 & 0 \\ \frac{dx_{o1}}{ds} & \frac{dx_{o2}}{ds} & \frac{dx_{o3}}{ds} & \frac{dx_{o4}}{ds} & \frac{dx_{o5}}{ds} & \frac{dT}{ds} & \frac{dR_f}{ds} \end{bmatrix}
\quad \dots (5.50a)$$

$$B_1 = \begin{bmatrix} -1 & 0 & 0 & 0 & 0 & 0 & 0 \\ 0 & -1 & 0 & 0 & 0 & 0 & 0 \\ 0 & 0 & -1 & 0 & 0 & 0 & 0 \\ 0 & 0 & 0 & -1 & 0 & 0 & 0 \\ 0 & 0 & 0 & 0 & -1 & 0 & 0 \\ 0 & 0 & 0 & 0 & 0 & 0 & 0 \\ 0 & 0 & 0 & 0 & 0 & 0 & 0 \end{bmatrix}
\quad \dots (5.50b)$$

The derivatives in the last column of the matrix B_o are determined as follows. Assuming that the initial condition x_o , minimal period T and the control parameter R_f have been found on a particular point on a branch we have,

$$\begin{aligned}
G(x_o, T, R_f, s) &= 0 \\
\Rightarrow \frac{\partial G}{\partial x_o} \cdot \frac{\partial x_o}{\partial s} + \frac{\partial G}{\partial T} \cdot \frac{\partial T}{\partial s} + \frac{\partial G}{\partial R_f} \cdot \frac{\partial R_f}{\partial s} &= 0 \\
\Rightarrow \begin{bmatrix} \frac{\partial x_o}{\partial s} \\ \frac{\partial T}{\partial s} \\ \frac{\partial R_f}{\partial s} \end{bmatrix} &= - \left[\begin{bmatrix} \frac{\partial G}{\partial x_o} & \frac{\partial G}{\partial T} \\ \frac{\partial G}{\partial x_o} & 1 \end{bmatrix}^{-1} \frac{\partial G}{\partial R_f} \right] \frac{\partial R_f}{\partial s}
\end{aligned}
\quad \dots (5.51)$$

The partial derivatives in Equation 5.51 are determined in terms of $\partial R_f / \partial s$. The vector is then normalized to have unit length. The quantities on the right hand side of Equation 5.51 are defined below.

$$\begin{aligned} \frac{\partial G}{\partial x_o} &= I - \frac{\partial x(1; x_o, R_f)}{\partial x_o} \\ \frac{\partial G}{\partial T} &= f(x(1), x_o, R_f) \end{aligned} \quad \dots (5.52)$$

The matrix $Y(\tau) = \frac{\partial x(\tau; \underline{x}_o^{(i)})}{\partial \underline{x}_o^{(i)}}$ in Equation 5.49 is the $n \times n$ fundamental solution defined by:

$$\begin{aligned} Y'(\tau) &= A(\tau)Y(\tau) \quad 0 < \tau < 1 \\ Y(0) &= I \quad A(\tau) = \frac{\partial f(\underline{x}(\tau); \underline{x}_o)}{\partial \underline{x}(\tau)} \end{aligned} \quad \dots (5.53)$$

$A(\tau)$ represents the Jacobian of the linearized system around the constructed periodic solution. In the actual computation, the $A(\tau)$ and the solution $\underline{x}(\tau; \underline{x}_o)$ are replaced by their numerical approximations obtained by solving the problem with the initially guessed solutions.

After computing $Y(\tau) = \frac{\partial x(\tau; \underline{x}_o^{(i)})}{\partial \underline{x}_o^{(i)}} \Big|_{\tau=1}$, it is substituted in Equation 5.49 for the gradient of G , which in turn

yields the new solution from Equation 5.48. The procedure is repeated until a convergence condition is met and continued as a function of the arc length s . The stability of the bifurcating periodic solutions is determined using Floquet theory [39]. After a periodic solution $x(t; x_o)$ with minimal period T is constructed, a by-product of the construction algorithm is the monodromy matrix Φ given by:

$$\Phi = \frac{\partial x(1; \underline{x}_o)}{\partial \underline{x}_o} \quad \dots (5.54)$$

The location of the eigenvalues of the monodromy matrix determine the stability of the periodic solution. If the eigenvalues of the monodromy matrix are inside the unit circle, the periodic solution is stable. As the control parameter R_f is varied, the eigenvalues of Φ move in the complex plane and may exit the unit circle in one of three ways as shown in Figure 5.33.

For the DC-DC buck converter with input filter, the eigenvalues of the monodromy matrix leave the unit circle through the $(1, 0)$ point. The system suffers a cyclic-fold bifurcation wherein a stable branch of periodic solutions loses stability and continues as an unstable branch of periodic solutions (Figure 5.32).

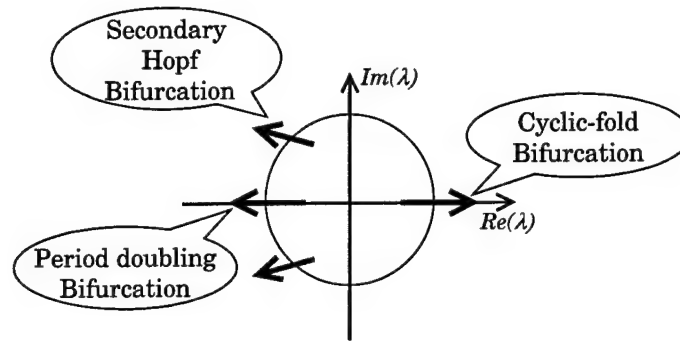


Figure 5.33. Bifurcation of Periodic Solutions

5.9.1.2 Comparison with Linear Analysis

Figure 5.34 illustrates the application of the impedance ratio Criterion. It can be seen that, according to Equation 5.1 the system is guaranteed to be stable for $R_f > 0.25$. The linear analysis technique provides information only about system stability as the control parameter is varied. Information regarding the type and multiplicity of solutions as provided by the bifurcation diagram cannot be obtained from linear analysis. Figure 5.35 shows a comparison between the linear and bifurcation analyses results. It is important to note from Figure 5.35 that a stable equilibrium solution (say X) can be perturbed strongly enough to drive the system to a periodic solution. On the other hand, an unstable equilibrium point (say Y) does not lead to catastrophic results when perturbed but only ends up in a stable periodic solution. Such an observation cannot be made from conventional linear analysis methods such as the Middlebrook Impedance Ratio Criterion. In addition, linear analysis provided a conservative estimate of system stability in this case.

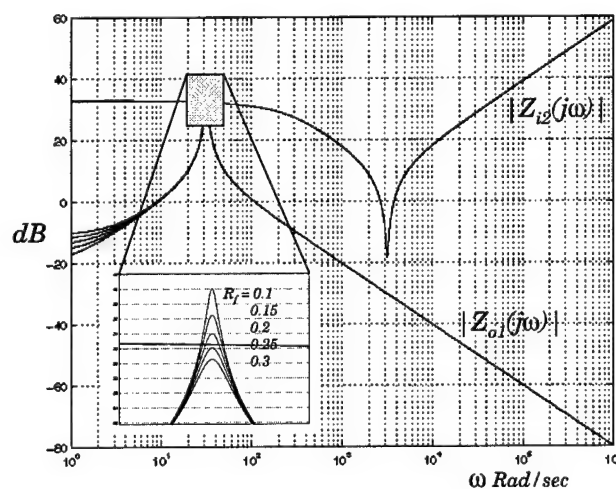


Figure 5.34. Middlebrook Criterion

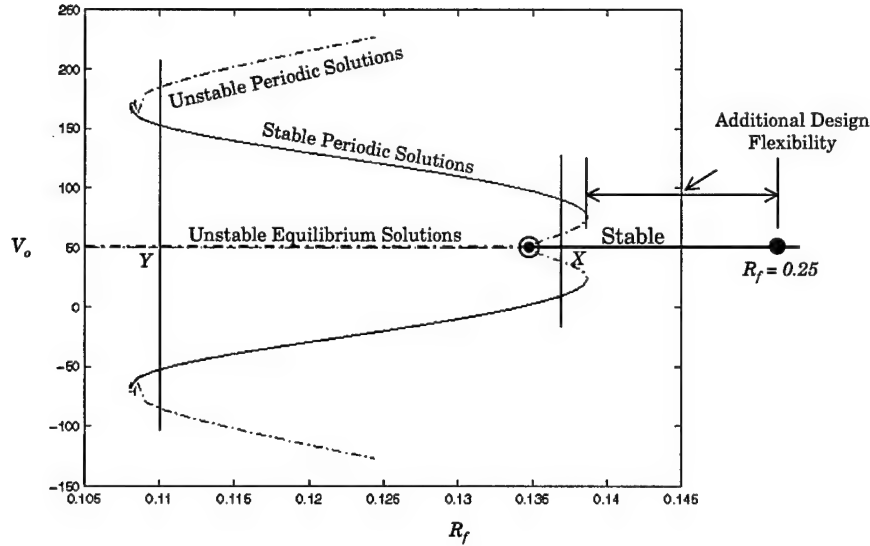


Figure 5.35. Comparison between Linear and Bifurcation Analysis

The Hopf point is at $R_f = 0.138$ where the equilibrium solution loses stability whereas the Middlebrook criterion provides a lower bound of $R_f = 0.25$. A clearer understanding of the system aided by the use of nonlinear analysis methods can hence help in newer design rules, control laws that optimize performance, cost, size and reliability.

5.9.2 Interaction at the DC Bus

The interaction at the DC bus, shown in Figure 5.36, between the bus regulator and a load converter is discussed in this section. The load subsystem represented by Subsystem 2 in Figure 5.36 is a regulated DC-DC converter with a front-end input filter. The other loads on the DC bus are modeled by a current source, negative impedance (other regulated power converters) or a simple resistance.

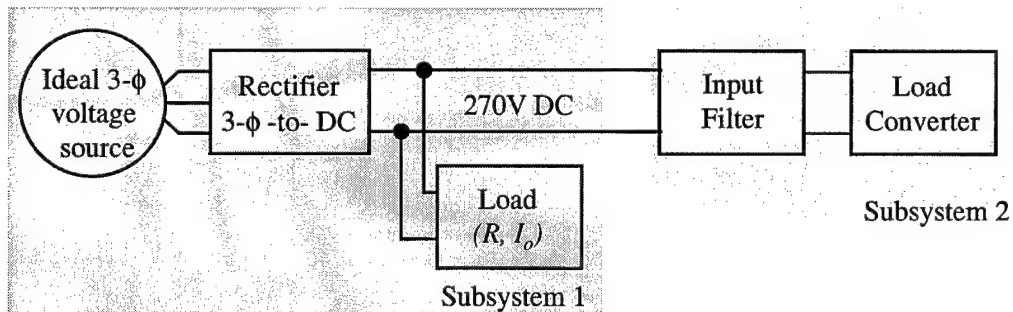


Figure 5.36. Simplified Power System Architecture

The three-phase boost rectifier is represented by its average model in rotating dq -coordinates synchronized with the input line voltages. The load converter is also represented by its corresponding average model.

The circuit schematic of the simplified power system is shown in Figure 5.37.

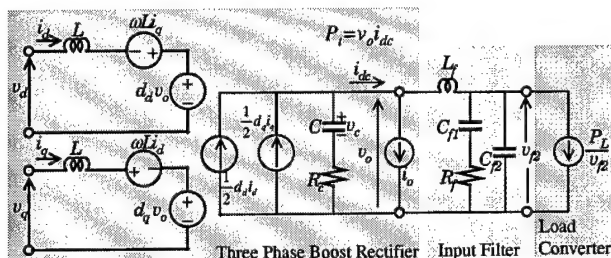


Figure 5.37. Circuit Schematic of Simplified Power System

The total power supplied by the boost rectifier is given by $P_r = v_o i_{dc}$ (Figure 5.37). The DC-DC converter in subsystem 2 is represented by a constant power load with the same modifications as in [37]. The input filter is a two-stage configuration with the damping resistance in a shunt path to minimize the power loss.

The first step in the analysis of the baseline system is the determination of the control parameter(s) for the bifurcation analysis. The three phase boost rectifier feeds the DC distribution bus of the baseline power system with a stiff regulated voltage of 270V.

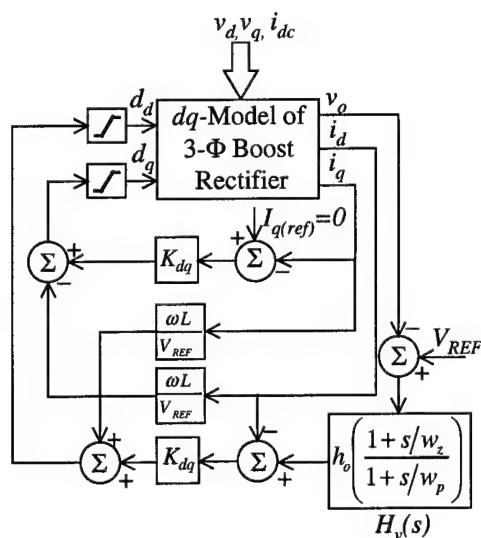


Figure 5.38. Control block diagram of three-phase boost rectifier

One of the critical performance indices of the rectifier is its bandwidth of regulation. This parameter can be related to the transient response and disturbance rejection properties of the rectifier. In addition, the bandwidth is intimately related to the stability of the rectifier and hence of the baseline system. The gain h_o

of the voltage controller $H_v(s)$ (Figure 5.38) is directly related to the bandwidth of the rectifier and hence is chosen as the control parameter for the bifurcation analysis of the baseline system. The stability analysis proceeds as follows: The stability of the equilibrium solutions of the baseline system is determined as a function of the control parameter, h_o . The total power P_i , supplied by the boost rectifier is divided equally between the constant current load i_o , and the constant power load P_L/v_{f2} . The complete bifurcation diagram for the baseline system for $P_i=8kW$ is shown in Figure 5.39a.

The equilibrium point loses stability through a Hopf bifurcation at $h_o=86.8295$ for $P_i=8kW$. The normal form equations (Equation 5.42) of the system at the Hopf point indicate that the bifurcation is supercritical (i.e.) the bifurcating periodic solutions are stable as shown in Figure 5.39a. The branch of periodic solutions is followed using the pseudo-arc length continuation procedure described in the previous section. The stability of the constructed periodic solutions is monitored by observing the corresponding Floquet multipliers. As mentioned in the previous section, the floquet multipliers move in the complex plane as a function of the control parameter and may exit the unit circle in one of three ways as shown in Figure 5.33. A period doubling bifurcation occurs at $h_o=88.7904$ where, one floquet multiplier exits the unit circle through $(-1,0)$. This is followed by another period doubling bifurcation to a period-4 solution. These periodic solutions are shown in Figure 5.39b.

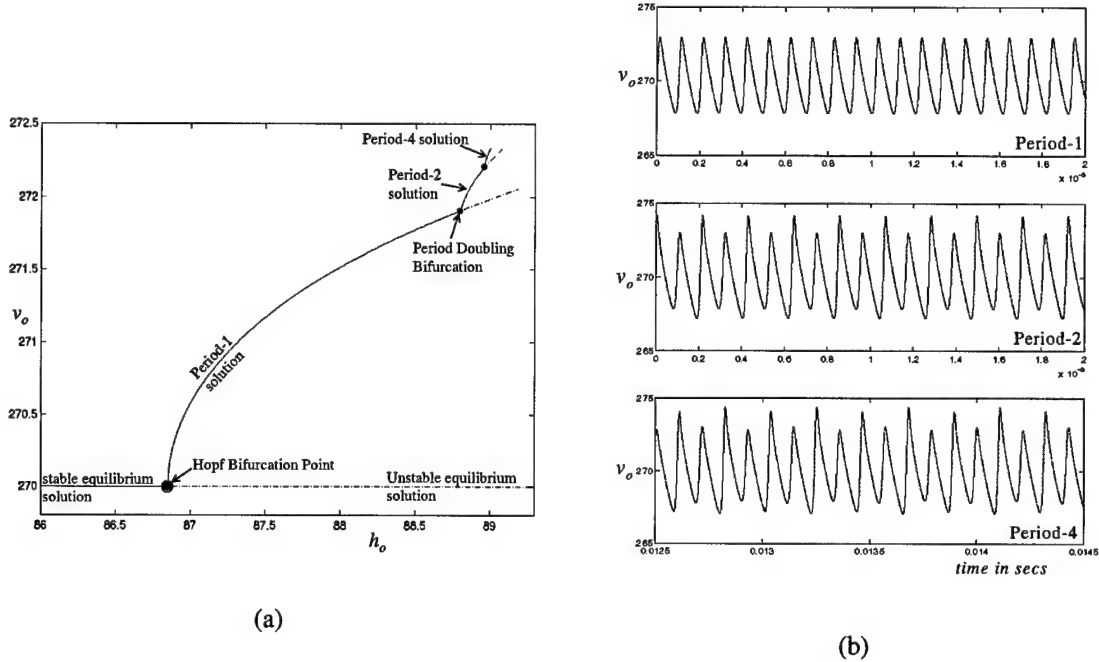


Figure 5.39. (a) Bifurcation Diagram of Baseline System as a function of h_o for $P_i=8kW$
(b) Periodic Solutions of Baseline System

5.9.2.2 Dependence on Parameter Values

The baseline system considered in this paper consists of two interconnected nonlinear subsystems namely, the three phase boost rectifier and the regulated load converter with input filter. The analysis method presented above considers the stability of the baseline system as a whole, regardless of the stability of the individual subsystems. To this end, as the control parameter is varied, the stability of the three phase boost rectifier as a standalone system terminated by the load P_r , is determined, in addition to that of the baseline system. The parameter values that yield the results shown in Figure 5.39 are such that, the equilibrium point of the boost rectifier as a standalone system loses its stability before that of the baseline system (i.e.) for $h_o < 86.8295$. Such a situation is only of academic interest as it defeats the entire purpose of subsystem integration in that, an unstable system (the boost rectifier) is integrated with a stable system (the filter-load converter subsystem) to form the stable baseline system. However, a different set of parameter values can result in an unstable baseline system while preserving the stability of the individual subsystems. It is the parameters of the boost rectifier that determine the manner in which the baseline system loses stability.

Since, the load on the DC bus is not constant at all times, the rectifier should provide "good" regulation of the DC bus voltage at all load levels. Since the baseline system is essentially nonlinear, the bandwidth of the regulator can be expected to change significantly with the load. Hence, it becomes important to study the effect of the regulation bandwidth of the rectifier on the stability of the baseline system for different values of power P_r . The values of h_o for which the baseline system loses stability were determined for different values of power P_r . For each value of P_r , the type of the Hopf bifurcation was determined by obtaining the normal form equations of the baseline system. The values of α_2 in the normal form equations are given in Table 5.1 for different values of power P_r .

In Table 5.1, case 1 is identified as the situation where the baseline system preserves its stability in spite of the boost rectifier being unstable, and that wherein the baseline system loses its stability with the individual subsystems being stable is identified as case 2. It can be seen from Table 5.1 that, the type of bifurcation for case 2 changes from subcritical to supercritical and back as the power is increased. Further investigation is necessary to identify the reasons for such a behavior. However, the normal form equations provide an idea about the post-bifurcation behavior of the system, which can be used to design fault-clearing systems in the event of an instability. In addition, it can be seen from Table 5.1, that the values of h_o for which the baseline system loses stability, decrease with increasing power. Hence, with the knowledge of the maximum possible load on the DC bus, h_o can be chosen such that the equilibrium solutions are stable at all load power levels or can be adaptively varied as a function of the load for optimal performance of the converter.

Table 5.1. α_2 for Case 1 and Case 2.

P_t (kW)	Case 1		Case 1	
	α_2	$h_{o(hopf)}$	$\alpha_2(10^{-6})$	$h_{o(hopf)}$
8	-0.01213	86.8295	26.9384	19.5325
16	-0.00818	45.8968	12.6145	8.5091
24	-0.00733	31.9366	4.6564	5.4051
32	-0.00854	24.6799	-3.0179	4.0491
40	-0.00773	19.9758	-6.4271	3.3109
48	-0.00214	16.5835	4.6585	2.8485
56	0.005724	14.0965	38.5256	2.5291

5.10 Conclusions

The problem of subsystem interaction was addressed in this chapter. A generic subsystem interface was considered and the traditional impedance ratio criterion that guarantees the stability of the interconnected system and minimal interaction was introduced. The interaction between the three-phase input filter and bus regulator was discussed. A multivariable impedance ratio criterion was derived. Due to the nonlinear nature of the systems, bifurcation methods were used to study the stability of a DC-DC converter with an input filter. The results obtained were then compared to the linear analysis results. The bifurcation analysis was extended to study the interaction at the DC bus between the bus regulator and a load converter in the presence of other loads in the system. Two distinct cases of loss of stability were identified and the dependence of system stability on parameter values was discussed. It was found that nonlinear methods provide information about the global behavior of the system. Knowledge of the system characteristics after the equilibrium point loses stability can be useful in designing fault-clearing mechanisms.

6 Conclusions

The principal goals of this project were the modeling, simulation and stability analysis of power distribution systems in 21st century airlifters. To start with a baseline power distribution architecture was identified in collaboration with Lockheed Martin Control Systems. The baseline architecture, built around the next generation 270V DC bus, consists of starter/generator units, bidirectional power converters to tightly regulate the 270V DC bus, storage batteries and a diverse range of loads including flight control electromechanical and electrohydraulic actuators, avionics, and environmental control systems. Smart actuators, which are widely used in aircraft for vibration suppression, are also included in the baseline system.

One of the distinguishing features of these power distributions systems was the regeneration of energy from the flight control actuators. As a result, the power distribution system is required to support bidirectional power flow. The presence of energy regeneration and a predominance of bidirectional power converters in the power system results in the subsystems to be tightly coupled and hence, exhibit strong interactions. The extensive simulation studies in Chapter 4 showed that a single solution would not suffice in mitigating the problems associated with bidirectional power flow. An optimal combination of solutions needs to be used to obtain a feasible design of the power distribution system components.

An optimization problem would then have to be formulated that takes into account the effects of the regenerative power flow. The performance specifications on the design would translate to optimization constraints. The design process would have to take into consideration the stability of the individual systems and of the integrated system as whole. Hence, the optimization constraints, in addition to the performance specifications, would include the stability indices. The results of stability analysis of interconnected systems presented in Chapter 5 would be used as the stability constraints for the optimization problem.

Considerable progress was made in the formulation of an optimization problem for the design of an interconnected system consisting of an input filter and a regulated DC-DC buck converter. The performance specifications for each of the subsystems were formulated as optimization constraints. The impedance ratio criterion was used to define the stability constraints of the interconnected system. To start with, the nonlinear results obtained in Chapter 5 were not used in formulating the stability constraints to keep the problem simple and mathematically tenable. The optimization results showed that optimizing the integrated system as a whole yielded a better design than integrating optimized systems. However, as the magnitude of the system increases optimizing the integrated system would pose serious computational difficulties. Hence, novel multi-level optimization procedures will have to be developed for the design of the complete power distribution system.

7 References

- [1] J. A. Weimer, "Power Management and Distribution for the More Electric Aircraft," Proceedings of the 30th Intersociety Energy Conversion Engineering Conference, 1995, pp. 273-277.
- [2] M. L. Maldonado, N. M. Shah, K. J. Cleek, P. S. Walia, G. Korba, "Power Management and Distribution System for a More Electric Aircraft (MADMEL) – Program Status," Proceedings of the 31st Intersociety Energy Conversion Engineering Conference, 1996, pp. 148-153.
- [3] J. S. Cloyd, "A Status of the United States Air Force's More Electric Aircraft Initiative," Proceedings of the 32nd Intersociety Energy Conversion Engineering Conference, 1997, pp. 681-686.
- [4] M. E. Elbuluk, M. D. Kankam, "Motor Drive Technologies for the Power-by-Wire (PBW) Program: Options, Trends, and Tradeoffs," Proceedings of the IEEE 1995 National Aerospace and Electronics Conference, NAECON'95, pp. 511-522.
- [5] G. L. Fronista and G. Bradbury, "An Electromechanical Actuator for a Transport Aircraft Spoiler Surface," Proceedings of the 32nd Intersociety Energy Conversion Engineering Conference, 1997, pp. 694-698.
- [6] K.C. Reinhardt, M. A. Marciniak, "Wide-Bandgap Power Electronics for the More Electric Aircraft," Proceedings of the 31st Intersociety Energy Conversion Engineering Conference, 1996, pp. 127-132.
- [7] R. A. Smith, H. J. Van Horn, "The J/IST of Improving JSF," Aerospace America, November 1997, pp. 20-22.
- [8] "MIL-STD-704E. Aircraft Electric Power Characteristics." Military standard.
- [9] J. G. Kassakian, M. F. Schlecht, G. C. Verghese, "Principles of Power Electronics," Addison-Wesley, 1991.
- [10] The MathWorks, Inc., "MATLAB User's Guide," The MathWorks, Inc., Natick, Mass., 1993.
- [11] The MathWorks, Inc., "SIMULINK User's Guide," The MathWorks, Inc., Natick, Mass., 1993.
- [12] The MathWorks, Inc., "Control System Toolbox User's Guide," The MathWorks, Inc., Natick, Mass., 1993.
- [13] P. C. Krause, "Analysis of Electrical Machinery," McGraw Hill, 1987.
- [14] S. Hiti, D. Borojevic, "Small-Signal Modeling and Control of Three-Phase PWM Converters," IEEE 1994 IAS Annual Meeting Proceedings, pp. 1143-1150.
- [15] S. Hiti, D. Borojevic, "Control of Front-End Three-Phase Boost Rectifier," APEC'94, pp. 927-933.
- [16] E. Richter and C. Ferreira, "Performance Evaluation of a 250kW Switched Reluctance Starter/Generator," IEEE 1995 IAS Annual Meeting Proceedings, pp. 434-440.
- [17] A. V. Radun, C. A. Ferreira, E. Richter, "Two-Channel Switched Reluctance Starter/Generator Results," IEEE Transactions on Industry Applications, vol. 34, no. 5, pp. 1026-1034.
- [18] A. Radun, "Generating with the Switched Reluctance Motor," IEEE APEC 1994 Annual Meeting Proceedings, pp. 41-47.
- [19] A. Radun, J. Rulison, and P. Sanza, "Switched Reluctance Starter/Generator," SAE Technical Papers, 1995, Paper No. 921974.
- [20] C. R. Elliott, J. M. Stephenson, and M. J. McClelland, "Advances in Switched Reluctance Drive System Dynamic Simulation," EPE 1995 Annual Meeting Proceedings, pp. 622-626.
- [21] A. V. Radun and Y. Q. Xiang, "Switched Reluctance Starter/Generator System Modeling Results," SAE Technical Papers, 1995, Paper No. 951407.
- [22] Middlebrook, R. D., "Input Filter Considerations in Design and Application of Switching Regulators," *IEEE Industry Application Society Annual Meeting*, October 11-14, 1976, Chicago, IL.
- [23] Middlebrook, R. D., "Design Techniques for Preventing Input-Filter Oscillations in Switched-Mode Regulators," *Proceedings of Powercon 5, the Fifth National Solid State Power Conversion Conference*, May 4-6, 1978, San Francisco, CA.
- [24] Erich, Sandra Y., and William M. Polivka, "Input Filter Design Criteria for Current-Programmed Regulators," *IEEE Transactions on Power Electronics*, vol. 7, No. 1, January 1992, pp. 143-151.
- [25] Jang, Yungtaek, and Robert E. Erickson, "Physical Origins of Input Filter Oscillations in Current Programmed Converters," *IEEE Transactions on Power Electronics*, Vol. 7, No. 4, October 1992, pp. 725-733.

- [26] Lewis, L.R., B.H. Cho, F.C. Lee, and B.A. Carpenter, "Modeling, Analysis and Design of Distributed Power Systems," *IEEE Power Electronics Specialists Conference, 1989. PESC'89*, vol I, pp. 152-159.
- [27] Florez-Lizarraga, Martin and Arthur F. Witulski, "Input Filter Design for Multiple-Module DC Power Systems," *IEEE Transactions on Power Electronics*, Vol.11, No. 3, May 1996, pp. 472-479.
- [28] S. Hiti, V. Vlatkovic, D. Borojevic and F. C. Lee, "A New Control Algorithm for Three Phase PWM Buck Rectifier with Input Displacement Factor Compensation", *Proceedings of the 11th VPEC Seminar*, 1993, pp. 19-25.
- [29] Mao H, et al., "Novel reduced-order small signal model of three phase PWM rectifiers and its application in control design and system analysis", *Proceedings of the 27th Power Electronics Specialists Conference*, June 1996, vol. 1, pp. 556-562
- [30] V. Vlatkovic, D. Borojevic and F. C. Lee, "Input Filter Design for Power Factor Correction Circuits", *Proceedings of the IECON '93*, November, 1993, pp.954-958.
- [31] Mohamed Belkhat, "Stability Criteria for AC power Systems with Regulated Loads", *PhD Dissertation*, Purdue University, 1997.
- [32] S. Hiti, D. Borojevic, "Small-signal modeling and control of three-phase PWM converters", *Proceedings of the 15th VPEC Seminar*, 1994, pp. 63-70.
- [33] Green, Limebeer, "Linear Robust Control", Prentice Hall Information and System Sciences Series, 1995.
- [34] MIL-STD704E, Military Standard, Aircraft Electric Power Characteristics, May 1, 1991
- [35] Gholdston E. W., et al., "Stability of large DC power systems using switching converters, with application to the International Space Station", *Proceedings of the 31st Intersociety Energy Conversion Engineering Conference*, vol. 1, August 1996, pp. 166-171.
- [36] Ashton R. W., et al., "The design and fabrication of a reconfigurable hardware testbed for the interaction analysis of power converters in a reduced-scale Navy dc distribution system, *Proceedings of the IEEE Symposium on Circuits and Systems*, vol. 3, 1998, pages 379-382.
- [37] Abed, E.H. et al, "Stability and Dynamics of Power Systems with Regulated Converters". *Proceedings of the IEEE Symposium on Circuits and Systems*, vol. 1, 1995, pages 143-145.
- [38] Belkhat, M. et al, "Large Signal Stability Criteria for Distributed System with Constant Power Loads, *Proceedings of the 26th Annual IEEE Power Electronics Specialists Conference*, Atlanta, GA, 1995, pages. 1333-1338.
- [39] "Applied nonlinear dynamics", Nayfeh, A.H et al., John Wiley, New York, 1995
- [40] Seydel Rudiger, "From Equilibrium to Chaos", Elsevier Science Publishing, 1988.
- [41] M. Al-Fayyumi, "Nonlinear dynamics and Interaction in Power Electronics Systems", M.S. Thesis, Department of Electrical and Computer Engineering, Virginia Tech, 1998.
- [42] Sriram Chandrasekaran, Douglas K. Lindner, Konstantin Louganski and, Dushan Boroyevich, "Subsystem Interaction Analysis in Power Distribution Systems of Next Generation Airlifters", To be presented at the European Power Electronics Conference, EPE '99, Lausanne, Switzerland, September 1999.
- [43] Sriram Chandrasekaran, Dusan Borojevic, Douglas. K. Lindner, "Input Filter Interaction in Three phase AC-DC Converters", *Proceedings of the Power Electronics Specialists Conference, PESC '99*, Charleston, South Carolina, June 1999, pp. 987-992.
- [44] Sriram Chandrasekaran, Douglas. K. Lindner, Dushan Boroyevich, "Analysis of Subsystem Integration in Aircraft Power Distribution Systems", *Proceedings of the International Symposium of Circuits and Systems, ISCAS '99*, Orlando, Florida, May 1999, vol. 5, pp. 82-85.
- [45] Douglas K. Lindner, Sriram Chandrasekaran, "Control of Regenerative Power from Piezoelectric Actuators", *Proceedings of the AIAA Adaptive Structures Forum in the 40th SDM Conference*, St. Louis, Missouri, April 1999.
- [46] Douglas K. Lindner, Sriram Chandrasekaran, "Power System Design Issues for Smart Materials", *Proceedings of the 1999 SPIE conference*, Newport Beach, California, March, 1999.

APPENDICES

Appendix A

Subsystem Parameters

Synchronous Generator

Parameter	Symbol	Unit	Nominal value
Armature phase resistance	R_s	Ohm	0.09113
Rotor speed	ω	rad/s	376.99
Armature phase leakage inductance	L_{ls}	H	0.9e-3
D axis coupling inductance	L_{md}	H	43e-3
Q axis coupling inductance	L_{mq}	H	21e-3
Field winding resistance (reflected to stator)	R_{fd}	Ohm	0.018
Field winding leakage inductance (reflected to stator)	L_{lfd}	H	3.4e-3
D axis damper winding resistance (reflected to stator)	R_{kd}	Ohm	0.08
Q axis damper winding resistance (reflected to stator)	R_{kq}	Ohm	0.08
D axis damper winding leakage inductance (reflected to stator)	L_{lkd}	H	0.16e-3
Q axis damper winding leakage inductance (reflected to stator)	L_{lkq}	H	0.35e-3
Additional resistance	R_a	Ohm	1e5
Field voltage (reflected to stator)	v_{fd}	V	1

Three Phase Boost Converter

Parameter	Symbol	Unit	Nominal value
One-phase inductance	L	H	18e-6
Output capacitance	C	F	350e-6
Output capacitor ESR	R_c	Ohm	0.01
Current feedback loops gain	K_{dq}	-	0.0126
Voltage loop proportional gain	K_{vp}	-	1
Voltage loop integral gain	K_{vi}	-	3300
Output voltage reference	$v_{o(ref)}$	V	270

DC Bus Cables

Parameter	Symbol	Unit	Nominal value
Resistance per foot	R	Ohm/ft	1.13e-3
Inductance per foot	L	H/ft	1e-9
Capacitance per foot	C	F/ft	1e-12
Cap. ESR per foot	R_C	Ohm/ft	negligible

Cable lengths:

- 10 feet for Inboard Spoilers (EMA)
- 40 feet for Elevators (EHA)

Flight Actuators

Input Filter

Parameter	Symbol	Unit	Nominal value
Inductance	L_i	H	1e-5
Inductor ESR	R_{li}	Ohm	0.1
Capacitance	C_i	F	1e-3
Capacitor ESR	R_{ci}	Ohm	0.01

DC Motor

Parameter	Symbol	Unit	Nominal value
Armature inductance	L	H	4.5e-4
Armature resistance	R	Ohm	0.5
Back emf constant	K_e	V/(rad/s)	0.129
Torque constant	K_t	in-lb/A	1.141
Motor group inertia	J_m	in-lb-s ²	2.43e-4
Motor group damping	B_m	in-lb-s	3.125e-4

Mechanical Linkage

Parameter	Symbol	Unit	Nominal value
Motor to Actuator gear ratio	N	rad/in	249.6 π
Actuator stiffness	K_{act}	lbf/in	9.0e5
Piston mass	M_p	lbf-s ² /in	5.43e-3
Piston damping	B_p	lbf-s/in	15

Surface load inertia	J_{sur}	in-lb-s ²	36.2
Surface load damping	B_{sur}	in-lb-s	1702
Horn radius	h	in	4.9
Horn stiffness	K_l	in-lb/rad	1.0e6
Structure stiffness	K_r	in-lb/rad	5.0e5
Gear efficiency	N_{mech}	-	0.85

EMA Feedback Controller

Parameter	Symbol	Unit	Nominal value
Motor current limit	-	A	19.3
Position forward gain	K_p	V/V	76
Velocity command limit	W_{lim}	V	+/-6.8
Velocity forward gain	K_v	V/V	122.5
Position feedback gain	H_p	V/in	1.6
Velocity feedback gain	H_v	V/(rad/s)	3.82e-3
Current feedback gain	H_i	V/A	0.25
Current forward gain	K_i	V/A	30

Appendix B

MATLAB Function for DQ-to-ABC Transformation

```
function [abc] = dq2abc(dq,w,t)
%DQ2ABC DQ-to-ABC transformation.
% [ABC] = DQ2ABC(DQ,W,T) performs DQ-to-ABC transformation for
% a balanced three-phase system as follows:
%
%      [cos wt      -sin wt      ]
%      [ABC] = [cos (wt-2pi/3) -sin (wt-2pi/3)] [DQ],
%      [cos (wt+2pi/3) -sin (wt+2pi/3)]
%
%      where T - time vector, W - angular frequency,
%      DQ - two-column matrix of a variable values in DQ coordinates,
%      ABC - three-column matrix of corresponding values in ABC
%      coordinates. The number of rows of DQ and ABC must be equal to
%      LENGTH(X).
%
% See also ABC2DQ.

% K.P. Louganski 1-05-98
% VPEC, Virginia Tech
```

```
error(nargchk(3,3,nargin));
```

```
wt=w*t;
phi=2*pi/3;
```

```
abc(:,1)= dq(:,1).*cos(wt)-dq(:,2).*sin(wt);
abc(:,2)= dq(:,1).*cos(wt-phi)-dq(:,2).*sin(wt-phi);
abc(:,3)= dq(:,1).*cos(wt+phi)-dq(:,2).*sin(wt+phi);
```

The function is developed for conversion of simulation results produced in dq coordinates into three-phase abc coordinates. Variable-step integration routines may be used. The time vector t must be saved during the simulation along with the two-column matrix of the time history of the variable in dq coordinates. After the simulation, an auxiliary equally spaced vector x spanning the range of t is created. The vector x should have a sufficient number of elements to accommodate the most rapid changes of the abc components. The two-column dq matrix is then converted into a three-column abc matrix by applying the “dq2abc” function to the dq values interpolated along x. An example below illustrates the usage of the function for plotting dq simulation results in abc reference frame.

```
% t - time vector obtained from simulation,
% V_dq - two-column matrix of a variable in DQ coordinates

x=[0:0.001*max(t):max(t)]';
figure
V_abc=dq2abc(interp1(t,V_dq,x),w,x);
plot(x,V_abc)
```

Appendix C

Synchronous Generator State-Space Model Derivation

In order to present the generator equations (10) in the standard state-space form, it is necessary to solve them for the state derivatives and collect the input and state variables into matrices. The five equations of (10) containing the state derivatives may be represented as follows:

$$\begin{bmatrix} a_{11} & 0 & a_{13} & 0 & a_{15} \\ 0 & a_{22} & 0 & a_{24} & 0 \\ a_{31} & 0 & a_{33} & 0 & a_{35} \\ a_{41} & 0 & a_{43} & 0 & a_{45} \\ 0 & a_{52} & 0 & a_{54} & 0 \end{bmatrix} \begin{bmatrix} x_1 \\ x_2 \\ x_3 \\ x_4 \\ x_5 \end{bmatrix} = \begin{bmatrix} b_1 \\ b_2 \\ b_3 \\ b_4 \\ b_5 \end{bmatrix}, \quad (\text{C-1})$$

where the auxiliary variables are

$$x_1 = \frac{di_{sd}}{dt}$$

$$x_2 = \frac{di_{sq}}{dt}$$

$$x_3 = \frac{di_{kd}}{dt}$$

$$x_4 = \frac{di_{kq}}{dt}$$

$$x_5 = \frac{di_{fd}}{dt}$$

$$a_{11} = -(L_{ls} + L_{md})$$

$$a_{13} = L_{md}$$

$$a_{15} = L_{md}$$

$$b_1 = -R_a i_d + (R_a + R_s) i_{sd} - \omega(L_{ls} + L_{mq}) i_{sq} + \omega L_{mq} i_{kq}$$

$$a_{22} = -(L_{ls} + L_{mq})$$

$$a_{24} = L_{mq}$$

$$b_2 = -R_a i_q + (R_a + R_s) i_{sq} + \omega(L_{ls} + L_{md}) i_{sd} - \omega L_{md} i_{fd} - \omega L_{md} i_{kd}$$

$$a_{31} = -L_{md}$$

$$a_{33} = L_{md}$$

$$a_{35} = L_{lfd} + L_{md}$$

$$b_3 = v_{fd} - R_{fd} i_{fd}$$

$$a_{41} = -L_{md}$$

$$a_{43} = L_{lkd} + L_{md}$$

$$a_{45} = L_{md}$$

$$b_4 = -R_{kd} i_{kd}$$

$$a_{52} = -L_{mq}$$

$$a_{54} = L_{lkq} + L_{mq}$$

$$b_5 = -R_{kq} i_{kq}$$

Solving the equation (C-1) symbolically in terms of the circuit parameters would be too cumbersome, and it is unnecessary since the parameters do not change during simulation. We obtain the solution by inverting the matrix of coefficients numerically:

$$X = A^{-1} \cdot B, \quad (C-2)$$

where

$$X = \begin{bmatrix} x_1 \\ x_2 \\ x_3 \\ x_4 \\ x_5 \end{bmatrix}, \quad A = \begin{bmatrix} a_{11} & 0 & a_{13} & 0 & a_{15} \\ 0 & a_{22} & 0 & a_{24} & 0 \\ a_{31} & 0 & a_{33} & 0 & a_{35} \\ a_{41} & 0 & a_{43} & 0 & a_{45} \\ 0 & a_{52} & 0 & a_{54} & 0 \end{bmatrix}, \quad B = \begin{bmatrix} b_1 \\ b_2 \\ b_3 \\ b_4 \\ b_5 \end{bmatrix}.$$

It can be seen that

$$\begin{aligned}
\begin{bmatrix} b_1 \\ b_2 \\ b_3 \\ b_4 \\ b_5 \end{bmatrix} &= \begin{bmatrix} R_a + R_s \\ \omega(L_{ls} + L_{md}) \\ 0 \\ 0 \\ 0 \end{bmatrix} \cdot i_{sd} + \begin{bmatrix} -\omega(L_{ls} + L_{mq}) \\ R_a + R_s \\ 0 \\ 0 \\ 0 \end{bmatrix} \cdot i_{sq} + \begin{bmatrix} 0 \\ -\omega L_{mq} \\ 0 \\ -R_{kd} \\ 0 \end{bmatrix} \cdot i_{kd} + \begin{bmatrix} \omega L_{mq} \\ 0 \\ 0 \\ 0 \\ -R_{kq} \end{bmatrix} \cdot i_{kq} + \begin{bmatrix} 0 \\ -\omega L_{md} \\ -R_{fd} \\ 0 \\ 0 \end{bmatrix} \cdot i_{fd} + \\
&\begin{bmatrix} -R_a \\ 0 \\ 0 \\ 0 \\ 0 \end{bmatrix} \cdot i_d + \begin{bmatrix} 0 \\ -R_a \\ 0 \\ 0 \\ 0 \end{bmatrix} \cdot i_q + \begin{bmatrix} 0 \\ 0 \\ 1 \\ 0 \\ 0 \end{bmatrix} \cdot v_{fd} = B_1 \cdot \begin{bmatrix} i_{sd} \\ i_{sq} \\ i_{kd} \\ i_{kq} \\ i_{fd} \end{bmatrix} + B_2 \cdot \begin{bmatrix} i_d \\ i_q \\ v_{fd} \end{bmatrix}, \\
\end{aligned} \tag{C-3}$$

where

$$B_1 = \begin{bmatrix} b_{11} & b_{12} & 0 & b_{14} & 0 \\ b_{21} & b_{22} & b_{23} & 0 & b_{25} \\ 0 & 0 & 0 & 0 & b_{35} \\ 0 & 0 & b_{43} & 0 & 0 \\ 0 & 0 & 0 & b_{54} & 0 \end{bmatrix}, \quad B_2 = \begin{bmatrix} b_{16} & 0 & 0 \\ 0 & b_{27} & 0 \\ 0 & 0 & b_{38} \\ 0 & 0 & 0 \\ 0 & 0 & 0 \end{bmatrix},$$

$$b_{11} = b_{22} = R_a + R_s$$

$$b_{21} = \omega(L_{ls} + L_{md})$$

$$b_{12} = -\omega(L_{ls} + L_{mq})$$

$$b_{23} = -\omega L_{mq}$$

$$b_{43} = -R_{kd}$$

$$b_{14} = \omega L_{mq}$$

$$b_{54} = -R_{kq}$$

$$b_{16} = b_{27} = -R_a$$

$$b_{38} = 1.$$

From equations (C-2) and (C-3) it is seen that

$$\frac{d}{dt} \begin{bmatrix} i_{sd} \\ i_{sq} \\ i_{kd} \\ i_{kq} \\ i_{fd} \end{bmatrix} = A^{-1} \cdot B_1 \cdot \begin{bmatrix} i_{sd} \\ i_{sq} \\ i_{kd} \\ i_{kq} \\ i_{fd} \end{bmatrix} + A^{-1} \cdot B_2 \cdot \begin{bmatrix} i_d \\ i_q \\ v_{fd} \end{bmatrix} = A_g \cdot \begin{bmatrix} i_{sd} \\ i_{sq} \\ i_{kd} \\ i_{kq} \\ i_{fd} \end{bmatrix} + B_g \cdot \begin{bmatrix} i_d \\ i_q \\ v_{fd} \end{bmatrix}, \quad (C-4)$$

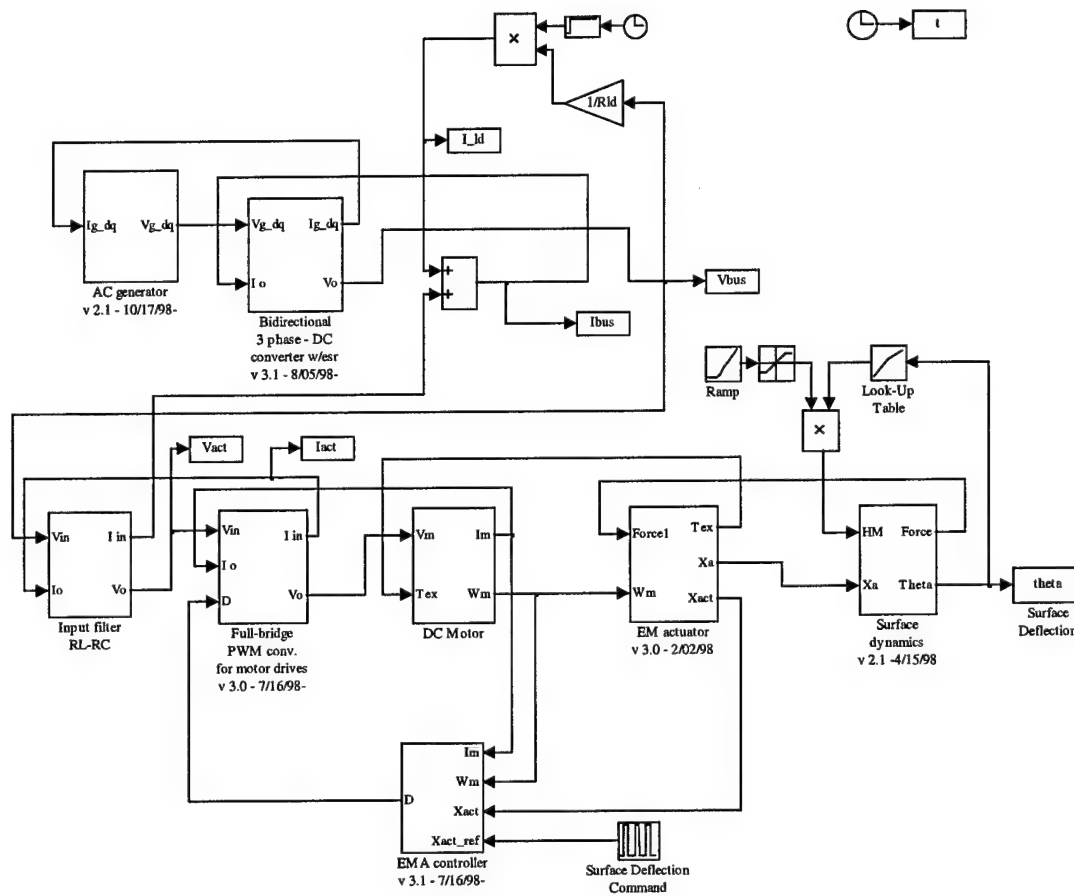
which is the state equation of the model. The output equation is obtained from the two equations of (10) containing the output variables. The state variables are obtained by adding them to the vector of output variables.

$$\begin{bmatrix} v_d \\ v_q \\ i_{sd} \\ i_{sq} \\ i_{kd} \\ i_{kq} \\ i_{fd} \end{bmatrix} = \begin{bmatrix} Ra & 0 & 0 & 0 & 0 \\ 0 & Ra & 0 & 0 & 0 \\ 1 & 0 & 0 & 0 & 0 \\ 0 & 1 & 0 & 0 & 0 \\ 0 & 0 & 1 & 0 & 0 \\ 0 & 0 & 0 & 1 & 0 \\ 0 & 0 & 0 & 0 & 1 \end{bmatrix} \begin{bmatrix} i_{sd} \\ i_{sq} \\ i_{kd} \\ i_{kq} \\ i_{fd} \end{bmatrix} + \begin{bmatrix} -Ra & 0 & 0 \\ 0 & -Ra & 0 \\ 0 & 0 & 0 \\ 0 & 0 & 0 \\ 0 & 0 & 0 \\ 0 & 0 & 0 \\ 0 & 0 & 0 \end{bmatrix} \begin{bmatrix} i_d \\ i_q \\ v_{fd} \end{bmatrix} = C_g \begin{bmatrix} i_{sd} \\ i_{sq} \\ i_{kd} \\ i_{kq} \\ i_{fd} \end{bmatrix} + D_g \begin{bmatrix} i_d \\ i_q \\ v_{fd} \end{bmatrix}$$

Appendix D

MATLAB Code Used for the Power Distribution Simulation and Analysis

Simulink Model of the PDS for a Parametric Sweep Analysis



MATLAB Files for Running a Parametric Sweep Analysis of the PDS

“sweepsys.m” – Running the Simulation

```
% Parametric sweep simulation
% Bidirectional Power Flow Analysis
% Required supplementary files:
%   model_name.mdl - Simulink model of the system
%   sysgen_par.m - synchronous generator parameter m-file
%   emaparam.m - EMA & DC motor parameter m-file
%   spikes.m - simulation results analysis
%   syspower.m - power flow analysis
clear all      % clear the workspace
close all     % close all windows
% SYSTEM PARAMETERS
% =====
% Synchronous Generator
syngen_par      % gen. parameters m-file
Vgref=100;
Kgref=1000;
% Three-phase - to - DC bidirectional converter
Vm = 200;      % input voltage
Vrref= 270;
Lbr = 18e-06;
Rbr = 0.2;      % BR inductor ESR in DQ
Cbr = 350e-06; % Output filter Capacitance
Rcbr= 0.01;    % Output cap. ESR
fs = 20e3;     % switching frequency
Kdq = 0.5*3*Lbr*2*pi*fs/Vrref;
Iqref = 0;
%% INPUT FILTER %%
Li = 1e-5;
Rli = 0.1;
Ci = 63e-6;
Rci = 0.01;
%% RESISTIVE LOAD %%
Rld = 72.9;    % 1kW load
% EMA parameters
emaparam      % EMA & DC motor parameters m-file
% PARAMETRIC SWEEP SIMULATION
% =====
% Data for analysis
deltav = 2;    % allowable bus voltage deviation for settling time calc.
Vbref = Vrref;
Vsp1max=[]; Vsp1min=[]; ts1=[]; % voltage spikes magn. and settling time
Vsp2max=[]; Vsp2min=[]; ts2=[];
Vsp3max=[]; Vsp3min=[]; ts3=[];
Vsp4max=[]; Vsp4min=[]; ts4=[];
Wbusp=[]; Wbusn=[]; buseff=[];
Wldp=[]; Wldn=[]; loadeff=[];
Wactp=[]; Wactn=[]; acteff=[];
Wbrp=[]; Wbrn=[]; breff=[];
Wcifp=[]; Wcifn=[]; cifeff=[];
Wifp=[]; Wifn=[]; ifeff=[];
Wcbrp=[]; Wcbrn=[]; cbreff=[];
Wwindp = []; Wwindn = [];
Wactel = [];
Wactm = [];
Wgmp=[]; Wgmn=[];
Wgp=[]; Wgn=[];
Wfip=[]; Wfin=[];
Wtot=[];
Wgls=[]; Wglk=[]; Wglf=[]; Wgl=[];
% Sweep parameter
par_name = 'Cbr'; % specify here the parameter to be swept
beg_val = 350e-06;
end_val = 0.8;
```

```

num_val = 20;
par_vect = logspace(log10(beg_val),log10(end_val),num_val);
par_vect = str2num(num2str(par_vect));
%pltype = 0;    % plotting with a linear x-scale
pltype = 1;    % plotting with a logarithmic x-scale
% Simulation parameters
dur=25e-1;
decim = 1;      % output to workspace decimation
cycle_number = 0;
    for par_val = par_vect;
        cycle_number = cycle_number+1;
        assignin('base',par_name,par_val);
        eval(par_name)
            options1 = simset('Solver','ode15s','RelTol',1e-3,'AbsTol',1e-4);
            sim('sysgen11a',dur,options1);

        spikes
        syspower2
% PLOTTING THE RESULTS
% =====
        figure
        spmax=5;
        subplot(spmax,1,1)
        plot(t,Vbus)
        grid
        ylabel('Vbus (V)')

        subplot(spmax,1,2)
        plot(t,Vbus.*Ibus/1000)
        grid
        ylabel('Pbus (kW)')

        subplot(spmax,1,3)
        plot(t,Im)
        grid
        ylabel('Im (A)')
        subplot(spmax,1,4)
        plot(t,theta*180/pi)
        grid
        ylabel('theta (deg)')
        subplot(spmax,1,5)
        plot(t,Xaref)
        grid
        ylabel('Xaref (in)')
        xlabel('time (sec)')
        zoom on
        end
        % Saving the data for future use
        save brcap20 par_name par_vect cycle_number pltype Vsp* Vbref ts* Wtot Wg* Wbus* Wfi*...
            Wact* Wwind*

```

“syngen_par.m” – Synchronous Generator Parameters

```

% Synchronous generator parameter file
% Parameters in DQ coordinate frame
Rs      = 0.09113;    % armature phase resistance
Lls     = 0.9e-3;    % armature phase leakage inductance
Lmd     = 43e-3;    % d axis coupling inductance
Lmq     = 21e-3;    % q axis coupling inductance
Rfd     = 0.018;    % field winding resistance (refl. to stator)
Lfld    = 3.4e-3;    % field winding leakage inductance (refl. to stator)
Rkd     = 0.08;    % d axis damper winding resistance (refl. to stator)
Rkq     = 0.08;    % q axis damper winding resistance (refl. to stator)
Likd    = 0.16e-3;    % d axis damper winding leak. induct. (refl. to stator)
Likq    = 0.35e-3;    % q axis damper winding leak. induct. (refl. to stator)
w       = 2*pi*60;    % rotor speed
Ra      = 1e5;    % additional resistance
Vfd     = 1;    % field voltage (refl. to stator)
% State space matrices

```

```

Agtmp=zeros(5);
Agtmp(1,1) = -Lls-Lmd;
Agtmp(1,3) = Lmd;
Agtmp(1,5) = Lmd;
Agtmp(2,2) = -Lls-Lmq;
Agtmp(2,4) = Lmq;
Agtmp(3,1) = -Lmd;
Agtmp(3,3) = Lmd;
Agtmp(3,5) = Lld+Lmd;
Agtmp(4,1) = -Lmd;
Agtmp(4,3) = Lld+Lmd;
Agtmp(4,5) = Lmd;
Agtmp(5,2) = -Lmq;
Agtmp(5,4) = Lld+Lmq;
Bg1 = zeros(5);
Bg1(1,1) = Ra+Rs;
Bg1(1,2) = -w*(Lls+Lmq);
Bg1(1,4) = w*Lmq;
Bg1(2,1) = w*(Lls+Lmd);
Bg1(2,2) = Ra+Rs;
Bg1(2,3) = -w*Lmd;
Bg1(2,5) = -w*Lmd;
Bg1(3,5) = -Rfd;
Bg1(4,3) = -Rkd;
Bg1(5,4) = -Rkq;
Bg2 = zeros(5,3);
Bg2(1,1) = -Ra;
Bg2(2,2) = -Ra;
Bg2(3,3) = 1;
Ag = inv(Agtmp)*Bg1;
Bg = inv(Agtmp)*Bg2;
Cg = zeros(7,5);
Cg(1,1) = Ra;
Cg(2,2) = Ra;
Cg(3:7,:) = eye(5);
Dg = zeros(7,3);
Dg(1,1) = -Ra;
Dg(2,2) = -Ra;

```

“emaparam.m” – EMA and DC Motor Parameters

% EMA parameters file (by Lockheed Martin Control Systems)

%% Inboard Spoiler Surface Parameters

```

Kp      = 76;           % V/V
wlim    = 6.8;          % V
Kv      = 122.5;        % V/V
Hp      = 1.6;           % V/in
Hv      = 0.00382;      % V/(rad/sec)
Jm      = 2.43e-4;       % in-lb-sec^2
Bm      = 3.125e-4;      % in-lb-sec
N       = 249.6*pi;      % rad/in
Kact     = 9e5;           % lbf/in
Mp      = 5.43e-3;       % lbf-sec^2/in
Bp      = 15;            % lbf-sec/in
Jsur    = 36.2;          % in-lb-s^2
Bsur    = 1702;          % in-lb-s
h       = 4.9;           % in
KI      = 1e6;           % in-lb/rad
Kr      = 5e5;           % in-lb/rad

```

% BDC Motor Parameters

```

Ka      = 20;           % V/V
L       = 0.00045;       % H
R       = 0.5;           % Ohms
Kt      = 1.141;         % in-lbf/amp
Ke      = 0.129;         % V/(rad/sec)
Ilim    = 19.3;          % Amp
Hi      = 0.25;          % V/A

```

Nmech = 0.85;

“spikes.m” – Calculation of the DC Bus Power Quality Characteristics

```
% Analysis of voltage spikes on DC bus obtained from simulation
%%      t -- time vector
%      Vbus -- DC bus voltage
t1beg = 0.5;           % beginning of the time interval #1
t1end = 0.8;           % end of the time interval #1
ind1 = find(t>=t1beg & t<=t1end); %vector of indices in the time span
Vsp1max = [Vsp1max max(Vbus(ind1))]; % max voltage during the transient
Vsp1min = [Vsp1min min(Vbus(ind1))]; % min voltage during the transient
ind1pos = find(Vbus(ind1)>(Vbref+deltav));
ind1neg = find(Vbus(ind1)<(Vbref-deltav));
ind1pn = [ind1pos ind1neg];
if isempty(ind1pn), ind1pn = 0; end
ts1 = [ts1 t(min(ind1)+max(ind1pn))-t(min(ind1)+min(ind1pn))]; % settling time
t2beg = 1.0;           % beginning of the time interval #2
t2end = 1.4;           % end of the time interval #2
ind2 = find(t>=t2beg & t<=t2end); %vector of indices in the time span
Vsp2max = [Vsp2max max(Vbus(ind2))];
Vsp2min = [Vsp2min min(Vbus(ind2))];
ind2pos = find(Vbus(ind2)>(Vbref+deltav));
ind2neg = find(Vbus(ind2)<(Vbref-deltav));
ind2pn = [ind2pos ind2neg];
if isempty(ind2pn), ind2pn = 0; end
ts2 = [ts2 t(min(ind2)+max(ind2pn))-t(min(ind2)+min(ind2pn))]; % settling time
t3beg = 1.5;           % beginning of the time interval #3
t3end = 1.8;           % end of the time interval #3
ind3 = find(t>=t3beg & t<=t3end); %vector of indices in the time span
Vsp3max = [Vsp3max max(Vbus(ind3))];
Vsp3min = [Vsp3min min(Vbus(ind3))];
ind3pos = find(Vbus(ind3)>(Vbref+deltav));
ind3neg = find(Vbus(ind3)<(Vbref-deltav));
ind3pn = [ind3pos ind3neg];
if isempty(ind3pn), ind3pn = 0; end
ts3 = [ts3 t(min(ind3)+max(ind3pn))-t(min(ind3)+min(ind3pn))]; % settling time
t4beg = 2.0;           % beginning of the time interval #4
t4end = 2.4;           % end of the time interval #4
ind4 = find(t>=t4beg & t<=t4end); %vector of indices in the time span
Vsp4max = [Vsp4max max(Vbus(ind4))];
Vsp4min = [Vsp4min min(Vbus(ind4))];
ind4pos = find(Vbus(ind4)>(Vbref+deltav));
ind4neg = find(Vbus(ind4)<(Vbref-deltav));
ind4pn = [ind4pos ind4neg];
if isempty(ind4pn), ind4pn = 0; end
ts4 = [ts4 t(min(ind4)+max(ind4pn))-t(min(ind4)+min(ind4pn))]; % settling time
```

“syspower2.m” – Bidirectional Power Flow Analysis

```
% Analysis of power flow in the system obtained from simulation
tmin = 0.5;           % beginning of the actuator operating cycle
tmax = 2.5;           % end of the actuator operating cycle
ind = find(t>=tmin & t<=tmax); %vector of indices in the time span
tnew = t(ind);
%%%%%%%%%%%%%%%%%%%%%%%%%%%%%%%%%%%%%%%%%%%%%%%%%%%%%%%%%%%%%%%%%%%%%%%%%%
% Generator losses
Pgl=(lg_dq(:,1).^2 + lg_dq(:,2).^2)*Rs*3/2; %losses in phase resistances
Pglk=((lk_dq(:,1).^2 + lk_dq(:,2).^2)*Rkd + (lk_dq(:,2).^2)*Rkq)*3/2; %losses in damper winding
Pglf=lfid.^2*Rfd; % losses in the field winding
Pgl = (Pgl + Pglk + Pglf)*2; % total generator losses
% x2 to account for other types of losses
Pnew = Pgl(ind);
```

GENERATOR

```

Wgls = [Wgls trapz(tnew,Pnew)]; % energy lost in phase resistances
Pnew = Pglk(ind);
Wgik = [Wgik trapz(tnew,Pnew)]; % energy lost in damper winding
Pnew = Pgl(ind);
Wglf = [Wglf trapz(tnew,Pnew)]; % energy lost in field winding
Pnew = Pgl(ind);
Wgl = [Wgl trapz(tnew,Pnew)]; % total energy lost in generator
% Energy coming from the engine %***
Pgm = Pg + Pgl; % mech. power delivered to the generator
Pnew = Pgm(ind); Ppos = Pnew.*(Pnew>0); Pneg = Pnew.*(Pnew<0);
Wgmp = [Wgmp trapz(tnew,Ppos)]; %*** % positive energy
Wgmn = [Wgmn -trapz(tnew,Pneg)]; %*** % negative (regenerated) energy
%%%%%%%%%%%% BOOST RECTIFIER %%%%%%%%%%%%%
% Energy flowing into the boost rectifier %***
Pnew = Pg(ind); Ppos = Pnew.*(Pnew>0); Pneg = Pnew.*(Pnew<0);
Wgp = [Wgp trapz(tnew,Ppos)]; %*** % positive energy
Wgn = [Wgn -trapz(tnew,Pneg)]; %*** % negative (regenerated) energy
% Energy coming from the boost rectifier to the load %***
Pbus = Vbus.*Ibus;
Pnew = Pbus(ind); Ppos = Pnew.*(Pnew>0); Pneg = Pnew.*(Pnew<0);
Wbusp = [Wbusp trapz(tnew,Ppos)]; %*** % positive energy
Wbusn = [Wbusn -trapz(tnew,Pneg)]; %*** % negative (regenerated) energy
%%%%%%%%%%%% INPUT FILTER %%%%%%%%%%%%%
% Energy coming into the filter from the DC bus %***
Pfi = Vbus.*(Ibus-Ild);
Pnew = Pfi(ind); Ppos = Pnew.*(Pnew>0); Pneg = Pnew.*(Pnew<0);
Wfip = [Wfip trapz(tnew,Ppos)]; %*** % positive energy
Wfin = [Wfin -trapz(tnew,Pneg)]; %*** % negative (regenerated) energy
%%%%%%%%%%%% ACTUATOR %%%%%%%%%%%%%
% Energy coming from the input filter %***
Pact = Vact.*Iact;
Pnew = Pact(ind); Ppos = Pnew.*(Pnew>0); Pneg = Pnew.*(Pnew<0);
Wactp = [Wactp trapz(tnew,Ppos)]; %*** % positive energy
Wactn = [Wactn -trapz(tnew,Pneg)]; %*** % negative (regenerated) energy
%%%%%%%%%%%% AIR FLOW %%%%%%%%%%%%%
Pwind = hm.*Wsur;
Pnew = Pwind(ind); Ppos = Pnew.*(Pnew>0); Pneg = Pnew.*(Pnew<0);
Wwindp = [Wwindp trapz(tnew,Ppos)]; % positive energy (passed to the wind)
Wwindn = [Wwindn -trapz(tnew,Pneg)]; % negative energy (received from the wind)

```

“plspikes.m” – Plotting Voltage Spikes Magnitude and Settling Time

```

% Plots voltage spikes magnitude and settling time
clear all
close all
load ifcap20 % Load workspace
% Voltage spikes magnitudes
figure(1)
Vsp2max = Vsp2max(1:cycle_number);
Vsp2min = Vsp2min(1:cycle_number);
if pltype == 0,
plot(par_vect(1:cycle_number),Vsp2max-Vbref,par_vect(1:cycle_number),Vsp2min- ...
Vbref, par_vect(1:cycle_number),Vsp2max-Vbref,'k^', ...
par_vect(1:cycle_number),Vsp2min-Vbref,'kv')
else semilogx(par_vect(1:cycle_number),Vsp2max-Vbref,par_vect(1:cycle_number),...
Vsp2min-Vbref, par_vect(1:cycle_number),Vsp2max-Vbref,'k^', ...
par_vect(1:cycle_number),Vsp2min-Vbref,'kv')
end
grid, ylabel('Magnitude (V)')
xlabel('Input Filter Capacitance (F)')
zoom on
% Voltage spikes settling time
figure(2)
ts2 = ts2(1:cycle_number);
if pltype == 0,
plot(par_vect(1:cycle_number),ts2, par_vect(1:cycle_number),ts2,'ko')
else semilogx(par_vect(1:cycle_number),ts2, par_vect(1:cycle_number),ts2,'ko')

```



```

end
grid, ylabel('Settling time (s)')
xlabel('Input Filter Capacitance (F)')
zoom on

```

“plenergy.m” – Plotting the Total Energy Flowing from the Engine

```

% Plots Energy Flow from the engine and back
clear all
close all
load ('ifcap20.mat')      % Load workspace
Wtot = 1;
figure(1)
spmax=3;
subplot(spmax,1,1)
Wplot = Wgmp./Wtot;
Wplot = Wplot(1:cycle_number);
if pltype == 0,
plot(par_vect(1:cycle_number),Wplot, par_vect(1:cycle_number),Wplot,'ko')
else semilogx(par_vect(1:cycle_number),Wplot, par_vect(1:cycle_number),Wplot,'ko')
end
grid, ylabel('Delivered Energy')
subplot(spmax,1,2)
Wplot = Wgmn./Wtot;
Wplot = Wplot(1:cycle_number);
if pltype == 0,
plot(par_vect(1:cycle_number),Wplot, par_vect(1:cycle_number),Wplot,'ko')
else semilogx(par_vect(1:cycle_number),Wplot, par_vect(1:cycle_number),Wplot,'ko')
end
grid, ylabel('Regenerated Energy')
subplot(spmax,1,3)
Wplot = Wgmn./Wgmp;
Wplot = Wplot(1:cycle_number);
if pltype == 0,
plot(par_vect(1:cycle_number),Wplot, par_vect(1:cycle_number),Wplot,'ko')
else semilogx(par_vect(1:cycle_number),Wplot, par_vect(1:cycle_number),Wplot,'ko')
end
grid, ylabel('% Regenerated')
xlabel('Input Filter Capacitance (F)')
zoom on
load ('ifcap20w.mat')      % Load workspace
Wtot = 1;
figure(2)
subplot(spmax,1,1)
Wplot = Wgmp./Wtot;
Wplot = Wplot(1:cycle_number);
if pltype == 0,
plot(par_vect(1:cycle_number),Wplot, par_vect(1:cycle_number),Wplot,'ko')
else semilogx(par_vect(1:cycle_number),Wplot, par_vect(1:cycle_number),Wplot,'ko')
end
grid, ylabel('Delivered Energy')
subplot(spmax,1,2)
Wplot = Wgmn./Wtot;
Wplot = Wplot(1:cycle_number);
if pltype == 0,
plot(par_vect(1:cycle_number),Wplot, par_vect(1:cycle_number),Wplot,'ko')
else semilogx(par_vect(1:cycle_number),Wplot, par_vect(1:cycle_number),Wplot,'ko')
end
grid, ylabel('Regenerated Energy')
subplot(spmax,1,3)
Wplot = Wgmn./Wgmp;
Wplot = Wplot(1:cycle_number);
if pltype == 0,
plot(par_vect(1:cycle_number),Wplot, par_vect(1:cycle_number),Wplot,'ko')
else semilogx(par_vect(1:cycle_number),Wplot, par_vect(1:cycle_number),Wplot,'ko')
end
grid, ylabel('% Regenerated')
xlabel('Input Filter Capacitance (F)')

```

zoom on

“plbalance.m” – Plotting the Energy Balance for Each Subsystem

```
% Plots energy balance for each subsystem
clear all
close all
load ('ifcap20.mat')          % Load workspace
Wtot = 1;
figure(1)
spmax=6;
subplot(spmax,1,1)
Wplot = ((Wgmp-Wgmn)-(Wgp-Wgn))./Wtot; % generator losses
Wplot = Wplot(1:cycle_number);
if pltype == 0,
plot(par_vect(1:cycle_number),Wplot, par_vect(1:cycle_number),Wplot,'ko')
else semilogx(par_vect(1:cycle_number),Wplot, par_vect(1:cycle_number),Wplot,'ko'); hold on
end
grid, ylabel('Generator')
subplot(spmax,1,2)
Wplot = ((Wgp-Wgn)-(Wbusp-Wbusn))./Wtot; % BR losses
Wplot = Wplot(1:cycle_number);
if pltype == 0,
plot(par_vect(1:cycle_number),Wplot, par_vect(1:cycle_number),Wplot,'ko')
else semilogx(par_vect(1:cycle_number),Wplot, par_vect(1:cycle_number),Wplot,'ko'); hold on
end
grid, ylabel('Boost Rectifier')
subplot(spmax,1,3)
Wplot = ((Wbusp-Wbusn)-(Wfip-Wfin))./Wtot; % dissipation in the load
Wplot = Wplot(1:cycle_number);
if pltype == 0,
plot(par_vect(1:cycle_number),Wplot, par_vect(1:cycle_number),Wplot,'ko')
else semilogx(par_vect(1:cycle_number),Wplot, par_vect(1:cycle_number),Wplot,'ko'); hold on
end
grid, ylabel('Load')
subplot(spmax,1,4)
Wplot = ((Wfip-Wfin)-(Wactp-Wactn))./Wtot; % filter losses
Wplot = Wplot(1:cycle_number);
if pltype == 0,
plot(par_vect(1:cycle_number),Wplot, par_vect(1:cycle_number),Wplot,'ko')
else semilogx(par_vect(1:cycle_number),Wplot, par_vect(1:cycle_number),Wplot,'ko'); hold on
end
grid, ylabel('Input Filter')
subplot(spmax,1,5)
Wplot = ((Wactp-Wactn)-(Wwindp-Wwindn))./Wtot; % EMA losses
Wplot = Wplot(1:cycle_number);
if pltype == 0,
plot(par_vect(1:cycle_number),Wplot, par_vect(1:cycle_number),Wplot,'ko')
else semilogx(par_vect(1:cycle_number),Wplot, par_vect(1:cycle_number),Wplot,'ko'); hold on
end
grid, ylabel('Actuator')
subplot(spmax,1,6)
Wplot = (Wwindp-Wwindn)./Wtot; % net energy passed to the wind
Wplot = Wplot(1:cycle_number);
if pltype == 0,
plot(par_vect(1:cycle_number),Wplot, par_vect(1:cycle_number),Wplot,'ko')
else semilogx(par_vect(1:cycle_number),Wplot, par_vect(1:cycle_number),Wplot,'ko'); hold on
end
grid, ylabel('Air Flow')
xlabel('Input Filter Capacitance (F)')
zoom on
load ('ifcap20w.mat')        % Load workspace again
Wtot = 1;
figure(1)
spmax=6;
subplot(spmax,1,1)
Wplot = ((Wgmp-Wgmn)-(Wgp-Wgn))./Wtot; % generator losses
Wplot = Wplot(1:cycle_number);
```

```

if pltype == 0,
plot(par_vect(1:cycle_number),Wplot, par_vect(1:cycle_number),Wplot,'ko')
else semilogx(par_vect(1:cycle_number),Wplot, par_vect(1:cycle_number),Wplot,'k^'); hold on
end
grid on, ylabel('Generator')
subplot(spmax,1,2)
Wplot = ((Wgp-Wgn)-(Wbusp-Wbusn))./Wtot; % BR losses
Wplot = Wplot(1:cycle_number);
if pltype == 0,
plot(par_vect(1:cycle_number),Wplot, par_vect(1:cycle_number),Wplot,'ko')
else
semilogx(par_vect(1:cycle_number),Wplot, par_vect(1:cycle_number),Wplot,'k^'); hold on
end
grid on, ylabel('Boost Rectifier')
subplot(spmax,1,3)
Wplot = ((Wbusp-Wbusn)-(Wfip-Wfin))./Wtot; % dissipation in the load
Wplot = Wplot(1:cycle_number);
if pltype == 0,
plot(par_vect(1:cycle_number),Wplot, par_vect(1:cycle_number),Wplot,'ko')
else
semilogx(par_vect(1:cycle_number),Wplot, par_vect(1:cycle_number),Wplot,'k^'); hold on
end
grid on, ylabel('Load')
subplot(spmax,1,4)
Wplot = ((Wfip-Wfin)-(Wactp-Wactn))./Wtot; % filter losses
Wplot = Wplot(1:cycle_number);
if pltype == 0,
plot(par_vect(1:cycle_number),Wplot, par_vect(1:cycle_number),Wplot,'ko')
else
semilogx(par_vect(1:cycle_number),Wplot, par_vect(1:cycle_number),Wplot,'k^'); hold on
end
grid on, ylabel('Input Filter')
subplot(spmax,1,5)
Wplot = ((Wactp-Wactn)-(Wwindp-Wwindn))./Wtot; % EMA losses
Wplot = Wplot(1:cycle_number);
if pltype == 0,
plot(par_vect(1:cycle_number),Wplot, par_vect(1:cycle_number),Wplot,'ko')
else
semilogx(par_vect(1:cycle_number),Wplot, par_vect(1:cycle_number),Wplot,'k^'); hold on
end
grid on, ylabel('Actuator')
subplot(spmax,1,6)
Wplot = (Wwindp-Wwindn)./Wtot; % net energy passed to the wind
Wplot = Wplot(1:cycle_number);
if pltype == 0,
plot(par_vect(1:cycle_number),Wplot, par_vect(1:cycle_number),Wplot,'ko')
else
semilogx(par_vect(1:cycle_number),Wplot, par_vect(1:cycle_number),Wplot,'k^'); hold on
end
axis([1e-5 1 -0.5 1])
grid on, ylabel('Air Flow')
xlabel('Input Filter Capacitance (F)')
zoom on

```

“plgenloss.m” – Plotting the Generator Losses

```

% Plots generator losses itemized
clear all
close all
load ('ifcap20.mat') % Load workspace
Wtot = 1;
figure(1)
spmax=4;
subplot(spmax,1,1)
Wplot = Wgl./Wtot; % total generator losses
Wplot = Wplot(1:cycle_number);
if pltype == 0,
plot(par_vect(1:cycle_number),Wplot, par_vect(1:cycle_number),Wplot,'ko')

```

```

else semilogx(par_vect(1:cycle_number),Wplot, par_vect(1:cycle_number),Wplot,'ko'); hold on
end
grid, ylabel('Generator Total')
subplot(spmx,1,2)
Wplot = Wgls./Wtot; % losses in phase resistances
Wplot = Wplot(1:cycle_number);
if pltype == 0,
plot(par_vect(1:cycle_number),Wplot, par_vect(1:cycle_number),Wplot,'ko')
else semilogx(par_vect(1:cycle_number),Wplot, par_vect(1:cycle_number),Wplot,'ko'); hold on
end
grid, ylabel('Phase Resistance')
subplot(spmx,1,3)
Wplot = Wgls./Wtot; % losses in damper winding
Wplot = Wplot(1:cycle_number);
if pltype == 0,
plot(par_vect(1:cycle_number),Wplot, par_vect(1:cycle_number),Wplot,'ko')
else semilogx(par_vect(1:cycle_number),Wplot, par_vect(1:cycle_number),Wplot,'ko'); hold on
end
grid, ylabel('Damper Winding')
subplot(spmx,1,4)
Wplot = Wgls./Wtot; % losses in field winding
Wplot = Wplot(1:cycle_number);
if pltype == 0,
plot(par_vect(1:cycle_number),Wplot, par_vect(1:cycle_number),Wplot,'ko')
else semilogx(par_vect(1:cycle_number),Wplot, par_vect(1:cycle_number),Wplot,'ko'); hold on
end
grid, ylabel('Field Winding')
xlabel('Input Filter Capacitance (F)')
zoom on
load ('ifcap20w.mat')          % Load workspace again
Wtot = 1;
figure(1)
spmx=4;
subplot(spmx,1,1)
Wplot = Wgls./Wtot;          % total generator losses
Wplot = Wplot(1:cycle_number);
if pltype == 0,
plot(par_vect(1:cycle_number),Wplot, par_vect(1:cycle_number),Wplot,'ko')
else semilogx(par_vect(1:cycle_number),Wplot, par_vect(1:cycle_number),Wplot,'k^'); hold on
end
grid on, ylabel('Generator Total')
subplot(spmx,1,2)
Wplot = Wgls./Wtot; % losses in phase resistances
Wplot = Wplot(1:cycle_number);
if pltype == 0,
plot(par_vect(1:cycle_number),Wplot, par_vect(1:cycle_number),Wplot,'ko')
else semilogx(par_vect(1:cycle_number),Wplot, par_vect(1:cycle_number),Wplot,'k^'); hold on
end
grid on, ylabel('Phase Resistance')
subplot(spmx,1,3)
Wplot = Wgls./Wtot; % losses in damper winding
Wplot = Wplot(1:cycle_number);
if pltype == 0,
plot(par_vect(1:cycle_number),Wplot, par_vect(1:cycle_number),Wplot,'ko')
else semilogx(par_vect(1:cycle_number),Wplot, par_vect(1:cycle_number),Wplot,'k^'); hold on
end
grid on, ylabel('Damper Winding')
subplot(spmx,1,4)
Wplot = Wgls./Wtot; % losses in field winding
Wplot = Wplot(1:cycle_number);
if pltype == 0,
plot(par_vect(1:cycle_number),Wplot, par_vect(1:cycle_number),Wplot,'ko')
else semilogx(par_vect(1:cycle_number),Wplot, par_vect(1:cycle_number),Wplot,'k^'); hold on
end
grid on, ylabel('Field Winding')
xlabel('Input Filter Capacitance (F)')
zoom on

```

“pleff.m” – Plotting Overall Efficiency of the System

% Plots Overall Efficiency of the System

```

clear all
close all
load ('ifcap20.mat')      % Load workspace
Wtot = 1;
figure(1)
Wplot = (Wgmp-((Wgmp-Wgmn)-(Wbusp-Wbusn)+(Wfip-Wfin)-(Wwindp-Wwindn)))/Wgmp;
Wplot = Wplot(1:cycle_number);
if pltype == 0,
plot(par_vect(1:cycle_number),Wplot, par_vect(1:cycle_number),Wplot,'ko')
else
semilogx(par_vect(1:cycle_number),Wplot, par_vect(1:cycle_number),Wplot,'ko'); hold on
end
grid, ylabel('Overall Efficiency')

xlabel('Input Filter Capacitance (F)')
zoom on
load ('ifcap20w.mat')      % Load workspace
Wtot = 1;
figure(1)
Wplot = (Wgmp-((Wgmp-Wgmn)-(Wbusp-Wbusn)+(Wfip-Wfin)-(Wwindp-Wwindn)))/Wgmp;
Wplot = Wplot(1:cycle_number);
if pltype == 0,
plot(par_vect(1:cycle_number),Wplot, par_vect(1:cycle_number),Wplot,'ko')
else
semilogx(par_vect(1:cycle_number),Wplot, par_vect(1:cycle_number),Wplot,'k^')
end
grid on, ylabel('Overall Efficiency')
xlabel('Input Filter Capacitance (F)')
zoom on

```

Appendix E

%% Matlab File for determining Stability of sample power distribution system %%%

clear all;
close all;

% EMA parameters file
%
% Secondary Actuator Simulation Parameters
%
% Inboard Spoiler Surface Parameters

global N Mp Bp Kact Kr;
global La Ra Jm Bm Kt Ke;
global Jsur Bsur h KI;
global Vg Ki Kv Kp th_ref;
global Hi Hp Hv;

PI = 3.14159265369;
Kp = 76; % V/V
wlim = 6.8; % V
% Kv = 490; % V/V
KI = 1;
Vg = 270;

Kv = 122.5; % V/V
Hp = 1.6; % V/in
Hv = 0.00382; % V/(rad/sec)
Jm = 2.43e-4; % in-lb-sec^2
Bm = 3.125e-4; % in-lb-sec
N = 249.6*PI; % rad/in
Kact = 9e5; % lbf/in
Mp = 5.43e-3; % lbf-sec^2/in
Bp = 15; % lbf-sec/in
Jsurr = 36.2; % in-lb-s^2
Bsur = 1702; % in-lb-s
h = 4.9; % in
KI = 1e6; % in-lb/rad
Kr = 5e5; % in-lb/rad
HM = 0;

% BDC Motor Parameters

Ka = 20; % V/V
La = 0.00045; % H
Ra = 0.5; % ohms
% Kt = 1.2; % in-lbf/amp

Kt = 1.141; % in-lbf/amp
% Ke = 0.188; % V/(rad/sec)

Ke = 0.129; % V/(rad/sec)

% Jm = 0.00142; % in-lbf-sec^2 - specified

above -
% Bm = 0.00473; % in-lbf-sec - specified

above -
% Ilim = 45; % amps
Ilim = 19.3; % Amps
Tlim = 22; % in-lb

Vlim = 270; % V
Hi = 0.25; % V/A
Nmech = 0.85;

nt = inf;

%% Filter parameters %%%

load theta_ref3_eq.mat;

wv = logspace(2,6,1e4);
m_zi = wv;
p_zi = wv;
m_zo = wv;
p_zo = wv;
P_p = 10;
Cfp = 1;

for j = 1:length(P_p);
for i = 1:length(Cfp);

theta_ref = 0;
Rcf1 = 0.4;
Lf1 = 10e-05;
Cf1 = 6.38e-05;
Cf2 = 6.38e-06;

Lf = Lf1;
Cf = Cf1;
Rcf = Rcf1;
RLf = 0.001;

%% The equilibrium solutions are determined below %%%

X = Xeq(1:3,1);
U0 = 0;
D = Xeq(4,1);
Im = X(1);
ILf_eq = D*Im;
Vcf_eq = 270;
ILf1_eq = ILf_eq;
Vcf1_eq = 270;
Vcf2_eq = 270;

[As2,Bs2,Cs2,Ds2] =
linmod('ema_simplified_sys21',[X;ILf1_eq;Vcf1_eq;Vcf2_
eq]',[270]);
ema_filt_model = ss(As2,Bs2,Cs2,Ds2);

Yi2_sys = ema_filt_model(4,1);
[num,den]= tfdata(Yi2_sys);
Zi2_sys = tf(den,num);
[mag_zi,ph_zi,wv] = bode(Zi2_sys,wv);
m_zi(:) = mag_zi(1,1,:);
p_zi(:) = ph_zi(1,1,:);

figure(5);
semilogx(wv,20*log10(m_zi)),hold on, grid on;

%%%

% Three-phase - to - DC bidirectional converter

Vm = 200; % input voltage
w = 2*pi*400; % Input line frequency
Vrref = 270;
Rld = 72.9; % Load resistance

Lbr = 18e-06;
Cbr = 350e-06; % Output filter Capacitance

fs = 20e3; % switching frequency
Ponom = 10e3; % nominal output power

```
ho      =      10;  
Cbr     =      350e-06;  
wz      =      2.5e3;  
wp      =      2.5e4;
```

```
Pload      =      60e3;
Vo_eq      =      270;
Iq_eq      =      0;
Io_eq      =      D*Im+(Pload/Vo_eq);
```

$$\begin{aligned} Dd_eq &= Vd_eq/No_eq; \\ Id_eq &= 2*Io_eq/Dd_eq; \end{aligned}$$

```
[Abf1,Bbf1,Cbf1,Dbf1] =linmod('ema_boost_simplified_filt_2',[X'  
ILf1_eq Vcf1_eq Vcf2_eq Id_eq Vo_eq Iq_eq Vc1_eq Vc2_eq],[0]);  
full1_sys = ss(Abf1,Bbf1,Cbf1,Dbf1);
```

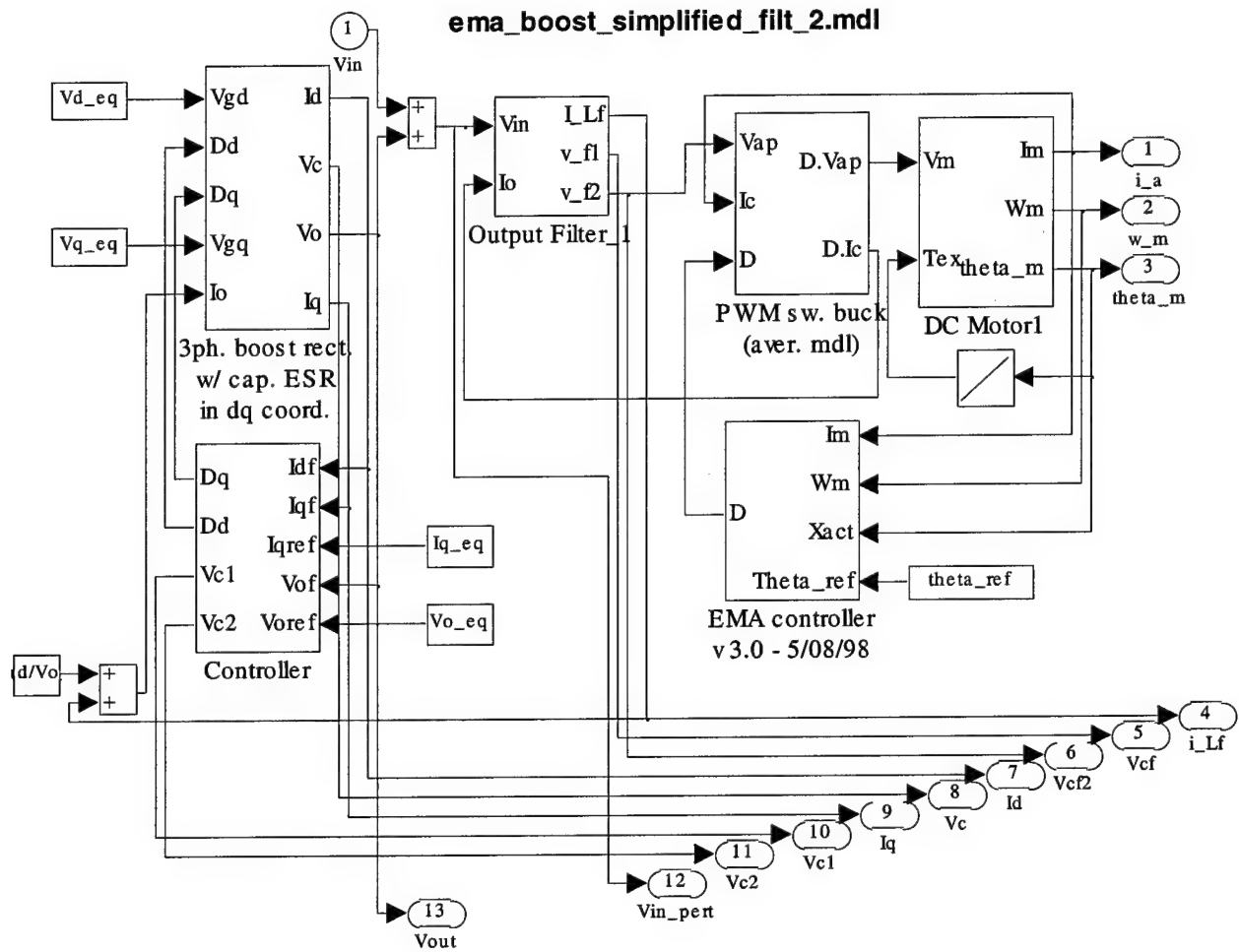
```
Vo_to_Vper = tf(full1_sys(13,1));
IL_to_Vper = tf(full1_sys(4,1));
Vin_to_Vper = tf(full1_sys(12,1));
```

```
[mag_zo,ph_zo,wv] = bode(Zoc_sys,wv);
m_zo(:) = mag_zo(1,1,:);
p_zo(:) = ph_zo(1,1,:);
```

```
figure(6);hold on;  
nyquist(series(Zoc_sys,inv(Zic_sys)),wv);
```

ema_simplified_sys21.mdl





Appendix F

%% Matlab Code to generate results for Input Filter Interaction
in Three Phase AC-DC converters %%

```
clear all;
close all;
```

```
global Lf Rf Vo Io Vgd Vgq Cf;
global w wLf wL wCf wCd Rd;
```

```
wv = logspace(2,6,1e04);
minus_pi = -180*ones(size(wv));
```

```
P_p = [5]; %% Constant current load %%
P_p = 1;
ho_p = [0.2];
```

```
for k = 1:length(P_p);
for l = 1:length(ho_p);
```

%% Three-phase - to - DC bidirectional converter %%

```
Vgd = 100;
Vgq = 0;
Vo = 270;
Io = 8e3/270;
Pr = 8e3;
```

```
w = 2*pi*400; % Input line frequency
```

```
L = 18e-06;
C = 350e-06; % Output filter Capacitance
```

```
%
Rc = 0.0;
wL = w*L;
```

```
Kdqq = -0.07;
Kdqd = -0.7;
Kqi = -200;
```

```
ho = 20;
wz = 2.0e3;
wp = 2.5e4;
```

%% Input Filter Parameters %%

```
Lf = 1e-06;
Ld = 50e-06;
Cf = 10e-06;
Rd = 0.5;
```

```
wLd = w*Ld;
wLf = w*Lf;
wCf = w*Cf;
wd = Rd/Ld;
%wd = 20000;
```

```
[Af,Bf,Cfm,Df] = linmod('In_filter4');
filter_sys = ss(Af,Bf,Cfm,Df);
[msp,psp,wv] = bode(filter_sys(3,2),wv);
zo_sp = [];
```

```
[m,p,wv] = bode(filter_sys(3,1),wv);
[y,i] = min(abs(2*pi*25e3-wv));
att(i) = m(i);
```

```
Af_dq = [Af*w*eye(size(Af));-w*eye(size(Af))
Af];
Bf_dq = [Bf zeros(size(Bf));zeros(size(Bf))
Bf];
Cfm_dq = [Cfm
zeros(size(Cfm));zeros(size(Cfm)) Cfm];
Df_dq = [Df zeros(size(Df));zeros(size(Df))
Df];
filter_dq_sys = ss(Af_dq,Bf_dq,Cfm_dq,Df_dq);
Zo_dq = filter_dq_sys([3 6],[2 4]);
Hf_dq = filter_dq_sys([3 6],[1 3]);
Zdd = Zo_dq(1,1);
```

```
[sv_zo,wv] = sigma(Zo_dq,wv);
[wn,del] = damp(filter_sys);
del_f(:,l) = del;
wn_f(:,l) = wn;
```

%% Equilibrium Solutions for Entire System %%

```
options(2) = 1e-09;
options(3) = 1e-09;
```

```
lfd = (1/2)*Vgd*(1-sqrt(1-
8*(Pr/Vgd^2)*Rd*(w/wd)^2/(1+(w/wd)^2)))/(Rd*(w/wd)^2/(1+(w/wd)^2));
```

```
Vf = Vgd-j*wLf*lfd-j*(w/wd)*Rd*lfd/(1+j*(w/wd));
lin = lfd-j*wCf*Vf;
ILd = lfd*1/(1+j*(w/wd));
```

```
ILdd_eq = real(ILd);
ILdq_eq = imag(ILd);
```

```
ld_eq = real(lin);
lq_eq = imag(lin);
```

```
Vd_eq = real(Vf);
Vq_eq = imag(Vf);
```

```
Vo_eq = Vo;
Io_eq = Io;
```

```
Dd_eq = Vd_eq/Vo;
Dq_eq = Vq_eq/Vo;
```

```
Vc1_eq = Vo_eq-ld_eq;
Vc2_eq = Vc1_eq;
```

```
lq(l) = lq_eq;
ld(l) = ld_eq;
```

```
Vq(l) = Vq_eq;
Vd(l) = Vd_eq;
```

```
P(l) = (1/2)*(Vd_eq*ld_eq+Vq_eq*lq_eq);
Q(l) = (1/2)*(Vq_eq*ld_eq-Vd_eq*lq_eq);
Im(l) = sqrt(ld_eq^2+lq_eq^2);
Pin(l) = (1/2)*Vgd*lfd;
```

```
Z_in = [ILdd_eq lfd Vd_eq ILdq_eq 0 Vq_eq];
```

```
[Aol,Bol,Col,Dol]= linmod('boost_ol_sys',[ld_eq lq_eq
Vo_eq],[Vd_eq Dd_eq Dq_eq Vq_eq Io_eq]);
```

```
ol_sys = ss(Aol,Bol,Col,Dol);
Gid_sys = ol_sys([1 2],[2 3]);
Gv_sys = ol_sys([3,2 3]);
Yi_sys = ol_sys([1 2],[1 4]);
Zo_sys = ol_sys(3,5);
Ai_sys = ol_sys([1 2],5);
```

```

Av_sys      =      ol_sys(3,[1 4]);

[AcI,BcI,CcI,DcI]=      linmod('boost_cl_sys',[Id_eq Iq_eq Vo_eq
Dq_eq Dd_eq],[Vd_eq Vq_eq lo_eq Id_eq]);
cl_sys      =      ss(AcI,BcI,CcI,DcI);

CLC_sys     =      cl_sys([1 2],[5 4]);

[AcIg,BcIg,CcIg,DcIg]=      linmod('boost_clg_sys',[Id_eq Iq_eq
Vo_eq Dq_eq Dd_eq],[Vd_eq Vq_eq lo_eq 0 0]);
clg_sys     =      ss(AcIg,BcIg,CcIg,DcIg);

CL_sys      =      clg_sys([1 2],[5 4]);
GvHi_sys    =      clg_sys([3],[5 4]);

[AfcIg,BfcIg,CfcIg,DfcIg]=      linmod('filt_boost_clg_sys',[Id_eq
Iq_eq Vo_eq Dq_eq Dd_eq Z_in],[Vd_eq Vq_eq lo_eq 0 0]);
fcIg_sys    =      ss(AfcIg,BfcIg,CfcIg,DfcIg);

FCL_sys     =      fcIg_sys([1 2],[5 4]);
fGvHi_sys   =      fcIg_sys([3],[5 4]);

[AvI,BvI,CvI,DvI]=      linmod('boost_vl_sys',[Id_eq Iq_eq Vo_eq
Dq_eq Dd_eq Vc1_eq Vc2_eq],[Vd_eq Vq_eq lo_eq Iq_eq
Vo_eq]);
vl_sys      =      ss(AvI,BvI,CvI,DvI);

VLC_sys     =      vl_sys(3,5);
Zo_sys      =      vl_sys(3,3);
Yi_sys      =      vl_sys([1 2],[1 2]);
Ydd         =      Yi_sys(1,1);
Ydq         =      Yi_sys(1,2);
Yqd         =      Yi_sys(2,1);
Yqq         =      Yi_sys(2,2);

sv_yi       =      sigma(Yi_sys,wv);

[AvIlg,BvIlg,CvIlg,DvIlg]=      linmod('boost_vlg_sys',[Id_eq Iq_eq
Vo_eq Dq_eq Dd_eq Vc1_eq Vc2_eq],[Vd_eq Vq_eq lo_eq Iq_eq
0]);
vlg_sys     =      ss(AvIlg,BvIlg,CvIlg,DvIlg);

VL_sys      =      vlg_sys(3,5);
GiHv_sys    =      vlg_sys([1 2],[5]);

[Afvlg,Bfvlg,Cfvlg,Dfvlg]=      linmod('filt_boost_vlg_sys',[Id_eq
Iq_eq Vo_eq Dq_eq Dd_eq Vc1_eq Vc2_eq Z_in],[Vd_eq Vq_eq
lo_eq Iq_eq 0]);
fvlg_sys    =      ss(Afvlg,Bfvlg,Cfvlg,Dfvlg);

FVL_sys     =      fvlg_sys(3,5);
fGiHv_sys   =      fvlg_sys([1 2],[5]);

[mz,pz,wv]  =      bode(Zo_dq(1,1),wv);
[nz,pz,wv]=      bode(Zo_dq(1,2),wv);
[my11,ny,wv]=      bode(Ydd,wv);
[my12,ny,wv]=      bode(Ydq,wv);
[my21,ny,wv]=      bode(Yqd,wv);
[my22,ny,wv]=      bode(Yqq,wv);

M           =      [];
N           =      [];
mydd        =      [];
mydq        =      [];
myqd        =      [];

myqq        =      [];

for i       =      1:length(mz);
zo_sp(i)=   msp(1,1,i);
M(i)       =      mz(1,1,i);
N(i)       =      nz(1,1,i);
mydd(i)    =      my11(1,1,i);
mydq(i)    =      my12(1,1,i);
myqd(i)    =      my21(1,1,i);
myqq(i)    =      my22(1,1,i);
end;

%[Afs,Bfs,Cfs,Dfs] =      linmod('filt_boost_sys4',[Id_eq
Vo_eq Iq_eq Vc1_eq Vc2_eq vqi_eq Z_in]);
%full_sys        =      ss(Afs,Bfs,Cfs,Dfs);
%Z_full(:,i)     =      eig(full_sys);

%loop_gain       =
tf(eye(2,2)+series(Yi_sys,Zo_dq));
%crit            =
loop_gain(1,1)*loop_gain(2,2)-
loop_gain(1,2)*loop_gain(2,1);
%crit_simple     =
1+Zo_dq(1,1)*Yi_sys(1,1)+Zo_dq(1,2)*Yi_sys(1,2);

%figure(3), hold on;
%nyquist(crit,wv,'r');
%nyquist(crit_simple,wv,'b');

figure(1);
semilogx(wv,20*log10(sv_zo(1,:)), 'r-',wv,20*log10(M+N), 'b-
.',wv,20*log10(zo_sp), 'k--'),grid on;

figure(2);
semilogx(wv,20*log10(sv_yi(1,:)), 'r',wv,20*log10(mydd), 'b'),grid on;

figure(3);
semilogx(wv,20*log10(M+N), 'r-',wv,-20*log10(mydd), 'b-'),grid on;

figure(5);
subplot(221),semilogx(wv,20*log10(mydd)),grid on;
subplot(222),semilogx(wv,20*log10(mydq)),grid on;
subplot(223),semilogx(wv,20*log10(myqd)),grid on;
subplot(224),semilogx(wv,20*log10(myqq)),grid on;

figure(4);
bode(VL_sys,wv,'-');
hold on;
bode(FVL_sys,wv,'--');

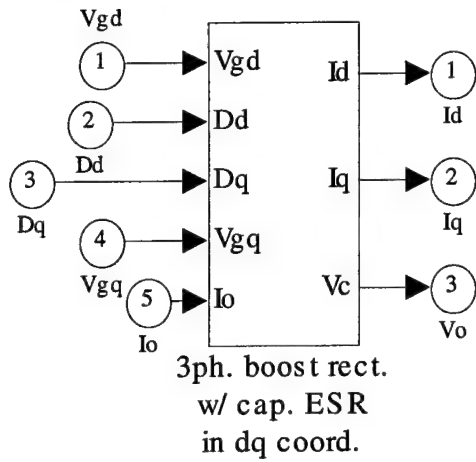
end;

%figure(1),hold on;
%plot(ho_p,Q),title('Reactive Power');
%figure(2),hold on;
%plot(ho_p,Iq),title('Q-axis Current');
%figure(3),hold on;
%plot(ho_p,Im),title('Input Current');
%figure(4),hold on;
%plot(ho_p,Pin-P),title('Power Loss in the Resistor');

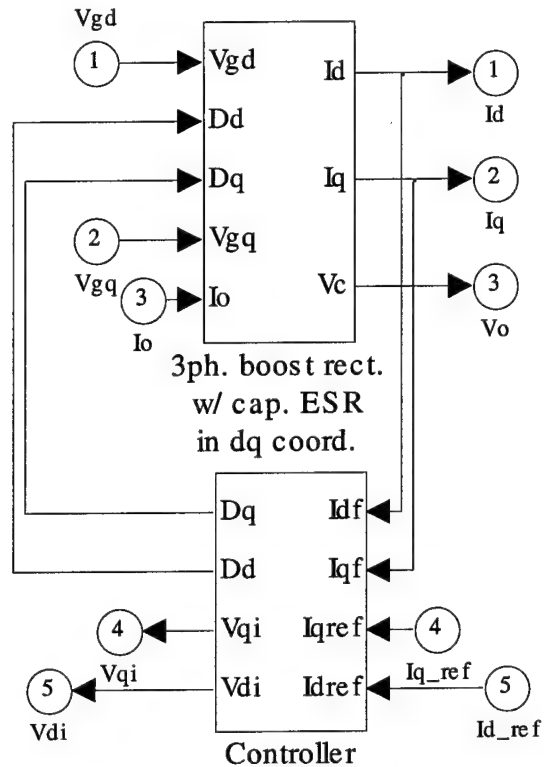
end;

```

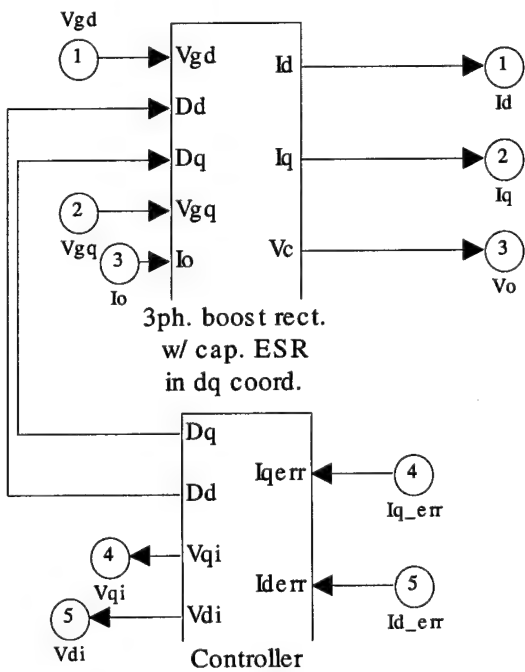
boost_ol_sys.mdl



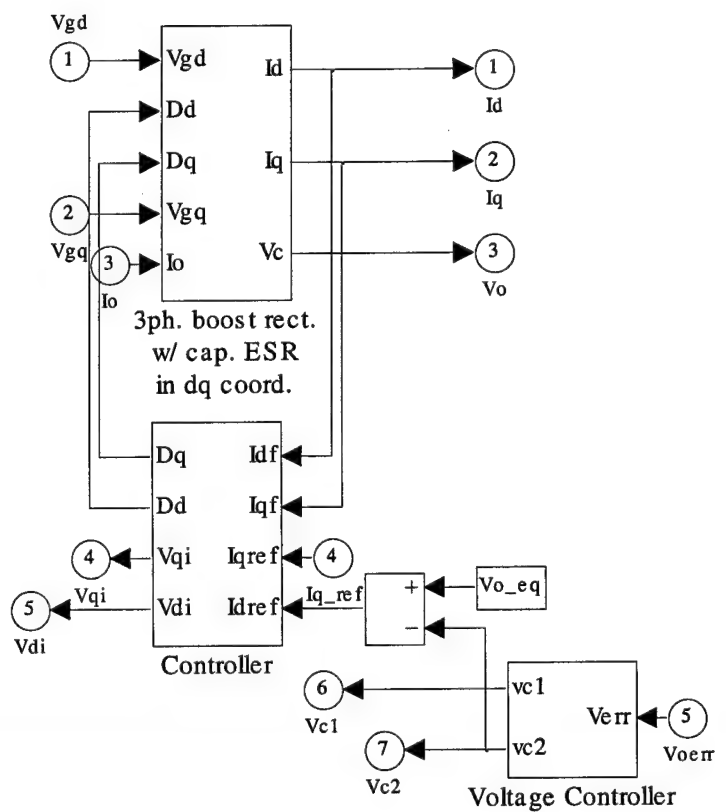
boost_cl_sys.mdl

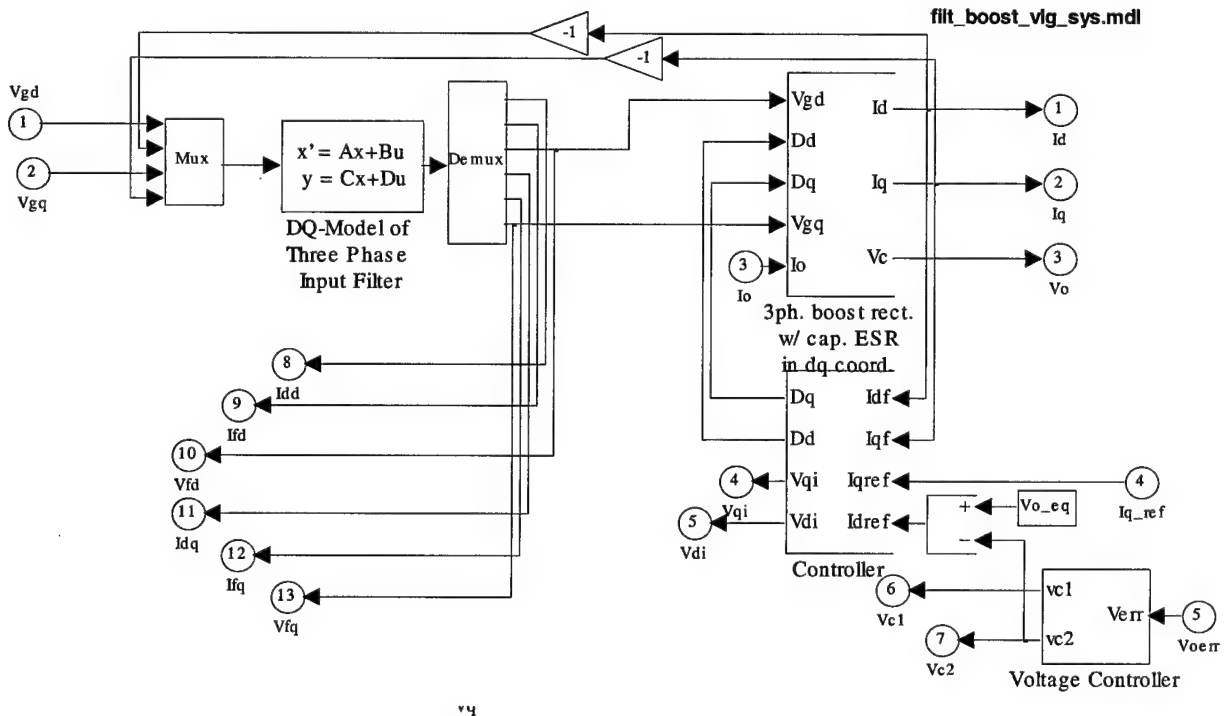
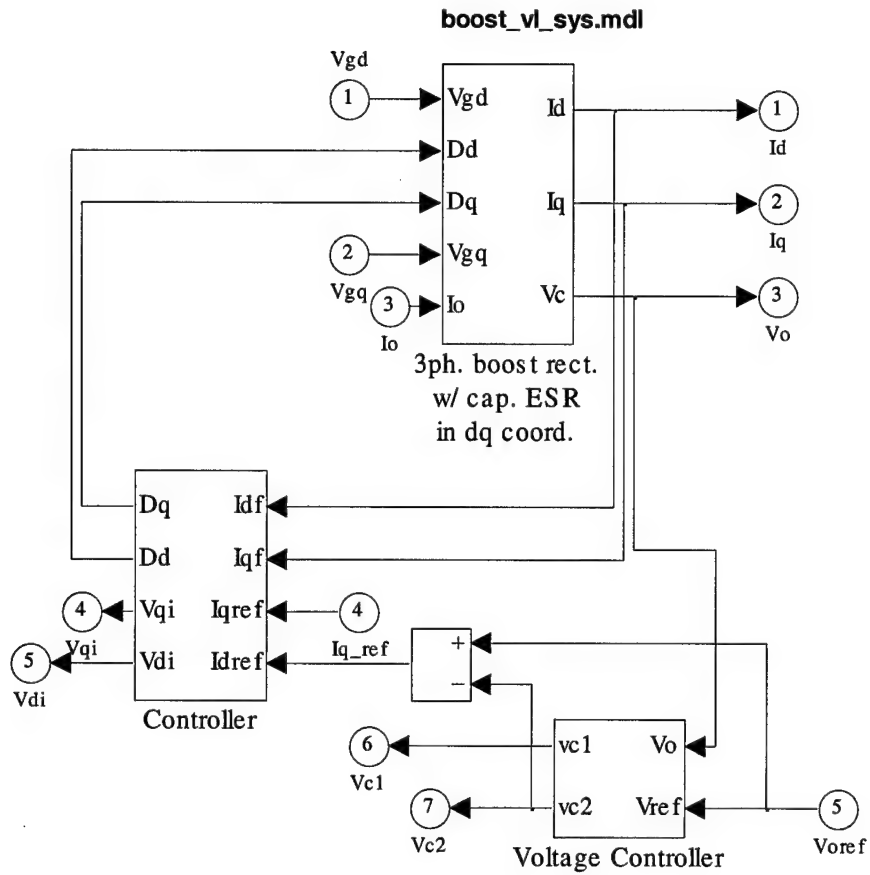


boost_clg_sys.mdl

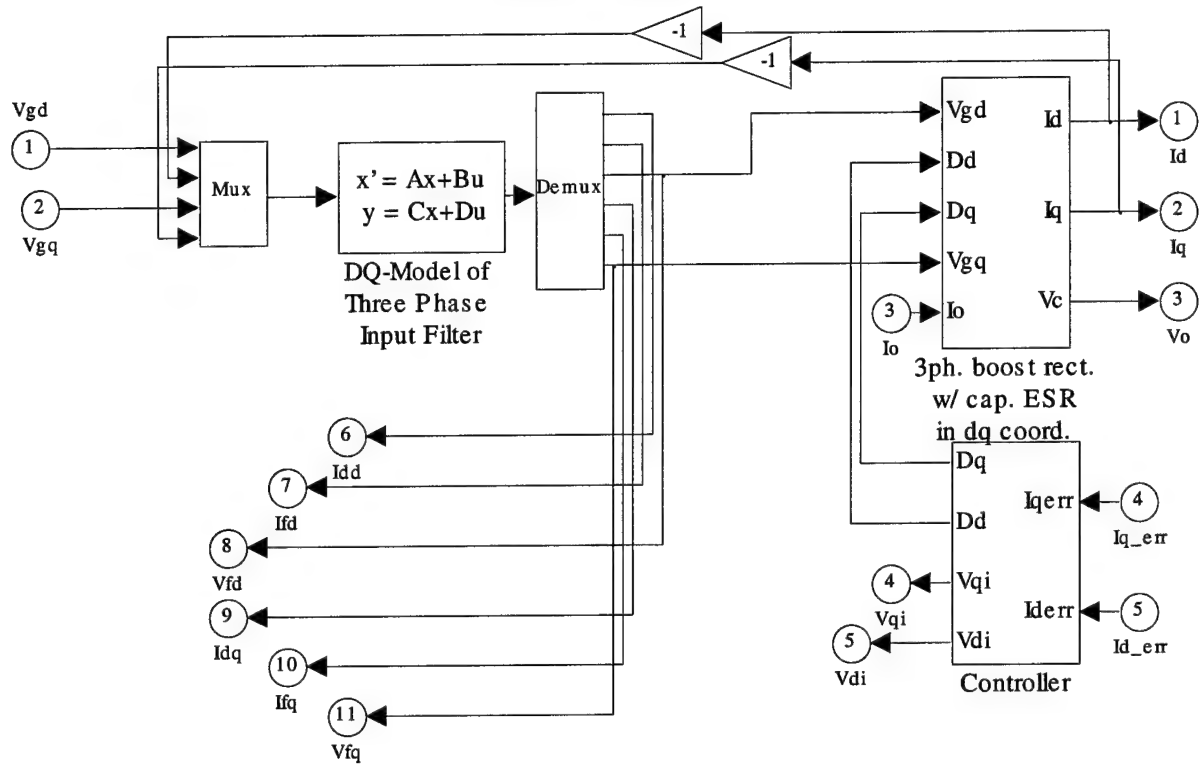


boost_vlg_sys.mdl

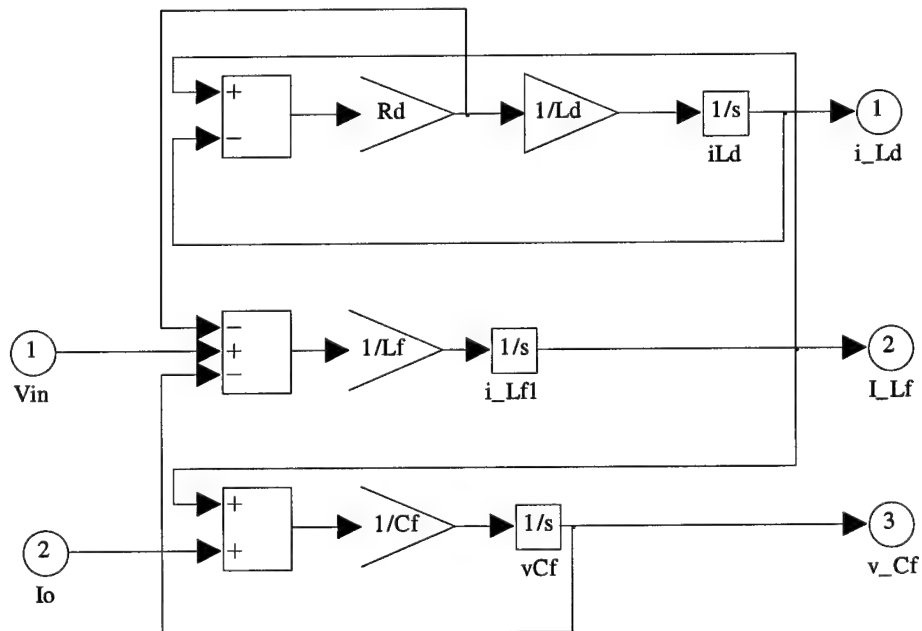




filt_boost_clg_sys.mdl



In_filter4.mdl



Appendix G

%% Matlab code for generating periodic solutions for DC-%% DC buck converter with input filter

```

%% Title : Simple Shooting method for determination of periodic solutions of a system of first order differential equations.
%% Author : Sriram Chandrasekaran
%% Date : 21st October, 1997
%% Periodic Solutions to a system of first order differential equations
%% are constructed by using the shooting method used to solve two point boundary value problems.
%% The following code implements the simple shooting method as described by Ascher, Mattheij and Russell from "Numerical Solution of boundary value problems for ordinary differential equations. pp 170-1
%% A DC-DC buck converter with an input filter is considered.
%% The parameters are defined below:
global U1 U2 U3;
global L C Lf Rf Rc RL R Cf;
global k Fm R1 R2 ho C1;
global RpRc RoverRRc khoFm m;
global dx_ds;
Vg = 150; % Input DC Voltage %
L = 0.1e-03; % Output Inductance %
C = 1e-03; % Output Capacitance %
R = 5; % Load Resistance %
k = 0.1; % Feedback Factor %
Vref = 5; % Reference Voltage %
%% Parameters of the PI compensator %%
R2 = 50e03; % Resistance at op-amp input %
R1 = 400; % Feedback path resistance %
C1 = 1e-06; % Feedback path capacitance %
Fm = 0.2; % 1/Ramp amplitude %
ho = R1/R2;
%% Parameters of the input filter %%
Lf = 0.1;
Cf = 0.01;
Rf = 0.139:0.001:0.180;
%% Parasitic Elements %%
RL = 0; % ESR of L %
Rc = 0; % ESR of C %
Io = 0; % Load disturbance %%
U1 = Vg;
U2 = Io;
U3 = Vref;
%% Definition of Equilibrium Solutions %%
RpRc = R*Rc/(R+Rc);
khoFm = k*ho*Fm;
RoverRRc = R/(R+Rc);
m = ((U3/k)+Io*R)*((U3/k)*(1+RL/R)+Io*RL);
X1 = (U3/(k*R))+U2; % Inductor Current %%
X2 = (U3/(k)); % Capacitor Voltage %%
X4 = (U1/2)+sqrt((U1/2)^2-m*Rf/R); % Filter Capacitor Voltage %%
X3 = (U1-X4)/Rf; % Filter Inductor Voltage %%
X5 = U3-X3/(Fm*X1); % Integrator Voltage %%
Q = (1/Cf)*(khoFm*RoverRRc*(2*Rc*X1+X2)+Fm*X5-((1+ho)*Fm*U3)-khoFm*RpRc*U2);
%% Shooting method starts here
%% The period of the solution is normalised to unity and the actual period T is obtained as a state variable by appropriately augmenting the original system.
%% "s" represents the starting guess for the initial conditions
%% s = [x10 x20 x30 x40 x50 T0];
%% The starting guesses for the states of the system are the equilibrium solutions
%% A branch of periodic solutions is followed by the arc length continuation procedure
%% We start with an initial guess for the initial conditions, period and the control parameter.
x0 = [30.6634 156.8718 86.2622 149.8281 -0.3193]';
T0 = 0.2361;
Rf0 = 0.1091;

```

```

%% The arc length is denoted by the symbol s %%
s = 0:0.01:50;
%% We need to find initial conditions such that the following equations
%% are satisfied.
%% We find the Jacobian Matrix of the system of equations shown below %%
%%  $F(x_0, x_2, x_3, x_4, x_5, T_0, R_f) = x(1, x_0) - x_0 = 0$ ;
%% We find the matrix  $[dy/dx]^{-1}$  %%
%% The state  $x(4)$  is maintained at 149.8281 throughout the continuation process %%
delta_s = 0.01*eye(5,5);
s_Rf = zeros(7,length(R_f));
floquet_m = zeros(5,length(R_f));
zeta = zeros(7,1);
Rf = Rf0;
inx = eye(7,7);
eta = 0.5;
for i = 1:length(s)-1;
    temp = s(i);
    in_x = [x0;x0+delta_s(:,1);x0+delta_s(:,2);x0+delta_s(:,3);x0+delta_s(:,5);x0];
    [t,x] = ode45('solve_system_arc1',0,1,in_x);
    xf = x(length(t),:);
    Y_b = 100*[xf(6:10)-xf(1:5) xf(11:15)-xf(1:5) xf(16:20)-xf(1:5) xf(21:25)-xf(1:5)]-[1 0 0 0;0 1 0 0;0 0 1 0;0 0 0 0;0 0 0 1];
    f_y = f_of_x(xf);
    yi_r = (xf(26:30) - xf(1:5))*1000;
    beta = [-inv([Y_b f_y])*yi_r;1];
    dx_ds = beta./norm(beta);
    edx_ds = [eta*[dx_ds(1) dx_ds(2) dx_ds(3) 0 dx_ds(4) dx_ds(5)]] (1-eta)*dx_ds(6);
    [ts,xs] = ode45('x_s',s(i),s(i+1),[x0(1) x0(2) x0(3) x0(5) T0 Rf]);
    xsf = xs(length(ts),:);
    xc = [xsf(1) xsf(2) xsf(3) 149.8281 xsf(4) xsf(5) xsf(6)]'
    xp = xc;
for j = 1:15;
    [tt,xx] = ode45('solve_system_new1',0,1,[xc;inx(:,1);inx(:,2);inx(:,3);inx(:,4);inx(:,5);inx(:,6);inx(:,7)]);
    xcf = xx(length(tt),:);
    Y_bc = [xcf(8:14) xcf(15:21) xcf(22:28) xcf(29:35) xcf(36:42) xcf(43:49) xcf(50:56)];
    B_a = [eye(5,5) [0 0 0 0 0]' [0 0 0 0 0]';[0 0 0 1 0 0 0];edx_ds];
    B_b = [-eye(5,5);zeros(2,5)] zeros(7,2);
    F_prime = B_a + B_b*Y_bc;
    last = sum((xc-xp).*edx_ds)-0.01;
    F_s = [ [xc(1:5) - xcf(1:5)]; xc(4)-xc(4); last];
    zeta = F_prime\(-F_s)
    xc = xc + zeta
    error = norm(zeta)
    if error < 0.02,
        break;
    end;
end;
s_Rf(:,i) = xc;
x0 = xc(1:5);
Rf = xc(7);
T0 = xc(6);
floquet_m(:,i) = eig(Y_bc(1:5,1:5));
save final5_arc s_Rf floquet_m R_f;
end;

function [xdot] = solve_system_arc1(t,x);
global U1 U2 U3;
global L C Lf Rc RL R Cf Rf;
global k Fm R1 R2 ho C1;
global RpRc RoverRRc khoFm;
xdot = zeros(30,1);
Rf1 = Rf+0.001;
% Define the state space equations %%
xdot(1) = (1/L)*(-(RL+RpRc)*x(1)-RoverRRc*x(2)-khoFm*RpRc*x(1)*x(4)-khoFm*RoverRRc*x(2)*x(4)-Fm*x(4)*x(5)+(1+ho)*Fm*x(4)*U3);
xdot(2) = (1/C)*RoverRRc*(x(1)-x(2)/R-U2);
xdot(3) = (1/Lf)*(-Rf*x(3)-x(4)+U1);
xdot(4) = (1/Cf)*(khoFm*RpRc*x(1)^2+khoFm*RoverRRc*x(1)*x(2)+x(3)+Fm*x(1)*x(5) -(1+ho)*Fm*U3*x(1)-khoFm*RpRc*U2*x(1));
xdot(5) = (1/C1)*(k*RpRc*(x(1)-U2)+k*RoverRRc*x(2)-U3)/R2;
xdot(6) = (1/L)*(-(RL+RpRc)*x(6)-RoverRRc*x(7)-khoFm*RpRc*x(6)*x(9)-khoFm*RoverRRc*x(7)*x(9)-Fm*x(9)*x(10)+(1+ho)*Fm*x(9)*U3);

```

```

xdot(7) = (1/C)*RoverRRc*(x(6)-x(7)/R-U2);
xdot(8) = (1/Lf)*(-Rf*x(8)-x(9)+U1);
xdot(9) = (1/Cf)*(khoFm*RpRc*x(6)^2+khoFm*RoverRRc*x(6)*x(7)+x(8)+Fm*x(6)*x(10)-(1+ho)*Fm*U3*x(6)-khoFm*RpRc*U2*x(6));
xdot(10) = (1/C1)*(k*RpRc*(x(6)-U2)+k*RoverRRc*x(7)-U3)/R2;
xdot(11) = (1/L)*(-(RL+RpRc)*x(11)-RoverRRc*x(12)-khoFm*RpRc*x(11)*x(14)-khoFm*RoverRRc*x(12)*x(14)-Fm*x(14)*x(15)+(1+ho)*Fm*x(14)*U3);
xdot(12) = (1/C)*RoverRRc*(x(11)-x(12)/R-U2);
xdot(13) = (1/Lf)*(-Rf*x(13)-x(14)+U1);
xdot(14) = (1/Cf)*(khoFm*RpRc*x(11)^2+khoFm*RoverRRc*x(11)*x(12)+x(13)+Fm*x(11)*x(15)-(1+ho)*Fm*U3*x(11)-khoFm*RpRc*U2*x(11));
xdot(15) = (1/C1)*(k*RpRc*(x(11)-U2)+k*RoverRRc*x(12)-U3)/R2;
xdot(16) = (1/L)*(-(RL+RpRc)*x(16)-RoverRRc*x(17)-khoFm*RpRc*x(16)*x(19)-khoFm*RoverRRc*x(17)*x(19)-Fm*x(19)*x(20)+(1+ho)*Fm*x(19)*U3);
xdot(17) = (1/C)*RoverRRc*(x(6)-x(17)/R-U2);
xdot(18) = (1/Lf)*(-Rf*x(18)-x(19)+U1);
xdot(19) = (1/Cf)*(khoFm*RpRc*x(16)^2+khoFm*RoverRRc*x(16)*x(17)+x(18)+Fm*x(16)*x(20)-(1+ho)*Fm*U3*x(16)-khoFm*RpRc*U2*x(16));
xdot(20) = (1/C1)*(k*RpRc*(x(16)-U2)+k*RoverRRc*x(17)-U3)/R2;
xdot(21) = (1/L)*(-(RL+RpRc)*x(21)-RoverRRc*x(22)-khoFm*RpRc*x(21)*x(24)-khoFm*RoverRRc*x(22)*x(24)-Fm*x(24)*x(25)+(1+ho)*Fm*x(24)*U3);
xdot(22) = (1/C)*RoverRRc*(x(21)-x(22)/R-U2);
xdot(23) = (1/Lf)*(-Rf*x(23)-x(24)+U1);
xdot(24) = (1/Cf)*(khoFm*RpRc*x(21)^2+khoFm*RoverRRc*x(21)*x(22)+x(23)+Fm*x(21)*x(25)-(1+ho)*Fm*U3*x(21)-khoFm*RpRc*U2*x(21));
xdot(25) = (1/C1)*(k*RpRc*(x(21)-U2)+k*RoverRRc*x(22)-U3)/R2;
xdot(26) = (1/L)*(-(RL+RpRc)*x(26)-RoverRRc*x(27)-khoFm*RpRc*x(26)*x(29)-khoFm*RoverRRc*x(27)*x(29)-Fm*x(29)*x(30)+(1+ho)*Fm*x(29)*U3);
xdot(27) = (1/C)*RoverRRc*(x(26)-x(27)/R-U2);
xdot(28) = (1/Lf)*(-Rf*x(28)-x(29)+U1);
xdot(29) = (1/Cf)*(khoFm*RpRc*x(26)^2+khoFm*RoverRRc*x(26)*x(27)+x(28)+Fm*x(26)*x(30)-(1+ho)*Fm*U3*x(26)-khoFm*RpRc*U2*x(26));
xdot(30) = (1/C1)*(k*RpRc*(x(26)-U2)+k*RoverRRc*x(27)-U3)/R2;
function [f] = f_of_x(x);
global U1 U2 U3;
global L C Lf Rc RL R Rf Cf;
global k Fm R1 R2 ho C1;
global RpRc RoverRRc khoFm;
f = zeros(5,1);
% Define the state space equations %%
f(1) = (1/L)*(-(RL+RpRc)*x(1)-RoverRRc*x(2)-khoFm*RpRc*x(1)*x(4)-khoFm*RoverRRc*x(2)*x(4)-Fm*x(4)*x(5)+(1+ho)*Fm*x(4)*U3);
f(2) = (1/C)*RoverRRc*(x(1)-x(2)/R-U2);
f(3) = (1/Lf)*(-Rf*x(3)-x(4)+U1);
f(4) = (1/Cf)*(khoFm*RpRc*x(1)^2+khoFm*RoverRRc*x(1)*x(2)+x(3)+Fm*x(1)*x(5)-(1+ho)*Fm*U3*x(1)-khoFm*RpRc*U2*x(1));
f(5) = (1/C1)*(k*RpRc*(x(1)-U2)+k*RoverRRc*x(2)-U3)/R2;
function [xdot] = solve_system_new1(t,x);
global U1 U2 U3;
global L C Lf Rc RL R Cf;
global k Fm R1 R2 ho C1;
global RpRc RoverRRc khoFm;
xdot = zeros(42,1);
% Define the state space equations %%
xdot(1) = (1/L)*(-(RL+RpRc)*x(1)-RoverRRc*x(2)-khoFm*RpRc*x(1)*x(4)-khoFm*RoverRRc*x(2)*x(4)-Fm*x(4)*x(5)+(1+ho)*Fm*x(4)*U3)*x(6);
xdot(2) = (1/C)*RoverRRc*(x(1)-x(2)/R-U2)*x(6);
xdot(3) = (1/Lf)*(-x(7)*x(3)-x(4)+U1)*x(6);
xdot(4) = (1/Cf)*(khoFm*RpRc*x(1)^2+khoFm*RoverRRc*x(1)*x(2)+x(3)+Fm*x(1)*x(5)-(1+ho)*Fm*U3*x(1)-khoFm*RpRc*U2*x(1))*x(6);
xdot(5) = (1/C1)*(k*RpRc*(x(1)-U2)+k*RoverRRc*x(2)-U3)*x(6)/R2;
xdot(6) = 0;
xdot(7) = 0;
%% Define the Jacobian matrix %%
Ja11 = -(1/L)*(RL+RpRc+khoFm*RpRc*x(4))*x(6);
Ja12 = -(1/L)*RoverRRc*(1+khoFm*x(4))*x(6);
Ja13 = 0;
Ja14 = -(1/L)*(khoFm*RoverRRc*(Rc*x(1)+x(2))-((1+ho)*Fm*U3+Fm*x(5))*x(6);
Ja15 = -(1/L)*Fm*x(4)*x(6);
Ja16 = (1/L)*(-(RL+RpRc)*x(1)-RoverRRc*x(2)-khoFm*RpRc*x(1)*x(4)-khoFm*RoverRRc*x(2)*x(4)-Fm*x(4)*x(5)+(1+ho)*Fm*x(4)*U3);
Ja17 = 0;
Ja21 = (1/C)*RoverRRc*x(6);
Ja22 = -(1/C)*RoverRRc*x(6)/R;
Ja23 = 0;
Ja24 = 0;

```



```

Ja25 = 0;
Ja26 = (1/C)*RoverRRc*(x(1)-x(2)/R-U2);
Ja27 = 0;
Ja31 = 0;
Ja32 = 0;
Ja33 = -(1/Lf)*x(7)*x(6);
Ja34 = -(1/Lf)*x(6);
Ja35 = 0;
Ja36 = (1/Lf)*(-x(7)*x(3)-x(4)+U1);
Ja37 = (1/Lf)*(-x(3)*x(6));
Ja41 = (1/Cf)*(khoFm*RoverRRc*(2*Rc*x(1)+x(2))+Fm*x(5)-((1+ho)*Fm*U3-khoFm*RpRc*U2)*x(6);
Ja42 = (1/Cf)*khoFm*RoverRRc*x(1)*x(6);
Ja43 = (1/Cf)*x(6);
Ja44 = 0;
Ja45 = (1/Cf)*Fm*x(1)*x(6);
Ja46 = (1/Cf)*(khoFm*RpRc*x(1)^2+khoFm*RoverRRc*x(1)*x(2)+x(3)+Fm*x(1)*x(5)-(1+ho)*Fm*U3*x(1)-khoFm*RpRc*U2*x(1));
Ja47 = 0;
Ja51 = (1/C1)*k*RpRc*x(6)/R2;
Ja52 = (1/C1)*k*RoverRRc*x(6)/R2;
Ja53 = 0;
Ja54 = 0;
Ja55 = 0;
Ja56 = (1/C1)*(k*RpRc*(x(1)-U2)+k*RoverRRc*x(2)-U3)/R2;
Ja57 = 0;
Ja = [Ja11 Ja12 Ja13 Ja14 Ja15 Ja16 Ja17;
      Ja21 Ja22 Ja23 Ja24 Ja25 Ja26 Ja27;
      Ja31 Ja32 Ja33 Ja34 Ja35 Ja36 Ja37;
      Ja41 Ja42 Ja43 Ja44 Ja45 Ja46 Ja47;
      Ja51 Ja52 Ja53 Ja54 Ja55 Ja56 Ja57;
      0 0 0 0 0 0 0;
      0 0 0 0 0 0 0];

xdot(8:14) = Ja*x(8:14);
xdot(15:21) = Ja*x(15:21);
xdot(22:28) = Ja*x(22:28);
xdot(29:35) = Ja*x(29:35);
xdot(36:42) = Ja*x(36:42);
xdot(43:49) = Ja*x(43:49);
xdot(50:56) = Ja*x(50:56);
function [xdot] = x_s(t,x);
global dx_ds;
xdot = zeros(6,1);
xdot = dx_ds.*x;

```

Appendix H

%% Bifurcation Diagram for Three phase boost driving %%

%% a DC-DC Buck with Input Filter %%

```
clear all;
global Vg Po;
global Lf1 Cf1 Cf2;
global Rf;
global dx_ds;
global Vd Vq Io Po w ki kv;
global Vref Iqref ho;
global Kdq wp wz L C Rc;
Vg = 270;
Po = 8e3;
Rf = 0.5;
Lf1 = 10e-06;
Cf1 = 100e-06;
Cf2 = 10e-06;
%% Operating Point values %%
If1_eq = Po/Vg;
Vf1_eq = Vg;
Vf2_eq = Vg;
% Three-phase - to - DC bidirectional converter
w = 2*pi*400; % Input line frequency
Vref = 270;
Iqref = 0;
L = 18e-06;
C = 350e-06;
wL = w*L;
Rc = 0.1;
ho = 45.8968;
wz = 2.5e3;
wp = 2.5e4;
Kdq = -0.007;
%% Equilibrium Solutions with an output filter %%
R_L = 10e20;
Pload = 8e3;
Vo_eq = 270;
Iq_eq = 0;
Io_eq = If1_eq+Pload/Vo_eq;
Vd_eq = 100;
Vq_eq = 0;
Dd_eq = Vd_eq/Vo_eq;
Id_eq = 2*(Io_eq)/Dd_eq;
Dq_eq = -wL*Id_eq/Vo_eq;
Vc1_eq = Vo_eq-Id_eq-Dd_eq/Kdq;
Vc2_eq = Vc1_eq;
Vd = Vd_eq;
Vq = 0;
Io = Pload/Vo_eq;
%% Shooting method starts here %%
%% The period of the solution is normalised to unity and the actual %
%% period T is obtained as a state variable by appropriately augmenting %
%% the original system. %
%% "x0" represents the starting guess for the initial conditions %
%% x0 = [x10 x20 x30 T0];
%% The starting guesses for the states of the system are the equilibrium solutions %%
%% A branch of periodic solutions is followed by the arc length continuation procedure %%
%% We start with an initial guess for the initial conditions, period and the
%% control parameter.
%% Initial Guess [i_Lf v_f1 v_f2] = [82.1315 270.0213 5.6913]
%% T0 = 1.5540e-04
x0 = [232.3456 272.0745 0.0406 1.8774 86.8255 35.1413 271.3489 275.1370];
T0 = 1.209726424099746e-04;
ho0 = 45.9968;
ho = ho0;
%% The arc length is denoted by the symbol s %%
s = 0:0.001:50;
%% We need to find initial conditions such that the following equations
%% are satisfied.
```

```

%% We find the Jacobian Matrix of the system of equations shown below %%
%% Fi(x01,x02,x03,x04,x05,T0,Rf0) = x(1,x0)-x0 = 0;
%% We find the matrix [dy/ds]-I %%
%% The state x(2) is maintained at 270 throughout the continuation process %%
delta_s = 0.005*eye(8,8);
s_ho = zeros(10,length(s));
floquet_m = zeros(8,length(s));
tolerance = 1e-09*ones(72,1);
options = odeset('RelTol',1e-06,'Abstol',tolerance);
zeta = zeros(10,1);
ho = ho0;
inx = eye(10,10);
eta = 0.5;
for i = 1:length(s)-1;
temp = s(i);
in_x = [x0;x0+delta_s(:,1);x0+delta_s(:,3);x0+delta_s(:,4);x0+delta_s(:,5);x0+delta_s(:,6);x0+delta_s(:,7);x0+delta_s(:,8);x0];
[t,x] = ode45('th_solve_system_arc1',[0 T0],in_x,options);
xf = x(length(t),:);
sub_b = [[1 zeros(1,6)];zeros(1,7);[zeros(6,1) eye(6,6)]];
Y_b = 200*[xf(9:16)-xf(1:8) xf(17:24)-xf(1:8) xf(25:32)-xf(1:8) xf(33:40)-xf(1:8) xf(41:48)-xf(1:8) xf(49:56)-xf(1:8) xf(57:64)-xf(1:8)]-sub_b;
f_y = th_of_x(xf);
yi_r = (xf(65:72) - xf(1:8))*10000;
beta = [-inv([Y_b f_y])*yi_r;1];
dx_ds = beta./norm(beta);
edx_ds = [[eta*[dx_ds(1) 0 dx_ds(2) dx_ds(3) dx_ds(4) dx_ds(5) dx_ds(6) dx_ds(7) dx_ds(8)]] (1-eta)*dx_ds(9)];
[ts,xs] = ode45('x_s',[s(i) s(i+1)],[x0(1) x0(3) x0(4) x0(5) x0(6) x0(7) x0(8) T0 ho]);
xsf = th_xs(length(ts),:);
xc = [xsf(1) 270.1592 xsf(2) xsf(3) xsf(4) xsf(5) xsf(6) xsf(7) xsf(8) xsf(9)];
xp = xc;
for j = 1:15;
xx_in = [xc;inx(:,1);inx(:,2);inx(:,3);inx(:,4);inx(:,5);inx(:,6);inx(:,7);inx(:,8);inx(:,9);inx(:,10)];
[tt,xx] = ode45('solve_system_new1',[0 1],xx_in);
xcf = xx(length(tt),:);
Y_bc = [xcf(11:20) xcf(21:30) xcf(31:40) xcf(41:50) xcf(51:60) xcf(61:70) xcf(71:80) xcf(81:90) xcf(91:100) xcf(101:110)];
B_a = [[eye(8,8) zeros(8,2)];[0 1 zeros(1,8)];edx_ds];
B_b = [-eye(8,8);zeros(2,8)] zeros(8,2);

F_prime = B_a + B_b*Y_bc;
last = sum((xc-xp).*edx_ds)-0.001;
F_s = [ xc(1:8) - xcf(1:8)]; xc(2)-xc(2); last];
zeta = F_prime\(-F_s)
xc = xc + zeta
error = norm(zeta)
if max(abs(zeta)) < 0.01,
break;
end;
end;

s_Rf(:,i) = xc;
x0 = xc(1:8);
ho = xc(10);
T0 = xc(9);
floquet_m(:,i) = eig(Y_bc(1:8,1:8));
save th_final_arc1 s_ho floquet_m;
end;

function [xdot] = th_solve_system_arc1(t,x);
global Vd Vq lo Po w ki kv;
global Vref lqref ho;
global Kdq wp wz L C Rc;
global Vg;
global Lf Cf1 Cf2;
global Rf;
global dx_ds;
hi = Kdq;
ho1 = ho+0.0001;
dd1 = hi*(Vref-ki*x(1)-x(5))+w*L*x(3)/Vref;
dq1 = hi*(lqref-ki*x(3))-w*L*x(1)/Vref;
xdot(1) = (1/L)*(Vd+w*L*x(3)-dd1*(x(2)+Rc*((dd1*x(1)+dq1*x(3))/2-x(6)-lo)));
xdot(2) = (1/C)*((dd1*x(1)+dq1*x(3))/2-x(6)-lo);
xdot(3) = (1/L)*(Vq-w*L*x(1)-dq1*(x(2)+Rc*((dd1*x(1)+dq1*x(3))/2-x(6)-lo)));
xdot(4) = (x(5)-x(4))*wz;

```

```

xdot(5) = -(x(4)+x(5))*wp+ho*(-Vref+kv*(x(2)+Rc*(-lo+(1/2)*(dd1*x(1)+dq1*x(3))-x(6))))*wp;
xdot(6) = (1/Lf)*(x(2)+Rc*(-lo+(1/2)*(dd1*x(1)+dq1*x(3))-x(6)))-x(8));
xdot(7) = (1/Cf1)*(x(8)-x(7))/Rf;
xdot(8) = (1/Cf2)*(x(6)-Po/x(8)-(1/Rf)*(x(8)-x(7)));
dd2 = hi*(Vref-ki*x(9)-x(13))+w*L*x(11)/Vref;
dq2 = hi*(lqref-ki*x(11))-w*L*x(9)/Vref;
xdot(9) = (1/L)*(Vd+w*L*x(11)-dd2*(x(10)+Rc*((dd2*x(9)+dq2*x(11))/2-x(14)-lo)));
xdot(10) = (1/C)*((dd2*x(9)+dq2*x(11))/2-x(14)-lo);
xdot(11) = (1/L)*(Vq-w*L*x(9)-dq2*(x(10)+Rc*((dd2*x(9)+dq2*x(11))/2-x(14)-lo)));
xdot(12) = (x(13)-x(12))*wz;
xdot(13) = -(x(12)+x(13))*wp+ho*(-Vref+kv*(x(10)+Rc*(-lo+(1/2)*(dd2*x(9)+dq2*x(11))-x(14))))*wp;
xdot(14) = (1/Lf)*(x(10)+Rc*(-lo+(1/2)*(dd2*x(9)+dq2*x(11))-x(14)))-x(16));
xdot(15) = (1/Cf1)*(x(16)-x(15))/Rf;
xdot(16) = (1/Cf2)*(x(14)-Po/x(16)-(1/Rf)*(x(16)-x(15)));
dd3 = hi*(Vref-ki*x(17)-x(21))+w*L*x(19)/Vref;
dq3 = hi*(lqref-ki*x(19))-w*L*x(17)/Vref;
xdot(17) = (1/L)*(Vd+w*L*x(19)-dd3*(x(18)+Rc*((dd3*x(17)+dq3*x(19))/2-x(22)-lo)));
xdot(18) = (1/C)*((dd3*x(17)+dq3*x(19))/2-x(22)-lo);
xdot(19) = (1/L)*(Vq-w*L*x(17)-dq3*(x(18)+Rc*((dd3*x(17)+dq3*x(19))/2-x(22)-lo)));
xdot(20) = (x(21)-x(20))*wz;
xdot(21) = -(x(20)+x(21))*wp+ho*(-Vref+kv*(x(18)+Rc*(-lo+(1/2)*(dd3*x(17)+dq3*x(19))-x(22))))*wp;
xdot(22) = (1/Lf)*(x(18)+Rc*(-lo+(1/2)*(dd3*x(17)+dq3*x(19))-x(22)))-x(24));
xdot(23) = (1/Cf1)*(x(24)-x(23))/Rf;
xdot(24) = (1/Cf2)*(x(22)-Po/x(24)-(1/Rf)*(x(24)-x(23)));
dd4 = hi*(Vref-ki*x(25)-x(29))+w*L*x(27)/Vref;
dq4 = hi*(lqref-ki*x(27))-w*L*x(25)/Vref;
xdot(25) = (1/L)*(Vd+w*L*x(27)-dd4*(x(26)+Rc*((dd4*x(25)+dq4*x(27))/2-x(30)-lo)));
xdot(26) = (1/C)*((dd4*x(25)+dq4*x(27))/2-x(30)-lo);
xdot(27) = (1/L)*(Vq-w*L*x(25)-dq4*(x(26)+Rc*((dd4*x(25)+dq4*x(27))/2-x(30)-lo)));
xdot(28) = (x(29)-x(28))*wz;
xdot(29) = -(x(28)+x(29))*wp+ho*(-Vref+kv*(x(26)+Rc*(-lo+(1/2)*(dd4*x(25)+dq4*x(27))-x(30))))*wp;
xdot(30) = (1/Lf)*(x(26)+Rc*(-lo+(1/2)*(dd4*x(25)+dq4*x(27))-x(30)))-x(32));
xdot(31) = (1/Cf1)*(x(32)-x(31))/Rf;
xdot(32) = (1/Cf2)*(x(30)-Po/x(32)-(1/Rf)*(x(32)-x(31)));
dd5 = hi*(Vref-ki*x(33)-x(37))+w*L*x(35)/Vref;
dq5 = hi*(lqref-ki*x(35))-w*L*x(33)/Vref;
xdot(33) = (1/L)*(Vd+w*L*x(35)-dd5*(x(34)+Rc*((dd5*x(33)+dq5*x(35))/2-x(38)-lo)));
xdot(34) = (1/C)*((dd5*x(33)+dq5*x(35))/2-x(38)-lo);
xdot(35) = (1/L)*(Vq-w*L*x(33)-dq5*(x(34)+Rc*((dd5*x(33)+dq5*x(35))/2-x(38)-lo)));
xdot(36) = (x(37)-x(36))*wz;
xdot(37) = -(x(36)+x(37))*wp+ho*(-Vref+kv*(x(34)+Rc*(-lo+(1/2)*(dd5*x(33)+dq5*x(35))-x(38))))*wp;
xdot(38) = (1/Lf)*(x(34)+Rc*(-lo+(1/2)*(dd5*x(33)+dq5*x(35))-x(38)))-x(40));
xdot(39) = (1/Cf1)*(x(40)-x(39))/Rf;
xdot(40) = (1/Cf2)*(x(38)-Po/x(40)-(1/Rf)*(x(40)-x(39)));
dd6 = hi*(Vref-ki*x(41)-x(45))+w*L*x(43)/Vref;
dq6 = hi*(lqref-ki*x(43))-w*L*x(41)/Vref;
xdot(41) = (1/L)*(Vd+w*L*x(43)-dd6*(x(42)+Rc*((dd6*x(41)+dq6*x(43))/2-x(46)-lo)));
xdot(42) = (1/C)*((dd6*x(41)+dq6*x(43))/2-x(46)-lo);
xdot(43) = (1/L)*(Vq-w*L*x(41)-dq6*(x(42)+Rc*((dd6*x(41)+dq6*x(43))/2-x(46)-lo)));
xdot(44) = (x(45)-x(44))*wz;
xdot(45) = -(x(44)+x(45))*wp+ho*(-Vref+kv*(x(42)+Rc*(-lo+(1/2)*(dd6*x(41)+dq6*x(43))-x(46))))*wp;
xdot(46) = (1/Lf)*(x(42)+Rc*(-lo+(1/2)*(dd6*x(41)+dq6*x(43))-x(46)))-x(48));
xdot(47) = (1/Cf1)*(x(48)-x(47))/Rf;
xdot(48) = (1/Cf2)*(x(46)-Po/x(48)-(1/Rf)*(x(48)-x(47)));
dd7 = hi*(Vref-ki*x(49)-x(53))+w*L*x(51)/Vref;
dq7 = hi*(lqref-ki*x(51))-w*L*x(49)/Vref;
xdot(49) = (1/L)*(Vd+w*L*x(51)-dd7*(x(50)+Rc*((dd7*x(49)+dq7*x(51))/2-x(54)-lo)));
xdot(50) = (1/C)*((dd7*x(49)+dq7*x(51))/2-x(54)-lo);
xdot(51) = (1/L)*(Vq-w*L*x(49)-dq7*(x(50)+Rc*((dd7*x(49)+dq7*x(51))/2-x(54)-lo)));
xdot(52) = (x(53)-x(52))*wz;
xdot(53) = -(x(52)+x(53))*wp+ho*(-Vref+kv*(x(50)+Rc*(-lo+(1/2)*(dd7*x(49)+dq7*x(51))-x(54))))*wp;
xdot(54) = (1/Lf)*(x(50)+Rc*(-lo+(1/2)*(dd7*x(49)+dq7*x(51))-x(54)))-x(56));
xdot(55) = (1/Cf1)*(x(56)-x(55))/Rf;
xdot(56) = (1/Cf2)*(x(54)-Po/x(56)-(1/Rf)*(x(56)-x(55)));
dd8 = hi*(Vref-ki*x(57)-x(61))+w*L*x(59)/Vref;
dq8 = hi*(lqref-ki*x(59))-w*L*x(57)/Vref;
xdot(57) = (1/L)*(Vd+w*L*x(59)-dd8*(x(58)+Rc*((dd8*x(57)+dq8*x(59))/2-x(62)-lo)));
xdot(58) = (1/C)*((dd8*x(57)+dq8*x(59))/2-x(62)-lo);
xdot(59) = (1/L)*(Vq-w*L*x(57)-dq8*(x(58)+Rc*((dd8*x(57)+dq8*x(59))/2-x(62)-lo)));
xdot(60) = (x(61)-x(60))*wz;

```

```

xdot(61) = (-x(60)+x(61))*wp+ho*(-Vref+kv*(x(58)+Rc*(-lo+(1/2)*(dd8*x(57)+dq8*x(59))-x(62))))*wp;
xdot(62) = (1/Lf)*(x(58)+Rc*(-lo+(1/2)*(dd8*x(57)+dq8*x(59))-x(62))-x(64));
xdot(63) = (1/Cf1)*(x(64)-x(63))/Rf;
xdot(64) = (1/Cf2)*(x(62)-Po/x(64)-(1/Rf)*(x(64)-x(63)));
dd9 = hi*(Vref-ki*x(65)-x(69))+w*L*x(65)/Vref;
dq9 = hi*(lqref-ki*x(67))-w*L*x(65)/Vref;
xdot(65) = (1/L)*(Vd+w*L*x(67)-dd9*(x(66)+Rc*((dd9*x(65)+dq9*x(67))/2-x(70)-lo)));
xdot(66) = (1/C)*(dd9*x(65)+dq9*x(67))/2-x(70)-lo;
xdot(67) = (1/L)*(Vq-w*L*x(65)-dq9*(x(66)+Rc*((dd9*x(65)+dq9*x(67))/2-x(70)-lo)));
xdot(68) = (x(69)-x(68))*wz;
xdot(69) = (-x(68)+x(69))*wp+ho1*(-Vref+kv*(x(66)+Rc*(-lo+(1/2)*(dd9*x(65)+dq9*x(67))-x(70))))*wp;
xdot(70) = (1/Lf)*(x(66)+Rc*(-lo+(1/2)*(dd9*x(65)+dq9*x(67))-x(70))-x(72));
xdot(71) = (1/Cf1)*(x(72)-x(71))/Rf;
xdot(72) = (1/Cf2)*(x(70)-Po/x(72)-(1/Rf)*(x(72)-x(71)));
function [f] = th_f_of_x(x);
global Vd Vq lo Po w ki kv;
global Vref lqref ho;
global Kdq wp wz L C Rc;
global Vg;
global Lf Cf1 Cf2;
global Rf;
global dx_ds;
f = zeros(8,1);
% Define the state space equations %%
dd1 = hi*(Vref-ki*x(1)-x(5))+w*L*x(3)/Vref;
dq1 = hi*(lqref-ki*x(3))-w*L*x(1)/Vref;
f(1) = (1/L)*(Vd+w*L*x(3)-dd1*(x(2)+Rc*((dd1*x(1)+dq1*x(3))/2-x(6)-lo)));
f(2) = (1/C)*((dd1*x(1)+dq1*x(3))/2-x(6)-lo);
f(3) = (1/L)*(Vq-w*L*x(1)-dq1*(x(2)+Rc*((dd1*x(1)+dq1*x(3))/2-x(6)-lo)));
f(4) = (x(5)-x(4))*wz;
f(5) = (-x(4)+x(5))*wp+ho*(-Vref+kv*(x(2)+Rc*(-lo+(1/2)*(dd1*x(1)+dq1*x(3))-x(6))))*wp;
f(6) = (1/Lf)*(x(2)+Rc*(-lo+(1/2)*(dd1*x(1)+dq1*x(3))-x(6))-x(8));
f(7) = (1/Cf1)*(x(8)-x(7))/Rf;
f(8) = (1/Cf2)*(x(6)-Po/x(8)-(1/Rf)*(x(8)-x(7)));
function [xdot] = th_solve_system_new1(t,x);
global Vd Vq lo Po w ki kv;
global Vref lqref ho;
global Kdq wp wz L C Rc;
global Vg;
global Lf Cf1 Cf2;
global Rf;
global dx_ds;
hi = Kdq;
xdot = zeros(110,1);
% Define the state space equations %%
dd1 = hi*(Vref-ki*x(1)-x(5))+w*L*x(3)/Vref;
dq1 = hi*(lqref-ki*x(3))-w*L*x(1)/Vref;
dec_d = w*L*x(3)/Vref;
dec_q = w*L*x(1)/Vref;
xdot(1) = (1/L)*(Vd+w*L*x(3)-dd1*(x(2)+Rc*((dd1*x(1)+dq1*x(3))/2-x(6)-lo))*x(9);
xdot(2) = (1/C)*((dd1*x(1)+dq1*x(3))/2-x(6)-lo)*x(9);
xdot(3) = (1/L)*(Vq-w*L*x(1)-dq1*(x(2)+Rc*((dd1*x(1)+dq1*x(3))/2-x(6)-lo))*x(9);
xdot(4) = (x(5)-x(4))*wz*x(9);
xdot(5) = (-x(4)+x(5))*wp+x(10)*(-Vref+kv*(x(2)+Rc*(-lo+(1/2)*(dd1*x(1)+dq1*x(3))-x(6))))*wp*x(9);
xdot(6) = (1/Lf)*(x(2)+Rc*(-lo+(1/2)*(dd1*x(1)+dq1*x(3))-x(6))-x(8))*x(9);
xdot(7) = (1/Cf1)*(x(8)-x(7))*x(9)/Rf;
xdot(8) = (1/Cf2)*(x(6)-Po/x(8)-(1/Rf)*(x(8)-x(7))*x(9);
xdot(9) = 0;
xdot(10) = 0;
%% Define the Jacobian matrix %%
Ja11 = (1/L)*((-1/2)*Rc*(-hi*ki*x(1)+dd1-dec_d)*(dd1)+hi*ki*(x(2)+Rc*(-lo+(1/2)*(x(3)*(dq1)+x(1)*(dd1))-x(6))))*x(9);
Ja12 = (1/L)*(-dd1)*x(9);
Ja13 = (1/L)*((w*L*(-1/2)*Rc*(-hi*ki*x(3)+dq1+dec_q)*(dd1)-(1/Vref)*(w*L*(x(2)+Rc*(-lo+(1/2)*(x(3)*(dq1)+x(1)*(dd1))-x(6))))*x(9);
Ja14 = 0;
Ja15 = (1/L)*(((1/2)*hi*Rc*x(1)*(dd1)+hi*(x(2)+Rc*(-lo+(1/2)*(x(3)*(dq1)+x(1)*(dd1))-x(6))))*x(9);
Ja16 = (1/L)*dd1*x(9);
Ja17 = 0;
Ja18 = 0;
Ja19 = (1/L)*(Vd+w*L*x(3)-(dd1)*(x(2)+Rc*(-lo+(1/2)*(x(3)*(dq1)+x(1)*(dd1))-x(6)))));
Ja110 = 0;

```

```

Ja21 = (1/2/C)*((-hi*ki*x(1)+dd1-dec_d)*x(9));
Ja22 = 0;
Ja23 = (1/2/C)*((-hi*ki*x(3)+dq1+dec_q)*x(9));
Ja24 = 0;
Ja25 = (1/2/C)*(-hi*x(1)*x(9));
Ja26 = -x(9)/C;
Ja27 = 0;
Ja28 = 0;
Ja29 = (1/C)*(-lo+(1/2)*(x(3)*(dq1)+x(1)*(dd1))-x(6));
Ja210 = 0;
Ja31 = (1/L)*((-w*L-(1/2)*Rc*(dq1)*(-hi*ki*x(1)+dd1-dec_d)+(1/Vref)*(w*L*(x(2)+Rc*(-lo+(1/2)*(x(3)*(dq1)+x(1)*(dd1))-x(6)))))*x(9));
Ja32 = (1/L)*(dq1*x(9));
Ja33 = (1/L)*((-1/2)*Rc*(dq1)*(-hi*ki*x(3)+dq1+dec_q)+hi*ki*(x(2)+Rc*(-lo+(1/2)*(x(3)*(dq1)+x(1)*(dd1))-x(6))))*x(9);
Ja34 = 0;
Ja35 = (1/2/L)*(hi*Rc*x(1)*(dq1)*x(9));
Ja36 = (1/L)*(Rc*(dq1)*x(9));
Ja37 = 0;
Ja38 = 0;
Ja39 = (1/L)*(Vq-w*L*x(1)-(dq1)*(x(2)+Rc*(-lo+(1/2)*(x(3)*(dq1)+x(1)*(dd1))-x(6)))));
Ja310 = 0;
Ja41 = 0;
Ja42 = 0;
Ja43 = 0;
Ja44 = -wz*x(9);
Ja45 = wz*x(9);
Ja46 = 0;
Ja47 = 0;
Ja48 = 0;
Ja49 = wz*(x(5)-x(4));
Ja410 = 0;
Ja51 = (1/2)*(kv*Rc*wp*(-hi*ki*x(1)+dd1-dec_d)*x(9)*x(10));
Ja52 = kv*wp*x(9)*x(10);
Ja53 = (1/2)*(kv*Rc*wp*(-hi*ki*x(3)+dq1+dec_q)*x(9)*x(10));
Ja54 = wp*x(9);
Ja55 = (-wp-(1/2)*hi*kv*Rc*wp*x(1)*x(10))*x(9);
Ja56 = -kv*Rc*wp*x(9)*x(10);
Ja57 = 0;
Ja58 = 0;
Ja59 = -wp*(x(5)-x(4))+wp*(-Vref+kv*(x(2)+Rc*(-lo+(1/2)*(x(3)*(dq1)+x(1)*(dd1))-x(6))))*x(10);
Ja510 = wp*(-Vref+kv*(x(2)+Rc*(-lo+(1/2)*(x(3)*(dq1)+x(1)*(dd1))-x(6))))*x(9);
Ja61 = (1/2/Lf)*(Rc*(-hi*ki*x(1)+dd1-dec_d)*x(9));
Ja62 = (1/Lf)*x(9);
Ja63 = (1/2/Lf)*(Rc*(-hi*ki*x(3)+dq1+dec_q)*x(9));
Ja64 = 0;
Ja65 = (1/2/Lf)*(-hi*Rc*x(1)*x(9));
Ja66 = (1/Lf)*(-Rc*x(9));
Ja67 = 0;
Ja68 = (1/Lf)*(-x(9));
Ja69 = (1/Lf)*(x(2)+Rc*(-lo+(1/2)*(x(3)*(dq1)+x(1)*(dd1))-x(6))-x(8));
Ja610 = 0;
Ja71 = 0;
Ja72 = 0;
Ja73 = 0;
Ja74 = 0;
Ja75 = 0;
Ja76 = 0;
Ja77 = (1/Rf/Cf1)*(-x(9));
Ja78 = (1/Rf/Cf1)*x(9);
Ja79 = (1/Rf/Cf1)*(x(8)-x(7));
Ja810 = 0;
Ja81 = 0;
Ja82 = 0;
Ja83 = 0;
Ja84 = 0;
Ja85 = 0;
Ja86 = (1/Cf2)*x(9);
Ja87 = (1/Cf2/Rf)*x(9);
Ja88 = (1/Cf2)*((-1/Rf)+(Po/x(8)^2))*x(9);
Ja89 = (1/Cf2)*(x(6)-(Po/x(8))-(1/Rf)*(x(8)-x(7)));
Ja810 = 0;

```

Ja91 = 0;
 Ja92 = 0;
 Ja93 = 0;
 Ja94 = 0;
 Ja95 = 0;
 Ja96 = 0;
 Ja97 = 0;
 Ja98 = 0;
 Ja99 = 0;
 Ja910 = 0;
 Ja101 = 0;
 Ja102 = 0;
 Ja103 = 0;
 Ja104 = 0;
 Ja105 = 0;
 Ja106 = 0;
 Ja107 = 0;
 Ja108 = 0;
 Ja109 = 0;
 Ja1010 = 0;
 Ja =

AIR FORCE OFFICE OF SCIENTIFIC
 RESEARCH (AFOSR)
 NOTICE OF TRANSMITTAL TO DTIC. THIS
 TECHNICAL REPORT HAS BEEN REVIEWED
 AND IS APPROVED FOR PUBLIC RELEASE
 IWA AFR 190-12. DISTRIBUTION IS
 UNLIMITED.
 YONNE MASON
 STINFO PROGRAM MANAGER

[Ja11 Ja12 Ja13 Ja14 Ja15 Ja16 Ja17 Ja18 Ja19 Ja110;
 Ja21 Ja22 Ja23 Ja24 Ja25 Ja26 Ja27 Ja28 Ja29 Ja210;
 Ja31 Ja32 Ja33 Ja34 Ja35 Ja36 Ja37 Ja38 Ja39 Ja310;
 Ja41 Ja42 Ja43 Ja44 Ja45 Ja46 Ja47 Ja48 Ja49 Ja410;
 Ja51 Ja52 Ja53 Ja54 Ja55 Ja56 Ja57 Ja58 Ja59 Ja510;
 Ja61 Ja62 Ja63 Ja64 Ja65 Ja66 Ja67 Ja68 Ja69 Ja610;
 Ja71 Ja72 Ja73 Ja74 Ja75 Ja76 Ja77 Ja78 Ja79 Ja710;
 Ja81 Ja82 Ja83 Ja84 Ja85 Ja86 Ja87 Ja88 Ja89 Ja810;
 0 0 0 0 0 0 0 0 0 0;
 0 0 0 0 0 0 0 0 0 0];

xdot(11:20) = Ja*x(11:20);
 xdot(21:30) = Ja*x(21:30);
 xdot(31:40) = Ja*x(31:40);
 xdot(41:50) = Ja*x(41:50);
 xdot(51:60) = Ja*x(51:60);
 xdot(61:70) = Ja*x(61:70);
 xdot(71:80) = Ja*x(71:80);
 xdot(81:90) = Ja*x(81:90);
 xdot(91:100) = Ja*x(91:100);
 xdot(101:110) = Ja*x(101:110);
 function [xdot] = th_x_s(t,x);
 global dx_ds;

xdot = zeros(9,1);
 xdot(1) = dx_ds(1)*x(1);
 xdot(2) = dx_ds(2)*x(2);
 xdot(3) = dx_ds(3)*x(3);
 xdot(4) = dx_ds(4)*x(4);
 xdot(5) = dx_ds(5)*x(5);
 xdot(6) = dx_ds(6)*x(6);
 xdot(7) = dx_ds(7)*x(7);
 xdot(8) = dx_ds(8)*x(8);
 xdot(9) = dx_ds(9)*x(9);

AFRL-SR-BL-TR-99-

P 1999

0236

REPORT DOCUMENTATION PAGE			OMB No. 0704-0188	
<small>The public reporting burden for this collection of information is estimated to average 1 hour per response, including the time for reviewing instructions, searching existing data sources, gathering and maintaining the data needed, and completing and reviewing the collection of information. Send comments regarding this burden estimate or any other aspect of this collection of information, including suggestions for reducing the burden, to Department of Defense, Washington Headquarters Service, Directorate for Information Operations and Reports (0704-0188), 1215 Jefferson Davis Highway, Suite 1204, Arlington, VA 22202-4302. Respondents should be aware that notwithstanding any other provision of law, no person shall be subject to any penalty for failing to comply with a collection of information if it does not display a currently valid OMB control number.</small>				
PLEASE DO NOT RETURN YOUR FORM TO THE ABOVE ADDRESS.				
1. REPORT DATE (DD-MM-YYYY) 01/09/99		2. REPORT TYPE Final		3. DATES COVERED (From - To) April 1997 - May 1999
4. TITLE AND SUBTITLE Subsystem Integration for Efficient Power Flow in 21st Century Airlifters		5a. CONTRACT NUMBER		
		5b. GRANT NUMBER F49620-97-0254		
		5c. PROGRAM ELEMENT NUMBER		
6. AUTHOR(S) Lindner, Douglas K. Frederick, Catherine Borojevic, Dusan Lu, Gordon..... Chandrasekaran, Sriram Louganski, Konstantin Korba, George		5d. PROJECT NUMBER		
		5e. TASK NUMBER		
		5f. WORK UNIT NUMBER		
7. PERFORMING ORGANIZATION NAME(S) AND ADDRESS(ES) Virginia Polytechnic Institute and State University 657 Whittemore Hall Blacksburg, VA 24061		8. PERFORMING ORGANIZATION REPORT NUMBER		
9. SPONSORING/MONITORING AGENCY NAME(S) AND ADDRESS(ES) Air Force Office of Scientific Research 801 North Randolph Street, Room 732 Arlington, VA 22203-1977		10. SPONSOR/MONITOR'S ACRONYM(S) AFOSR		
		11. SPONSOR/MONITOR'S REPORT NUMBER(S)		
12. DISTRIBUTION/AVAILABILITY STATEMENT Approved for public release, distribution unlimited				
13. SUPPLEMENTARY NOTES				
14. ABSTRACT In this report we are concerned with modeling, simulation and dynamic stability of next generation DC power distribution systems for 21 st century airlifters. These new power distribution systems allow for two way power flow between the generator, power distribution system, and loads (actuators, avionics, environmental control system). This two way power flow implies that all of these subsystems dynamically interact with each other. An extensive simulation block library was developed including models of generators, power converters, filters, and electromechanical and electrohydraulic actuators. A methodology based on bifurcation analysis for investigating the dynamic stability of two nonlinear subsystems is also presented.				
15. SUBJECT TERMS Power distribution systems, power converters, nonlinear stability				
16. SECURITY CLASSIFICATION OF:			17. LIMITATION OF ABSTRACT	18. NUMBER OF PAGES
a. REPORT	b. ABSTRACT	c. THIS PAGE		
UNCLASSIFIED				
19a. NAME OF RESPONSIBLE PERSON H.T. Hurd			19b. TELEPHONE NUMBER (include area code) 540-231-5283	